Properties of Cerium Containing Lead Free Solder

by

Huxiao Xie

A Dissertation Presented in Partial Fulfillment
of the Requirements for the Degree
Doctor of Philosophy

Approved October 2012 by the
Graduate Supervisory Committee:

Nikhilesh Chawla, Chair
Stephen Krause
Kiran Solanki
Kabir Mirpuri

ARIZONA STATE UNIVERSITY

December 2012

ABSTRACT

With increasing concerns of the intrinsic toxicity of lead (Pb) in electronics, a series of tin (Sn) based alloys involving silver (Ag) and copper (Cu) have been proposed as replacements for Pb-Sn solder and widely accepted by industry. However, they have a higher melting point and often exhibit poorer damage tolerance than Pb-Sn alloys. Recently, a new class of alloys with trace amount of rare-earth (RE) elements has been discovered and investigated. In previous work from Prof. Chawla's group, it has been shown that cerium (Ce)-based Pb-free solder are less prone to oxidation and Sn whiskering, and exhibit desirable attributes of microstructural refinement and enhanced ductility relative to lanthanum (La)-based Sn-3.9Ag-0.7Cu (SAC) alloy. Although the formation of $RESn_3$ was believed to be directly responsible for the enhanced ductility in RE-containing SAC solder by allowing microscopic voids to nucleate throughout the solder volume, this cavitation-based mechanism needs to be validated experimentally and numerically. Additionally, since the previous study has exhibited the realistic feasibility of Ce-based SAC lead-free solder alloy as a replacement to conventional SAC alloys, in this study, the proposed objective focuses on the in in-depth understanding of mechanism of enhanced ductility in Ce-based SAC alloy and possible issues associated with integration of this new class of solder into electronic industry, including: (a) study of long-term thermal and mechanical stability on industrial metallization, (b) examine the role of solder volume and wetting behavior of the new solder, relative to Sn-3.9Ag-0.7Cu alloys, (c) conduct experiments of new solder alloys in the form of mechanical

shock and electromigration. The research of this new class alloys will be conducted in industrially relevant conditions, and the results would serve as the first step toward integration of these new, next generation solders into the industry.

ACKNOWLEDGEMENTS

I would like to acknowledge my adviser, Dr. Nikhilesh Chawla, for providing me with the opportunity to conduct this work. Without his constant encouragement and support, I cannot achieve today's accomplishments. I would like to thank the committee members Drs. Stephen Krause, Kiran Solanki and Kabir Mirpuri.

I am grateful for the financial support for this research from the Semiconductor Research Corporation (SRC) under task # 1292.068 (Drs. P. Brofman, A. Aleksov, K. Mirpuri, M. Renavikar, M. Varughese, and K. Zeng, industrial liaisons, and Drs. S. List and J. Candelaria, Program Managers). I gratefully acknowledge the use of facilities within the Center for Solid State Science and Center for Solid State Semiconductor Research at Arizona State University, especially David Wright for his assistance with evacuating the quartz tubes.

I would like to acknowledge Dr. Yu-Lin Shen, who did the Finite Element modeling in chapter 4, and Dr. Ling Jiang, who did the wetting tests in chapter 6. I would like to thank the members of the Mechanical Behavior of Materials Group, especially Dr. Kyle Yazzie, Dustin Friedman and Eric Padilla, for their helps in running the mechanical shock and x-ray tomography tests. Finally, I'd like to give special thanks to my family (my wife, Mom and Dad) for their love and support.

TABLES OF CONTENTS

Page

LIST OF TABLES xii

LIST OF FIGURES xiv

CHAPTERS

1. INTRODUCTION 1

2. REVIEW OF LITERATURE 4

2.1 Thermal Stability of SAC and RE-Containing SAC Solder Alloys on Industrial Metallizations 4

2.1.1 Industrial under-bump metallizations 4

2.1.2 Isothermal aging behavior of Pb-free solders on Cu and Ni-P metallizations 6

2.1.3 Isothermal aging behavior of RE containing Pb-free solders on Cu and Ni-P metallizations 8

2.2 Wetting Behavior of SAC and RE-Containing SAC Solder Alloys 9

2.3 Volume Effect on Microstructural and Mechanical Properties of Pb-Free Solders 10

2.4 Mechanical Shock Behavior of SAC and RE-Containing SAC Solder Joints 13

Page

2.4.1 Testing methods of mechanical shock 13

2.4.2 Mechanical shock behavior of Pb-free solders 14

2.4.3 Effect of solder alloy composition on shock behavior.....................14

2.5 Electromigration Behavior of SAC and RE-Containing SAC Solder Joints..15

2.5.1 Fundamentals of electromigration in solder joints...........................15

2.5.2 Electromigration behavior of RE-Containing SAC solder 16

2.5.3 Characterization techniques used in electromigration studies 17

3. RESEARCH OBJECTIVES AND APPROACH..18

3.1 Mechanism Study of Enhanced Ductility of Ce-Containing SAC Solder 19

3.1.1 Ce-containing SAC solder alloy fabrication 19

3.1.2 Lap-shear joints fabrication 20

3.1.3 Lap-shear and interrupted shear tests..22

3.2 Study of Thermal and Mechanical Stability of Ce-containing Solder on Cu and Ni-P Substrate 22

3.2.1 SAC and SAC-Ce/Ni-P lap-shear joints fabrication 22

3.2.2 Effect of thermal aging on microstructural and mechanical behavior of Ce-containing SAC solder joints.................................23

Page

3.3 Study of physical properties of Ce-containing SAC solder 23

3.3.1 Evaluation of wettability of Ce-containing SAC solder on Cu substrate 23

3.3.2 Characterize the melting and solidification behavior of SAC-Ce solder 24

3.3.3 Volume effect on microstructure refinement in Ce-Containing SAC solder joints 24

3.4 Mechanical Shock Behavior of SAC and Ce-containing SAC Solder Joints 26

3.4.1 Butt solder joint fabrication 26

3.4.2 Mechanical shock testing 28

3.5 Effect of Electromigration on Microstructure Evolution of SAC and SAC-Ce Solder Joints 28

3.5.1 Fabrication of micron-size butt joints for electromigration testing 28

3.5.2 Electromigration testing 29

3.5.3 Characterize microstructural evolution of Ce-containing SAC solder induced by electromigration 31

3.5.4 Characterize current density inside solder joint using finite element method 31

Page

3.6 Effect of Complaint Intermetallic Phases on the Enhanced Ductility of SAC Solder Joints 32

3.6.1 Preparation of Mn and Ca-containing SAC solder alloys...............32

3.6.2 Determine the elastic properties of intermetallic compounds formed in the solder alloys using nanoindentation.........................33

3.6.3 Comparison of shear behavior of Ca and Mn-containing SAC solder joints shear tests 34

4. MECHANISMS OF DEFORMATION IN HIGH-DUCTILITY CE-CONTAINING SN-3.9AG-0.7CU SOLDER ALLOYS 35

4.1 Abstract 35

4.2 Introduction 35

4.3 Materials and Experimental Procedure 37

4.4 Results and Discussion..40

4.4.1 Interrupt shear testing 40

4.4.2 Effect of Cu_6Sn_5 layer thickness on shear behavior of SAC and SAC-Ce joints..46

4.4.3 Finite element analysis...49

4.4.4 Damage evolution for SAC and SAC-0.5Ce solder joints...............57

4.5 Conclusions 57

Page

4.6 References 59

5. THERMAL AND MECHANICAL STABILITY OF CE-CONTAINING SN-3.9AG-0.7CU LEAD-FREE SOLDER ON CU AND ELECTROLESS NI-P METALLIZATIONS.....................................63

5.1 Abstract 63

5.2 Introduction 63

5.3 Materials and Experimental Procedure 65

5.4 Results and Discussion..67

5.4.1 Microstructural characterization of as-reflowed solder joints 67

5.4.2 Microstructural evolution of solder joints after thermal aging 76

5.4.3 Mechanical evolution of solder joint after thermal aging 80

5.5 Conclusions 86

5.6 Reference..87

6. EFFECT OF CERIUM ADDITION ON WETTING, UNDERCOOLING AND VOLUME EFFECT OF SN-3.9AG-0.7CU LEAD-FREE SOLDER..90

6.1 Abstract 90

6.2 Introduction 90

6.3 Materials and Experimental Procedure 92

Page

6.4 Results and Discussion 94

6.4.1 Wetting behavior of Sn-3.9Ag-0.7Cu and Sn-3.9Ag-0.7Cu-0.5Ce alloys 94

6.4.2 Differential scanning calorimetry 98

6.4.3 Solder volume effect on microstructural refinement in Sn-3.9Ag-0.7Cu and Sn-3.9Ag-0.7Cu-0.5Ce/Cu joints 103

6.5 Conclusions 109

6.6 References: 109

7. MECHANICAL SHOCK BEHAVIOR OF SN-3.9AG-0.7CU AND SN-3.9AG-0.7CU-0.5CE SOLDER JOINTS 112

7.1 Abstract 112

7.2 Introduction 112

7.3 Materials and Experimental Procedure 114

7.4 Results and Discussion 118

7.4.1 Microstructure characterization 118

7.4.2 Mechanical tensile behavior of Sn-3.9Ag-0.7Cu and Sn-3.9Ag-0.7Cu solder joints 121

7.4.3 Fractographic analysis 124

7.5 Conclusions 129

Page

7.6 References 131

8. ELECTROMIGRATION BEHAVIOR OF SN-3.9AG-0.8CU AND SN-3.9AG-0.8CU-0.5CE LEAD-FREE SOLDER JOINTS 134

8.1 Abstract 134

8.2 Introduction 134

8.3 Materials and Experimental Procedure 136

8.4 Results and Discussion...139

8.4.1 Finite Element Modeling results 139

8.4.2 Microstructural evolution of Sn-3.9Ag-0.7Cu and Sn-3.9Ag-0.7Cu-0.5Ce during electromigration...142

8.4.3 Electromigration behavior of Sn-3.9Ag-0.7Cu and Sn-3.9Ag-0.7Cu-0.5Ce solders 151

8.5 Conclusions 156

8.6 References 157

9. ENHANCING THE DUCTILITY OF SN-AG-CU LEAD-FREE SOLDER JOINTS BY ADDITION OF COMPLIANT INTERMETALLICS...160

9.1 Abstract 160

9.2 Introduction 160

Page

9.3 Materials and Experimental Procedure 162

9.4 Results and Discussion 166

9.4.1 Microstructural characterization 166

9.4.2 Nanoindentation 173

9.4.3 Mechanical shear behavior of Ca and Mn-containing Sn-3.9Ag-0.7Cu solder joints 182

9.5 Conclusions 187

9.6 Reference 187

10. CONCLUDING REMARKS 190

10.1 Summary of Research Findings 190

10.2 Recommendations 192

REFERENCES 195

LIST OF TABLES

Table Page

1. Summary of shear behavior of SAC and SAC-Ce solder joints. 42

2. Summary of monotonic shear test of Sn-3.9Ag-0.7Cu and Sn-3.9Ag-0.7Cu-0.5Ce solder joints. 47

3. Summary of microstructure characterization results for as-reflowed and thermal-aged Sn-3.9Ag-0.7Cu and Sn-3.9Ag-0.7Cu-0.5Ce/Cu and Ni-P joints. 72

4. Composition of $(Cu,Ni)_6Sn_5$ layer in as-reflowed and thermal-aged Sn-3.9Ag-0.7Cu and Sn-3.9Ag-0.7Cu-0.5Ce/Ni-P joints.........................75

5. Monotonic shear results for as-reflowed and thermal-aged Sn-3.9Ag-0.7Cu and Sn-3.9Ag-0.7Cu-0.5Ce/Cu joints. 82

6. Monotonic shear results for as-reflowed and thermal-aged Sn-3.9Ag-0.7Cu and Sn-3.9Ag-0.7Cu-0.5Ce/Ni-P joints. 86

7. The DSC results for Sn-3.9Ag-0.7Cu and Sn-3.9Ag-0.7Cu-0.5Ce solders. 103

8. Microstructure characterization comparison of Sn-3.9Ag-0.7Cu and Sn-3.9Ag-0.7Cu-0.5Ce solder joints with different thicknesses.......107

9. Summary of microstructure characterization results for as-reflowed and thermal-aged Sn-3.9Ag-0.7Cu and Sn-3.9Ag-0.7Cu-0.5Ce solder joints. 121

10. Dynamic tensile results for Sn-3.9Ag-0.7Cu and Sn-3.9Ag-0.7Cu-0.5Ce solder joints. 124

Table Page

11. EDS analysis of Mn-Sn and Ca-Sn intermetallic phases in as-processed alloys. 167

12. Summary of microstructure characterization for as-processed solder alloys. 170

13. Summary of microstructure characterization results for reflowed solder joints. 172

14. Young's moduli and hardness of intermetallics in Pb-free solder and pure Sn. 177

15. Monotonic shear results for Sn-3.9Ag-0.7Cu and Sn-3.9Ag-0.7Cu-0.5Ca and Mn. 185

LIST OF FIGURES

Figure Page

1. Schematic diagram of the spread area test. 11

2. Schematic of Cu jig used for assembling lap-shear solder joint 21

3. Diagram of an apparatus for measuring wettability of solders on Cu substrate. 25

4. Schematic of solder sandwich and Al holder. 27

5. Procedure of processing silicon V-groove using photolithography and KOH etching techniques. 30

6. Reflow profile for lap shear specimens. The input profile is shown in black, while the actual temperature profile is shown in red. 39

7. Typical shear stress-shear strain curves and fracture surfaces after monotonic shear testing: (a) SAC and (b) SAC-0.5Ce solder joints. The SAC-0.5Ce joints exhibit higher ductility. Fracture of SAC occurs very close to the Cu_6Sn_5/solder interface. 41

8. Optical microscopy images of interrupted shear testing of Sn-3.9Ag-0.7Cu and Sn-3.9Ag-0.7Cu-0.5Ce at different strain values (Arrows indicating shear direction of joints). The SAC-Ce allow shows homogeneous strain distribution while SAC fails bey strain localization close to the copper/solder interface. 44

9. Scanning electron microscopy images of interrupted shear test of $CeSn_3$ intermetallic particles in Sn-3.9Ag-0.7Cu-0.5Ce solder joints. Note plasticity around the particles, debonding, and fracture.........45

Figure Page

10. Backscatter electronic microscopy images for Cu_6Sn_5 intermetallic layer of Sn-3.9Ag-0.7Cu solders with different dwell time......................48

11. Shear stress vs. shear strain curves of Sn-3.9Ag-0.7Cu and Sn-3.9Ag-0.7Cu-0.5Ce solder joints reflowed with different dwell time. 50

12. Schematic of the solder joint model, along with the loading and boundary conditions, used in the lap-shear modeling...............................52

13. Contour plots of equivalent plastic strain in the solder containing $LaSn_3$ intermetallic particles with area fractions of (a) 0, (b) 5% and (c) 8%, when the applied nominal shear strain is at 0.08...................54

14. (a) Area fractions of the solder matrix having equivalent plastic strain greater than 0.15 (the red color regions in Fig. 13) in the three models. (b) The average equivalent plastic strain values within the same solder matrix regions in (a)..56

15. Damage accumulation schematic for Sn-3.9Ag-0.7Cu and Sn-3.9Ag-0.7Cu-0.5Ce solder joints. 58

16. Optical microscopy images of as-reflowed Sn-3.9Ag-0.7Cu (top raw) and Sn-3.9Ag-0.7Cu-0.5Ce (bottom raw). 69

17. Backscatter electron microscopy images of as-reflowed Sn-3.9Ag-0.7Cu and Sn-3.9Ag-0.7Cu-0.5Ce on Cu substrate.................................71

Figure Page

18. Backscattered electron microscopy images of as-reflowed Sn-3.9Ag-0.7Cu and Sn-3.9Ag-0.7Cu-0.5Ce reflowed on electroless Ni-P substrate. 74

19. Optical microscopy images of thermal aged Sn-3.9Ag-0.7Cu (left column) and Sn-3.9Ag-0.7Cu-0.5Ce (right column) reflowed on Cu (top row) and electroless Ni-P substrate (bottom row). 77

20. Backscattered electron microscopy images of aged Sn-3.9Ag-0.7Cu (left column) and Sn-3.9Ag-0.7Cu-0.5Ce (right column) on Cu (top row) and electroless Ni-P (bottom row). 78

21. Backscattered electron microscopy images of $CeSn_3$ intermetallic particle formed in as-reflowed (left column) and aged (right column) and Sn-3.9Ag-0.7Cu-0.5Ce on Cu (top row) and electroless Ni-P (bottom row). 81

22. Shear-stress-vs-shear-strain curve for as-reflowed and thermal aged Sn-3.9Ag-0.7Cu and Sn-3.9Ag-0.7Cu-0.5Ce/Cu joints tested in monotonic shear. 84

23. Shear-stress-vs-shear-strain curve for as-reflowed and thermal aged Sn-3.9Ag-0.7Cu and Sn-3.9Ag-0.7Cu-0.5Ce/Ni-P joints tested in monotonic shear 85

24. Typical optical image of molten solder on Cu substrate for contact angle measurement. Note receding contact angle due to Marangoni flow. 95

Figure Page

25. Schematic of measuring wetting angle of molten solder on Cu substrate based on optical images. 97

26. Wetting behavior of solder on Cu substrate as function of dwell time above solder melting point. 99

27. Quantitative measurement of contact angle and spreading area ratio of Sn-3.9Ag-0.7Cu and Sn-3.9Ag-0.7Cu-0.5Ce solder reflowed on Cu substrate. 100

28. The DSC thermograms for Sn-3.9Ag-0.7Cu (red) and Sn-3.9Ag-0.7Cu-0.5Ce (blue). 102

29. Optical images of Sn-3.9Ag-0.7Cu (top row) and Sn-3.9Ag-0.7Cu-0.5Ce (bottom row) solder joints with different solder thicknesses: 0.2 mm, 0.5 mm, 0.75 mm and 1.00 mm. 105

30. Backscattered electron microscopy images of Sn-3.9Ag-0.7Cu (left column) and Sn-3.9Ag-0.7Cu-0.5Ce (right column) joints with different solder thicknesses: 0.2 mm, 0.5 mm, 0.75 mm, 1.0 mm. 108

31. Schematic showing how dynamic solder joint strength is controlled by bulk solder strength at lower strain rate and by strength of interfacial intermetallic layer at higher strain rates 115

32. As-processed optical images of left: Sn-3.9Ag-0.7Cu and Right: Sn-3.9Ag-0.7Cu-0.5Ce solder joints 119

33. Backscatter electron microscopy images of as-reflowed Sn-3.9Ag-0.7Cu (left) and Sn-3.9Ag-0.7Cu-0.5Ce (right) solder joints 120

Figure Page

34. Tensile stress vs. strain curve for Sn-3.9Ag-0.7Cu and Sn-3.9Ag-0.7Cu-0.5Ce/Cu solder joints tested at different strain rate (from 10^{-3} to 12 s^{-1}) 123

35. Tensile fracture morphology of Sn-3.9Ag-0.7Cu (top row) and Sn-3.9Ag-0.7Cu-0.5Ce (bottom row) solder joints at different strain rates. 126

36. Ultimate tensile strength and strain-to-failure of Sn-Ag-Cu and Sn-Ag-Cu-0.5Ce solder joints, plotted as a function of strain rates. The fracture schematics for Sn-Ag-Cu and Sn-Ag-Cu-0.5Ce solder joints are shown at top and bottom, respectively. 130

37. Image of butt solder/Cu joint showing direction of virtual cross-sectioning. 2D virtual cross-section data is also shown, along with segmented gray scale image and 3D reconstructed structure of solder joint 140

38. Finite element modeling results of current density inside Sn-3.9Ag-0.7Cu solder (a) with porosity; (b) without porosity 144

39. Backscatter electron microscopy images of cross-section of Sn-3.9Ag-0.7Cu/Cu solder joint after current stressing for: (a) 0 hour; (b) 48 hours; and (c) 96 hours. 146

40. Backscatter electron microscopy images of the cross-section of Cu/Sn-3.9Ag-0.7Cu-0.5Ce/Cu butt joints after current stressing at current 10 A and 100 °C for: 0 hour and 300 hours. 147

Figure Page

41. Backscatter electron microscopy images of central region of Sn-3.9Ag-0.7Cu and Sn-3.9Ag-0.7Cu-0.5Ce joints after current stress for 200 hours (Arrow indicating current direction). 149

42. Backscatter electron microscopy images of anode side of Cu/Sn-3.9Ag-0.7Cu-0.5Ce/Cu butt joints after current stressing for 100 hours..150

43. Sn-3.9Ag-0.7Cu void growth over time, showing 3-D rendering (top) and cathode void top view (bottom)...154

44. Sn-3.9Ag-0.7Cu-0.5Ce void growth over time, showing 3-D rendering (top) and cathode void top view (bottom). 155

45. As-processed optical images of left: Sn-3.9Ag-0.7Cu-0.5Mn and Right: Sn-3.9Ag-0.7Cu-0.5Ca, and EDS spots scan results on intermetallic phases...168

46. As-processed optical images of left: furnace cooled Sn-3.9Ag-0.7Cu-2Mn and Right: furnace cooled Sn-3.9Ag-0.7Cu-2Ca. 169

47. SEM image of cross-section of as-polished Ca-Sn intermetallic and EDS line scan results for partially oxidized Ca-Sn intermetallic alone the yellow arrow. Note that SEM image is viewed in a tilted angle (θ = 52°). 171

48. As-reflow optical images of left: Sn-3.9Ag-0.7Cu-0.5Mn and Right: Sn-3.9Ag-0.7Cu-0.5Ca solder joints..174

Figure Page

49. SEM images of the Cu substrate/solder interface in reflowed joints for Sn-3.9Ag-0.7Cu-0.5Mn (left) and Sn-3.9Ag-0.7Cu-0.5Ca (right). 176

50. Representative load vs. displacement curves for pure Sn, $MnSn_2$ and $CaSn_3$, indented to a depth up to 1500 nm. Note large variation in maximum load for each phase. 178

51. Nanoindentaion behavior of pure Sn, $CaSn_3$ and $MnSn_2$ intermetallics, (a) left: Young's modulus-displacement curve and (b) right: hardness-displacement curve. Young's modulus and hardness value were averaged from the plateau between 300-600 nm for Sn and $MnSn_2$, 800-1200 nm for $CaSn_3$....................180

52. Scanning electron micrographs of indentations in (a) pure Sn, (b) $CaSn_3$ and (c) $MnSn_2$ intermetallics. Pile-up can be seen around the indentation edge in pure Sn. Sn whisker can be seen in $CaSn_3$, while cracks present around the indent in $MnSn_2$....................183

53. Ultimate shear strength and strain to failure of solder joints, plotted as a function of Young's modulus of intermetallics. Increase in Young's modulus of intermetallics increase the USS but reduce the strain to failure of solder joints. 185

1. INTRODUCTION

Solder is an interconnection material that has been used in electronic packaging industry for several decades. Tin (Sn) based solder alloys are the most common choice for all proposed solder candidates due to the alloy's great wetting charactistics and tendency for the formation of bonding intermetallic compounds with copper, nickel and other metallizations that used in electronic industry, in addition to commanding a relatively low cost [1]. Before the potential hazards to the environment and human health of lead's (Pb) containing products were fully realized and had become a wide spread concern, the Pb-Sn eutectic alloy was one of the most successful eutectic solder alloys used by mankind from ancient times (due to its ease in terms of processabiliy) [2]. Although Pb can reduce the melting point of Sn when used as an alloying element and improve physical properties without affecting the solder chemistry, legislations have been pursued most heavily in the European countries and even worldwide during the last 15 years to eliminate lead in electronics. Up to now, and with increased attention in recent years, a series of Sn base alloys involving silver (Ag) and copper (Cu) have been widely accepted as replacements for Sn-Pb solder [3, 4]. However, there is a significant marked decrease in the performance of the Sn-Ag-Cu (SAC) alloy, compared to the Pb-Sn alloy. Most notably, the higher melting temperature, higher undercooling required for solidification, and of particular interest, a low ductility, yielding consequently poor mechanical shock resistance [5, 6].

Recently, rare earth (RE) doped Pb-free solder alloys have gained significant attention from worldwide researchers due to their superior physical

and mechanical properties [7-10]. Previous investigations have shown that adding RE elements can refine the microstructure of Pb-free solders [11-14], yield refined intermetallic particles [15-18], reduce the melting temperature [19, 20], decrease the thickness of the Cu_6Sn_5 layer that forms at the Cu substrate and solder interface [21], and improved wetting behavior [14, 20, 22], improved electromigration resistance [23] and superior mechanical performance [12-14, 24, 25] when the RE content is less than 0.5 wt pct. In particular, enhanced mechanical properties, such as tensile strength [12, 14], ductility [24, 25] and creep resistance [17, 24] of RE-containing solders have been reported.

In the previous work of Chawla and others have shown that Pb-free solder alloys with small amounts of La [26] and Ce [10] elements possess refined microstructure, reduced Cu_6Sn_5 intermetallic compound layer thickness, and significantly increased ductility of solder joints compared to the SAC solder alloy. Most importantly, Ce-based alloys are less prone to oxidation [27] but still exhibit the desirable attributes of microstructural refinement and increased strain-to-failure relative to SAC solder alloy. Such enhanced ductility has profound implications for improving the mechanical shock resistance of SAC solder joints. This is by far one of the most important properties for a solder to possess for the suitable performance of devices, which experience vibrations, bumping and even dropping in real deployment. This property is an important topic of particular interest which must be further investigated using mechanical shock behavior studies.

The proposed mechanism of the enhanced ductility in RE-containing SAC solder joint is based on observations of the fracture surface [21] showing according to which voids nucleate at the $RESn_3$ intermetallic particles. However, the mechanisms of this cavitation must to be validated both experimentally and with numerical simulations based on suitable models.

In previous studies at the realistic feasibility of Ce-based SAC Pb-free solder alloy as a replacement to conventional SAC alloys has been demonstrated. However, a survey of the literature shows that there is a lack of fundamental understanding on the thermal stability, physical properties and reliability of Ce-containing lead-free alloy, including isothermal and mechanical stability, wettability, the volume effect on microstructural refinement and reliability issues in the form of mechanical shock and electromigration tolerance of Ce-containing SAC alloy. This dissertation focuses on the possible issues associated with the integration of this novel class of solder alloy into the electronic industry and will contribute to the ever increasing body of knowledge under the banner of Pb-free solders, which is of pressing importance to improve the health of our world.

2. REVIEW OF LITERATURE

In recent years, a series of eutectic and near-eutectic Sn-Ag-Cu (SAC) alloys have been proposed as acceptable replacements for the Pb-Sn solder by industry and are considered to be one of the most successful lead-free solder alloy systems [3, 28-32]. The primary reason of that this alloy of ternary composition rather than binary composition is due to the realization of the lowest observed melting point for this material system [3], as well as superior mechanical performance including improved creep and fatigue resistance [33, 34]. However, the excessive addition of Cu and Ag often results in the formation of rigid large Ag_3Sn plates and Cu_6Sn_5 bricks, which may cause mechanical degradation of, solder joints [35, 36]. This literature review mainly focuses on the observed microstructures and properties of SAC and SAC alloyed with a fourth element to investigate potentially improved performance.

2.1 Thermal Stability of SAC and RE-Containing SAC Solder Alloys on Industrial Metallizations

2.1.1 Industrial under-bump metallizations

The metallic substrate is an essential component of flip-chip technology, which must be able to provide an excellent solderable surface to form a good metallurgical bond. During the reflow process, molten Sn reacts with a Cu substrate and forms a nodular Cu_6Sn_5 intermetallic (IMC) layer at the interface of the solder and Cu substrate [37]. During thermal aging, this brittle Cu_6Sn_5 IMC layer grows and an additional Cu_3Sn interfacial IMC layer can form between the Cu_6Sn_5 IMC layer and the Cu substrate [33]. The rapid formation of the IMC

layer and the consequent consumption of Cu metallization is due to fast diffusion of Cu within the molten solder as well as in solid-state solder, which has tremendous repercussions on the mechanical and electromigration behavior of the ensuing solder joint.

To minimize the rapid IMC layer growth in Cu under-bump metallization (UBM), an alternative Ni-based UBM has been widely used in industry as a diffusion barrier against the Cu atoms. Amoung the Ni-based UBM, electroless nickel-phosphorus (Ni-P) with an immersion Au layer is considered as a promising UBM because of its low cost compared to vacuum deposited Ni and electroplated Ni, and its exceptional mechanical properties. The thin Au layer serves as a wetting and oxidation protection layer [38]. The interfacial reactions between Ni-P and lead-free solders have been widely studied [39-50]. During the reflow process, the Au layer is completely dissolved in the solder and forms $AuSn_4$ or $(Au,Ni)Sn_4$ IMC particles [39-41]. A thin P-rich Ni-P layer is formed between IMC layer and original Ni-P layer as a result of the diffusion of Ni. Since the composition and morphology of the interfacial intermetallic depends on the solder composition in the Pb-free solder. Without Cu, a thin needle-shaped Ni_3Sn_4 layer is formed at the Ni-P/solder interface during reflow. However, the IMC layer formed with the Cu-containing solder is very complicated as there is a ternary reaction between Ni, Cu and Sn at the interface. Different results in terms of IMC phase have been reported in numerous previous studies, such as $Ni_4Cu_7Sn_6$, $(Ni,Cu)_3Sn_4$, $(Cu,Ni)_6Sn_5$ and $Cu_{26}Ni_{26}Sn_{47}$ [42-46]. Researchers have shown that the IMCs formed at the interface is dependent on the Cu concentration

in the solder alloy [47]. Zeng et al. [45] observed that $(Cu,Ni)_6Sn_5$ and $(Ni,Cu)_3Sn_4$ were formed above and below 0.6 at.% Cu in the solder, respectively. Yu et al. [48] reported that when the concentration of Cu is between 0.3 wt.% and 0.7 wt.%, the IMC layer becomes a discontinuous $(Cu,Ni)_6Sn_5$ layer forming over a continuous $(Ni,Cu)_3Sn_4$ layer. Jeon et al. [49] and Alam et al. [50] suggested that $(Cu,Ni)_6Sn_5$ is the most stable phase, and $(Ni,Cu)_3Sn_4$ was formed when the Cu inside solder was completely consumed. They found that the morphology of $(Cu,Ni)_6Sn_5$ is faceted while $(Ni,Cu)_3Sn_4$ is needlelike.

2.1.2 Isothermal aging behavior of Pb-free solders on Cu and Ni-P metallizations

Isothermal aging has been widely used as a successful method to study long-term thermal and mechanical stability of solder joints. Isothermal aging test conditions vary from room temperature to 200°C with up to 2000 hours of aging [51-54]. During solid-state aging under elevated temperature, microstructural evolutions such as solder matrix coarsening [52, 55, 56], growth of Cu_6Sn_5 and Cu_3Sn intermetallic layers at the solder/Cu interface [55, 57, 58] and consequently Kirkendall voids growth [59, 60] will all be accelerated. Although only a few studies have been conducted on interfacial reactions between electroless Ni UBM and SAC alloy during aging, it was found that the IMC growth on the Ni UBM is effectively minimized when the temperature is low [61, 62]. The growth of IMC layer and composition change in IMC layer are almost negligible, when the aging temperature is lower than 125°C [61,62,47]. After the consumption of Cu is completed inside solder with extended annealing, a continuous $(Ni,Cu)_3Sn_4$ IMC

is formed between $(Cu,Ni)_6Sn_5$ IMC layer and Ni-P layer [42, 49, 62, 63]. As a by-product of Ni diffusion from the Ni-P to IMC/Ni-P interface, a thick P-rich Ni-P (Ni_3P) layer with Kirkendall voids is observed after reflow and annealing [47, 64], which may potentially deteriorate the mechanical performance of Pb-free solder joints.

As a result of the coarsening of SAC's microstructure due to thermal aging, properties like the hardness of the solder matrix [53, 65-67], tensile strength [52], stiffness [51], yield stress, and creep resistance [56] decrease while elongation [68] increases. However, the growth of the interfacial intermetallic layer complicates the effect of aging on the mechanical behavior of solder joints. Deng et al. [53] showed that in quasi-static shear testing, the decrease in shear strength is controlled by solder coarsening instead of intermetallic growth. However, for high strain rate tests (drop test, ball shear/pull test), it was found that mechanical behavior of solder joint is controlled by IMC layer thickness [59], rather than the bulk of the solder joint as in quasi-static testing. Dutta et al. [56] suggested that the effect of aging on dynamic fracture toughness depends on the loading angles, and softening is associated with coarsening which enhances toughness in mode I. Ou et al. [69] also observed increase in impact toughness with increase in aging time. Additionally, it was found that Kirkendall voids formed during the reflow process and during aging may reduce the strength of solder joint and degrade drop test performance significantly [70, 71]. Amgai et al. [72] and Anderson et al. [60] reported that by adding a suitable 4th element (Ni,

Co and Fe) to the SAC alloy, the formation and growth of Kirkendall voids was retarded, and drop test performance was consequently improved.

2.1.3 Isothermal aging behavior of RE containing Pb-free solders on Cu and Ni-P metallizations

Due to the reactive nature of RE elements with oxygen [27], the mechanical properties of RE containing solders are degraded even at room temperature by RE oxidation and Sn whiskering. Thus, it is critical to understand long-term microstructural and mechanical reliability of RE containing solder during isothermal aging. It was shown that the IMC layer growth is inhibited as a result of higher activation energy of the IMC layer in RE containing solder [73] because of the aggregation of RE at the interface between solder and Cu_6Sn_5 interfacial layer, and lower activity of Sn in RE containing solder [20, 74, 75]. However, this is not sufficient to explain the retarded growth rate of the Cu_3Sn IMC layer observed during annealing. Pei et al. [76] systematically studied the effect of La on the microstructural evolution during thermal aging and proved that Sn grain size remains stable and coarsening rate of IMC particles is reduced with additional La content. A similar effect on coarsening rate of IMC particles was also observed by Hao et al. [75]. It has also been reported that the addition of RE elements did not alter the composition of the interfacial IMC layer formed on the Ni-P substrate but did in fact reduce thickness of IMC layer [8, 77].

Only a limited number of reports focusing on mechanical behavior evolution of RE containing lead-free solders during isothermal aging have been published. Li et al. [78] showed that although the shear strength of the as-

reflowed SAC-RE solder joints is lower than that of SAC joints, the deterioration rate of shear strength in SAC solder joints is suppressed with addition of RE elements. A series of studies [8] on aging behavior of RE containing SnAg and SnCu solder joints on Ni metallization showed that RE containing solder joints have higher shear strength than joints without RE elements for all aging times.

2.2 Wetting Behavior of SAC and RE-Containing SAC Solder Alloys

To obtain successful soldering, a certain degree of wetting of molten solder on the metallization is required. Thus, wetting behavior of RE containing solders has been intensively studied and compared with conventional lead-free solder. There are two common tests to evaluate wettability of novel solders based on a review of the relevant literature: spread area test and wetting balance test [79-87]. Only spread area test is utilized for determining the wettability of Ce-containing solder in this thesis and described here in detail, due to its ease in terms of accessibility.

In spread area test [8], a solder disc is brought to melt and spread over the substrate with flux applied first in between. The ability of the molten solder to wet the substrate is measured by determining the ratio of the as-bonded contact area to the original contact area and the contact angle between substrate and liquid solder. The relationship between contact angle θ, and the surface energies between liquid-vapor γ_{lv}, solid-vapor γ_{sv} and liquid-solid γ_{ls}, is given by Young's equation as follows:

$$\cos\theta_c = \frac{\gamma_{SV} - \gamma_{SL}}{\gamma_{LV}}$$

A good wetting behavior should have a small contacting angle and large spreading ratio. As shown in Fig. 1, a contact angle θ of 0° indicates a complete wetting, while 180° indicates no wetting at all.

Spreading area studies on RE containing lead-free solder showed that the addition of RE alloying elements can enhance the wetting behavior of the solder alloy when the RE addition is low, because the high activity of RE elements can significantly decrease surface tension [14, 15, 24, 25, 81, 82]. However, with increasing content of RE, the spreading area decreases due to the formation of RE oxides during soldering. The suggested optimal RE concentration based on wetting behavior is no more than 1.0 wt.% [24]. Wang et al. [83] observed a minimum contact angle and maximum spread area with 0.5 wt.% RE addition in SnAg solder. A similar trend was also found in wetting balance tests on RE containing lead-free solder by measuring wetting force [12, 84-87].

2.3 Volume Effect on Microstructural and Mechanical Properties of Pb-Free Solders

Due to the increasing functions in smaller electronic devices, both through-hole and ball grid array (BGA) pad pitch decrease with time. The International Technology Roadmap for Semiconductors indicates that the I/O pitch size will decrease down to 20 μm [88]. Additionally, electronic components vary in their sizes, from plastic quad flat pack to BGA and flip-chip, which results in a different microstructural and mechanical behavior. Studies on solidification behavior on solder joint with different size showed that by reducing the size of the solder sphere, both the cooling rate and the degree of undercooling for

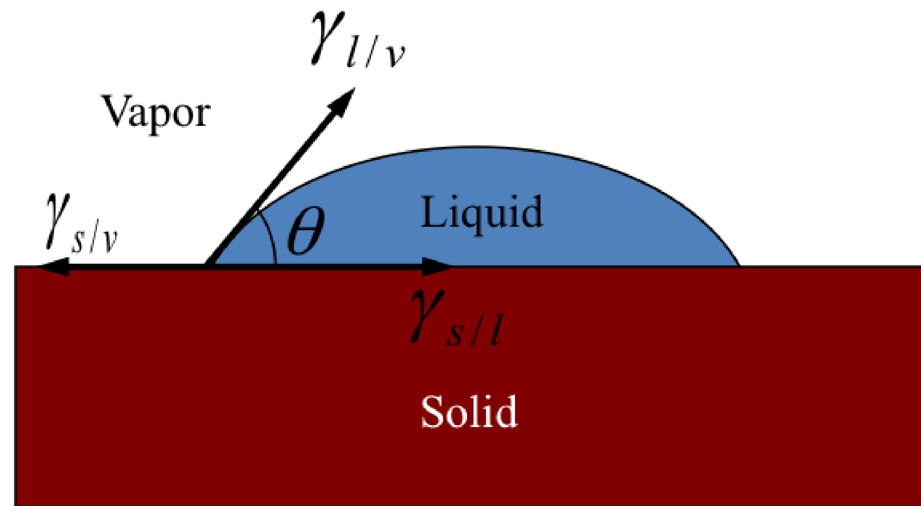

Figure 1. Schematic diagram of the spread area test.

solidification increased significantly, which resulted in a refinement of microstructure [89, 90]. Decreasing volume of solder joints lead to finer microstructure [89], the formation of large Ag_3Sn plates [91], slower metallization consumption rate and thicker IMC interfacial layer [92], as reported in previous investigations.

It is also well known that mechanical properties obtained from bulk solder are incapable of estimating the mechanical behavior when the size of solder is less than 100 μm due to the volume effect [93, 94]. In a typical solder joint, solders are highly constrained by a stiff metallization (i.e. Cu) and the plasticity of the solder is thus restricted. The effect of dimensional constraints on the tensile strength of solder joints has been investigated experimentally [95, 96] and numerically [97]. The ultimate tensile strength and yield strength increase with decreasing gap size owing to increasing mechanical constraint. Decrease in the thickness of the solder joint also leads to brittle fracture at the IMC/solder interface, resulting in a decrease in fracture strain. Systematically experiments and modeling studies conducted by Chawla et al. [98, 99] on lap-shear joints showed that the difference between applied shear strain and the actual solder strain increases with a decrease in solder gap thickness, and thicker joints would generate more accurate results (closer to true shear response). The volume effect on ultimate shear strength is similar to that on tensile strength because shear strength increased with a decrease of solder volume [100].

Very few studies have been carried out on investigating the influence of solder composition on the volume effect. Mueller et al. [89] showed that in

SnAgCu-Ni solder, Sn grains maintain stable size with decrease in solder ball size, indicating that the volume effect can be suppressed with a trace amount addition of Ni. However, a thorough study on the volume effect of RE-containing SnAgCu solder joints is to our knowledge non-existent.

2.4 Mechanical Shock Behavior of SAC and RE-Containing SAC Solder Joints

2.4.1 Testing methods of mechanical shock

Mechanical shock resistance of solder joint has been considered as critical reliability issue to the portable electronic devices. Mechanical shock occurrs when electronic devices are dropped during manufacturing or usage, which leading to complete failure of the total electronic package due to fracture of critical components including solder joints. Typically, the range of strain rate that solders experience during mechanical shock or drop is approximately 10^{-1} to 10^{2} s^{-1} [101]. Drop testing, single solder ball pull and shear tests have been used in the industry to provide qualitative results for quality control. A major disadvantage of these methods is that non-uniform strain experienced by solder joints cannot be measured [102-104]. Miniature impact tests are used to quantify the impact energy of solder [105], however, the major drawback of impact tests is that the total fracture energy can not be easily separated from the fracture energy of the solder joint [106]. Compared to the previously mentioned methods, screw-driven and servohydraulic methods are particularly useful for studying mechanical shock of solders due to well controlled strain rates and loads during shock tests [107].

2.4.2 Mechanical shock behavior of Pb-free solders

Generally, with increasing strain rates from the quasi-static (10^{-3} s^{-1}) region to the dynamic (200 s^{-1}) region, the ultimate tensile strength of solder joint increases significantly because of strain hardening [107]. Studies on the effect of microstructure showed a strong correlation between microstructure and shock performance. It was witnessed that thicker IMC layers induced by aging or processing parameters decreased shock resistance owing to the changes in the intermetallic layer morphology [108, 109]. Suh et al. suggested that Ag content plays an important role in drop performance, because increase in Ag content increases the strength of bulk solder and therefore increase the probalility of IMC layer fracture [110]. Chong et al. [111] and Chin et al. [112] stated that the formation of brittle $(Ni,Cu)_3Sn_4$ IMC layer between Ni-P and solder hindered the drop performance. Huang et al. [113] studied the effect of microstructure and loading condition on shock performance of SAC solder joints by measuring mixed-mode fracture toughness. They found out that fracture toughness decreases with the increase in mode-mixity, fine microstructure and IMC layer thickness.

2.4.3 Effect of solder alloy composition on shock behavior

Although a very few researchers have studied shock performance of RE-containing SAC solder, it has been shown that the shock performance of lead-free solder can be improved by adding trace amount of 4th additional elements. Liu et al. showed that trace amount addition of Ce [114], Y [115], Mn [114, 116] and Ti [116, 117], can improve the drop resistance of Sn-rich lead free solder. They reported that the drop performance of SAC105 + 0.25Mn is even better than that

of $Sn_{37}Pb$ solder joints. Amagai et al. [118] found that addition of Co, Ni and Pt elements can improve the drop performance of Pb-free solder by suppressing the growth of IMC layer. Additionally, shock performance of solder joints can be expected to be improved by alloying elements that can reduce IMC layer thickness and limit Kirkendall void formation, such as Ni, Ge [119], Co, Fe [60], In [118], and Zn [120].

2.5 Electromigration Behavior of SAC and RE-Containing SAC Solder Joints

2.5.1 Fundamentals of electromigration in solder joints

Due to increase in number of input/output interconnects in a small electronic device, the average current density in a solder bump is high enough for failure by electromigration to occur [121]. Failure mechanisms of electromigration in solder joints can be classified into two types: pancake-type voids formation by current-induced Sn self-diffusion [122-124], and extensive metallization consumption [125, 126], such as Cu and Ni at cathode side. The two major degradation mechanisms of electromigration is controlled by temperature [127] and Sn grain orientation [128]. Geometry induced current crowding effect was found to exist in flip-chip solder bump [129] and it significantly decrease the solder bump life time [130] by rising local temperature [131, 132] and accelerating the diffusion rate of Cu and Sn [133, 134].

The effect of intermetallics on electromigration and atomic diffusion in lead-free solder has gained sufficient attention. Hung et al. [135] found that coarse Cu-Zn IMC precipitates formed during solidification could block electromigration induced by Sn flux in which Sn extrusion sites were created from precipitates and

were randomly distributed within solder. Chen et al. [136] reported that plate-like Ag_3Sn compound can intercept the Bi migration from the cathode side to anode side. A similar effect was also observed in Sb [137], Ni [138], and Cu_6Sn_5 [139] particle-reinforced lead-free solder during electromigration, suggesting that electromigration performance of solder can be enhanced with the formation of rigid intermetallic precipitates.

2.5.2 Electromigration behavior of RE-Containing SAC solder

Electromigration behavior of SAC Pb-free solder has been studied and compared with conventional SnPb solder [140, 141]. They found the pancake-type void formation in SAC solder is much lower than that of SnPb solder if tested at the same condition, owing to the higher homologous temperature of SAC solder. Additionally, due to mechanically harder Sn matrix and surface oxide, the compressive stress at the anode of SAC is relieved by squeezing out the hillocks instead of budging of the solder surface [142]. Thus, electromigration studies on SAC were mainly focused on polarized effect on IMC growth [143, 144] and effective charge number in SAC solder, which can only be determined through the measurement of the movement of markers [145-147].

Studies on RE-additions to SAC alloys show a large discrepancy in reported electromigration behavior. Lin et al. reported that the electromigration resistance of SAC [148] and SnZn [149] solder decreased with addition of 0.5 wt% Ce, which is attributed to higher number of diffusion paths in Ce-containing solder. However, He et al. [23] observed enhanced electromigration resistance in

RE containing SnBi solder because of suppressed dislocations movement and the occurrence of grain boundary sliding.

2.5.3 Characterization techniques used in electromigration studies

To characterize electromigration behavior, several novel characterization techniques have been applied for the electromigration studies besides the well known traditional 2D imaging tools, such as optical and scanning electron microscopy. The electromigration induced strain distribution was established using the digital image correlation (DIC) method, and large strains were observed at large pores and at the corner of the solder joint [143]. Interestingly, a 3D x-ray tomography imaging technique was conducted on SnPb solder bump after electromigration stressing [150]. Location, shape and size evolution of voids formed during electromigration can be revealed in three dimensions and measured by reconstructing 3D structure of solder bump after current stressing. Thus, the products of effective diffusivity and effective charge number, as well as back-stress gradient and activation energy can be more accurately calculated. Additionally, x-ray diffraction can be utilized to investigate stress evolution [151] and in-situ Sn grain orientation [152].

3. RESEARCH OBJECTIVES AND APPROACH

Investigation performed in Prof. Chawla's group has shown that Sn-3.9Ag-0.7Cu alloy alloyed with very small amount of Ce possesses unique mechanical properties and oxidation resistance. This study's primary foucs is regarding the possible issues associated with integration of the new class of Pb-free solders into the electronic packaging. The main objectives of this investigation are:

1. In-depth study on the mechanism of enhanced ductility in Ce-containing Sn-3.9Ag-0.7Cu using interrupted shear test and finite element modeling.
2. A thorough understanding of the viability of RE-containing solders reflowed on industrial metallizations, including thermal and mechanical stability of Ce-containing Sn-3.9Ag-0.7Cu solder on Cu and electroless Ni metallization.
3. Understand and compare the wetting behavior of both the Ce-containing Sn-3.9Ag-0.7Cu and Sn-3.9Ag-0.7Cu solders. This would include measurements of both contact angle and spread area ratio.
4. Quantify the role of solder volume on the microstructure of Sn-3.9Ag-0.7Cu and Ce-containing Sn-3.9Ag-0.7Cu solders. Quantitative characterization of critical microstructural features of Ce containing Sn-3.9Ag-0.7Cu solder joints with different thickness would be conducted.

5. Conduct mechanical shock tests on Ce-containing Sn-3.9Ag-0.7Cu solder, in comparison to Sn-3.9Ag-0.7Cu solder. Tests would be carried out using a servohydraulic load frame with specially designed low mass grips.
6. Evaluate the electromigration performance of Ce-containing Sn-3.9Ag-0.7Cu solder in comparison to Sn-3.9Ag-0.7Cu, with the utilization of the V-groove processing technique. The void growth would be revealed by lab-scale x-ray tomography.
7. Understand the effect of compliant intermetallic phases on the enhanced ductility of Sn-3.9Ag-0.7Cu solder. The mechanical properties of solder alloys containing soft and hard intermetallics would be studied and compared with conventional Sn-3.9Ag-0.7Cu solder.

A detailed description of the major objectives is listed below.

3.1 Mechanism Study of Enhanced Ductility of Ce-Containing SAC Solder

3.1.1 Ce-containing SAC solder alloy fabrication

Vacuum-melted ingots of Sn-3.9-0.7Cu with trace amounts of Ce (0.5 wt.%) were prepared for following studies. High purity Sn-3.9Ag-0.7Cu ingots (Indium, Clinton, NY) were cut into small rectangular pieces (6.5 mm × 6.5 mm × 13 mm) and mixed with Ce shot (ESPI, Ashland, OR). Due to the reactive nature of pure Ce with oxygen, the materials were mixed in a quartz ampoule (12 mm in diameter) under a sealed glove box with helium atmosphere. The quartz ampoules then were evacuated to 10^{-5} torr and sealed. The sealed ampoules were heated to

1000 °C for 4 h, and periodically mixed by rotation of the ampoule in order to homogenize the liquid metal. The ampoules were water quenched. The ingots were removed from the ampoule, and sectioned.

3.1.2 Lap-shear joints fabrication

Lap-shear and interrupted shear tests were performed on solder/Cu single lap shear joint. As-processed solder ingots were machined into 6.35 mm × 6.35mm × 0.5mm squares. The oxidation caused by machining process was removed by polishing, and ultrasonically cleaned in acetone. Oxygen free copper bars (50.8 mm in length and 6.35 mm in thickness) were polished to a 0.05 μm finish with colloidal silica solution. A graphite mask was applied to the Cu bar, leaving a 6.35 mm ×6.35 mm area for reflow. A rosin mildly activated (RMA) flux was applied to the unmasked portions of the Cu bars to improve the wetting between the Cu bars and solder. The joint was assembled with the aid of a reflow fixture, as shown in Fig. 2 to minimize misalignment, and maintain a consistent solder thickness of approximately 500 μm. The entire assembly was heated on a hot plate. The typical reflow profile consists of heating the jig to 170 °C for 2 minutes to allow excess flux to vaporize, then heating to 20 °C above the melting point and holding for 40 s and cooling in air on Al blocks. The actual temperature of solder during reflow was monitored by inserting a thermal couple inside it, and a reproducible cooling rate of 0.7 °C/s. To understand the role of thinner intermetallic layer in Ce-containing solder joint on the enhanced ductility, mechanical shear behaviors of SAC and SAC-Ce solder joints with constant Cu_6Sn_5 intermetallic layer thickness was studied and compared. SAC solder joint

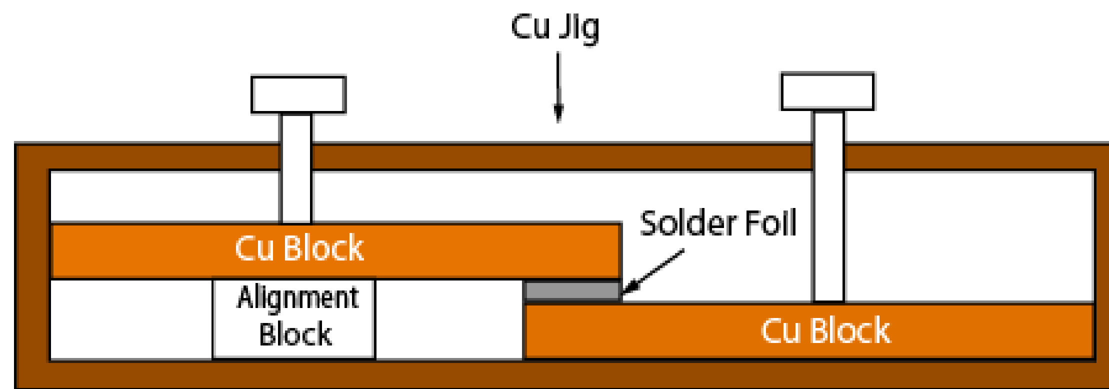

Figure 2. Schematic of Cu jig used for assembling lap-shear solder joint

with consistent intermetallic layer thickness as SAC-0.5Ce was obtained by reducing dwell time at melting point from 40 s to 10 s.

3.1.3 Lap-shear and interrupted shear tests

Shear testing was conducted using a servo-hydraulic load frame at room temperature and a nominal shear strain rate of 10^{-3} s^{-1}. For the interrupted shear testing, one side of the Sn-3.9Ag-0.7Cu and Sn-3.9Ag-0.7Cu-0.5Ce joints was polished to a 0.05 μm finish with colloidal silica solution before shear testing. When the desired shear strain values (2%, 10%, 50%) were reached, the experiment was interrupted, and the microstructure was examined by optical microscopy and SEM.

3.2 Study of Thermal and Mechanical Stability of Ce-containing Solder on Cu and Ni-P Substrate

3.2.1 SAC and SAC-Ce/Ni-P lap-shear joints fabrication

Bulk ingots of each solder and lap-shear solder/Cu joints were prepared following same procedure as described above. Electroless Ni-P substrate was fabricated by depositing Ni-P layers on the polished copper bars with an immersion Au plating on top to avoid oxidation of the nickel surface. The reflow procedure of solder/Ni-P joints was consistent with typical reflow for solder/Cu joints as described above. The thickness of Ni-P and Au layer, as well as P content in Ni-P layer was measured by scanning electron microscope and energy dispersive spectroscopy.

3.2.2 Effect of thermal aging on microstructural and mechanical behavior of Ce-containing SAC solder joints

High temperature stability of solder joint was examined by aging joints for 250 hours at 95 °C in furnace. After thermal aging, the solder joints were sectioned and polished to a 0.05 μm finish with colloidal silica solution for microstructure characterization. Strength and ductility of as-reflowed and thermal aged joints was evaluated by shear test using a servo-hydraulic load frame at room temperature and a nominal shear strain rate of 10^{-3} s^{-1}. Quantitative microstructure characterization of intermetallic phases was conducted using image analysis software (ImageJ, Gaithersburg, MD). Optical and SEM micrographs were segmented into binary images and the particles of interest were fit to ellipse, to estimate their size and aspect ratio.

3.3 Study of physical properties of Ce-containing SAC solder

3.3.1 Evaluation of wettability of Ce-containing SAC solder on Cu substrate

The wetting behavior of SAC-0.5Ce was studied by reflowing solder discs on a Copper substrate, and compared to SAC. The ingots of each material were prepared as described above. Each ingot was sectioned into small disks approximately 10 mm in diameter and 0.6 mm in thickness. The disks were polished and ultrasonically cleaned by acetone before reflow. The copper substrate (20 mm × 20 mm × 7.7 mm) was polished to a final finish with 0.05 μm colloidal silica solution. The specimens were placed on the center of the copper block, and rosin mildly activated (RMA) flux was applied on the surface of the copper substrate. The solder discs were heated up to 250 °C at a heating rate of

1 °C/s, and then cooled at a nominal cooling rate of 3 °C/s. The specimens were maintained above 220 °C for 140 s. The melting solder discs were illuminated by a source of visible light, and the contact angles were recorded by a CCD camera equipped with an appropriate set of lenses, as shown in Fig. 3. Both spreading area ratio of the as-bonded contact and contact angel of SAC and SAC-0.5Ce on Cu substrate were measured to indicate the wetting behavior of solder.

3.3.2 Characterize the melting and solidification behavior of SAC-Ce solder

Differential scanning calorimetry (DSC) was used to determine the onset melting point as well as undercooling value for the solder with 0.5 wt pct Ce additions and compare it to the SAC alloy. The measurements were conducted in a dry argon atmosphere gas on the calorimeter (model DSC-7, PerkinElmer). Sample of 10 to 20 mg were punched from the as-cast and slightly polished solder disc and were ultrasonically cleaned in acetone. Samples were weighted and placed into Aluminum pans. An empty Aluminum pan was used as a reference Samples were then heated and cooled at rates of 0.5 and 1 °C/s in the temperature range of 298 K to 573 K (25 °C to 300 °C) to simulate lap shear specimen cooling condition.

3.3.3 Volume effect on microstructure refinement in Ce-Containing SAC solder joints

A Cu/solder/Cu sandwich-like structure will be used to study volume effect on microstructural evolution of Ce-containing Sn-3.9Ag-0.7Cu solder joint with different solder volume, in comparison with Sn-3.9Ag-0.7Cu solder. The ingots of each material will be prepared as described above.

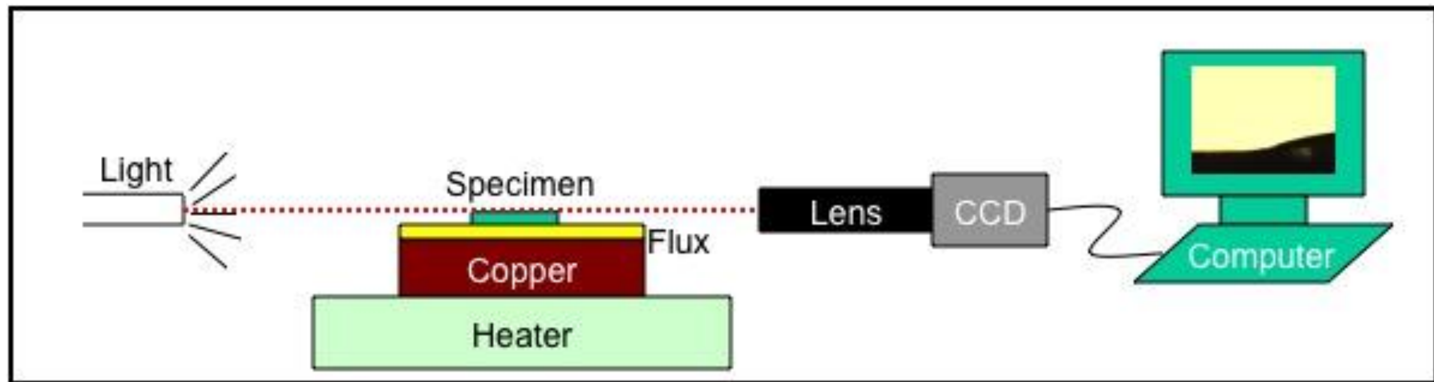

Figure 3. Diagram of an apparatus for measuring wettability of solders on Cu substrate

Sn-3.9Ag-0.7Cu-0.5Ce and Sn-3.9Ag-0.7Cu solder foils, 6.35 mm in diameter and with different thickness (0.2 mm, 0.5 mm, 0.75 mm, 1.00 mm), will be reflowed between two polished Cu pellets in a 6061 Al alloy holder to ensure a alignment during reflow and cooling, as shown in Fig. 4 at a nominal cooling rate of 4 °C/s. The sandwich-like solder joints will be sectioned into two specimens, then mounted and polished for examining in a optical microscopy and scanning electron microscopy to qualify microstructure and IMC thickness evolution.

3.4 Mechanical Shock Behavior of SAC and Ce-containing SAC Solder Joints

3.4.1 Butt solder joint fabrication

As-processed SAC solder and SAC-Ce solder ingots were machined into 6.35 mm × 0.5 mm discs. The oxidation caused by machining process was removed by polishing and ultrasonically cleaned in acetone. Oxygen-free-high-conductive (OFHC) copper bars (25 mm long and 6.35 mm diameter) were mechanically polished to a 0.05 μm finish with colloidal silica solution. A rosin mildly activated flux was applied to the polished portion of Cu bars to improve the wetting between the Cu bars and solder. The butt joints for mechanical tensile tests were assembled with the aid of a reflow fixture to minimize misalignment and maintain a consistent solder thickness of approximately 50 μm. The entire assembly was heated on a programmable digital hot plate the solder reached its melting temperature. The typical reflow profile consists of heating the jig to 170 °C for 2 minutes to allow excess flux to vaporize, then heating to 20 °C above the melting point and holding for 40 s, removed from the hot plate and cooling in

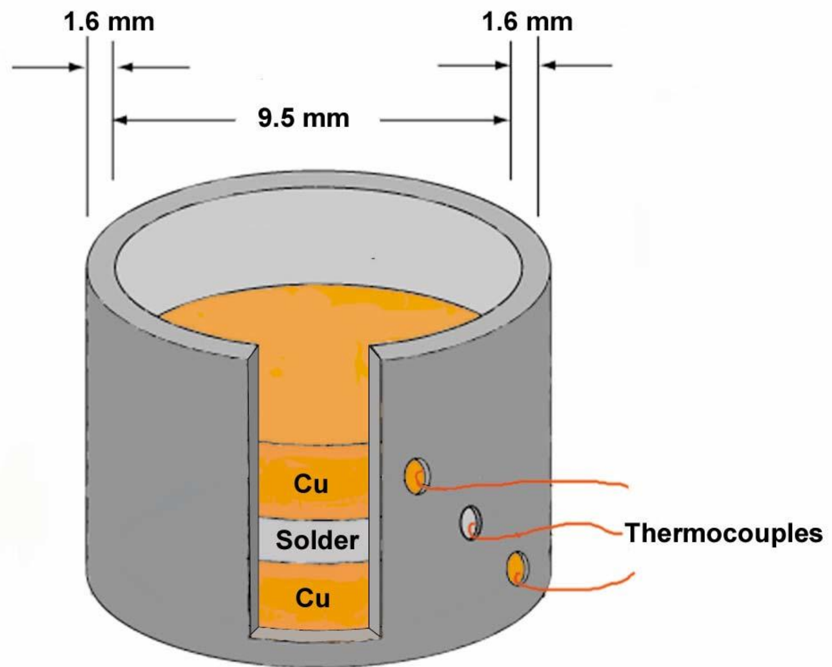

Figure 4. Schematic of solder sandwich and Al holder.

air on aluminum block at ~1 °Cs^{-1}. The actual temperature of solder during reflow was monitored by inserting a thermal couple inside it.

3.4.2 Mechanical shock testing

Mechanical tensile tests were conducted on solder joints over the range of stain rates (10^{-3}-$12s^{-1}$), using an MTS 810 hydraulic machine. Tests were conducted in strain control mode at 10^{-3} and 10^{-1} s^{-1} using an extensometer. Tests at 1.5 and 12 s^{-1} were conducted in displacement control mode. For high strain rate tests, a small section of the joint was polished to a 0.05 µm colloidal silica finish to permit visualization of the joint interfaces for the measurement of strain and strain rate, instead of using an extensometer. A Questar QM100 traveling microscope was used in conjunction with a Phantom Miro2 high-speed camera to measure strain from the displacement of the joint interfaces. A slack adapter was utilized to ensure that a well-controlled, linear strain rate was achieved. After tests, fracture surface of each joint was analyzed by scanning electron microscopy and energy dispersive spectroscopy to determine the failure mechanisms. Energy dispersive X-ray spectroscopy (EDS) was used to identify the composition of the IMC layer and precipitates on the fracture surfaces.

3.5 Effect of Electromigration on Microstructure Evolution of SAC and SAC-Ce Solder Joints

3.5.1 Fabrication of micron-size butt joints for electromigration testing

To study the effects of electromigration the microstructural change of Ce-containing Sn-3.9Ag-0.7Cu solder, micron-size Cu/Solder/Cu butt joints (500 µm in diameter) were fabricated, using a V-groove testing methodology [17, 18].

Silicon V-groove was made on a silicon wafer using photolithography and wet KOH etching techniques, as shown in Fig. 5. The as-processed solder ingots were machined in to 500 μm thick solder disc, then punched to small solder disc with 500 μm in diameter. The copper wire end (500 μm in diameter) was polished to a 0.05 μm finish with colloidal silica solution. A rosin mildly activated (RMA) flux was applied to the Cu end bars to improve the wetting between the Cu wires and solder. The butt joints were assembled by aligning two Cu wires and solder disc on Si V-groove, then reflowed on a hotplate using a reflow profile consists of heating the fixture to 170 °C for 2 minutes to allow the excess flux to vaporize, then heating to 20 °C above the melting point and holding for 50 s, then cooling in air on Al blocks. A reproducible cooling rate of 1.4 °C/s was obtained.

3.5.2 Electromigration testing

Before electromigration tests, joints were re-enforced by a high temperature epoxy resin to avoid brittle failure while transferring the sample to the characterization tools. The as-reflowed sample was then polished down until half of the solder joint was grounded in order to reach high enough current density (10^4 A/cm^2), as well as for microstructure examination using microscopies. Butt joint and test fixture were preheated inside a furnace at 100 °C for 1 hour to stabilize the sample and minimize thermal shock damage to the joints. Electromigration tests were performed at elevated temperature (100 °C) with a constant current that depends on the sample geometry. The actual temperature of specimen during testing was monitored by attaching a thermocouple at cathode side of solder joint.

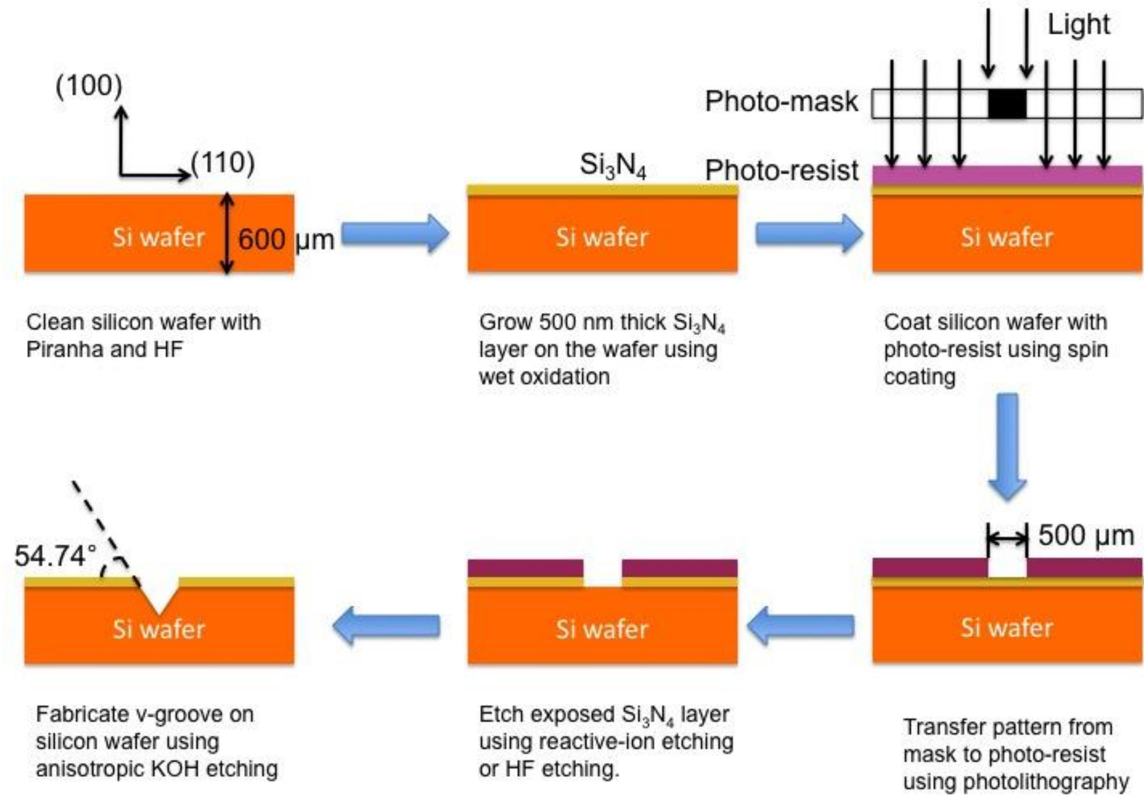

Figure 5. Procedure of processing silicon V-groove using photolithography and KOH etching techniques.

3.5.3 Characterize microstructural evolution of Ce-containing SAC solder induced by electromigration

The microstructural evolution of the Ce-containing solder joint during electromigration was examined by optical and scanning electron microscopy during current stressing, and compared with conventional Sn-3.9Ag-0.7Cu joints. The electromigration induced voids growth was examined by X-ray tomography technique. To reconstruct 3D structure of solder joints, 3D projection images of solder joints were collected by a MicroXCT system at Intel (Xradia). After data collection, it will be reconstructed by a commercial tomography reconstruction software (MIMICS) to create a 3D representation of the object. With 3D structure of solder joints, the growth rate of current induced voids at cathode side can be measured.

3.5.4 Characterize current density inside solder joint using finite element method

After obtaining 3D reconstructed microstructure, Finite Element Modeling was utilized to predict the current density distribution based on the actual geometry and distribution of voids in the solder joint. To conduct Finite element analysis on the sample, the volume mesh of the reconstructed model was generated by commercial meshing software (Hypermesh) using linear tetrahedral elements. The meshed model will be then exported to Abaques for current density analysis. In the model, a concentrated current was applied on the cathode side of solder, while the anode side was set to be zero potential boundary condition to get

a current flow from cathode to anode. The electronic conductivity of SAC and SAC-Ce solder was taken to be $8.66 \times 10^6/\Omega \bullet m$ and $8.39 \times 10^6/\Omega \bullet m$, respectively.

3.6 Effect of Complaint Intermetallic Phases on the Enhanced Ductility of SAC Solder Joints

3.6.1 Preparation of Mn and Ca-containing SAC solder alloys

Ca and Mn were selected as doping elements for SAC alloy due to the unique mechanical properties of their intermetallic compounds formed in SAC alloy. Vacuum-melted ingots of SAC with 2 wt.% Ca and Mn were prepared for nanoindentation, in order to obtaine relatively large intermetallic particles. For mechanical testing, we have shown that alloying additions of less than 0.5 wt.% provide the best enhancement in ductility. So for shear tests, samples of SAC with 0.5 wt.% Ca and Mn were fabricated. High purity SAC ingots were cut into small rectangular pieces ($6.5 \times 6.5 \times 13$ mm) and were mixed with Ca and Mn shot (ESPI, Ashland, OR). Due to their high reactivity, Ca, Mn and solder were mixed in a sealed glove box in helium atmosphere, and then sealed in a quartz ampoule (12 mm in diameter). With a stopcock the quartz ampoule was evacuated to 10^{-5} torr and sealed. The sealed ampoules were heat treated at 700°C for 4 hours, and periodically mixed by rotating the ampoule, in order to homogenize the liquid metal. The ampoules were then furnace cooled for nanoindentation (to obtain larger particles) or water quenched for mechanical shear tests. The samples were removed from the ampoule, and sectioned.

3.6.2 Determine the elastic properties of intermetallic compounds formed in the solder alloys using nanoindentation.

Nanoindentation was conducted on intermetallics in the as-processed Ca and Mn containing SAC ingots, as well as on pure Sn. The ingots were sectioned and polished to a final finish of 0.05 μm colloidal silica. Samples were mounted on aluminum stubs for testing using a mounting adhesive. Nanoindentation was carried out by selecting 20 intermetallic particles randomly. The center of each of these intermetallics was indented. The nanoindenter was first calibrated by measuring Young's modulus and hardness of a silica standard at a strain rate of $0.05s^{-1}$. A continuous stiffness measurement (CSM) technique was used during indentation. With the CSM, a load is applied to the indenter tip to drive the indenter into the specimen surface while concurrently superimposing an oscillating force with a small amplitude (significantly smaller than the nominal load). An accurate measurement of the contact stiffness at all indentation depths is provided by separating the in-phase and out-of-phase components of the load-displacement data. The advantage of CSM is that an instaneous measurement of modulus and hardness can be obtained during indentation. Thus, multiple indentations at different depths are not necessary.

For all indentations, Young's modulus was calculated as a function of indentation depth, to determine the onset of any pile-up, sink-in or cracking during indentation, as well as the thickness of oxidation layer. Indentation was carried out using a Berkovich indenter to an average depth of 1000-1500 nm per indentation. Young's modulus for an individual indentation was taken as the

average value over a depth range where the modulus was independent of depth, i.e, approximately 500-1300 nm. An SEM equipped with Focused Ion Beam (FIB) and EDS was used after indentation to ensure that the indentations were located on the intermetallics, and to analyze the deformation during indentation. Indentation size was much smaller than the size of the individual intemetallic particles, so sink-in of the particle during testing was not likely to take place.

A FIB was used to cross-section oxidized samples of Sn-3.9Ag-0.7Cu-0.5Ca to study the thickness of oxide layer. Samples were first coated with a 1-μm-thick Pt layer using the ion beam to protect from subsequent beam damage. A trench was milled using the ion beam at 30 kV and a current of 5 nA. The initial cleaning cross-section was performed at 30kV and 0.3 nA, with subsequent cleaning sections using smaller currents to a final ion bean current of 30 pA.

3.6.3 Comparison of shear behavior of Ca and Mn-containing SAC solder joints shear tests

In order to understand the relationship between soft intermetallic particle and enhanced ductility, it is necessary to conduct mechanical tests on the solder alloys with soft and hard particles, to simulate the effect of adding RE-Sn intermetallics to the microstructure. Shear testing was conducted using a servo-hydraulic load frame (MTS systems) at room temperature and a shear strain rate of 10^{-3} s^{-1} in displacement control mode. To compensate for the variability in joint geometry, the joint thickness and reflowed area were measured in each case, after the experiment, to accurately measure the applied stress and strain.

4. MECHANISMS OF DEFORMATION IN HIGH-DUCTILITY CE-CONTAINING SN-3.9AG-0.7CU SOLDER ALLOYS

4.1 Abstract

Rare earth-containing Pb-free solders have gained widespread attention due to their superior ductility relative to conventional Pb-free alloys. Our previous work has shown that new Ce-based alloys are also extremely oxidation resistant compared to La or Y-containing alloys. In this study, we report on a mechanism-based model for the large increases in ductility with small addition of rare-earth element to Sn-3.9Ag-0.7Cu. The mechanisms of ductility enhancement by Ce were observed in a scanning electron microscope, in interrupted shear-tests, where $CeSn_3$ particles served as microscopic fracture and void nucleation sites. Micro-mechanical modeling using the finite element method was used to examine the plastic strain field in solder affected by the particles. The concentrated deformation band was seen to be disturbed by the particles, resulting in a more uniform deformation pattern with reduced strains and thus enhanced ductility of the lap-sheared joint.

4.2 Introduction

The toxic nature of lead has prompted the electronic packaging industry to seek environmentally-friendly Pb-free alloys as replacements to Pb-Sn solder alloy. Although a series of near-eutectic Sn-Ag-Cu (SAC) alloys are being used [1], there are some drawbacks for SAC alloys. These include higher melting temperature and poor mechanical shock resistance, relative to Pb-Sn alloys [2-4].

Rare-earth (RE) elements have been used as fourth alloying element to SAC as a means of enhancing both physical and mechanical properties [5-8]. Past investigations have shown that by adding RE elements the microstructure of SAC solder can be refined [5-11]. Wetting behavior [11-14] and mechanical performance [9-11, 15] can be improved when the RE content is less than 0.5 wt%. In particular, enhanced mechanical properties, such as tensile strength [9,11], ductility [15,16], and creep resistance [15,17], of RE-containing solders have been reported.

In our previous work [18,19], we have shown that small additions of La and Ce (0.1 and 0.5 wt. %) to SAC alloy refine the Sn dendrite microstructure, reduce the Cu_6Sn_5 intermetallic compound layer thickness, and significantly increase the ductility of solder joints compared to SAC alloy. The oxidation resistance of La-containing solders is relatively low and the resulting $LaSn_3$ particles are prone to whiskering during oxidation [20-22]. Ce-based alloys are less prone to oxidation but still exhibit the desirable attributes of microstructural refinement and increased strain-to-failure, relative to SAC, as in the La-containing solders [8, 23].

For La-containing Sn-Ag-Cu solder, we hypothesized that the main mechanism for the higher ductility in these solders is based on microscopic voids nucleating at $LaSn_3$ throughout the solder volume [18]. This cavitation based mechanism, however, needs to be validated experimentally. Additionally, the role of reduced Cu_6Sn_5 intermetallic layer in RE-containing alloy is still unknown. In this study, we have conducted systematic interrupted shear experiments, coupled

with microstructural characterization using scanning electron microscopy (SEM), on Ce-containing SAC. The behavior of the RE-containing materials was compared to that of SAC solder alloys. It will be shown that plasticity around $CeSn_3$ intermetallic particles, as well as debonding and fracture of the particles takes place. The shear strain is distributed more homogeneously in the RE-containing solders, compared with SAC. The effect of reduced Cu_6Sn_5 intermetallic layer on enhanced ductility is also examined, and it will be shown that it was $CeSn_3$ intermetallic particles, not thinner Cu_6Sn_5 interfacial layer that improved ductility. Finally, finite-element method (FEM) was used to model the effects of $CeSn_3$ intermetallic compound on strain distribution. The FEM results qualitatively corroborate the experimentally-observed behavior.

4.3 Materials and Experimental Procedure

Vacuum-melted ingots of Sn-3.9Ag-0.7Cu with trace amounts of Ce (0.5 wt.%) were prepared. High purity Sn-3.9Ag-0.7Cu ingots (Indium) were cut into small rectangular pieces (6.5 mm × 6.5 mm × 13 mm) and mixed with Ce shot (ESPI, Ashland, OR). Due to the reactive nature of pure Ce with oxygen, the materials were mixed in a quartz ampoule (12 mm in diameter) under a sealed glove box with helium atmosphere. The quartz ampoule was then evacuated to 10^{-5} torr and sealed. The sealed ampoules were heat treated at 1000 °C for 4 h, and periodically mixed by rotation of the ampoule, in order to homogenize the liquid metal. The ampoules were then water quenched. The solder ingots were removed from the ampoule, and sectioned.

Mechanical testing was conducted on solder/Cu single lap shear joints. As-processed solder ingots were machined into 6.35 mm × 6.35 mm × 0.5 mm squares. These were lightly polished to remove oxidation caused by the machining process, and ultrasonically cleaned in acetone. Oxygen free copper bars (50.8 mm and 6.35 mm in thickness) were polished to a 0.05 μm finish with colloidal silica solution, and etched in 2 vol.% nitric acid for 10 seconds to remove residual oxides. A graphite mask was applied to the Cu bars, leaving a 6.35 mm × 6.35 mm area for reflow. A rosin mildly activated (RMA) flux was applied to the unmasked portions of the Cu bars to improve the wetting between the Cu and the solder. The joint was assembled with the aid of a reflow fixture, to minimize misalignment, and maintain a consistent solder thickness of approximately 500 μm. The entire assembly was heated on a hot plate with a reflow profile as shown in Fig. 6. The assembly was held at 170 °C for 120 seconds, to allow excess flux to vaporize. The temperature was then raised until the solder reached 220 °C and was held for 40 seconds. The assembly was then removed from the hot plate and air-cooled on an aluminum heat sink. The actual temperature of solder during reflow was monitored by inserting a thermal couple inside it, and a reproducible cooling rate of 0.7 °C/s was obtained. The cooling rate was measured from the peak temperature to 150 °C, because the joint microstructure does not change significantly below this temperature during cooling [24-26]. A reproducible solder thickness of 500 μm was obtained in all joints. SAC solder joint with consistent intermetallic layer thickness as SAC-0.5Ce was obtained by reducing dwell time at melting point from 40 s to 10 s.

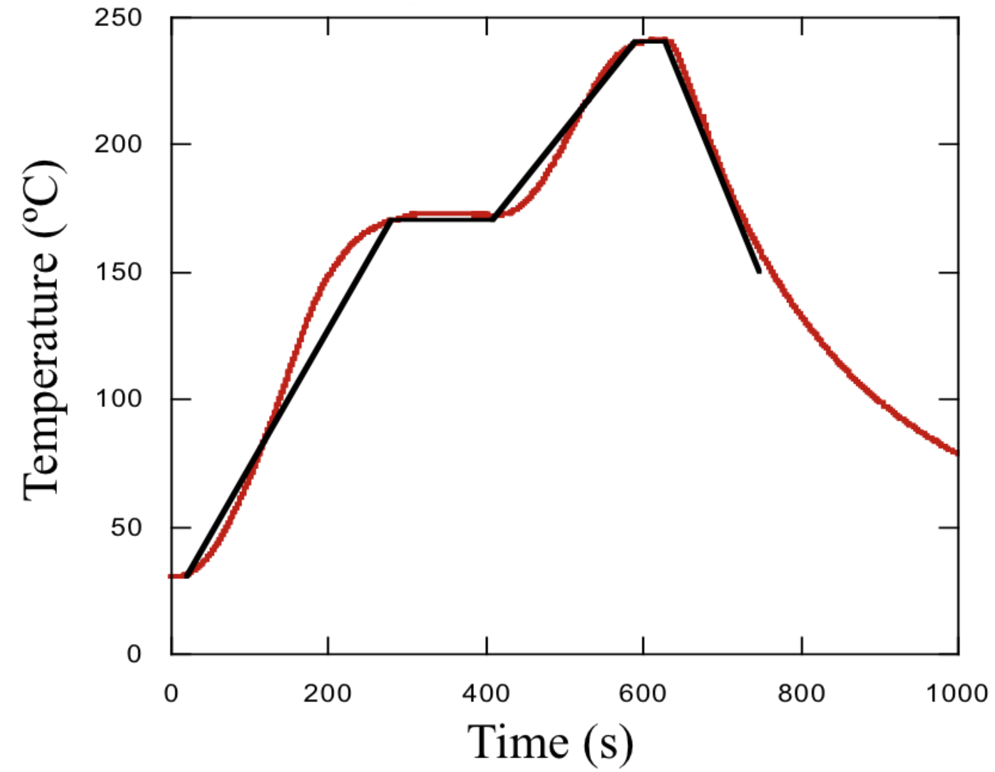

Figure 6. Reflow profile for lap shear specimens. The input profile is shown in black, while the actual temperature profile is shown in red.

Shear testing was conducted using a servo-hydraulic load frame at room temperature and a nominal shear strain rate of 10^{-3} s^{-1}. For the interrupted shear testing, one side of the Sn-3.9Ag-0.7Cu and Sn-3.9Ag-0.7Cu-0.5Ce joints was polished to a 0.05 μm finish with colloidal silica solution before shear testing. When the desired shear strain values (2%, 10%, 50%) were reached, the experiment was interrupted, and the microstructure was examined by optical microscopy and SEM.

4.4 Results and Discussion

4.4.1 Interrupt shear testing

Representative shear stress shear strain curves for of SAC and SAC-0.5Ce are shown in Fig. 7. Table 1 summarizes some of the mechanical properties measured, such as ultimate shear strength and strain-to-failure. The strain-to-failure was defined as the strain when the stress reached 1 MPa. Our results on Ce-containing solder were similar to what we reported on La-doped materials [8]. The ultimate shear strength decreases with an increase in Ce content. Alloys containing 0.5 wt% Ce showed an approximate decrease of 25% in strength compared to SAC solder. More importantly, the strain-to-failure of SAC-0.5Ce increased significantly, nearly 50% over that of SAC. To give a better view of enhanced ductility, the work of fracture of SAC-0.5Ce joints was also measured by integration of the stress-strain curve and compared with SAC joints. As shown in the Table 1, the addition of Ce not only significantly enhanced strain-to-failure but also the toughness of SAC solder joints.

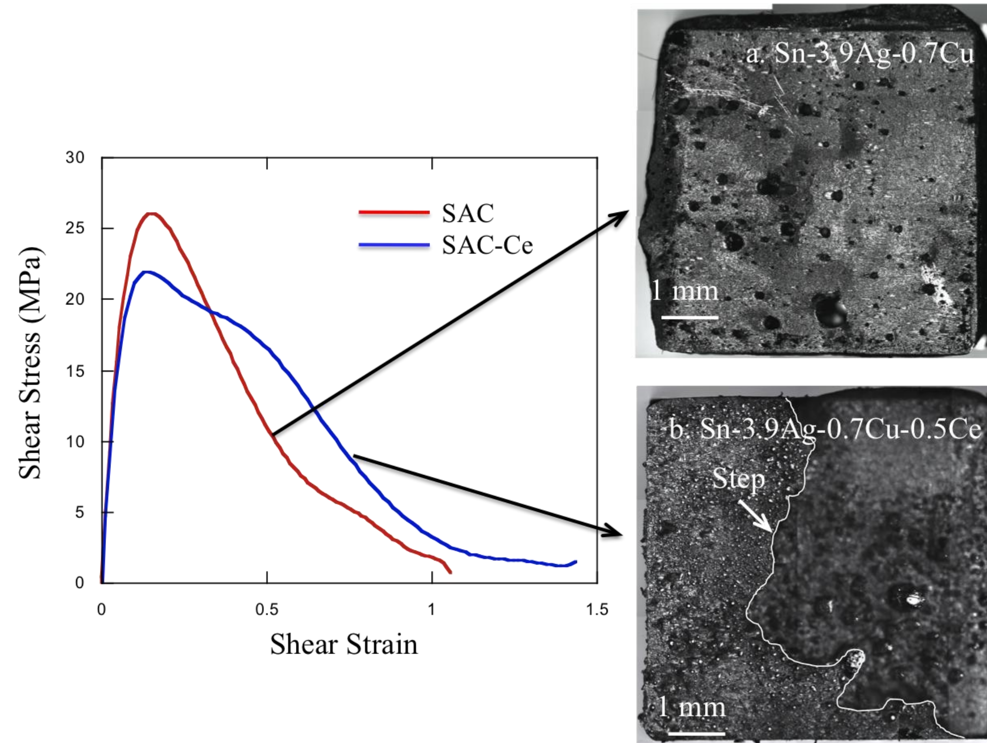

Figure 7. Typical shear stress-shear strain curves and fracture surfaces after monotonic shear testing: (a) SAC and (b) SAC-0.5Ce solder joints. The SAC-0.5Ce joints exhibit higher ductility. Fracture of SAC occurs very close to the Cu_6Sn_5/solder interface.

Table 1. Summary of shear behavior of SAC and SAC-Ce solder joints.

Solders	Ultimate Shear Strength (MPa)	Strain-to-Failure (%)	Work of Fracture (J/m^3)
SAC	24.2 ± 5.2	104.5 ± 3.7	14.2 ± 2.9
SAC-0.5Ce	21.8 ± 2.3	164.9 ± 58.9	21.6 ± 8.9

Examination of the fractured surfaces, Fig. 7, of the SAC-0.5Ce and SAC joints revealed classical ductile and brittle fracture, respectively. For Sn-3.9Ag-0.7Cu-0.5Ce the fracture occurred through the bulk solder, which resulted in a relatively tortuous fracture path, with visible steps on the fracture surface. Fracture in Sn-3.9Ag-0.7Cu occurred close to the interfacial region between the solder and Cu_6Sn_5 intermetallic, exposing the tips of the Cu_6Sn_5 nodules in some areas [27].

We previously proposed a hypothesis for the increased ductility of SAC by RE elements, such as La and Ce [18,19]. This hypothesis was based on the mechanisms of localized nucleation and growth of microscopic voids at $RESn_3$ intermetallic particles, which minimize strain localization and crack growth along the brittle Cu_6Sn_5 intermetallic/solder interface. To validate this hypothesis experimentally, interrupted shear tests were conducted on SAC and SAC-0.5Ce solders. The samples were initially polished on a side and the microstructure, at each strain value, was studied by optical microscopy and SEM. The microstructural evolution of deformation in the SAC solder, observed by optical microscopy, is shown in Fig. 8. The deformation of SAC in the linear-elastic regime appeared to be quite small. At the ultimate shear strength of the solder,

extensive plastic deformation was observed. The distribution of the deformation is not uniform, with a large degree of strain intensification near the solder/Cu interface. This effect becomes more obvious at higher strain values. This is indicative of a large degree of plastic strain localization at the solder/Cu interface. Thus, the plastic deformation in the solder is quite localized and inhomogeneous, which causes fracture in SAC to be localized to a very small fraction of the joint.

In the SAC-0.5Ce the degree of deformation becomes noticeable after the yield point. It is interesting to note, however, that the deformation of the solder is more homogeneously distributed and less concentrated at the intermetallic/solder interface, compared to SAC solder, even at higher shear strain (50%). The decrease in strain localization suppresses and delays the onset of crack growth along the brittle Cu_6Sn_5 intermetallic/solder interface.

The reason for the deformation being "spread out" over the entire joint volume of Sn-Ag-Cu-0.5Ce solder was further investigated using SEM. Figure 9 shows SEM images of as-deformed $CeSn_3$ particles at different shear strain values. In the linear elastic region, no deformation of $CeSn_3$ particles was observed. A significant amount of plastic strain appears to be present in the Sn matrix region surrounding the particles. Some evidence of debonding and fracture of $CeSn_3$ particles was also observed at higher strain (50%). Cracked particles don't carry any load, therefore the strength of the Ce containing Sn-Ag-Cu is lower than that of Sn-Ag-Cu. The plasticity around the particle, debonding and intermetallic fracture all contribute to an increase in fracture energy. Plastic deformation surrounding the particles helps in the homogenization of

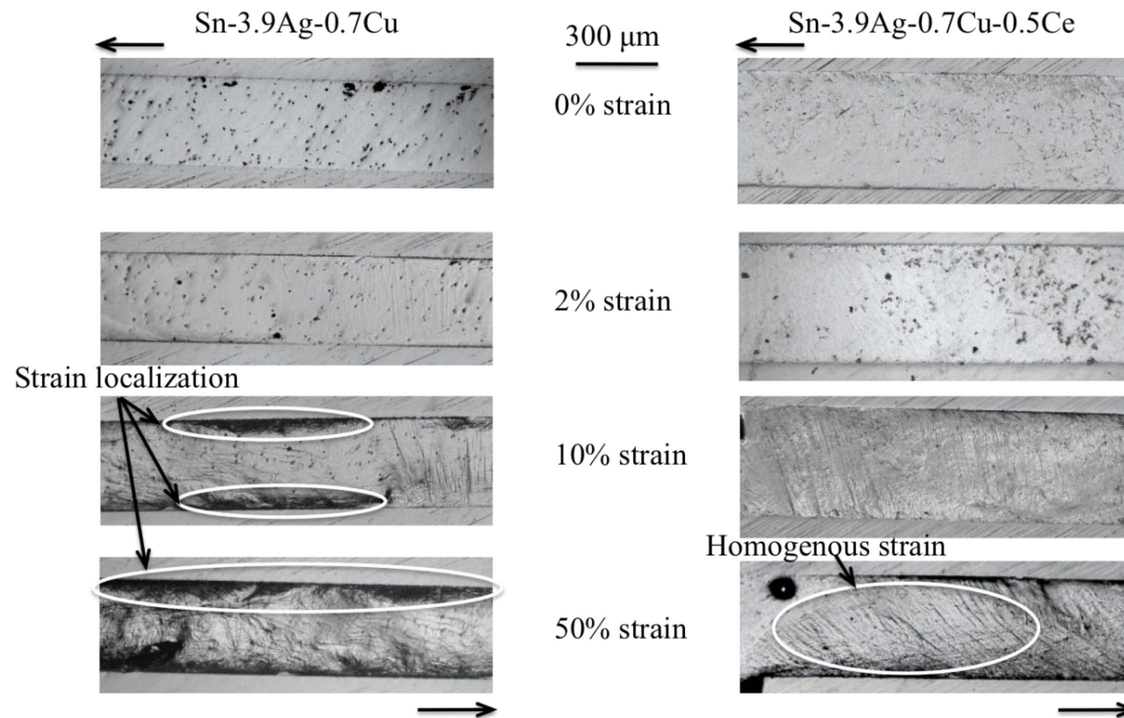

Figure 8. Optical microscopy images of interrupted shear testing of Sn-3.9Ag-0.7Cu and Sn-3.9Ag-0.7Cu-0.5Ce at different strain values (Arrows indicating shear direction of joints). The SAC-Ce allow shows homogeneous strain distribution while SAC fails bey strain localization close to the copper/solder interface.

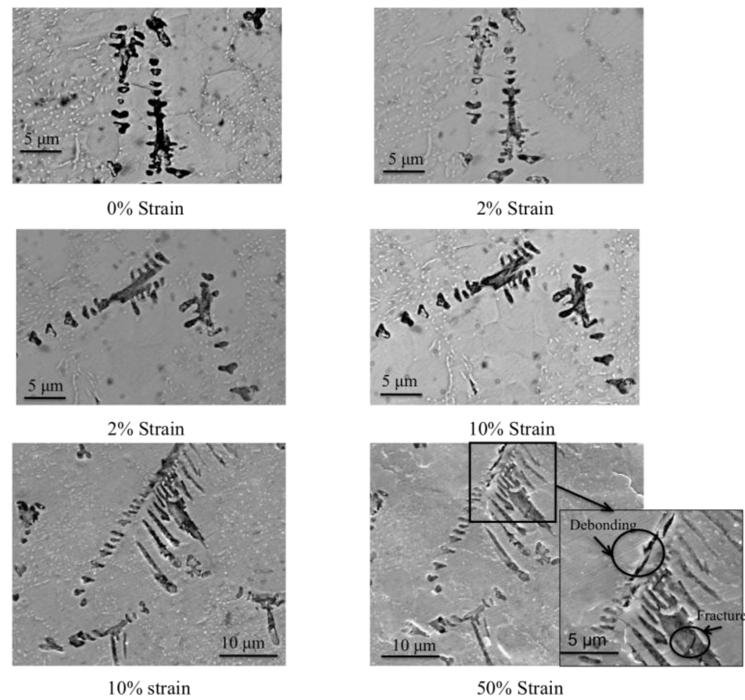

Figure 9. Scanning electron microscopy images of interrupted shear test of $CeSn_3$ intermetallic particles in Sn-3.9Ag-0.7Cu-0.5Ce solder joints. Note plasticity around the particles, debonding, and fracture.

deformation, and minimization of strain localization at the solder/Cu_6Sn_5 interface. This is further discussed in the following section on finite element modeling of deformation.

4.4.2 Effect of Cu_6Sn_5 layer thickness on shear behavior of SAC and SAC-Ce joints

In this section, we discuss the shear behavior of the solder alloys. It has been shown that the intermetallic layer thickness plays an important role in the mechanical behavior of solder joints, especially at high strain rate tests [30,31]. In addition the formation of Kirkendall voids may increase with increasing thickness of the intermetallic layer, which can also reduce the ductility of solder joint [29,32, 33]. Therefore, it is important to understand the effects of thinner Cu_6Sn_5 intermetallic layer on enhanced ductility in SAC-Ce. To eliminate the effect of Cu_6Sn_5 intermetallic layer thickness, mechanical shear behavior of SAC and SAC-0.5Ce alloy must be compared with constant Cu_6Sn_5 intermetallic layer thickness. In the previous work, we have shown that the thickness of intermetallic can be controlled by dwell time above the melting point of solder or thermal aging [34]. However, for thermal-aging, the microstructure of the bulk solder, such as Sn dendrites and Ag_3Sn particles, also coarsens. To obtain SAC and SAC-0.5Ce with constant intermetallic layer thickness and compatible microstructure, Sn-3.9Ag-0.7Cu solder joints were processed by modified reflow profiles, i.e. when the Sn is molten over shorter periods of time in contact with Cu, less intermetallic layer grows at Cu/Solder interface. Here the solder

microstructure of both SAC and SAC-0.5Ce solder joints is controlled by a constant cooling rate [35].

As shown in the Fig. 10, with decrease in dwell time in the reflow profile of SAC solder, the intermetallic layer thickness decreased gradually without significantly altering the morphology of the Cu_6Sn_5 nodules nor the microstructure of solder matrix [36], thereby providing a means to isolate the effect of intermetallic layer thickness. By measuring the thickness of intermetalliclayer with different dwell time, it was found that the intermetallic layer thickness of SAC solder with 10s dwell time is close to that of SAC-0.5Ce solder joint formed by a typical reflow profile (40s dwell time). The representative shear stress strain curves of SAC and SAC-Ce with different intermetallic layer thicknesses are shown in Fig. 11, and results are summarized in Table 2. It is clear that strain-to-failure of SAC solder joint did not increase with a decrease in intermetallic layer thickness, indicating that intermetallic thickness does not play a critical role in the enhanced ductility observed in SAC-0.5Ce solder.

Table 2. Summary of monotonic shear test of Sn-3.9Ag-0.7Cu and Sn-3.9Ag-0.7Cu-0.5Ce solder joints.

Solder alloys	Dwell time (second)	Cu_6Sn_5 layer thickness (μm)	Ultimate shear strength (MPa)	Strain to failure (%)
SAC	40	4.0 ± 2.1	24.2 ± 5.2	104.5 ± 3.7
	10	2.7 ± 0.9	22.8 ± 2.7	92.8 ± 51.5
SAC-0.5Ce	40	2.6 ± 1.0	21.8 ± 2.3	164.9 ± 58.9

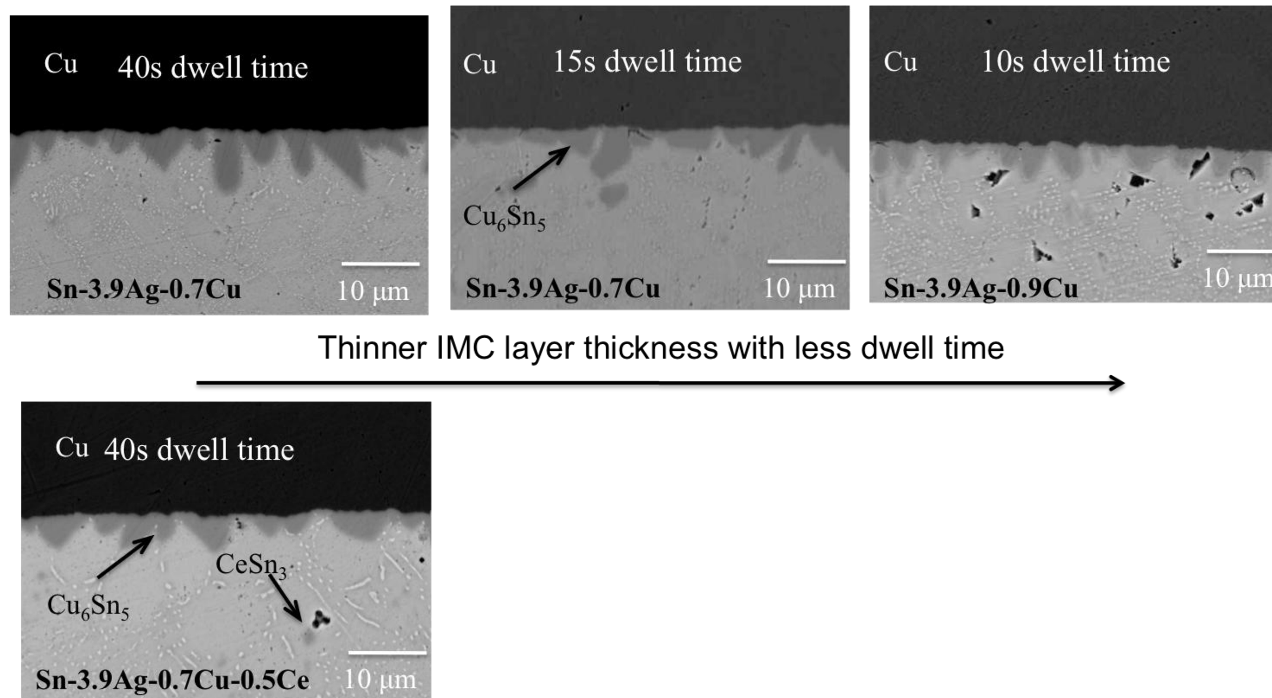

Figure 10. Backscatter electronic microscopy images for Cu_6Sn_5 intermetallic layer of Sn-3.9Ag-0.7Cu solders with different dwell time.

It has also been shown that the solder joint behavior is strain-rate-dependent, being controlled by either solder or the intermetallic layer [31,37]. At the lower strain rate regime (quasi-static), the mechanical properties of solder joint are controlled by the deformation of the solder matrix, while at higher strain rates, the Cu_6Sn_5 intermetallic layer controls the deformation behavior of the joint. Additionally, the intermetallic layer controls the quasi-static mechanical behavior of solder joint only when the layer thickness is large enough (greater than 10 μm) [44]. Since the strain rate used in this study is in quasi-static regime (10^{-3} s^{-1}) and the intermetallic layer thickness is relatively small (4 μm for SAC joint), it is not surprising that intermetallic layer thickness does not contribute to the enhanced ductility in SAC-Ce solder joint.

4.4.3 Finite element analysis

To provide a mechanistic rationale for the proposed ductility enhancement mechanism caused by the $CeSn_3$ particles, numerical finite element modeling was carried out. The model configuration, as well as the loading and boundary conditions, are schematically shown in Fig. 12. The solder is bonded to two large copper substrates, and experiences the same kind of shear deformation as in the actual experiment. In the modeling horizontal displacements (Δl in the *x*-direction) were imposed at the far right end of the lower copper substrate. The *x*-direction motion of the far left edge of the upper copper was forbidden, but movement in the *y*-direction was allowed except that the lower-left corner of the upper copper was totally fixed. The model dimensions are: h = 0.5 mm, w = 1 mm, H = 2.5 mm and L = 0.5 mm. The relative thicknesses of solder and substrate

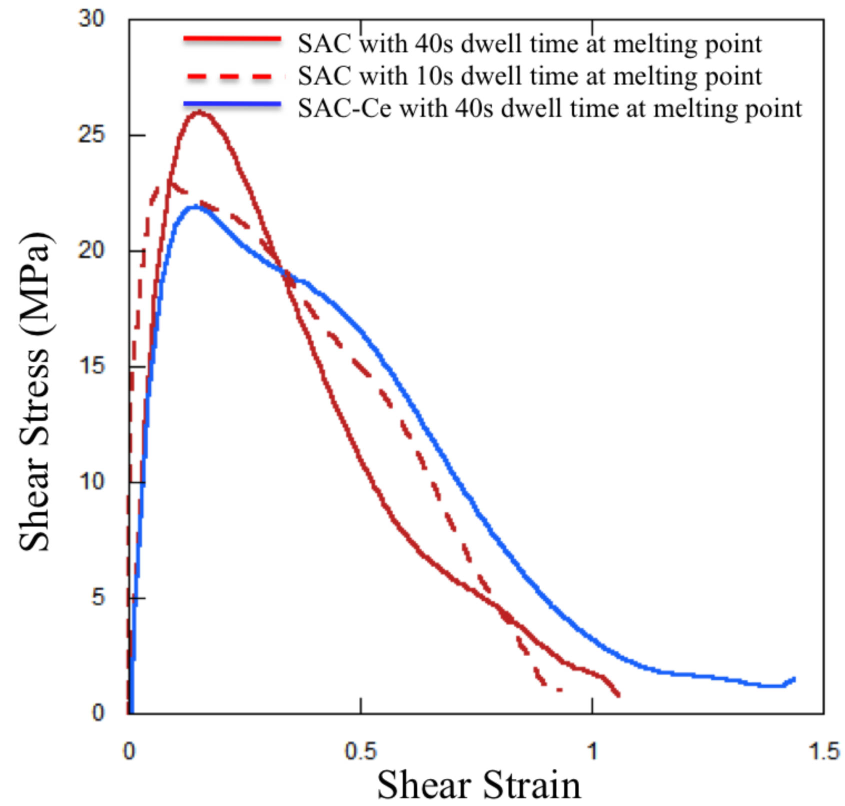

Figure 11. Shear stress vs. shear strain curves of Sn-3.9Ag-0.7Cu and Sn-3.9Ag-0.7Cu-0.5Ce solder joints reflowed with different dwell time.

were chosen such that apparent bending resulting from the shear loading is kept at minimum. The calculations were based on the plane strain condition, which effectively simulates the nominal simple shearing mode of the solder [38-40]. The nominal shear strain during deformation is defined to be $\Delta l/h$. In the model Cu is taken to be elastic, with Young's modulus of 114 GPa and Poisson's ratio of 0.31. The solder alloy is assumed to be elastic-perfectly plastic, with Young's modulus 48 GPa, Poisson's ratio 0.36, and yield strength 47.9 MPa. For simplicity the rate-independent material behavior is not included here, as it will not affect the salient results considered in the present analysis. Two forms of particle dispersion are considered (see Fig. 13 below), one with an area fraction of 5% (model A) and the other 8% (model B). The size, geometry, and spatial distribution of the particles are arbitrary. In actual materials, the particles are much smaller and more densely distributed than those adopted here. Nevertheless, the present models suffice for qualitative illustration of the particle-mediated deformation field developed in the solder. The particles are also elastic-perfectly plastic, with their properties estimated from nanoindentation measurements [28]. Their Young's modulus, Poisson's ratio and yield strength are, respectively, 64 GPa, 0.3, and 356 MPa. Note that the yield strength of the particles is much greater than that of the solder matrix. In the model the solder was discretized into 5000 four-noded linear elements, and each Cu substrate was discretized into 2400 elements. The mesh convergence was checked by another set of preliminary calculations using twice the number of elements in the model. The finite element program Abaqus [41] was employed for the modeling.

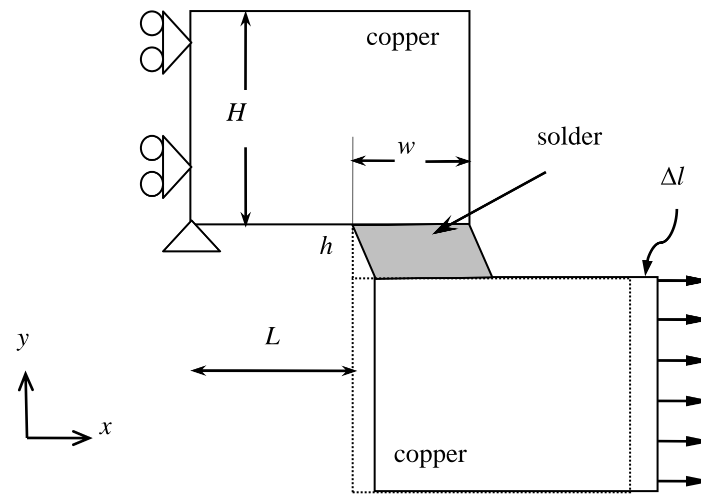

Figure 12. Schematic of the solder joint model, along with the loading and boundary conditions, used in the lap-shear modeling.

The results are shown in Fig. 13. In Fig. 13(a) the contour plot of equivalent plastic strain in the solder for the case without intermetallic particles, when the applied nominal shear strain is 0.08, is presented. The corresponding contour plots for model A (5 % particles) and model B (8% particles) are shown in Figs. 13(b) and (c), respectively. In Fig. 13(a) two distinct plastic deformation bands inside the homogeneous solder, originating from the four corners but predominantly parallel to the interfaces, are evident. Eventual failure can be expected to follow the strong plastic band which leads to a fracture path close to the interface, as was observed experimentally in Fig. 8. When discrete compliant particles exist, Figs. 13(b) and (c), the plastic flow field is seen to be disturbed to a great extent. The concentrated band becomes branched due to the blocking particles, and the maximum plastic strain is significantly reduced. This trend is more apparent in the case of more finely distributed particles (Fig. 13(c)). In general, the plastic deformation field becomes more uniform when the particles exist.

Results in Fig. 13 may also be presented in a more quantitative way. Figure 14(a) shows the area fractions of the solder matrix in which the equivalent plastic strain is above 0.15 (i.e., the red color regions in Fig. 14), for the case of no particles as well as for models A and B. It is clear that the pure solder (free of particles) possesses the largest area fraction with high plastic strains. The existence of particles results in a significant decrease in the high-strain region, especially in the case of more finely distributed particles (model B). Figure 14(b) shows the averaged equivalent plastic strains within the solder areas considered in

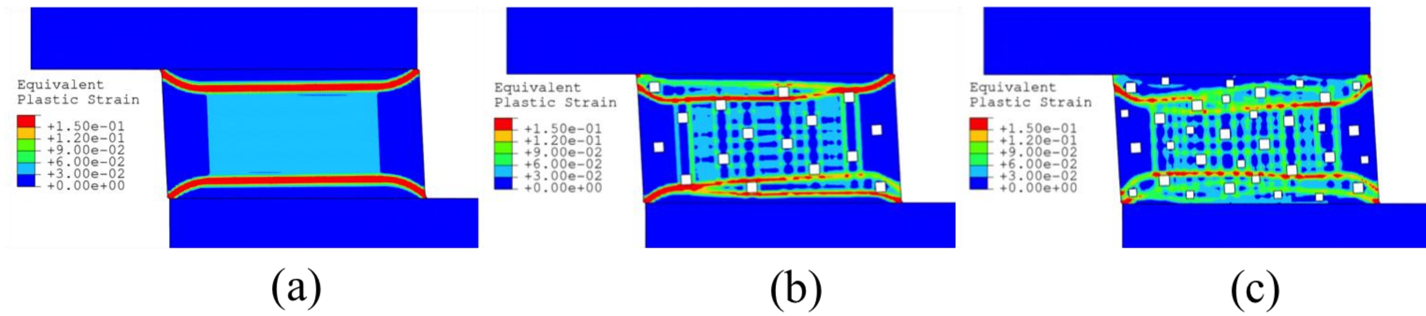

Figure 13. Contour plots of equivalent plastic strain in the solder containing $LaSn_3$ intermetallic particles with area fractions of (a) 0, (b) 5% and (c) 8%, when the applied nominal shear strain is at 0.08.

Fig. 14(a) (i.e., areas having equivalent plastic strains greater than 0.15, or the red color regions in Fig. 13). The pure solder is seen to have the greatest strain value, 0.224, and the values for models A and B are 0.211 and 0.190, respectively. Therefore not only does the incorporation of particles decrease the largest area of high plastic strains, but its average strain value is also lower. It can thus be expected that the initiation of damage in the solder with finer particles will be delayed. This naturally leads to an improvement of overall ductility under the same type of lap-shear loading. The proposed mechanism in Section 4.4.1 is seen to be consistent with the present modeling results.

There is an interesting observation worthy of discussion. Conventional thinking stipulates that reinforcing a ductile matrix with strong particles results in composite strengthening (such as in typical particle-reinforced metal matrix composites). Ductility will then be reduced due partly to the localization of plastic flow field within which an elevated plastic strain level commonly exists, leading to easier damage initiation. In the present experiment and modeling, however, an opposite trend is seen. The primary difference between the present study and those of particle-reinforced composites lies in the deformation pattern caused by the different macroscopic loading mode [42]. Within the context of typical particle strengthening, deformation is nominally uniform in the homogeneous matrix when no particles are present (typical tensile testing of bulk specimens). The presence of particles perturbs the deformation and induces locally higher plastic strains. In substrate constrained deformation, however, such as the current lap-sheared solder or tensile loading of a butt-joint solder, deformation is

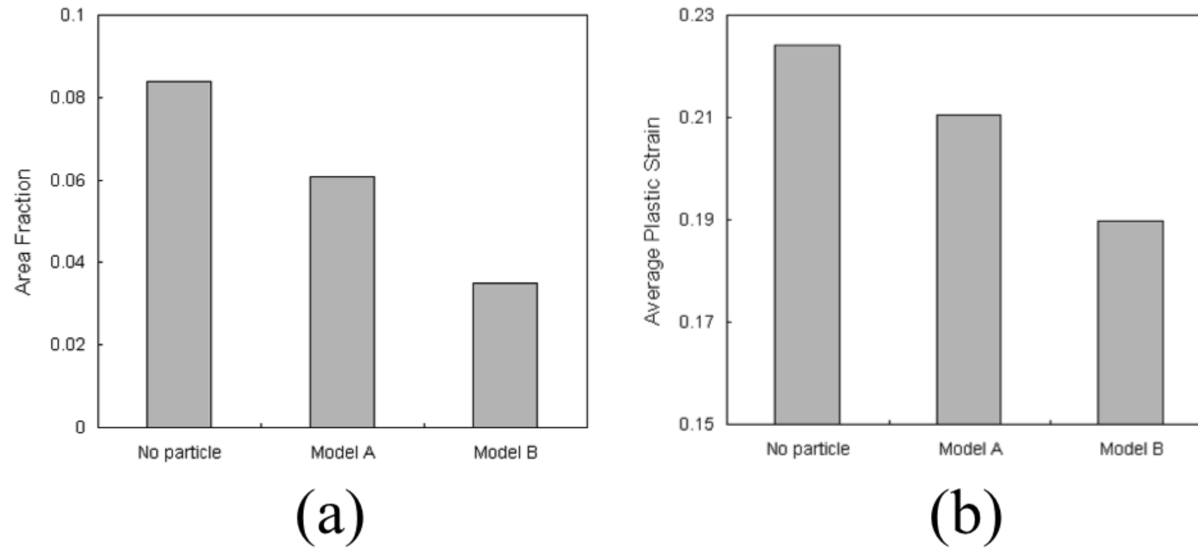

Figure 14. (a) Area fractions of the solder matrix having equivalent plastic strain greater than 0.15 (the red color regions in Fig. 13) in the three models. (b) The average equivalent plastic strain values within the same solder matrix regions in (a).

inherently highly localized in the homogeneous matrix free of particles (Fig. 13(a)). The added particles then serve to diffuse the strain concentration and result in locally lower plastic strains, which aids in delaying fracture.

4.4.4 Damage evolution for SAC and SAC-0.5Ce solder joints

Here, we propose a modified fracture model for the Ce-containing solders based on the observations from interrupted shear tests [42] and findings from this study. The schematic of damage accumulation is shown in Fig. 15. For the SAC solder alloy, the crack initiated and propagated close to the intermetallic/solder interface due to the strain localization at the interface [43, 44]. Thus, in the SAC solder alloy, fracture is localized in a very small fraction of the joint, causing low ductility in the solder joint. In Ce-containing SAC solder, the cracking and debonding of $CeSn_3$ intermetallic particles contributed significantly to the amount of plastic deformation, thus allowing deformation to be distributed uniformly over the entire joint's volume. Due to minimized plastic strain localization, the crack grew away from the brittle Cu_6Sn_5 intermetallic/solder interface resulting in enhanced ductility for the SAC-0.5Ce solder joints.

4.5 Conclusions

The monotonic shear behavior of Ce containing SAC solder was investigated, and compared with that of pure SAC alloy. Based on the experiment and modeling results, the following conclusions can be drawn. The SAC alloy with Ce additions exhibited higher strain-to-failure and lower strength compared with SAC.

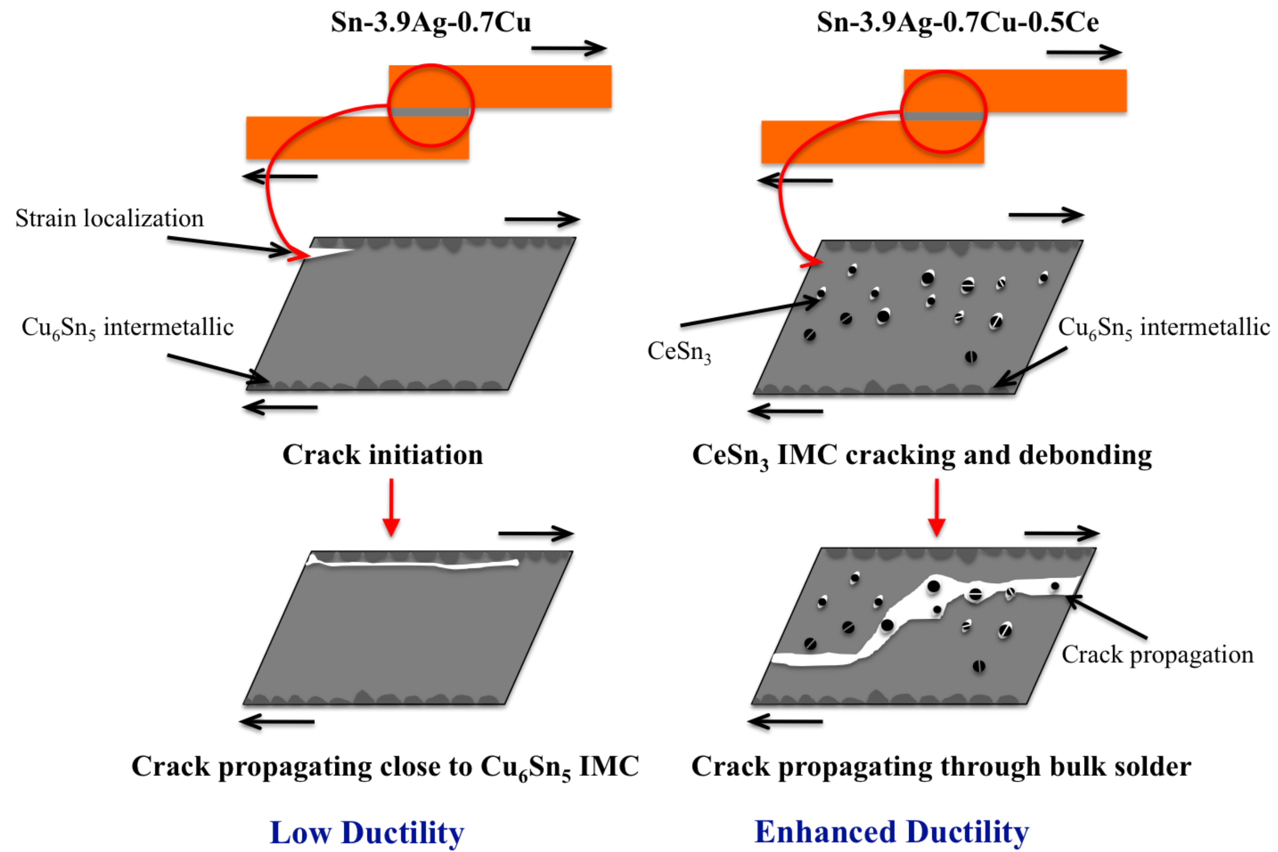

Figure 15. Damage accumulation schematic for Sn-3.9Ag-0.7Cu and Sn-3.9Ag-0.7Cu-0.5Ce solder joints.

1. The interrupted shear testing and characterization by optical microscopy and SEM shows that the $CeSn_3$ intermetallic particles are directly responsible for the higher ductility observed in Ce-containing SAC alloy. Plasticity around the particles, debonding, and fracturing of $CeSn_3$ intermetallic particles contribute to an increase in fracture energy as well as homogenization of the plastic strain in the solder region.
2. Studies on the effect of thinner Cu_6Sn_5 intermetallic layer thickness on ductility showed that is not due to the thin Cu_6Sn_5 intermetallic layer, but the preexisting $CeSn_3$ intermetallic particles.
3. Numerical finite element modeling illustrated that the existence of intermetallic particles in the solder serves to disturb the concentrated plastic deformation band during the lap-shear loading. The overall plastic flow field becomes more uniform, with a reduced maximum strain magnitude. Delayed fracture can thus be expected, leading to enhanced ductility.

4.6 References

1. H. Ma, J.C. Suhling, J. Mater. Sci., 2009, 44: 1141.

2. D.H. Kim, P. Elenuysm S, Barrett, IEEE Trans Electron. Packaging Manufacturing, 2002, 25, 84.

3. M.E. Loomans, M.E. Fine, Metall. Mater. Trans., 2000, 31A, 1155.

4. N. Chawla, Int. Mater. Rev., 2009, 54, 368.

5. F. Guo, M. Zhao, Z. Xia, Y. Ler, X. Li, Y. Shi, JOM, 2009, 61, 39.

6. C.M.L. Wu, D.Q. Yu, C.M.T. Law, L. Wang, Mater. Sci. Eng., 2004, 44, 1.

7 L. Zhang, S. Xue, L.-L, Gao, G. Zeng, Z. Sheng, Y. Chen, S.-L, Yu, J. Mater. Sci. Mater. Electron., 2009, 20, 685.

8. M.A. Dudek, N. Chawla, Metall. Mater. Trans., 2010, 41A, 610.

9. L.-L Gao, S.-B Xue, L. Zhang, Z. Sheng, G. Zeng, F. Ji, J. Mater. Sci. Mater. Electron., 2010, 21, 643.

10. L. Zhang, S.-B Xue, L.-L Gao, Y. Chen, S.-L. Yu, Z. Sheng, G. Zeng, J. Mater. Sci. Mater. Electron., 2009, 20, 1193.

11. Y. Shi, J. Tian, H. Hao, Z. Xia, Y. Lei, F. Guo, J. Alloys Compd., 2008, 454, 180

12. C.M.L. Wu Y.W. Wong, J. Mater. Sci. Mater. Electron., 2007, 80, 398.

13. C.M.L. Wu, J. Electron. Mater., (2002), 31, 921.

14. A. Ramirez, H. Mavoori, S. Jin, Appl. Phys. Lett., 2002, 80, 398.

15. Z. Chen, Y. Shi, Z. Xia, Y. Yan, J. Electron. Mater., 2003, 32, 235.

16. X.-Y Zhao, M.-Q. Zhao, X.-Q. Cui, T.-H. Xu, M.-X. Tong, Trans. Nonferrous Met. Soc. China, 2007, 17, 805.

17. D.Q. Yu, J. Zhao, L. Wang, J. Alloys Compd., 2004, 376, 170.

18. M.A. Dudek, R.S. Sidhu, N. Chawla, M. Renavikar, J. Electron. Mater., 2006, 35, 2088.

19. M.A. Dudek, R.S. Sidhu, N. Chawla, JOM, 2006, 58, 57.

20. T. Chuang, Scripta Mater., 2006, 55, 983.

21. M.A. Dudek, N. Chawla, Acta Mater., 2009, 57, 4588.

22. M.A. Dudek, N. Chawla, J. Electron. Mater., 2009, 38, 210.

23. M.A. Dudek, N. Chawla, Mater. Charac., 2006, 59, 1364.

24. F. Ochoa, X. Deng, N. Chawla, J. Electron. Mater., 2004, 33, 1596.

25. X. Deng, G. Piotrowski, J.J. Williams, N. Chawla, J. Electron. Mater., 2003, 32, 1403.

26. N. Chawla, F. Ochoa, V.V. Ganesh, X. Deng, M. Koopman, K.K. Chawla, S. Scarritt, J. Mater. Sci. Mater. Electron. 2004, 15, 385.

27. X. Deng, R.S. Sidhu, P. Johnson, N. Chawla, Metall. Mater. Trans., 2005, 36A, 55.

28. M.A. Dudek, N. Chawla, Intermetall. 2010, 18, 1016.

29. M. Amagai, Microelectron. Reliab., 2002, 42, 607.

30. S. Fubin, S.W.R. Lee, In Electronic components and technology conference 2006 proceedings, 2006,1196.

31. K.E. Yazzie, H.E. Fei, H. Jiang, N. Chawla, Acta Mater., 2012, 60, 4336.

32. I. Anderson, J. Harringa, J. of Electron. Mater., 2006, 35(1), 94.

33. M. Amagai, Y. Toyoda, T. Ohnishi, S. Akita, In Electronic Components and Technology conference, 2004 Proceeding, 54th, 2004, 2, 1304.

34. F. Ochoa, X. Deng, N. Chawla, J. Electron. Mater., 2004, 33(12), 1596.

35. X. Deng, R.S. Sindu, P. Johnson, N. Chawla, Metall. Mater. Trans. A, 2005, 36(1), 55.

36. D. Ma, W.D. Wang, S.K. Lahiri, J. Appl. Phys., 2002, 91, 3312.

37. K.E. Yazzie, H.X. Xie, J. Williams, N. Chawla, Scripta Mater., 2012, 66, 586.

38. Y.-L. Shen, N. Chawla, E. S. Ege, X. Deng, Acta Mater. 2005, 53, 2633.

39. W. H. Moy, Y.-L. Shen, Microelectron. Reliab. 2007, 47, 1300.

40. Y.-L. Shen, K. Aluru, Microelectron. Reliab. 2010, 50, 2059.

41. Abaqus 6.8, User’s Manual, Dassault Systèmes Simulia Corp., Providence, RI.

42. H.X. Xie, N. Chawla, Y.-L. Shen, Microelectron. Reliab., 2011,51,1142.

43. N. Chawla, Y.-L. Shen, X. Deng, E.S. Ege, J. Electron. Mater., 33(12), 1589.

44. Y.-L. Shen, N. Chawla, E.S. Ege, X. Deng, Acta Mater., 53(9), 2633.

5. THERMAL AND MECHANICAL STABILITY OF CE-CONTAINING SN-3.9AG-0.7CU LEAD-FREE SOLDER ON CU AND ELECTROLESS NI-P METALLIZATIONS

5.1 Abstract

Rare-earth containing solders have been shown to exhibit improvements in both physical and mechanical properties. However, the reactive nature of RE elements with oxygen may degrade the mechanical properties even under room temperature aging. In this article, we report on the microstructure and mechanical properties of as-processed and thermal aged Ce-containing Sn-3.9Ag-0.7Cu solder reflowed on electroless Ni-P and Cu metallizations. The microstructure of both as-reflowed and thermal aged Ce-containing Sn-3.9Ag-0.7Cu solder joints are more refined compared with conventional Sn-3.9Ag-0.7Cu solder joints. The $(Cu,Ni)_6Sn_5$ intermetallic layer formed at Cu/Ce-containing solder interface is thinner than that of Sn-3.9Ag-0.7Cu solder. The monotonic shear behavior of as-reflowed and thermal aged Sn-3.9Ag-0.7Cu-0.5Ce/Cu and electroless Ni-P lap shear joints was studied, and compared with Sn-3.9Ag-0.7Cu. It was found that both as-reflowed and thermal aged Ce-containing Sn-3.9Ag-0.7Cu exhibit higher strain-to-failure compared with Sn-3.9Ag-0.7Cu solder joints.

5.2 Introduction

In recent years, a series of eutectic of near-eutectic Sn-Ag-Cu alloys have been proposed as replacements of Pb-Sn solder, due to their superior creep and fatigue resistance [1-5]. However, adding excessive amount of Ag and Cu often

results in formation of rigid large Ag_3Sn plates and Cu_6Sn_5 particles, which also result in low ductility and poor mechanical shock resistance [6, 7].

In our previous work, we have shown that Sn-3.9Ag-0.7Cu Pb-free solder alloys doped with small amounts of La [8, 9] and Ce [10] elements posses refined microstructure, reduced Cu_6Sn_5 intermetallic compound (IMC) layer thickness, and, most importantly, significantly increased ductility compared to Sn-3.9Ag-0.7Cu alloy. Such enhanced ductility has profound implications for improving the mechanical shock resistance of solder joints.

Due to the reactive nature of rare-earth element with oxygen [11], rare-earth containing solder may experience severe oxidation and degradation in mechanical properties, wettability [12-15] and rapid formation of Sn whiskers on the solder surfaces [16, 17]. We have reported that Ce-based solder alloys are much less prone to oxidation but still exhibit the desirable attributes of microstructural refinement and increased ductility relative SAC as in the La-based solders [11]. However, little work has been conducted on the thermal stability of Ce containing solder, especially mechanical stability. Much work remains to be done in order to understand the effect of thermal aging on the microstructure and mechanical properties of rare-earth containing solder joint.

Additionally, electroless Ni-P metallization has been widely used as diffusion barrier for Cu due to its excellent properties and low cost [18, 19]. It is well known that interfacial reaction between Sn-rich alloys and Ni-P metallization results in the formation of Ni-Sn or Ni-Sn-Cu intermetallic layers. The nature of this reaction depends on the Cu content in the lead-free solder, and a thin P-rich

layer formed between the IMC and the Ni-P layer formed during the reflow process [20-22]. Relatively few studies have been done on the solderability and mechanical properties of Ce-containing lead-free solder joint on Ni-P metallization. It has been reported, however, that the addition of RE elements do not alter the composition of the intermetallic layer formed on electroless Ni-P substrate, The addition of RE does reduce the rate of increase in IMC thickness, and decrease in shear strength of SnAgCu solder during thermal aging [14, 23].

In this study, we investigated the interfacial reaction between Ce-containing Sn-3.9Ag-0.7Cu and eletroless Ni-P metallization. Isothermal aging was conducted on Sn-3.9Ag-0.7Cu and Sn-3.9Ag-0.7Cu-0.5Ce solder joint on Cu and Ni-P metallization. The microstructure and mechanical properties of Sn-3.9Ag-0.7Cu-0.5Ce solder joints was studied, and compared with that of Sn-3.9Ag-0.7Cu solder joints. It will be shown that the ductility of Ni-P based solder joint can be significantly enhanced with adding trace amount of Ce. Ce-containing solder have excellent oxidation resistance so that thermal aged Ce-containing solder still exhibited larger strain-to-failure in comparison with aged Sn-3.9Ag-0.7Cu solder joints.

5.3 Materials and Experimental Procedure

Vacuum-melted ingots of Sn-3.9Ag-0.7Cu and Sn-3.9Ag-0.7Cu with 0.5 wt% Ce were prepared. High purity Sn-3.9Ag-0.7Cu ingots (Indium) were cut into small rectangular pieces (6.5mm × 6.5mm ×13mm) and mixed with Ce shot (ESPI, 99.995% pure). Due to the reactive nature of pure Ce with oxygen, the materials were mixed in a quartz ampoule (12 mm in diameter) under a sealed

glove box in helium atmosphere. The quartz ampoule was then evacuated to 10^{-5} Torr and sealed. The sealed ampoules were heat treated at 1,000°C for 4 h, and periodically mixed by rotation of the ampoule, in order to homogenize the liquid metal. The ampoules werewater quenched, removed from the ampoule, and sectioned. The Sn-Ag-Cu ingot was prepared by the same process as the Sn-3.9Ag-0.7Cu-0.5Ce ingot.

Thermal and mechanical stability tests were performed on solder/metallization single lap shear joint. Two different metallizations were studied: oxygen free Cu and electroless Ni-P plated Cu bars. Oxygen free copper bars (50.8 mm and 6.35 mm in thickness) were polished to a 0.05 μm finish with colloidal silica solution. Electroless Ni-P substrate was fabricated by depositing 7 μm Ni-P layer on the polished Copper bars with an immersion Au-Pd layer (0.1 μm) plating on top to avoid oxidation of the nickel surface. A graphite mask was applied to the Cu or Ni-P bars, leaving a 6.35 mm by 6.35 mm area for reflow. A rosin mildly activated (RMA) flux was applied to the unmasked potions of the Cu or Ni-P bars to improved wetting between the metallization and the solder. The entire assembly was heated on a digital hot plate. The standard reflow profile is described as follow: the assembly was held at 170°C for 120 seconds to allow excess flux to vaporize. The temperature was then raised over the melting point of Sn-3.9Ag-0.7Cu (240 °C) and held for 40 seconds. The assembly was then removed from the hot plate and air cooled on an aluminum heat sink. The temperature in the solder was monitored using a thermocouple, and a reproducible cooling rate of 0.6 °C/s was obtained. The cooling rate was measured from the

peak temperature to 150 °C, because the joint microstructure does not change significantly below this temperature during cooling [24, 25].

Microstructure characterization was conducted on the lap-shear joints reflowed on Cu or Ni-P substrate before and after thermal aging. Lap-shear joints were sectioned and polished to a final finish of 0.05 μm colloidal silica. Optical microscopy, scanning electron microscopy (SEM), and image analysis were conducted to quantify the microstructure. This included secondary Sn dendrite size and $CeSn_3$ intermetallic size. Energy dispersive spectroscopy (EDS) analysis was also used to confirm the composition of the electroless plated Ni-Au metallization and intermetallic layer. Quantitative microstructure characterization was conducted using image analysis software (ImageJ, Gaithersburg, MD). Both optical and SEM micrographs were segmented into black and white images. The intermetallic phases of interest were fit to ellipses to estimate their size and aspect ratio.

The strength and ductility of as-reflowed and thermal aged joints were evaluated by monotonic shear test using a servo-hydraulic load frame at a nominal shear strain rate of 10^{-1} s^{-1}.

5.4 Results and Discussion

5.4.1 Microstructural characterization of as-reflowed solder joints

Representative microstructures of as-reflowed Sn-3.9Ag-0.7Cu and Sn-3.9Ag-0.7Cu-0.5Ce solder joints are shown in Fig. 16. As expected, the microstructure of near-eutectic Sn-3.9Ag-0.7Cu solder joint on both Cu and Ni-P metallization consisted of Sn-dendrites and a eutectic mixture of Ag_3Sn and

Cu_6Sn_5 intermetallics distributed in a Sn-rich matrix. Electroless Ni-P substrate had no noticeable effect on the microstructure of the as-reflowed solder, although a small amount of $AuSn_4$ intermetallic particles formed in the solder matrix. The alloys doped with Ce formed dendritic RE-Sn intermetallic particles. The Ce-Sn phase diagram predicts the formation of an intermetallic phase, $CeSn_3$, for Sn concentrations greater than 73 wt% Sn. EDS results confirmed that the atomic ratio between Sn and Ce is approximately 3:1. The Sn dendrite size for as-reflowed solder joints is shown in Table 1. A smaller Sn dendrite size in as-processed Ce-containing joints indicates that the microstructure was refined by addition of RE element. The microstructural refinement of Sn matrix in Ce-containing solder joint is due to the large amount of heterogeneous nucleation sites provided by $CeSn_3$ [9] and reduced undercooling [26].

Figures 17 and 18 show the metallization/solder interface for Cu and Ni-P substrates. Both Sn-3.9Ag-0.7Cu and Sn-3.9Ag-0.7Cu-0.5Ce reacted with the Cu substrate forming a thin Cu_6Sn_5 layer with nodular morphology. The intermetallic layer thickness was measured from SEM images and is shown in Table 3. Note that the intermetallic layer thickness in Ce-containing Sn-3.9Ag-0.7Cu is approximately 50% lower than that of the Sn-3.9Ag-0.7Cu alloy. Thickness of brittle Cu_6Sn_5 intermetallic layer plays a crucial role in mechanical shock behavior of lead-free solder joint, that strength of solder joint under high-strain rate tests is controlled by the strength of intermetallic layer and joints with thicker intermetallic layer are more prone to brittle fracture in the joints [27]. Therefore, thinner Cu_6Sn_5 intermetallic layer in Ce-containing could potentially improve the

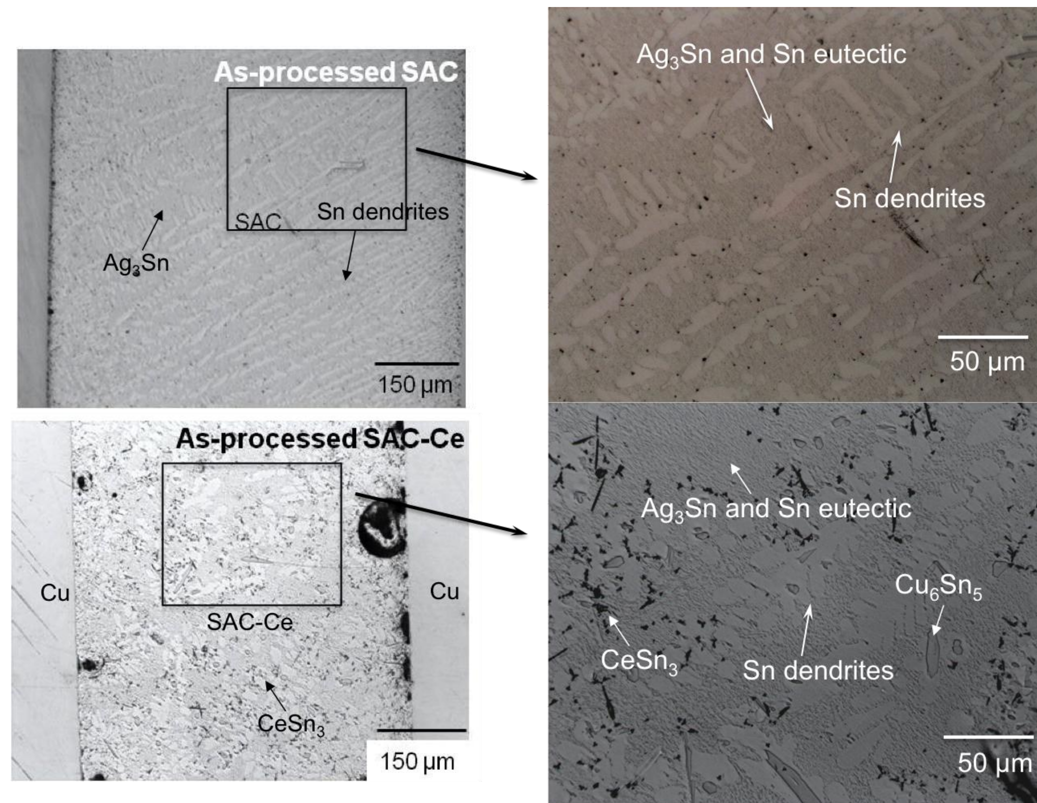

Figure 16. Optical microscopy images of as-reflowed Sn-3.9Ag-0.7Cu (top raw) and Sn-3.9Ag-0.7Cu-0.5Ce (bottom raw).

mechanical shock resistance of Sn-3.9Ag-0.7Cu solder joint [28]. Decreasing in intermetallic layer thickness of rare-earth solder systems has been widely reported in the literature [29, 30]. The reason for this phenomenon was explained by the aggregation of rare earth element between solder and Cu_6Sn_5 interfacial layer and therefore retard the growth of Cu_6Sn_5 layer [31,32]. However, such rare-earth rich layer was failed to observe at solder/metallization interfacial region. As mentioned above, Ce was aggregated inside the Sn-rich solder in the form of $CeSn_3$ intermetallic which agrees very well with Sn-Ce phase diagram. Additionally, a detailed TEM analysis indicating that the tin grains nucleate and grow from the faceted edges of the $RESn_3$ IMC [9]. Thus, we believe that reduced intermetallic thickness in Ce-containing solder joints can be explained by a lower time for solder remains in liquid state due to lower undercooling in Ce-doped solder alloy, and a lower time for the reaction between solder and metallization consequently [10]. Upon reflow, the intermetallic layer formed at the solder/Ni-P interface had a very different morphology than the scallop-like Cu_6Sn_5 layer observed on Cu substrate, as shown in Fig. 18. The morphology of intermetallic formed in Sn-3.9Ag-0.7Cu and Sn-3.9Ag-0.7Cu-0.5Ce on Ni-P substrate was similar, with a faceted-like morphology. As with the Cu_6Sn_5 intermetallic layer, the IMC layer thickness on Ni-P substrate was measured from SEM images and summarized in Table 3. As expected, the intermetallic layer on Ni-P substrate is significantly thinner than that on Cu substrate due to the existence of the Ni diffusion barrier. It is interesting to note that the thickness of intermetallic layer in

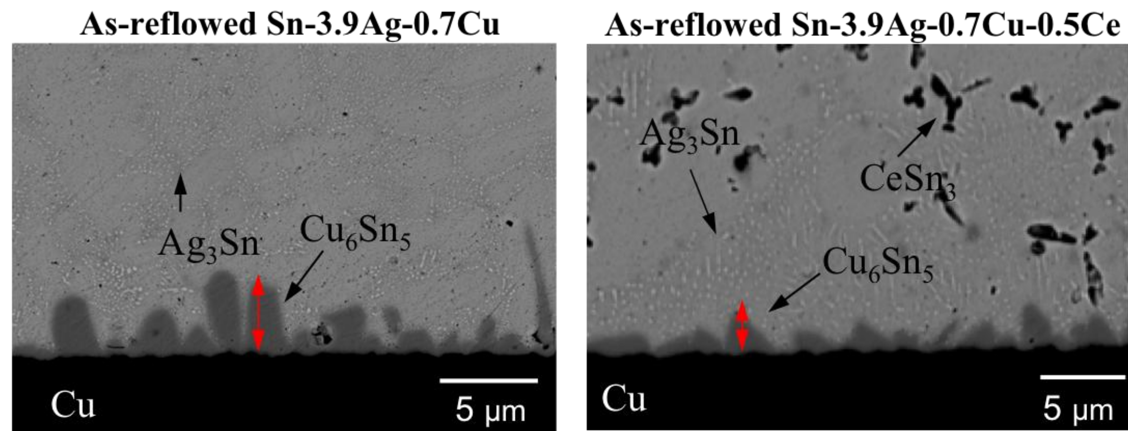

Figure 17. Backscatter electron microscopy images of as-reflowed Sn-3.9Ag-0.7Cu and Sn-3.9Ag-0.7Cu-0.5Ce on Cu substrate.

Table 3. Summary of microstructure characterization results for as-reflowed and thermal-aged Sn-3.9Ag-0.7Cu and Sn-3.9Ag-0.7Cu-0.5Ce/Cu and Ni-P joints.

		Sn-3.9Ag-0.7Cu				Sn-3.9Ag-0.7Cu-0.5Ce			
		As-reflowed		Thermal-aged		As-reflowed		Thermal-aged	
		Cu	Ni-P	Cu	Ni-P	Cu	Ni-P	Cu	Ni-P
β-Sn dendrites	Secondary dendrite length (μm)	15.5±7.4	21.8±13.5	24.7±9.4	25.6±10.2	11.7±8.3	13.6±5.8	21.9±13.5	19.9±8.7
	Secondary dendrite spacing (μm)	10.4±4.9	13.7±7.0	14.2±6.7	14.8±6.6	8.9±4.6	9.5±3.0	12.8±9.3	15.8±6.1
IMC layer	Thickness (μm)	4.0±2.1	2.2±0.4	6.3±2.3	2.1±0.5	2.6±1.0	1.5±0.6	4.1 ±1.7	2.1±0.8
$CeSn_3$ IMC particle size	Major axis (μm)	N/A	N/A	N/A	N/A	2.5±1.2	3.5±2.8	2.5±1.6	3.4±1.4
	Minor axis (μm)	N/A	N/A	N/A	N/A	1.3±0.5	1.9±0.9	1.2±0.4	2.1±0.6
	Aspect ratio	N/A	N/A	N/A	N/A	2.1±1.2	1.8±0.1	2.1±1.0	1.7±0.4

as-processed Sn-3.9Ag-0.7Cu-0.5Ce is even smaller than that of Sn-3.9Ag-0.7Cu solder/Ni-P joint. The composition of this IMC layer was investigated using EDS line scans, as shown in Fig. 18. It is quite clear that Sn, Cu and Ni is uniformly distributed in the IMC layer indicating that only one type of intermetallic formed during reflow. After reflow, the immersion Au layer was rapidly dissolved in the solder and formed $AuSn_4$ IMC particles inside the solder matrix. A P-rich (Ni_3P) region is present in between Cu-Ni-Sn IMC layer and the Ni-P layer due to Ni diffusion from original Ni-P to intermetallic layer [33]. As a result of self-diffusion of Ni atoms in Ni-P layer, Kirkendall voids could form and grow inside P-rich layer during reflow and thermal annealing [33, 34]. Large amount of Kirkendall voids existing in P-rich layer could deteriorate the mechanical performance of Ni-P based solder joints. It is also interesting to note that a significant amount of Cu existed in the intermetallic layer. There are two available Cu resources in the Ni-P based solder joint, the oxygen-free copper substrate beneath the Ni-P layer and Cu in the Sn-3.9Ag-0.7Cu solder matrix. The Ni layer plated on Cu metallization is fairly thick and remains after reflow. Thus, it is unlikely for Cu to diffuse from Cu metallization through this barrier and react with the molten solder. Studies on interfacial reaction between solders without Cu and Ni-P showed that only needle-like Ni_3Sn_4 was formed [35]. Thus, we believe that Cu diffused from the solder instead of the Cu metallization. The detailed composition of intermetallic layer was further investigated by EDS, as summarized in Table 4. The atomic ratio distribution of Sn, Ni, Cu indicates that $(Cu,Ni)_6Sn_5$ intermetallic is formed between the solder and Ni-P. This finding

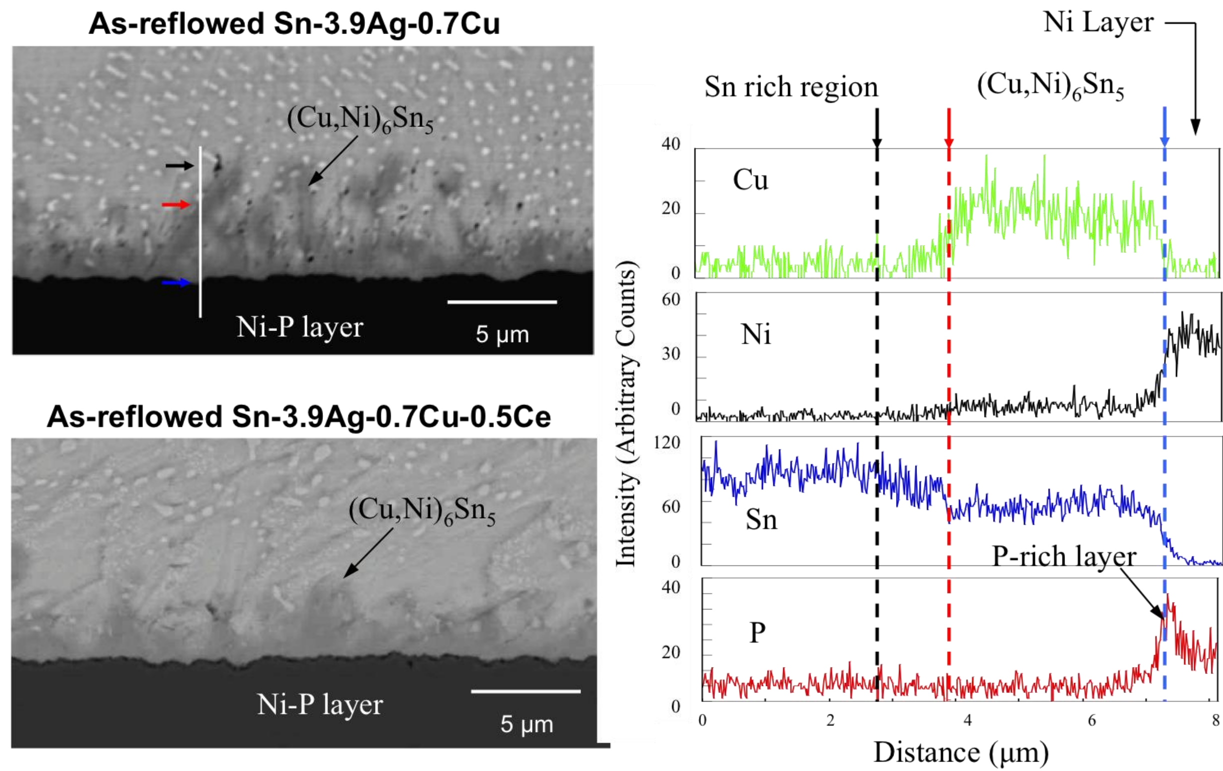

Figure 18. Backscattered electron microscopy images of as-reflowed Sn-3.9Ag-0.7Cu and Sn-3.9Ag-0.7Cu-0.5Ce reflowed on electroless Ni-P substrate.

agrees very well with results from the literature, where it was shown that $(Cu,Ni)_6Sn_5$ intermetallic is formed when the Cu content is higher than 0.7 wt.% [20, 36]. The intermetallic layer formed in Sn-3.9Ag-0.7Cu solder joint was composed of approximately 42 at.% Sn, 25 at.% Ni, and 33 at.% Cu. On other hand, the intermetallic layer formed in Ce-containing SAC solder had a composition of approximately 49 at.% Sn, 17 at.% Ni, and 33 at.% Cu. Clearly the amount of Ni in as-reflowed Sn-3.9Ag-0.7Cu joint is higher than that of Sn-3.9Ag-0.7Cu -0.5Ce joint. The difference in composition and intermetallic thickness between Sn-3.9Ag-0.7Cu and Sn-3.9Ag-0.7Cu-0.5Ce solder joints can both be explained by the significantly reduced undercooling in Ce-containing Sn-3.9Ag-0.7Cu, which results in less time for Ni to diffuse through intermetallic. Therefore, one may expect that the formation of a P-rich layer and potential Kirkendall voids to be retarded in as-processed Ce-containing solder joint during reflow.

Table 4. Composition of $(Cu,Ni)_6Sn_5$ layer in as-reflowed and thermal-aged Sn-3.9Ag-0.7Cu and Sn-3.9Ag-0.7Cu-0.5Ce/Ni-P joints.

Alloys	SnL (At%)	NiK (At%)	CuK (At%)
As-reflowed SAC	41.8 ± 1.9	25.3 ± 2.4	32.9 ± 0.6
As-reflowed SAC-Ce	48.7 ± 3.7	16.8 ± 1.4	32.8 ± 4.7
Aged SAC	42.6 ± 1.6	20.6 ±0.7	36.8 ± 1.3
Aged SAC-Ce	45.9 ± 3.1	18.4 ±1.4	35.7 ± 2.1

5.4.2 Microstructural evolution of solder joints after thermal aging

Thermal aging of Sn-3.9Ag-0.7Cu and Sn-3.9Ag-0.7Cu-0.5Ce solders reflowed on Cu and Ni-P joints was performed at 95°C for 250 hours. Typical microstructures of thermal aged solder joints are shown in Fig. 19 (optical microscopy images) and Fig. 20 (backscattered electron microscopy images). Table 3 summarizes quantitative microstructural feature of thermal aged SAC and SAC-Ce solder joints, including $CeSn_3$ IMC size, aspect ratio, interfacial IMC layer thickness. Sn dendrite size in solders/Cu joints increased after annealing indicating the microstructure of aged solder joints coarsened. The IMC layer thickness for both Sn-3.9Ag-0.7Cu and Sn-3.9Ag-0.7Cu-0.5Ce solder joints increased and morphology of Cu_6Sn_5 IMC layer remained scalloped after thermal aging. Note that the IMC layer thickness in thermal aged Ce-containing Sn-3.9Ag-0.7Cu joint is still lower than that of aged SAC joints due to the thinner initial intermetallic layer. The microstructure of thermally aged Ce-containing Sn-3.9Ag-0.7Cu is still finer than that of aged Sn-3.9Ag-0.7Cu. There was no evidence that the addition of trace amount of Ce accelerated or retarded solder microstructure coarsening and IMC layer growth.

The quantitative measurements of $(Cu,Ni)_6Sn_5$ layer thickness before and after aging are shown in Table 3. For the Ni-P metallization, no noticeable Ni layer consumption can be observed and the growth of $(Cu,Ni)_6Sn_5$ intermetallic layer in Sn-3.9Ag-0.7Cu during thermal aging is relatively undetectable, compared with the Cu_6Sn_5 intermetallic layer. This is due to relative low thermal aging temperature. As indicated in literature [21], the growth of $(Cu,Ni)_6Sn_5$

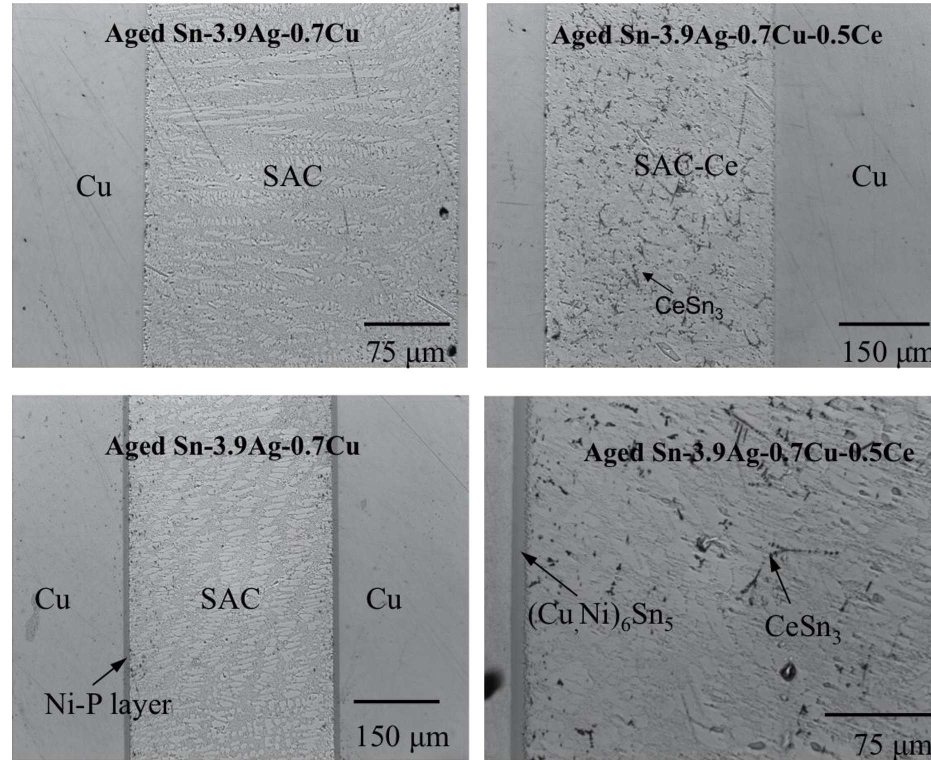

Figure 19. Optical microscopy images of thermal aged Sn-3.9Ag-0.7Cu (left column) and Sn-3.9Ag-0.7Cu-0.5Ce (right column) reflowed on Cu (top row) and electroless Ni-P substrate (bottom row).

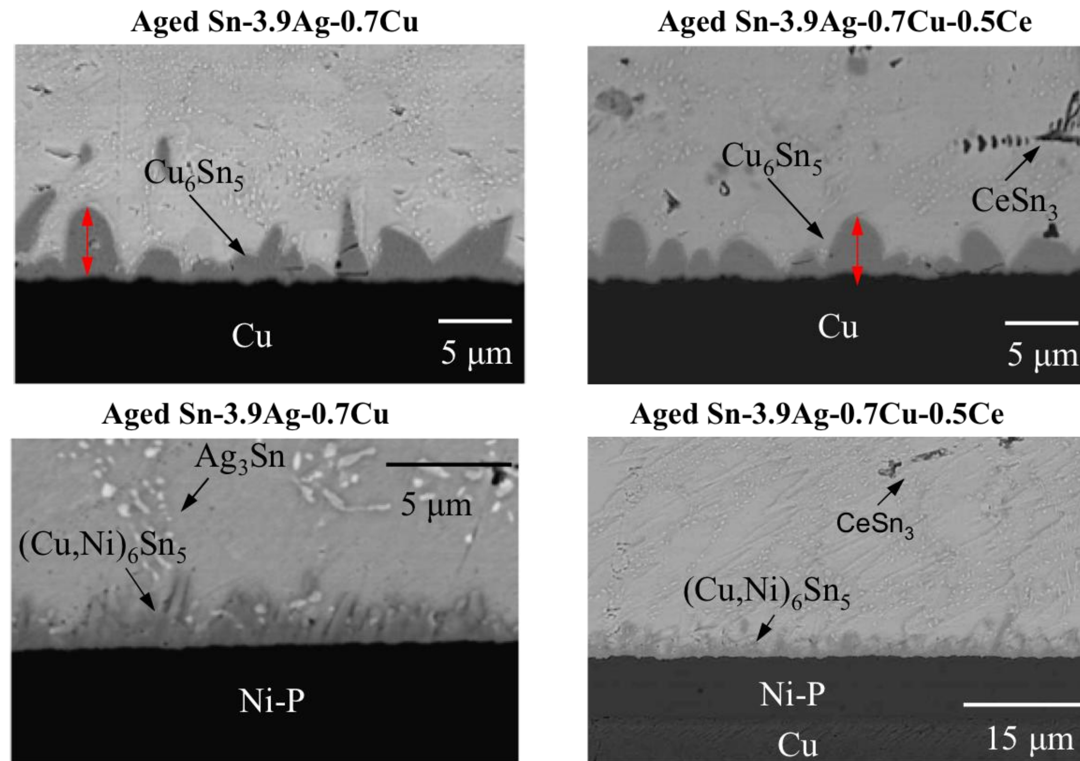

Figure 20. Backscattered electron microscopy images of aged Sn-3.9Ag-0.7Cu (left column) and Sn-3.9Ag-0.7Cu-0.5Ce (right column) on Cu (top row) and electroless Ni-P (bottom row).

intermetallic layer is negligible when the aging temperature is lower than 125 °C. However, note that the initial thinner $(Cu,Ni)_6Sn_5$ layer in Sn-3.9Ag-0.7Cu-0.5Ce solder joints grew up to 2.4 μm after thermal aging which is in the same magnitude as the aged SAC solder joint. As discussed previously, the thinner $(Cu,Ni)_6Sn_5$ IMC layer in as-reflowed Sn-3.9Ag-0.7Cu-0.5Ce joint is due to insufficient time for Cu diffusing from solder matrix to the interface. During thermal aging, remaining Cu in the solder matrix kept on diffusing to interfacial region, results in the growth of IMC layer in Ce-containing solder. On the other hand, IMC layer thickness in Sn-3.9Ag-0.7Cu remained stable during thermal aging. This implies that the growth of $(Cu,Ni)_6Sn_5$ layer on the Ni-P substrate is controlled by the long range Cu diffusion from solders matrix to interfacial region during reflow and low temperature annealing.

The $CeSn_3$ particle size before and after thermal aging was measured based on backscattered scanning electron microscopy images by ImageJ, as shown in Fig. 21. To quantitative measure the microstructure, the BSEM image was segmented into black and white images. Then the $CeSn_3$ IMC particles were fit to ellipses to estimate their size and aspect ratio. Table 3 summarizes the results from quantitative measurement of $CeSn_3$ particle size for both as-reflowed and thermal-aged joints on different metalllizations. For both Cu and Ni-Au metallization, the size of $CeSn_3$ (major axis, minor axis and aspect ratio) is almost identical for as-reflowed and thermal-aged joints, indicating no coarsening of $CeSn_3$ particles during thermal aging. Also note that little oxidization of $CeSn_3$ intermetallic particles took place during thermal aging, and there was no hillock-

type Sn whiskers growth observed surround rare-earth particles. This result is consistence with our previous study on oxidation behavior of rare-earth containing SAC solder alloy that Ce-containing solder has excellent oxidization resistance [11].

5.4.3 Mechanical evolution of solder joint after thermal aging

The representative shear stress-shear strain curves of Sn-3.9Ag-0.7Cu and Sn-3.9Ag-0.7Cu-0.5Ce on Cu metallization are shown in Fig. 22. Table 5 summarizes the mechanical properties of the joints, including ultimate shear strength, strain-to-failure, and work of fracture. Work of fracture was calculated by integration of the stress-strain curve. For the as-reflowed solder/Cu joints, the ultimate shear strength decreased slightly, while the strain-to-failure and work of fracture increased significantly by doping with Ce, nearly 150% over that of the SAC joints. In our previous study on the mechanisms of enhanced ductility of Ce-containing solder joints [37], we have shown that the decrease in ultimate shear strength in as-reflowed Ce-containing solder joints is due to $CeSn_3$ intermetallic particles fracture and debonding under loading, and the increase in ductility with adding Ce is a result of the more homogeneously distributed plastic strain due to relatively soft $CeSn_3$ intermetallic particles. Moreover, as indicating by nanoindentation results [38], the $CeSn_3$ intermetallic are relatively compliant, with Young's modulus significantly lower than that of Ag_3Sn and Cu_6Sn_5 intermetallics. It is likely that appreciable amount of deformation takes place in these Ce-containing phases as well, contributing to the enhancement in work of

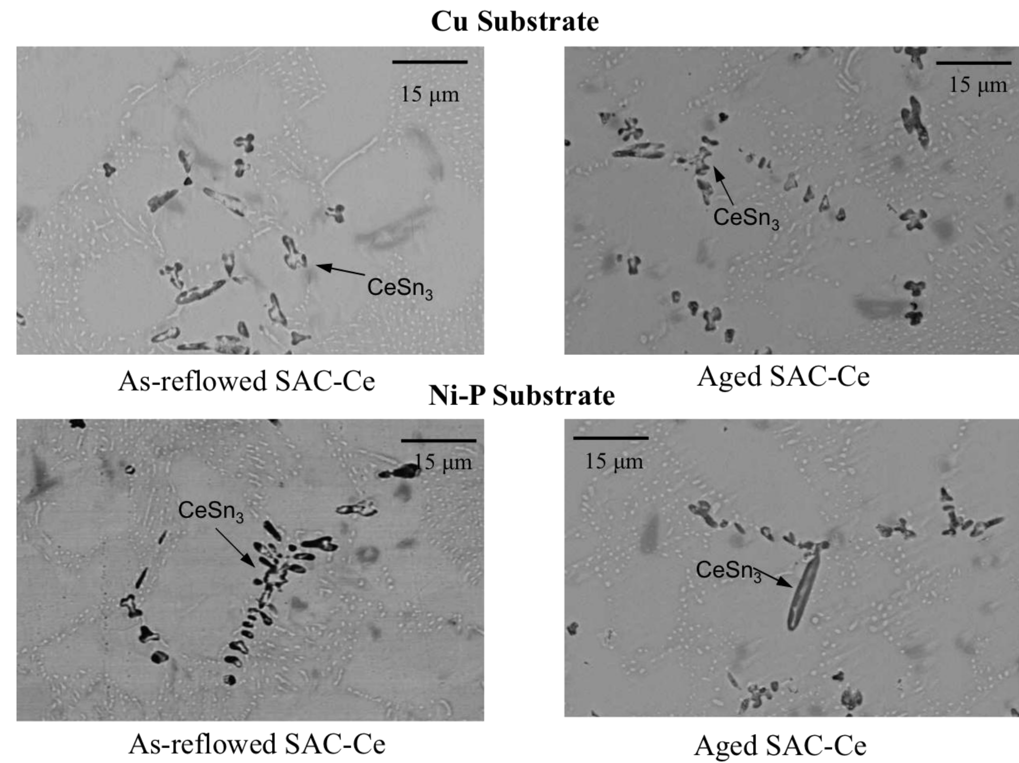

Figure 21. Backscattered electron microscopy images of $CeSn_3$ intermetallic particle formed in as-reflowed (left column) and aged (right column) and Sn-3.9Ag-0.7Cu-0.5Ce on Cu (top row) and electroless Ni-P (bottom row).

fracture. Our preliminary results have shown that such enhanced ductility could improve the shock resistance of Sn-3.9Ag-0.7Cu solder joints [28].

Table 5. Monotonic shear results for as-reflowed and thermal-aged Sn-3.9Ag-0.7Cu and Sn-3.9Ag-0.7Cu-0.5Ce/Cu joints.

	Sn-3.9Ag-0.7Cu		Sn-3.9Ag-0.7Cu-0.5Ce	
	As-reflowed	Thermal-aged	As-reflowed	Thermal-aged
Ultimate Shear Strength (MPa)	23.4 ± 4.0	25.2 ± 3.0	22.7 ± 3.5	21.9 ± 3.5
Strain to Failure (Pct)	103.3 ± 77.3	129.5 ± 30.4	155.5 ± 35.1	197.7 ± 38.0
Work of fracture (J/m^3)	14.2 ± 2.9	22.0 ±7.0	21.6 ± 8.9	23.4 ± 6.6

After thermal aging, both Sn-3.9Ag-0.7Cu and Sn-3.9Ag-0.7Cu-0.5Ce solder joints experienced a decrease in ultimate shear strength but increase strain-to-failure and work of fracture, which can be explained by solder matrix softening [39, 40]. Due to the concern of oxidation induced degradation in mechanical performance of rare-earth containing solder joint, it is important to compare mechanical property of aged Ce-containing solder with conventional lead-free solder joints. It is interesting to note that over all strain-to-failure and work of fracture of aged Sn-3.9Ag-0.7Cu-0.5Ce solder joint is still larger than that of aged Sn-3.9Ag-0.7Cu joints, indicating that Ce element did not undergo severe oxidation. Thus, it is safe to state that the ability of $CeSn_3$ particles on enhanced ductility was not compromised by thermal aging.

The representative shear behaviors of Sn-3.9Ag-0.7Cu and Sn-3.9Ag-0.7C-0.5Ce on electroless Ni-P metallization are shown in Fig. 23, respectively. Table 6 summarized shear behavior of the joints, including ultimate shear strength, strain-to-failure and work of fracture. The trend of mechanical evolution of Sn-3.9Ag-0.7Cu and Sn-3.9Ag-0.7Cu-0.5Ce solder joints on electroless Ni-P metallization is similar to those on Cu metallization. As mentioned above, the microstructure characterization did not reveal significant difference between Cu and Ni-P metallization except the interfacial intermetallic layer and trace amount $AuSn_4$ particles formed during reflow process, because the microstructure of solder matrix is controlled by cooling rate and aging history which is same for both metallizations. The quasi-static shear behavior of solder joint is primarily controlled by the mechanical properties of the solder body, instead of the intermetallic layer [41]. Therefore, the improvement of ductility in Ni-P based Sn-3.9Ag-0.7Cu solder joint with adding trace amount Ce element, as well as lower ultimate shear strength can be expected. Similar as Cu based solder joint, the strain-to-failure and work of fracture of aged Ce-containing solder is larger than that of aged Sn-3.9Ag-0.7Cu solder joint. Nonetheless, the addition of Ce does not deteriorate the mechanical shear performance Sn-3.9Ag-0.7Cu solder joints after elevated temperature aging.

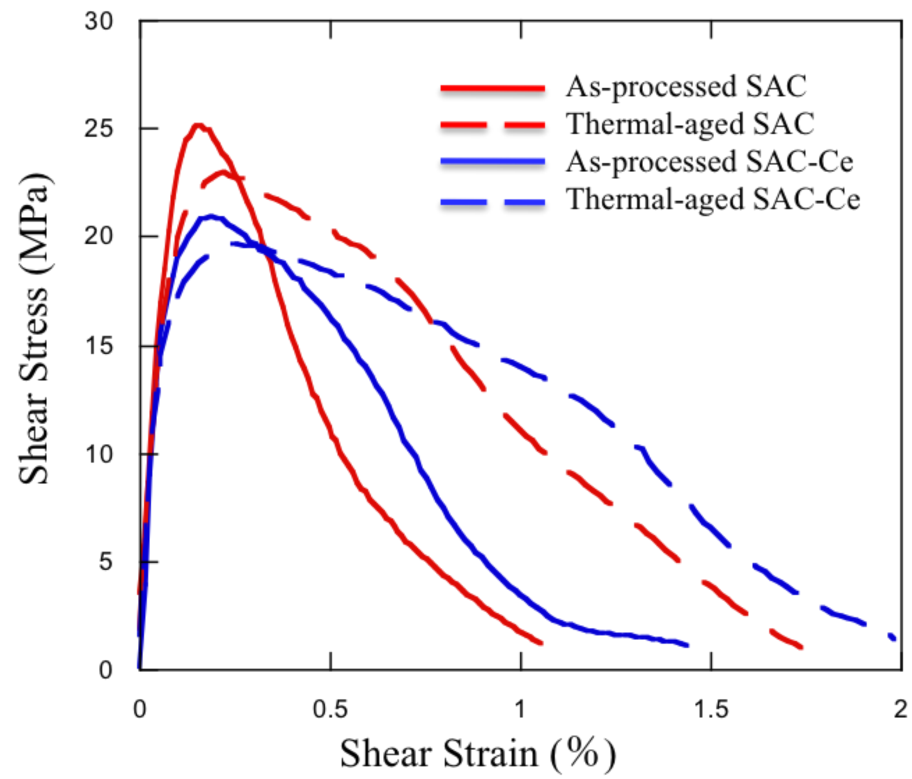

Figure 22. Shear-stress-vs-shear-strain curve for as-reflowed and thermal aged Sn-3.9Ag-0.7Cu and Sn-3.9Ag-0.7Cu-0.5Ce/Cu joints tested in monotonic shear.

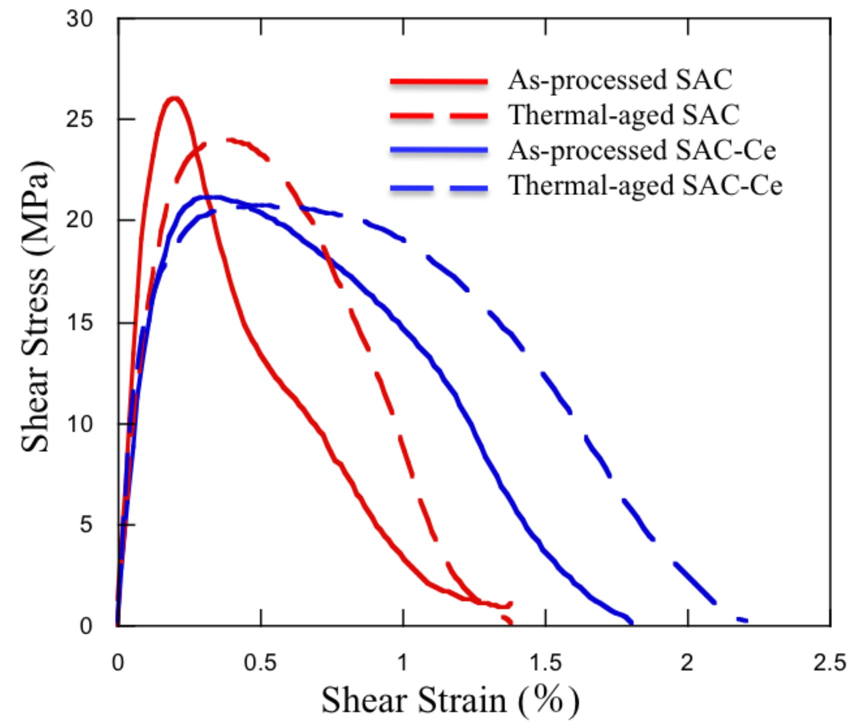

Figure 23.Shear-stress-vs-shear-strain curve for as-reflowed and thermal aged Sn-3.9Ag-0.7Cu and Sn-3.9Ag-0.7Cu-0.5Ce/Ni-P joints tested in monotonic shear.

Table 6. Monotonic shear results for as-reflowed and thermal-aged Sn-3.9Ag-0.7Cu and Sn-3.9Ag-0.7Cu-0.5Ce/Ni-P joints.

	Sn-3.9Ag-0.7Cu		Sn-3.9Ag-0.7Cu-0.5Ce	
	As-reflowed	Thermal-aged	As-reflowed	Thermal-aged
Ultimate Shear Strength (MPa)	26.0 ±4.8	25.9± 3.5	24.5± 4.1	21.9± 4.5
Strain to Failure (Pct)	120.6 ± 59.9	129.7± 33.5	152.5 ± 37.2	195.3 ± 39.5
Work of fracture (J/m^3)	15.8 ±11.1	22.5 ±8.1	21.1 ±7.2	30.2 ±9.4

5.5 Conclusions

The reliability performances of Ce-containing Sn-3.9Ag-0.7Cu/Cu and Ni-P joints was studied in form of isothermal aging, and compared with conventional Sn-3.9Ag-0.7Cu joints. The following conclusions are drawn from the experimental results:

- Addition of Ce results in Sn microstructure refinement and reduced intermetallic layer thickness on both Cu and electroless Ni-P substrate.
- Interfacial intermetallic layer formed between solders/Ni-P is identified as $(Cu,Ni)_6Sn_5$ for both Sn-3.9Ag-0.7Cu and Sn-3.9Ag-0.7Cu-0.5Ce solder by EDS results.
- The overall intermetallic layer in aged Sn-3.9Ag-0.7Cu/Cu joints is lower than that of aged Sn-3.9Ag-0.7Cu joint due to thinner initial layer.

- Monotonic-shear results of as-reflowed joints show that Ce-containing Sn-3.9Ag-0.7Cu joints exhibit enhanced ductility on both Cu and Ni-P substrate.
- Ce-containing Sn-3.9Ag-0.7Cu have excellent oxidation resistance that mechanical performance of Ce-containing joints does not deteriorate by isothermal aging.

5.6 Reference

1. H. Ma, J. Suhling, J. Mater. Sci., 2009, 44, 1141.
2. S. Kang, A. Sarkhel, J. Electron. Mater., 1994, 23, 701.
3. S. Wiese, K.J. Wolter, Microelectron. Reliab., 2004, 44, 1923.
4. S. Kang, IBM J. Res. Dev., 2005, 49, 607.
5. N. Chawla, Int. Mater. Rev., 2009, 54, 368.
6. I. E. Anderson, J. Mater. Sci.: Mater. Electron., 2007, 18, 55.
7. N.C. Lee, Mater.Adv. Packaging, 2009 p. 181.
8. M. Dudek, R.S. Sidhu, N. Chawla, M. Renavikar, J. of Electron. Mater., 2006, 35 2088.
9. M. Dudek, R. Sidhu, N. Chawla, JOM, 2006, 58, 57.
10. M. Dudek, N. Chawla, Metall. Mater. Trans. A, 2010, 41, 610.
11. M. Dudek, N. Chawla, J. of Electron. Mater., 2009, 38, 210.
12. Y. Shi, J. Tian, H. Hao, Z. Xia, Y. Lei, F. Guo, J. Alloys Compd., 2008, 453, 180.
13. L. Gao, S. Xue, L. Zhang, Z. Sheng, G. Zeng, F. Ji, J. Mater. Sci.: Mater. Electron., 2010, 21, 643.
14. C.M.L. Wu, D.Q. Yu, C.M.T. Law, L. Wang, Mater. Sci. Eng.: R, 2004, 44 1.

15. D.Q. Yu,, J. Zhao, L. Wang, J. of Alloys Compd.,2004, 376170.

16. T.-H. Chuang, Scripta Mater., 2006, 55, 983.

17. T.-H. Chuang, Metall. Mater. Trans. A, 2007, 38, 1048.

18. C.-Y. Lee, K.-L. Lin, Thin Solid Films, 1994, 249, 201.

19. A.J.G. Strandjord, S. Popelar, C. Jauernig, Microelectron. Reliab., 2002, 42, 265.

20. K. Zeng,, V. Vuorinen, J.K. Kivilahti. Electronic Components and Technology Conference, Proceedings, 2001.

21. A. Sharif, Y.C. Chan, M.N. Islam, M.J. Rizvi, J. Alloys Compd., 2005, 388, 75.

22. Y.-D. Jeon, S. Nieland, A. Ostmann, H. Reichi, K.-W Paik, et al., J. Electron. Mater., 2003, 32, 548.

23. C.M.T. Law, C.M.L. Wu, Proceeding of the Sixth IEEE CPMT Conference. 2004.

24. F. Ochoa,, X. Deng, N. Chawla, J. Electron. Mater., 2004, 33, 1596.

25. X. Deng, G. Piotrowski, J.J. Williams, N. Chawla, J. Electron. Mater. 2003, 32, 1403.

26. H.X. Xie, L. Jiang, N. Chawla, Unpublished research, 2012.

27. K.E. Yazzie, H.X. Xie, N. Chawla, Scripta Mater., 2012, 66, 586.

28. H.X. Xie, N. Chawla, unpublished research, 2012.

29. C. Wu, Y. Wong, J. Mater. Sci.: Mater. Electron., 2007, 18, 77.

30. L. Zhang, S. Xue, G. Zeng, L. Gao, Y. Huan, J. Alloys Compd., 2012, 510, 38.

31. B. Lu, H. Li, J. Wang, H. Zhu, X. Jiao, J. Central South University of Technology, 2008, 15, 313.

32. H. Hao, Y. Shi, Z. Xia, Y. Lei, F. Guo, J. of Electron. Mater., 2008, 37, 2.

33. A. Kumar, M. He, Z. Chen, Surface and Coatings Technology, 2005. 198(1-3), 283.

34. P. Sun, C. Anderson, X. Wei, Z. Cheng, D. Shangguan, J. Liu, J. Alloys Compd., 2006, 425(1-2), 191.

35. A. Kumar, M. He, Z. Chen, Surf. Coat. Technol., 2005, 198 283.

36. D.Q. Yu, C.M.L Wu, D.P. He, N. Zhao, L. Wang, J.K.L. Lai, J. Mater. Res., 2005, 20, 8.

37. H.X. Xie, N. Chawla, Y.-L Shen, Microelectron. Reliab., 2011, 51, 5.

38. M. Dudek, N. Chawla, Intermetallics, 2010, 18, 1016.

39. I. Dutta, P. Kumar, G. Subbarayan, JOM, 2009, 61, 29.

40. O. Shengquan, Y. Xu, K.N. Tu, M.O. Alam, Y.C. Chan, Electronic Components and Technology Conference, Proceedings. 2005.

41. X. Deng, R. Sidhu, P. Johnson, N. Chawla, Metall. Mater. Trans. A, 2005, 36, 55.

6. EFFECT OF CERIUM ADDITION ON WETTING, UNDERCOOLING AND VOLUME EFFECT OF SN-3.9AG-0.7CU LEAD-FREE SOLDER

6.1 Abstract

In this article, we report the effect of cerium (Ce) addition on wettability, microstructure and mechanical properties of Sn-3.9Ag-0.7Cu (SAC) solders. It was found that the wettability of Ce-containing solder on Cu substrate is comparable to that of SAC solder. The microstructure of lap-shear joints containing 0.5 wt. pct Ce rare-earth elements showed finer microstructure and a thinner Cu_6Sn_5 intermetallic layer at the Cu/solder interface. Using differential scanning calorimetry (DSC), it was found that the magnitude of undercooling was significantly reduced with the addition of Ce. The monotonic shear behavior of reflowed Sn-3.9Ag-0.7Cu-0.5Ce (SAC-Ce)/Cu lap shear joints was studied, and compared with the SAC alloy. Ce-containing alloys exhibited a slight decrease in the ultimate shear strength, but higher elongation and work of fracture compared with SAC. The effect of Cu_6Sn_5 intermetallic layer thickness on ductility was also studied. It was found that the presence of $CeSn_3$ intermetallic particles, and not the thin Cu_6Sn_5 intermetallic layer, were responsible for the improved ductility demonstrated by Ce-containing solders.

6.2 Introduction

With the increasing concerns over the intrinsic toxicity of Pb [1], several novel Sn-rich Pb-free solders have been developed as replacements for Pb-Sn solder in electronic industry [2-3]. Among those Pb-free solder alloys, Sn-Ag-Cu alloys have been considered as one of the most promising alternatives for Pb-Sn

solder [4-5]. However, due to the brittle nature of Ag and Cu containing intermetallic compounds, the Sn-Ag-Cu alloys often exhibit poorer damage tolerance than Pb-Sn [6-7].

In recent years, rear-earth (RE) elements have been selected as a fourth alloying element for the Sn-Ag-Cu solder system to improve both physical and mechanical properties [8-18]. It has been shown that the addition of different RE elements can decrease the alloy melting temperature [8-9], enhance the wetting behavior [9-12], refine solder microstructures [12-15], and, in particular, improve mechanical performance [10, 12, 15-18]. Regarding mechanical properties, improvements in tensile strength [12,15-17], ductility [16,18], and creep resistance [16,17] due to addition of RE elements in SAC alloys have been reported.

In our previous reports, it has been shown that both shear strain-to-failure and work of fracture of Sn-3.9Ag-0.7Cu sold joints can be significantly increased by adding trace amount of La and Ce (nearly 50% over that of SAC, with a small penalty in ultimate shear strength) [20-22]. Additionally, Ce-based alloys are less prone to oxidation and Sn whiskering [23,24] and have excellent thermal stability [22], compared with other RE containing SAC alloys. Thus, Ce-containing SAC solders are promising alloys, due to their excellent mechanical properties as well as better oxidation resistance. However, few studies on the wettability of rare-earth containing solders have shown a large discrepancy [25,26]

Due to the increasing functionality in small electronic devices, solder pitch size will decrease down significantly [27]. Volume variations in solder joint

causes a different microstructural and mechanical behavior [28-30]. To our knowledge, a thorough study on the volume effect of RE-containing SAC solder is almost non-existent.

In this study, wettability, solidification and volume effect of Ce-containing SAC solders were examined. The effect of Ce addition (0.5 wt. pct) on microstructure and physical behavior of SAC alloy was investigated and compared to SAC alloy. It will be shown that the refined microstructure of SAC-0.5Ce solder is due to reduced undercooling for solidification from increase in heterogeneous nucleation sites. The size of the solder volume has significant effect on the microstructure evolution within SAC solder joint.

6.3 Materials and Experimental Procedure

Vacuum-melted ingots of Sn-3.9Ag-0.7Cu with trace amount of Ce (0.5 wt.%) were prepared. High purity SAC ingots (Indium, Ithica, NY) were cut into small rectangular pieces (6.5 × 6.5 × 13 mm) and mixed with Ce shot (ESPI, Ashland, OR). Due to the reactive nature of pure Ce with oxygen, the materials were mixed in a quartz ampoule (12 mm in diameter) under a sealed glovebox with helium atmosphere. The quartz ampoule was then evacuated to 10^{-5} torr and sealed. The sealed ampoules were heat treated at 1000°C for 4 hours, and periodically mixed by rotation of the ampoule, in order to homogenize the liquid metal. The ampoules were then water quenched, removed from the ampoule, and sectioned.

The wetting behavior of SAC-0.5Ce was studied by reflowing solder discs on a Copper substrate, and compared to SAC. The ingots of each material were

prepared as described above. Each ingot was sectioned into small disks approximately 10 mm in diameter and 0.6 mm in thickness. The disks were polished and ultrasonically cleaned by acetone before reflow. The copper substrate (20 mm × 20 mm × 7.7 mm) was polished to a final finish with 0.05 μm colloidal silica solution. The specimens were placed on the center of the copper block, and rosin mildly activated (RMA) flux was applied on the surface of the copper substrate. The solder discs were heated up to 250°C at a heating rate of 1°C/s, and then cooled at a nominal cooling rate of 3°C/s. The specimens were maintained above 220 °C for 140 s. The molten solder discs were illuminated by a source of visible light, and the contact angles were recorded by a CCD camera equipped with an appropriate set of lenses. Both spreading area ratio of the as-bonded contact and contact angle of SAC and SAC-0.5Ce on Cu substrate were measured to quantify the wetting behavior of the solder.

Differential scanning calorimetry (DSC) was used to determine the onset of melting and the degree of undercooling for both SAC and SAC-Ce solder alloys. The measurements were conducted in a dry argon atmosphere gas in a calorimeter (model DSC-7, Perkin Elmer). Samples (10 to 20 mg) were punched from the as-cast ingots, slightly polished, and ultrasonically cleaned in acetone. Samples were weighed and placed on Aluminum pans. Samples were then heated and cooled at rates of 0.5 °C/s in the temperature range of 298 K to 573 K (25 °C to 300 °C).

A Cu/solder/Cu sandwich-like structure was used to study volume effect on the microstructural evolution in Ce-containing SAC and SAC solder joints

with different solder volume. SAC-0.5Ce and SAC solder foils, 6.35 mm in diameter and with different thickness (0.2 mm, 0.5 mm, 0.75 mm and 1.00 mm), were reflowed between two polished Cu pellets in a 6061 Al alloy holder to ensure an alignment during reflow and cooling, at a nominal cooling rate of 4 °C/s. The sandwich-like solder joints were sectioned into two specimens, then mounted and polished to a 0.05 microns colloidal silica. These specimens were then examined in an optical microscope and scanning electron microscope to quantify the microstructure of solder matrix and IMC layer thickness.

6.4 Results and Discussion

6.4.1 Wetting behavior of Sn-3.9Ag-0.7Cu and Sn-3.9Ag-0.7Cu-0.5Ce alloys

In order to form a good intermetallic bond between the substrate and the solder, the solder must have adequate wettability on the substrate during reflow process. It is important to investigate the wetting behavior of rare earth-containing alloys, due to concern over the reactive nature of rare-earth elements with oxygen and the possible negative effect on wetting behavior. In this study, the wetting behavior of SAC and SAC-0.5Ce solders on Cu metallization was studied. Typical images recorded during the reflow process are shown in the Fig. 24.

Due to the temperature difference between solder/air interface and solder/substrate contact surface, thermal capillary motion of the molten solder surface resulted in a receding contact angle at solder/Cu interface [31]. Since the reflectivity of the Cu substrate is low, it is very difficult to define a triphase line and then draw a "tangent line" (red arrows in Fig. 24) to measure the contact angle. Normally, the contact angle of solder has been measured by

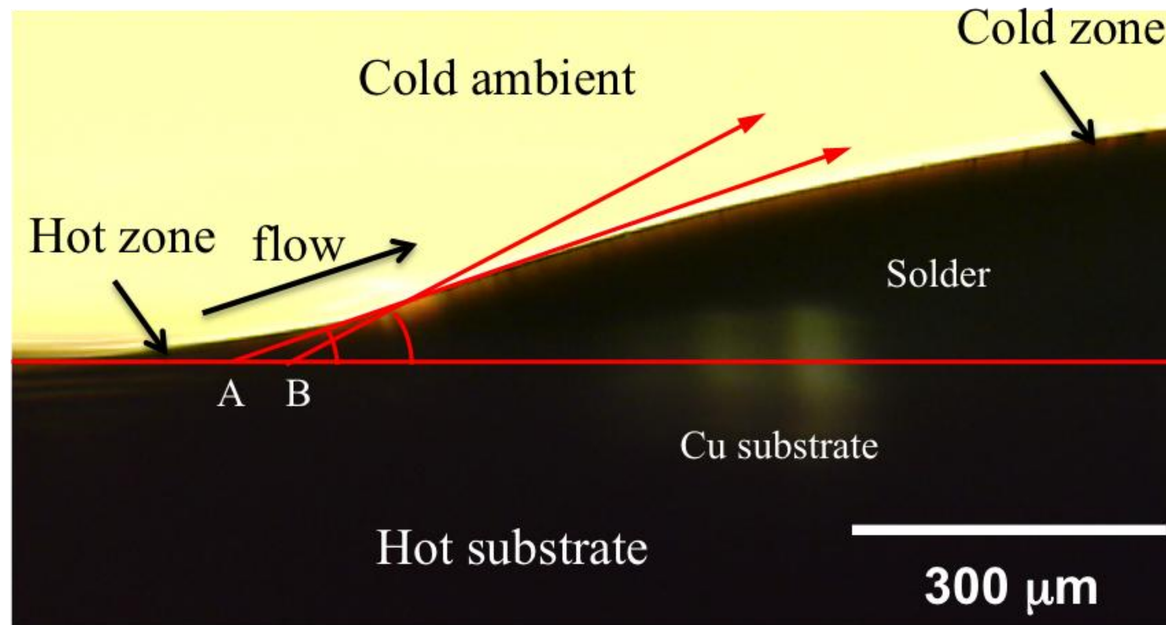

Figure 24. Typical optical image of molten solder on Cu substrate for contact angle measurement. Note receding contact angle due to Marangoni flow.

cross-sectioning of samples after solidification [32]. To accurately measure the contact angle between molten solder and Cu substrate, a procedure was developed to draw the tangent line at the interface, as shown in Fig. 25. The original image was segmented using image analysis software (ImageJ, Gaithersburg, MD), and the profile of the solder surface was subtracted from the segmented image. Assuming that the molten solder has a spherical shape, a circle of best fit of the solder surface profile was then obtained. The origin of the coordinate system was defined as the intersection of the best-fit circle and the top surface of the Cu substrate. A tangent line was drawn at this point. The sine of the contact angle is then given by:

$$\sin\theta = \frac{x_c - x_0}{R} = \frac{\sqrt{R^2 - y_c^2}}{R}$$

where R is the radius of best-fit circle and (x_c, y_c) is the coordinate of center of the circle. Another important parameter affecting the contact angle is the dwell time above the melting point. A series of in-situ images of the solder melting process, as well as the contact angle curve as a function of dwell time for molten solder on Cu substrate are shown in Fig. 26. Note the “plateau” regions in Fig. 26, where the contact angle is independent of depth after approximately 6 seconds of dwell time. The wetting angle was determined by taking the average values of wetting angles in the plateau region.

The as-bonded contact area of solder can also be measured to give us another measure of wetting. The contact angle and ratio of the as-bonded to original contact area of both SAC and SAC-Ce solder alloys are shown in Fig. 27.

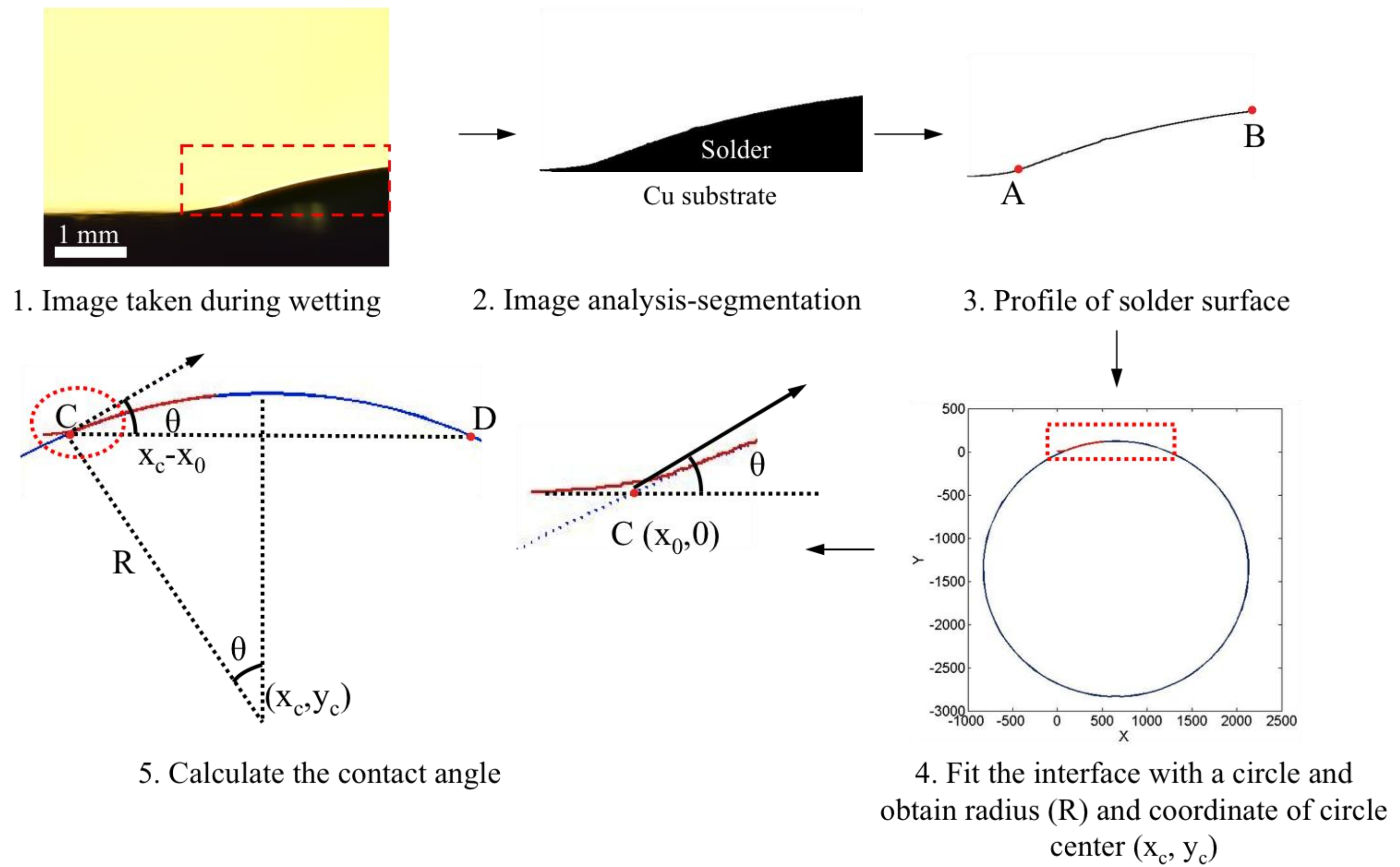

Figure 25. Schematic of measuring wetting angle of molten solder on Cu substrate based on optical images.

It is clear that the wettability of SAC-0.5Ce solder is comparable with SAC, and the formation of $CeSn_3$ intermetallics does not deteriorate the wettability of SAC solder on Cu substrate.

Previous studies on RE-containing solders show a large discrepancy in reported wetting behavior. For example, studies on RE-containing solder showed that the addition of RE alloying elements can enhance the wetting behavior of the solder alloy when the RE addition is low [12, 13, 15, 32, 33], while another showed no evidence of such improvement in wettability [16]. It is interesting to note that the variability in wetting behavior is likely attributed to a discrepancy in microstructure [12-16], i.e., formation of discrete RE-Sn intermetallics. The enhancement in wetting behavior of solder alloy by the addition of RE elements was only observed in the alloys with low content of RE, and most importantly, without the formation of RE-Sn intermetallics [13, 15, 16 32], indicating that wettability of solder alloy may be somehow deteriorated by RE-Sn intermetallics. However, results in this study and previous studies [16] show that the wettability is not affected by the addition of Ce up to 0.5 wt.%, even with the existence of $CeSn_3$ intermetallics.

6.4.2 *Differential scanning calorimetry*

Generally, the microstructure of solder joins is controlled by the solidification behavior of the solder during the reflow process. It has been reported that the microstructure of solder can be significantly refined by introducing a 4th alloying element, such as REs [20], Co [34], Mn, Ti [35], Ni [36], and Zn [37].

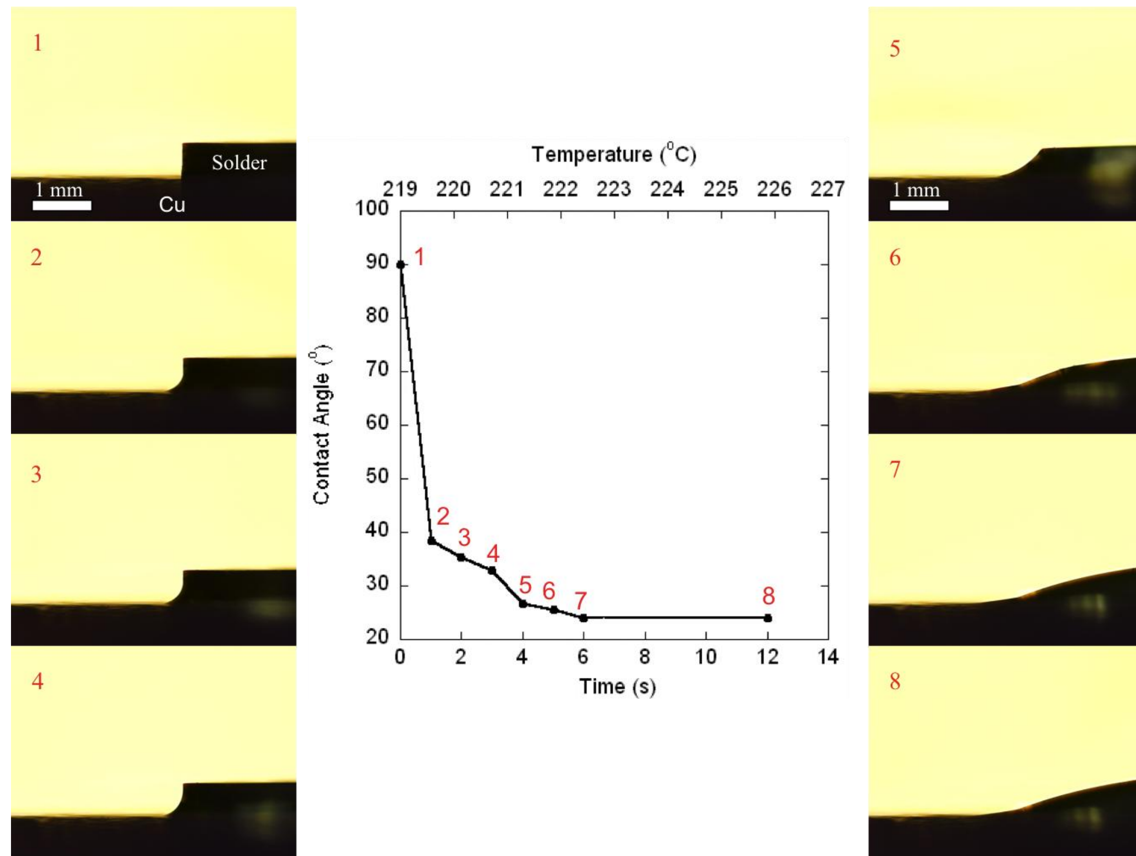

Figure 26. Wetting behavior of solder on Cu substrate as function of dwell time above solder melting point.

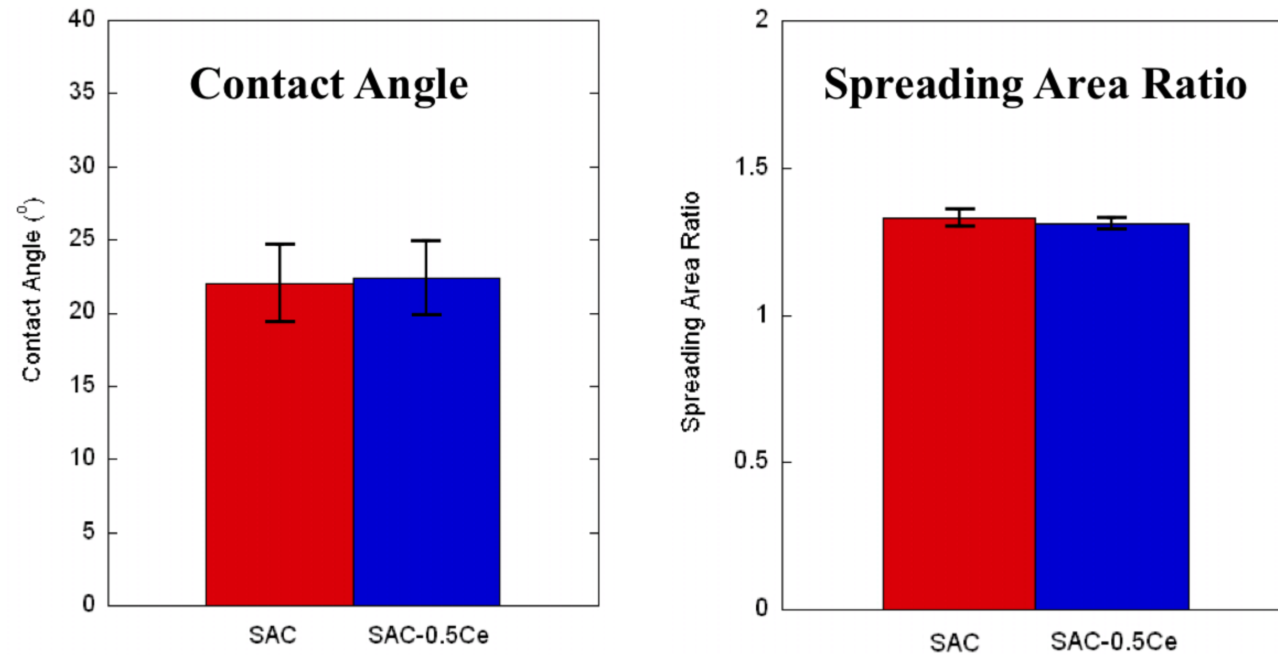

Figure 27. Quantitative measurement of contact angle and spreading area ratio of Sn-3.9Ag-0.7Cu and Sn-3.9Ag-0.7Cu-0.5Ce solder reflowed on Cu substrate.

The critical nucleus size in heterogeneous nucleation is given by:

$$r^* = \left(\frac{2\gamma_{SL}T_m}{L_V}\right)\frac{1}{\Delta T}$$

Where γ_{SL} is the solid/liquid interfacial energy, L_v is the latent heat of fusion per unit volume, T_m and ΔT are the melting temperature and degree of undercooling, respectively. It is clear that, for a given critical size, undercooling can be reduced by heterogeneous nucleation. Although it has been previously reported that the Sn grains in RE-containing alloys nucleate and grow from the faceted edges of the primary RE-Sn intermetallics during solidification [21], the undercooling of RE containing solder has not been studied in detail [30].

DSC was used to investigate the solidification behavior of both solder alloys. The heat-flow-vs-temperature curves, on both heating and cooling, for SAC and SAC-0.5Ce solders at different scanning rates are shown in Fig. 28. The results are summarized in Table 7. The melting onset temperature (T_m) and solidification onset temperature (T_s) are indicated in the Fig. 28. The undercooling (ΔT) is defined as the temperature gap between Tm and Ts:

$$\Delta T = T_m - T_S$$

Both SAC and SAC-0.5Ce show a single endothermic peak at the onset of melting for SAC alloy. The addition of RE elements to SAC did not significantly alter the melting characteristics, as the onset melting point was almost identical for both SAC and SAC-0.5Ce solders. However, it is interesting to note that the Ce-containing SAC alloy had a significantly higher onset point for solidification, compared with SAC solder, indicating that the undercooling value of SAC was significantly decreased by adding 0.5wt% Ce. This result indicates that

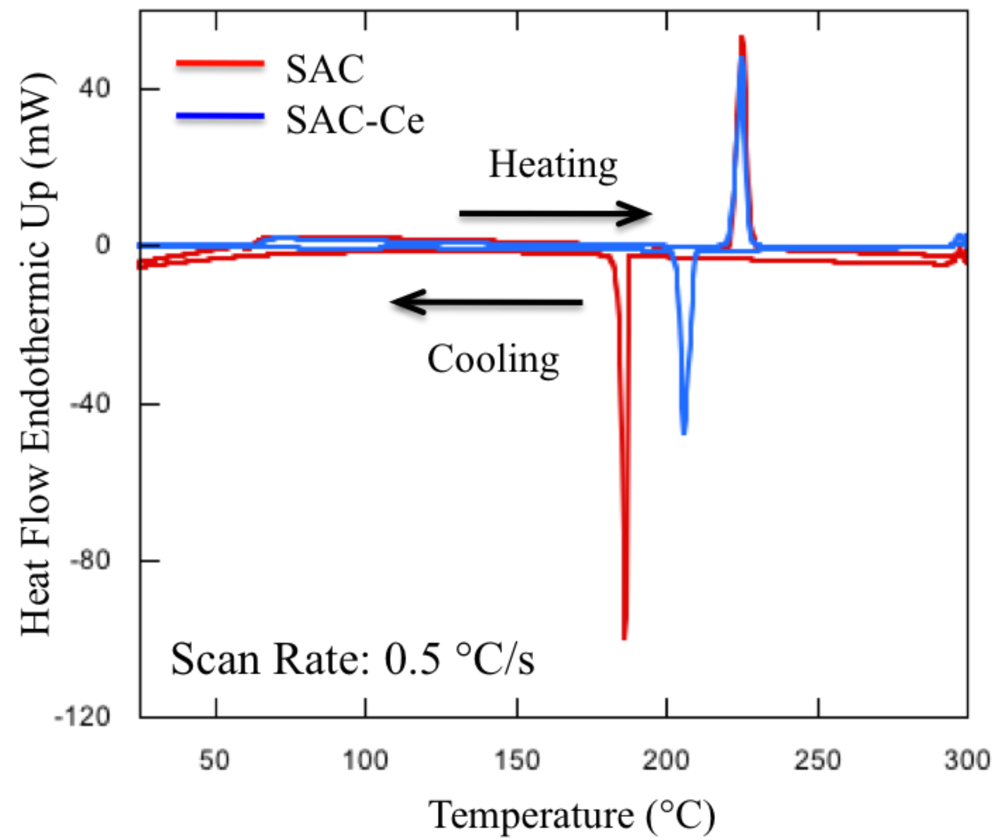

Figure 28. The DSC thermograms for Sn-3.9Ag-0.7Cu (red) and Sn-3.9Ag-0.7Cu-0.5Ce (blue).

pre-formed $CeSn_3$ intermetallics can promote the solidification of solder more rapidly through heterogeneous nucleation at $CeSn_3$ particles, which results in the finer microstructure and potentially suppress the formation of large Ag_3Sn plates, which will be shown in the following section.

Table 7. The DSC results for Sn-3.9Ag-0.7Cu and Sn-3.9Ag-0.7Cu-0.5Ce solders.

Solders	Onset Liquidus (°C)	Onset Solidification (°C)	Undercooling (°C)
Sn-3.9Ag-0.7Cu	222	187	35
Sn-3.9Ag-0.7Cu-0.5Ce	223	210	13

6.4.3 Solder volume effect on microstructural refinement in Sn-3.9Ag-0.7Cu and Sn-3.9Ag-0.7Cu-0.5Ce/Cu joints

The size of the solder volume has a significant effect on the microstructure of solder joints, varied by altering the cooling rate and undercooling behavior. Therefore, the volume effect on the microstructural evolution of Ce-containing SAC/Cu joints with different gap thickness (0.2 mm, 0.5 mm, 0.75 mm, and 1.00 mm) was studied using optical and scanning electronic microscopy. By varying the thickness of solder gap, different ratios of solder volume to Cu pad area can be achieved. Fig. 29 shows optical microscopy images of cross-section views of SAC and SAC-Ce joints with different solder thicknesses. Quantitative measurements of β-Sn dendrites size resulted, $CeSn_3$ IMC particle size and the thickness of Cu_6Sn_5 IMC layer at solder/Cu interface are summarized in Table 8. As a result of large supercooling experinced in near-eutectic Sn-3.9Ag-0.7Cu solder, the microstructure was dominated by β-Sn dendrites surrounded with a

mixture of eutectic Ag_3Sn, Cu_6Sn_5 and Sn. The cross-section images of SAC solder joints show an increasingly heterogeneous microstructure in the central region with increasing thickness of joints. It is interesting to note that in the central region of 1.00 mm thick SAC joint coarse microstructure that large Ag_3Sn plates embedded in coarse β-Sn dendrites have been formed upon solidification. The formation of Ag_3Sn plates may deteriorate mechanical properties of SAC joints [38, 39]. The finer microstructure of Ce-containing solder, specifically the suppression of Ag_3Sn plate and the decrease in the spacing of the Sn dendrites, can be explained by the reduced undercooling in RE-containing solder. The microstructure in solder/Cu interfacial regions was found to be much finer. It was found that the spacing of the β-Sn dendrites was smaller compared to center region and was solidified from interface to centre, which is normally observed in faster cooled samples (e.g. water quenched) [40]. It is believed that cooling rate close to the solder/Cu interface is higher than that of the central region due to poor thermal conductivity of solder alloy. Temperature gradient between the outer and central regions results in directional dendritic growth at the interface of solder/Cu. The area of coarsened β-Sn dendrites in central region was gradually minimized with decreasing the thickness, and only fine directional β-Sn dendrites were observed in the joint with 200 μm thickness, indicating that it was cooling rate that controlled solidification behavior of SAC joint with decreasing solder volume. In contrast with SAC alloy, the microstructure in SAC-Ce/Cu joint with thick solder gap was finer than that of SAC joints, and microstructure of SAC-Ce solder joint was less affected by temperature gradient and variation in solder

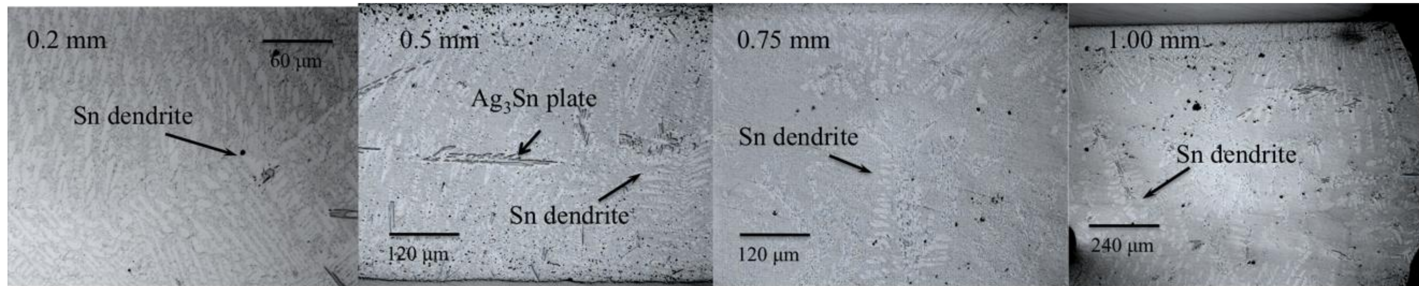

Sn-3.9Ag-0.7Cu

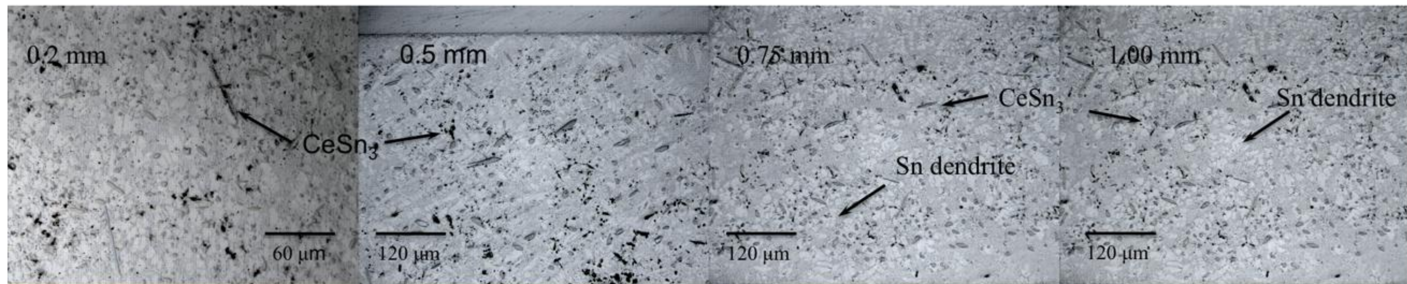

Sn-3.9Ag-0.7Cu-0.5Ce

Figure 29. Optical images of Sn-3.9Ag-0.7Cu (top row) and Sn-3.9Ag-0.7Cu-0.5Ce (bottom row) solder joints with different solder thicknesses: 0.2 mm, 0.5 mm, 0.75 mm and 1.00 mm.

thickness. As shown in Fig. 29, small and random orientated β-Sn dendrites homogenously distributed in the center and interface regions. Large Ag_3Sn plates were not observed even in the thickest SAC-Ce joints, as a result of the lower undercooling value. Most importantly, it was found the microstructure of SAC-Ce joints was relatively less sensitive to the volume change. Note that SAC-Ce solder joint with largest solder volume remains solidified with a fine β-Sn dendrites structure. This indicates that the volume effect is suppressed by the addition of Ce. It is interesting to note that Sn dendrite sizes in SAC and SAC-Ce solder joints with minimum solder thickness are comparable, indicating that refinement effect by $CeSn_3$ particles is not as pronounced as in thicker joint. This might be attributed to increase in the relative size of $CeSn_3$ intermetallic with decreasing solder volume, which means relative less heterogeneous nucleation sites in the smaller solder joints. Therefore, $CeSn_3$ intermetallic size needs to be decreased to improve the refinement effect in the smaller solder joints.

The volume effect on the thickness of Cu_6Sn_5 IMC layer formed at solder/Cu interface was also studied using backscattered electron microscopy, as shown in Fig. 30. The IMC layer thickness of SAC and SAC-Ce joints do not show strong differences with varying thickness of solder gap, which may be due to relatively short dwell time above the melting point of solders in this case. It was found that the IMC layer thickness in Ce-containing solder joints was alwaysless than that of SAC joints regardless of solder volume. Moreover, the size and geometry of $CeSn_3$ IMC particle was not affected by the volume of solder.

Table 8. Microstructure characterization comparison of Sn-3.9Ag-0.7Cu and Sn-3.9Ag-0.7Cu-0.5Ce solder joints with different thicknesses.

		Sn-3.9Ag-0.7Cu				Sn-3.9Ag-0.7Cu-0.5Ce			
	Solder thickness	0.2mm	0.5mm	0.75mm	1.00mm	0.2mm	0.5mm	0.75mm	1.00mm
Sn-rich dendrite	Secondary dendrite length (μm)	8.5±3.3	13.0±7.6	15.6±11.0	33.4±21.4	10.1±4.0	11.4±6.1	11.0±7.0	11.8±6.8
	Arm spacing (μm)	6.3±1.9	8.1±4.0	11.6±6.5	24.8±14.6	7.5±2.9	7.7±3.8	8.5±4.7	8.3±3.3
IMC Thickness (μm)		3.7±0.8	4.7±3.2	3.9±1.6	4.6±2.5	2.9±0.7	2.4±0.6	2.2±0.9	2.8±0.8
$CeSn_3$ particle size	Major axis (μm)	N/A	N/A	N/A	N/A	1.4±0.6	2.1±0.9	1.8 ±0.8	2.5 ± 1.1
	Minor axis (μm)	N/A	N/A	N/A	N/A	0.6±0.3	0.9 ± 0.4	0.8 ± 0.3	1.1 ± 0.6
	Aspect ratio	N/A	N/A	N/A	N/A	2.5±1.5	2.7 ±1.9	2.6 ± 1.5	2.8 ± 2.1

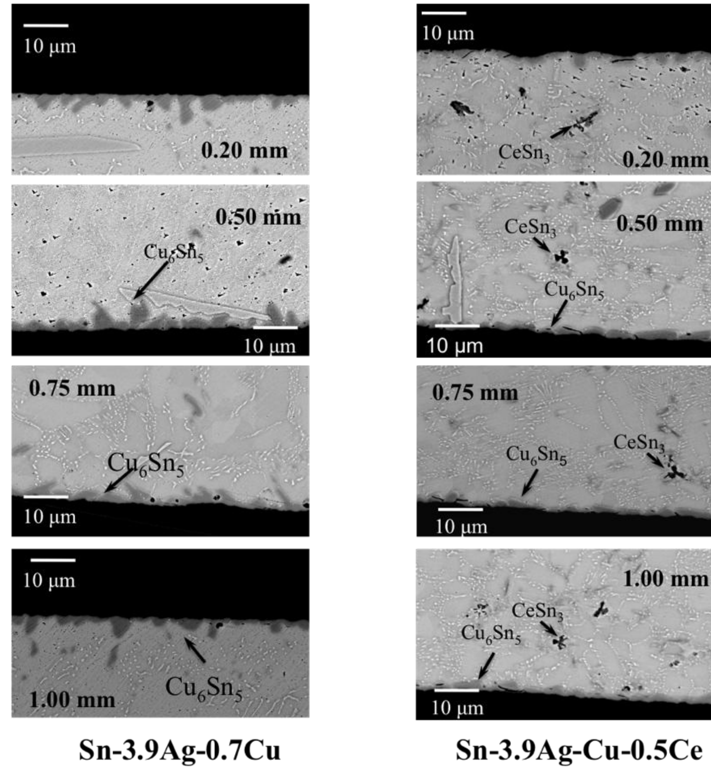

Figure 30. Backscattered electron microscopy images of Sn-3.9Ag-0.7Cu (left column) and Sn-3.9Ag-0.7Cu-0.5Ce (right column) joints with different solder thicknesses: 0.2 mm, 0.5 mm, 0.75 mm, 1.0 mm.

6.5 Conclusions

The mechanisms for formation of refined microstructure, wettability of the novel Ce containing Pb-free solder, as well as volume effect were investigated. Based on the experimental results, the following conclusions can be drawn:

1. The results of wetting behavior of SAC and SAC-0.5Ce indicate that SAC-Ce solder has comparable wetting behavior to SAC solder on Cu substrate.
2. DSC results revealed that refined microstructure in Ce-containing alloys is due to reduced undercooling value.
3. The microstructure of SAC can be refined with Ce addition. DSC result reveals that the refined microstructure as well as thinner Cu_6Sn_5 intermetallic layer may both be due to the reduction in undercooling, by increasing the amount of heterogeneous nucleation sites, i.e. $CeSn_3$ intermetallic.
4. The SAC-Ce alloy showed constant microstructure refinement with variation of solder volume, indicating that both the microstructure of the solder matrix and the interfacial intermetallic layer thickness is less affected by the variation of solder volume.

6.6 References:

1. E.P. Wood, K.L. Nimmo, J. Electron. Mater., 1994, 23(8), 709.
2. M. Abtew, G. Selvaduray, Mater. Sci. Eng., 2000, 20(5-6), 95.
3. N.-C. Lee, Soldering Surf. Mount Technol., 1997, 9(2), 65.
4 H. Ma, J. C. Suhling, J. Mater. Sci., 2009, 44(5), 1141.

5. N. Chawla, Int. Mater. Rev., 2009, 54, 368.

6. N.-C. Lee, International Microsystems, Packaging, Assembly and Circuits Technology (IMPACT) conference, (2007), Oct, 44.

7. I.E. Anderson: J. Mater. Sci., Mater. Electron., 2007, 18, 55.

8. M. Dittes, H. Walter, Soldering Surf. Mount. Technol., 2003, 15(1), 77.

9. C.M.L. Wu, Y.W. Wong, J. Mater. Sci. Mater. Electron., 2007, 18(1), 77.

10. C.M.L. Wu, D.Q. Yu, C.M.T. Law, L. Wang, J. Electron. Mater., 2002, 31, 921.

11. A. Ramirez, H. Mavoori, S. Jin, Appl. Phys. Lett., 2002, 80 (3), 398.

12. Y. Shi, J. Tian, H. Hao, Z. Xia, Y. Lei, F. Guo, J. Alloys Compd., 2008, 453(1-2), 180.

13. L. Zhang, S.-B. Xue, L.-L. Gao, Y. Chen, S.-L. Yu, Z. Sheng, G. Zeng, J. Mater. Sci. Mater. Electron., 2009, 20, 1193-9.

14. L.-L Gao, S.-B Xue, L. Zhang, Z.-X, Xiao, W. Dai, F. Ji, H. Ye, G. Zeng: J. Mater. Sci. Mater. Electron., 2010, 21(9), 910.

15. L.-L Gao, S.-B Xue, L. Zhang, Z. Sheng, G. Zeng, F. Ji, J. Mater. Sci. Mater. Electron., 2010, 21(7), 643.

16. Z. Chen, Y. Shi, Z. Xia, Y. Yan, J. Electron. Mater., 2003, 32(4), 235.

17. X.-Y. Zhao, M.-Q. Zhao, X.-Q. Cui, T.-H. Xu, M.-X. Tong, Trans. Nonferrous Met. Soc. China, 2007, 17(4), 805.

18. D.Q. Yu, J. Zhao, L. Wang, J. Alloys Compd., 2004, 376(1-2), 170.

19. M.A. Dudek, R.S. Sidhu, N. Chawla, M. Renavikar: J. Electron. Mater., 2006, 35(12), 2088.

20. M.A. Dudek, N. Chawla, Metall. Mater. Trans. A, 2010, 41(3), 610.

21. M.A. Dudek, R.S. Sidhu, N. Chawla, JOM, 2006, 58(6), 57.

22. H.X. Xie, N. Chawla, K. Mirpuri, J. Electron. Mater., 2012, online first.

23. M.A. Dudek, N. Chawla, Acta. Mater., 2009, 57, 4588.

24. M.A. Dudek, N. Chawla, J. Electron. Mater., 2009, 38(2), 210.

25. Z. Chen, Y. Shi, Z. Xia, Y. Yan, J. Electron. Mater., 2003, 32(4), 235.

26. L. Wang, D.Q. Yu, J. Zhao, M.L. Huang, Mater. Lett., 2002. 56(6), 1039.

27. A.O. Aggarwal, P.M. Raj, V.S.D. Ravi, S. Koh, R. Mukkapudi, R.R. Tummala, in Electronic Components and Technology Conference, 2005. Proceedings. 55th. 2005.

28. M. Mueller, S. Wiese, M. Roellig, K.-J. Wolter, in Electronic Components and Technology Conference, 2007. ECTC '07. Proceedings. 57th. 2007.

29. Z. Huang, P.P. Conway, E. Jung, R.C. Thomson, C. Liu, T. Loeher, M. Minkus, J. Electron. Mater., 2006.,35(9),1761.

30. M. Islam, A. Sharif, Y. Chan, J. Electron. Mater., 2005. 34(2), 143.

31. Karl J. Puttlitz, K.A.S., Marcel, Dekker, Handbook of lead-free solder technology for microelectronic assemblies. 2004, CRC Press, 349.

32. Wang L. D.Q. Yu, J. Zhao, M.L. Huang, Mater. Lett., 2002, 56(6), 1039.

33. H. Hao, J. Tian, Y.W. Shi, Y.P. Lei, Z.D. Xia, JEM, 2007, 36(7), 766.

34. I.E. Anderson, J. Mater. Sci.: Mater. Electron., 2007, 18, 55.

35. L-W. Lin, J-M. Song, Y-S. Lai, Y.-T. Chiu, N.-C. Lee, J-Y. Uan, Microelectron. Relib., 2009, 49, 235.

36. M.G. Cho, S.K. Kang, S-K. Seo, D-Y. Shih, H.M. Lee: J. Mater. Research, 2009, 24(2), 534.

37. S.K. Kang, D.-Y. Shih, D. Leonard, D.W. Henderson, T. Gosselin, S-I. Cho, J. Yu, W.K. Choi, JOM, 2004, 56(6), 34.

38. K.S. Kim, S.H. Huh, K. Suganuma, J. Alloys Compd., 2003. 352(1-2), 226.

39. D.Q. Yu, L. Wang, J. Alloys Compd., 2008. 458(1-2), 542.

40. M. Muller, S. Wiese, K.J. Wolter, in Electronics Systemintegration Technology Conference, 2006. 1st. 2006.

7. MECHANICAL SHOCK BEHAVIOR OF SN-3.9AG-0.7CU AND SN-3.9AG-0.7CU-0.5CE SOLDER JOINTS

7.1 Abstract

Sn-Ag-Cu lead-free solder have been shown to have inferior mechanical shock resistance to that of Pb-Sn alloy. Sn-rich solders containing rare earth elements have been shown to have superior mechanical properties when compared to conventional Sn-Ag-Cu solder, in terms of strain-to-failure. In this study, we report on the mechanical shock behavior of Sn-3.9Ag-0.7Cu and Ce-containing Sn-3.9Ag-0.7Cu alloys over the strain rate range of 10^{-3}-$12 s^{-1}$. Failure mechanisms of solders in different strain regimes are investigated based on the fractography analysis. It will be shown that the shock performance of Sn-3.9Ag-0.7Cu solders can be improved with addition of trace amount of Ce in the solder matrix controlled regime. The role of $CeSn_3$ intermetallics on the enhanced dynamic performance is discussed.

7.2 Introduction

In recent years, a series of eutectic or near-eutectic Sn-rich solder alloys containing Ag and Cu have been proposed as replacements for Pb-Sn solder [1-3]. However, adding excessive amount of Cu and Ag results in the formation of Ag_3Sn and Cu_6Sn_5 intermetallics, which may cause mechanical degradation of solder joints [4-6], in particular, lower ductility, and poor damage tolerance [7,8].

To further improve the mechanical and physical properties of Sn-Ag-Cu Pb-free solder, Pb-free solder alloys containing rare earth elements have been proposed and studied [9-11]. Preliminary investigations have shown that the

addition of trace amounts of rare earth (RE) elements can refine the microstructure of the solder alloy [12-15], refine intermetallic particle size [16-19], enhance wettability [15,20,21] and electromigration resistance [22], and improve mechanical properties [23-25]. Our previous work has also shown that Pb-free solder alloys doped with small amount of La and Ce possess refined microstructure, reduced thickness of Cu_6Sn_5 intermetallic layer, and most importantly, better ductility in comparison to conventional Sn-3.9Ag-0.7Cu alloy [25-27]. In addition, Ce-containing Sn-Ag-Cu alloys are less prone to oxidation [28] and exhibit excellent thermal stability [29] relative to other rare earth containing Sn-Ag-Cu, e.g., La and Y-containing solders.

Mechanical shock resistance, which is directly related to the ductility of solders [30], has been considered as a critical reliability issue to the electronic devices, since solder joints may experience mechanical shock when a device is mishandled or dropped during manufacturing or usage [31-33]. An improvement in shock resistance in Pb-free solder joint over a range of strain rates is needed. Although enhanced ductility in Ce-containing Sn-Ag-Cu solder has profound implications for improving the mechanical shock resistance, such improvement needs to be validated experimentally. However, the mechanical shock behavior of solder alloys bonded to the substrates by IMC layer is quite complex. It has been hypothesized that the solder joint behavior is strain-rate dependent, being controlled by either solder or the IMC layer. A schematic representation of this behavior is shown in Fig. 31 [1]. Our work on the mechanical shock behavior of Sn-rich alloys has shown that at lower strain rates the strength is controlled by the

ductile deformation of the solder, while at high strain rates it is controlled by the strength of the IMC layer [34,35]. Thus, it is important to study the shock behavior of Sn-3.9Ag-0.7Cu and Ce-containing Sn-3.9Ag-0.7Cu alloys at different strain rate regimes.

In this study, the mechanical shock behavior of Sn-3.9Ag-0.7Cu and Sn-3.9Ag-0.7Cu-0.5Ce solder joints was systematically investigated over the strain rate range of 10^{-3} to 12 s^{-1}. The fracture mechanisms were characterized by fractographic analysis using scanning electronic microscopy (SEM) and energy dispersive X-ray spectroscopy (EDS). It will be shown that an increase in strain rate leads to a transition from solder-controlled to intermetallic layer-controlled fracture in both Sn-Ag-Cu and Ce-containing Sn-Ag-Cu alloys. Also, a significant increase in strain-to-failure can be obtained with a small addition of Ce in the solder matrix-controlled regime. The mechanisms for the enhanced shock performance in Ce-containing solder are also discussed in detail.

7.3 Materials and Experimental Procedure

Vacuum-melted ingots of Sn-3.9Ag-0.7Cu and Sn-3.9Ag-0.7Cu with 0.5 wt% Ce were prepared. High purity Sn-3.9Ag-0.7Cu ingots (Indium Corp., Utica, NY, USA) were cut into small rectangular pieces (6.5mm × 6.5mm ×13mm) and mixed with Ce shot (ESPI, 99.995% pure). Due to the reactive nature of pure Ce with oxygen, the materials were mixed in a quartz ampoule (12 mm in diameter) under a sealed glovebox with helium atmosphere. The quartz ampoule was then evacuated to 10^{-5} Torr and sealed. The sealed ampoules were heat treated at 1000 °C for 4 h, and periodically mixed by rotation of the ampoule, in order to

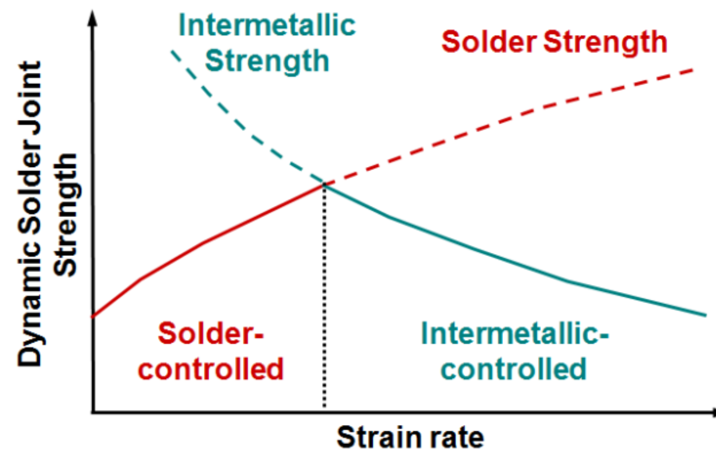

Figure 31 Schematic showing how dynamic solder joint strength is controlled by bulk solder strength at lower strain rate and by strength of interfacial intermetallic layer at higher strain rates.

homogenize the liquid metal. The ampoules were then water quenched. The solder ingots were then removed from the ampoules and sectioned.

As-processed Sn-3.9Ag-0.7Cu solder and Sn-3.9Ag-0.7Cu-0.5Ce solder ingots were machined into 6.35 mm × 0.5 mm discs. The oxidation caused by the machining process was removed by polishing and ultrasonically cleaned in acetone. Oxygen-free-high-conductive (OFHC) copper bars (25 mm long and 6.35 mm diameter) were mechanically polished to a 0.05 μm finish with colloidal silica solution. A rosin mildly activated (RMA) flux was applied to the polished portion of the Cu bars to improve the wetting between the Cu and solder. Butt joints for mechanical tensile tests were assembled with the aid of a reflow fixture to minimize misalignment and maintain a consistent solder thickness of approximately 50 μm. The entire assembly was heated on a programmable digital hot plate (Torrey Pines Scientific, San Marcos, CA, USA) until the solder reached its melting temperature. The typical reflow profile consisted of heating the sample to 170 °C for 2 minutes to allow excess flux to vaporize, then heating to 20 °C above the melting point and holding for 40 s, removing from the hot plate and cooling in air on an aluminum block. The approximate cooling rate of the solder was 1 $°Cs^{-1}$.

The microstructure of as-reflowed solder joints was characterized using optical and SEM (FEI-XL30, Hillsboro, Oregon). The features of interest included secondary Sn dendrite size and arm spacing, RE intermetallic size, and Cu_6Sn_5 intermetallic layer thickness. Quantitative microstructural characterization was conducted using image analysis software (ImageJ, NIH, Bethesda, MD,

USA). Optical and SEM micrographs were thresholded and segmented into binary images and the particles of interest were fit to ellipses, to estimate their size and aspect ratio. The intermetallic layer was also isolated by segmenting backscattered SEM micrographs, and the thickness of intermetallic layer was then measured using ImageJ.

Mechanical shock experiments were conducted on solder joints over a range of stain rates (10^{-3}-12 s^{-1}), using an MTS 810 servohydraulic machine (MTS Systems, Minneapolis MN). Tests were conducted in strain control mode at 10^{-3} and 10^{-1} s^{-1} using an extensometer. Tests at 1.5 and 12 s^{-1} were conducted in displacement control mode. For the higher strain rate tests, a small section of the joint was polished to a 0.05 μm colloidal silica finish to permit visualization of the joint interfaces for the measurement of strain and strain rate, instead of using an extensometer. A Questar QM100 (New Hope, PA, USA) traveling microscope was used in conjunction with a Phantom Miro2 (Wayne, NJ, USA) high-speed camera to measure strain from the displacement of the joint interfaces. A slack adapter was utilized to ensure that a well-controlled, linear strain rate was achieved. After tests, fracture surface of each joint was analyzed by scanning electron microscopy and energy dispersive spectroscopy to determine the failure mechanisms. Energy dispersive X-ray spectroscopy (EDS) was used to identify the composition of the IMC layer and precipitates on the fracture surfaces.

7.4 Results and Discussion

7.4.1 Microstructure characterization

Fig. 32 shows representative microstructures of the as-reflowed Sn-3.9Ag-0.7Cu and Sn-3.9Ag-0.7Cu-0.5Ce solders joints. A typical microstructure of as-processed Sn-3.9Ag-0.7Cu solder ingot consists of Sn dendrites surrounded by a eutectic mixture of Ag_3Sn and Cu_6Sn_5 intermetallics in a Sn-rich matrix. Ce-containing intermetallic phases were formed with the addition of trace amount of Ce. These intermetallics were uniformly distributed in the Sn matrix, as shown in Fig. 32. Three dimension visualization and TEM studies of $RESn_3$ intermetallic showed that they are complex dendrites with a faceted geometry [26,36]. In the as-reflowed Sn-Ag-Cu and Ce-containing Sn-Ag-Cu solder joints, a nodular type Cu_6Sn_5 intermetallic layer was formed at the Cu/Solder interface, as shown in Fig. 33. Table 9 summarizes quantitative measurements of microstructural features after reflow for conventional Sn-Ag-Cu and 0.5 wt.% Ce containing alloys, including the Sn dendrite size and arm spacing, and the Cu_6Sn_5 intermetallic layer thickness. It is interesting to note that the average Sn dendrite size in Ce-containing Sn-3.9Ag-0.7Cu solder joint is approximately 35 % smaller than that of Sn-Ag-Cu solder joint, indicating that the microstructure of Sn matrix is finer in Ce-containing alloy compared with the base Sn-Ag-Cu alloy. It is believed that the Sn grains in RE-containing alloy are nucleating and growing from the faceted edges of the RE-containing intermetallics during solidification [26]. Thus, the decrease in the Sn dendrite size and spacing is due to the large number of heterogeneous nucleation sites provided by RE-Sn intermetallics. Also note that

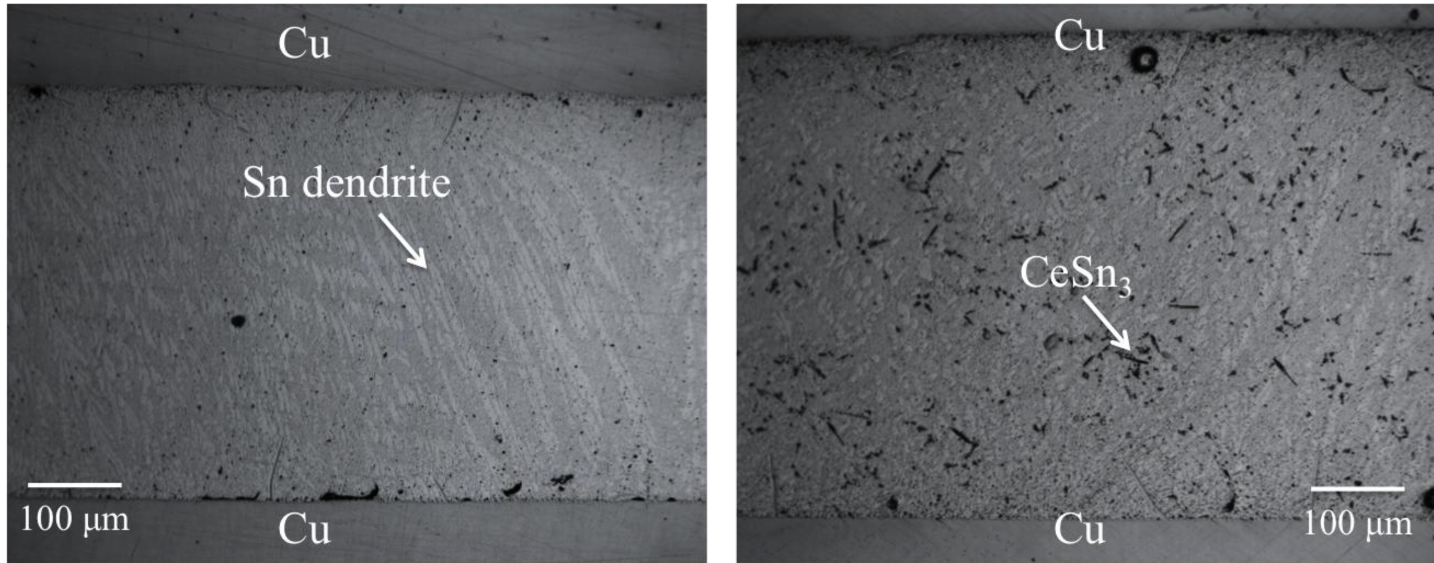

Figure 32. As-processed optical images of left: Sn-3.9Ag-0.7Cu and Right: Sn-3.9Ag-0.7Cu-0.5Ce solder joints

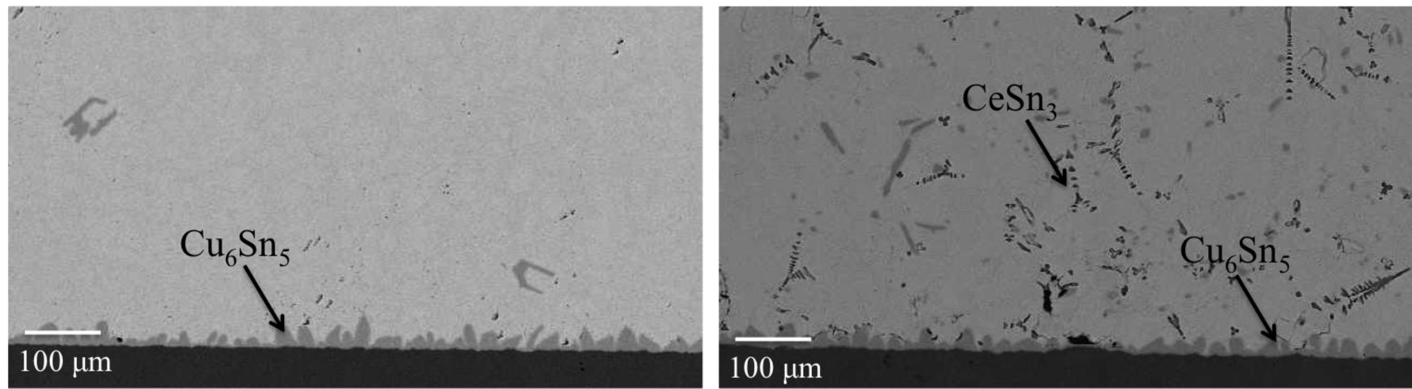

Figure 33. Backscatter electron microscopy images of as-reflowed Sn-3.9Ag-0.7Cu (left) and Sn-3.9Ag-0.7Cu-0.5Ce (right) solder joints

in the Ce-containing alloy, the Cu_6Sn_5 intermetallic thickness is approximately 25 % smaller compared to that of Sn-Ag-Cu alloy. It has been reported that the lower intermetallic thickness in Ce-containing solder is due to the lower degree of undercooling and less time for reaction between molten Sn and the Cu substrate [27]. Although it was believed that lower brittle intermetallic layer thickness could have a substantial impact on the mechanical behavior of joints, systematic studies on the effect of IMC thickness showed that the intermetallic layer plays a less important role when the thickness of intermetallic layer is relatively thin (<10 μm), i.e., in this IMC thickness range the mechanical behavior is solder-controlled [35].

Table 9. Summary of microstructure characterization results for as-reflowed and thermal-aged Sn-3.9Ag-0.7Cu and Sn-3.9Ag-0.7Cu-0.5Ce solder joints.

<table>
<tr><th colspan="2"></th><th>Sn-3.9Ag-0.7Cu</th><th>Sn-3.9Ag-0.7Cu-0.5Ce</th></tr>
<tr><td rowspan="2">β-Sn dendrites</td><td>Secondary dendrite length (μm)</td><td>18.8 ± 2.8</td><td>12.4 ± 3.9</td></tr>
<tr><td>Secondary dendrite spacing (μm)</td><td>11.9 ± 2.3</td><td>8.3 ± 1.6</td></tr>
<tr><td>IMC layer</td><td>Thickness (μm)</td><td>4.3 ± 1.8</td><td>3.3 ± 1.3</td></tr>
</table>

7.4.2 Mechanical tensile behavior of Sn-3.9Ag-0.7Cu and Sn-3.9Ag-0.7Cu solder joints

In this section, we discuss the mechanical shock properties of the Sn-3.9Ag-0.7Cu and Sn-3.9Ag-0.7Cu-0.5Ce solder joints at different strain rates. A detailed description of the testing methods can be found elsewhere [35].

Representative tensile stress-strain curves of solder joints are shown in Fig. 34. The tensile behavior is summarized in Table 10, including ultimate tensile strength and strain-to-failure. In order to quantitatively compare the strains at failure, a procedure was developed to determine the onset of failure. The strain to failure was taken as a deviation of 5 % from a linear regression fit to the end of the stress-strain curve [25]. It have been previously reported that for the quasi-static shear behavior of solder joints, small additions of Ce can significantly increase the strain-to-failure with a slight drop in shear strength [27]. The results on quasi-static tensile behavior showed a similar trend to the shear behavior of Ce-containing solder joints. The ultimate tensile strength of joints decreased with a small addition of Ce. The alloy containing 0.5 wt.% Ce showed approximately 30% decrease in tensile strength compared to Sn-Ag-Cu solder. More importantly, the strain-to-failure of Sn-Ag-Cu-0.5Ce increased by over 100% to that of Sn-Ag-Cu. Such an increase in strain-to-failure in Sn-Ag-Cu-0.5Ce solder joints indicates that the ductility of Sn-Ag-Cu solder can be significantly improved by adding trace amount of Ce.

With increasing strain rate, the dynamic strengths of as-reflowed solder joints first increased in the strain rate range 10^{-3} to 1.5 s^{-1}, then decreased in the strain rate range 1.5 to 12 s^{-1} for both Sn-Ag-Cu and Ce-containing Sn-Ag-Cu solder alloys. Although the dynamic strength of Ce-containing Sn-Ag-Cu is still lower than that of Sn-Ag-Cu alloy at intermediate strain rate, the strength of both alloys is comparable at highest strain rate. This trend indicated that the 10^{-3}-1.5 s^{-1} is solder-controlled and the higher range, over 12 s^{-1}, is intermetallic-controlled.

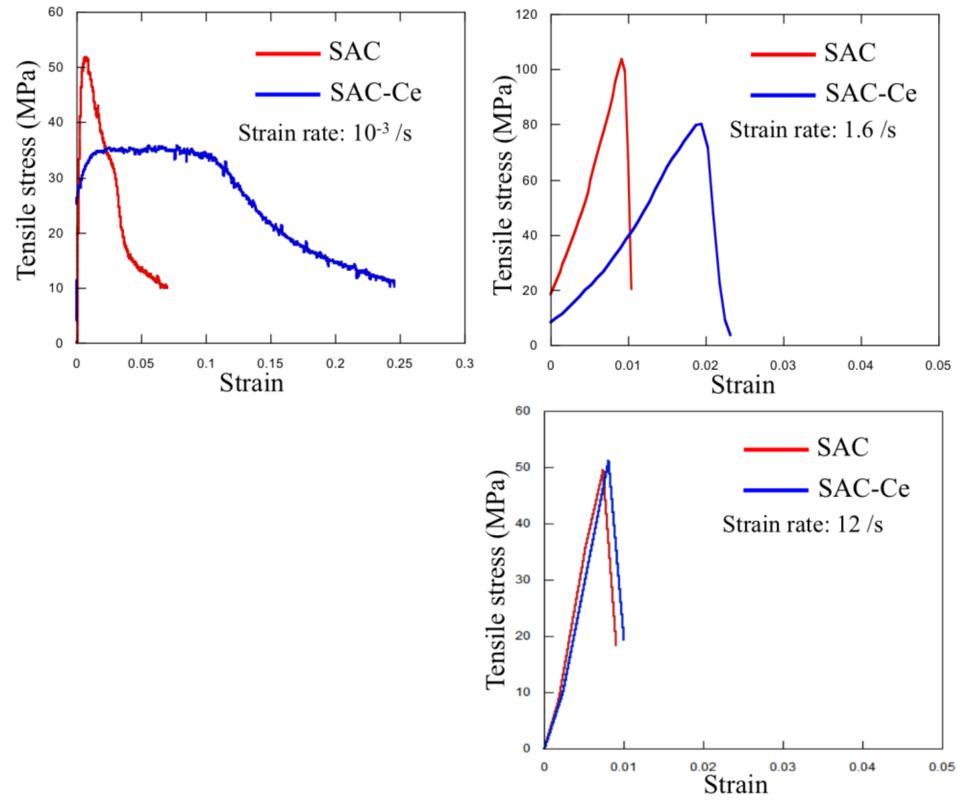

Figure 34. Tensile stress vs. strain curve for Sn-3.9Ag-0.7Cu and Sn-3.9Ag-0.7Cu-0.5Ce/Cu solder joints tested at different strain rate (from 10^{-3} to 12 s^{-1})

This discussed in more detail in the next session on fractographic analysis. Strain-to-failure of both Sn-Ag-Cu and Sn-Ag-Cu-0.5Ce alloys decreased with increasing strain rate, due to the transition of failure mode from ductile to brittle. It is interesting to note that Ce-containing alloy still showed impressive gain in strain-to-failure, nearly 100% over that of Sn-Ag-Cu when the strain rate was at around 1.5 s^{-1}. Such gains in strain-to-failure started to decrease in the intermetallic-controlled regime, i.e. only 20 % improvement is gained at $12s^{-1}$. The mechanism of enhanced shock resistance in Ce-containing Sn-Ag-Cu alloy will be further discussed in the fractographic analysis section below.

Table 10. Dynamic tensile results for Sn-3.9Ag-0.7Cu and Sn-3.9Ag-0.7Cu-0.5Ce solder joints

	Ultimate tensile strength (MPa)			Stain to failure		
Strain rate (s^{-1})	10^{-3}	1.6	12	10^{-3}	1.6	12
SAC	50.0 ± 1.4	111.5 ± 12.0	48.3 ± 3.4	9.0 ± 2.8	0.9 ± 0.2	0.8 ± 0.2
SAC-0.5Ce	37.0 ± 3.5	74.0 ± 4.6	52.0 ± 2.1	20.6 ± 10.2	2.1 ± 0.6	0.9 ± 0.3

7.4.3 Fractographic analysis

The fracture surface of as-reflowed Sn-Ag-Cu and Ce-containing Sn-Ag-Cu solder joints were examined to elucidate the relationship between fracture mechanism and mechanical performance. Fig. 35 shows representative fracture surfaces of Sn-Ag-Cu and Ce-containing Sn-Ag-Cu solder joints at different strain rates. At lower strain rates, the fracture surfaces revealed a classical void

nucleation, growth, and coalescence process in the solder region of both Sn-Ag-Cu and Sn-Ag-Cu-0.5Ce alloys. However, cracking in the Sn-Ag-Cu joint was observed to propagate along the interfacial region between the solder and Cu substrate. Energy dispersive X-ray spectroscopy (EDS) identified broken Cu_6Sn_5 nodules tips at the bottom of dimples. This indicated that voids in Sn-Ag-Cu joints were nucleated in Solder/Cu interfacial regime due the stress concentrations created by the Cu_6Sn_5 nodules, followed by crack propagation into the intermetallic layer as the voids grew and coalesced. In contrast, fracture in Ce-containing Sn-Ag-Cu joints occurred through the solder, instead of solder/Cu interface. Voids caused by the fracture process are much larger in scale than for the Sn-Ag-Cu joints, and $CeSn_3$ intermetallic particles were also identified at the bottom of most dimples in the Sn-Ag-Cu-0.5Ce joints using EDS. This fractography indicated that $CeSn_3$ intermetallics are directly responsible for the increase in ductility in Sn-Ag-Cu-0.5Ce joints. Previously, it has been reported that the ductility enhancement in Ce-containing solder joints is due to relatively more homogeneous plastic deformation band, which is disturbed by $CeSn_3$ intermetallic particles during the lap-shear loading [37]. Similar to our work on lap-shear experiments, one can expect that the large plastic deformation bands exist at the Sn-Ag-Cu solder/copper interface during tensile loading. Such a unique deformation pattern is due to the substrate constraint imposed by the geometry of the solder joint [38] and responsible for the fracture morphology in

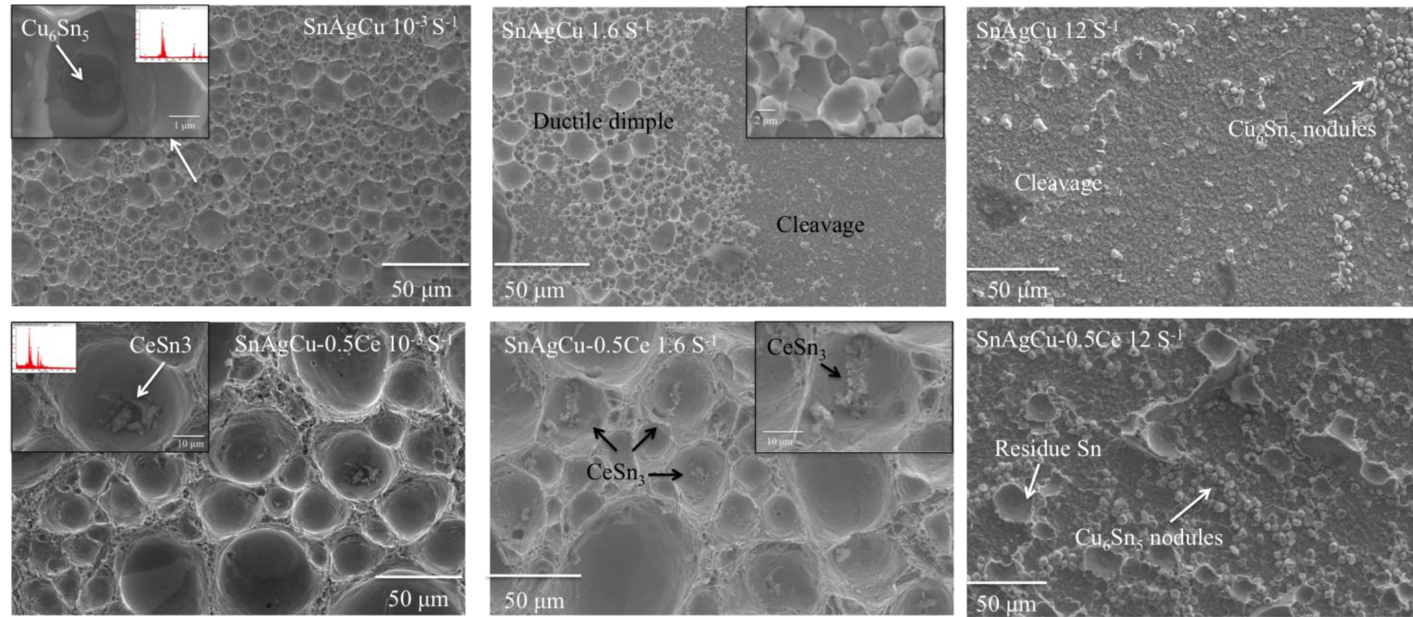

Figure 35. Tensile fracture morphology of Sn-3.9Ag-0.7Cu (top row) and Sn-3.9Ag-0.7Cu-0.5Ce (bottom row) solder joints at different strain rates.

Sn-Ag-Cu joints [39]. Thus, $CeSn_3$ intermetallic particles serve to diffuse the strain concentration, as well as creating voids nucleation sites during the fracture process, which result in delayed fracture and enhanced ductility in the Ce-containing alloy.

Increasing the strain rate changed the fracture morphology from ductile to cleavage, as shown in Fig. 35. The transition in fracture morphology has also been reported by several authors [40,41]. At intermediate strain rate, fracture in Sn-Ag-Cu alloy occured in the interior of Cu_6Sn_5 intermetallic layer due to an increase in stress triaxiality in the solder matrix, less time for stress relaxation, and highly localized brittle fracture at the intermetallic layer. In general, the fracture surface in Sn-Ag-Cu joint at intermediate strain rate consisted of a mixture of ductile dimples and fully exposed or fractured Cu_6Sn_5 nodules. At the strain rate corresponding to the transition between solder-controlled and intermetallic-controlled strength region, the area ratio of ductile to cleavage fracture in the intermetallic was found to be ~1 (by image analysis), indicating that both fracture mechanisms contributed equally to the overall strength of the joint at this strain rate. A decrease in strain-to-failure with an increase in strain rate can be also explained by the increase in area fraction of cleavage fracture and less ductile dimple fracture. It is important to note that large dimples with $CeSn_3$ intermetallic particles at the bottom still can be found in the fracture surface of Ce-containing Sn-Ag-Cu solder joints at intermediate strain rate. It is not surprising that $CeSn_3$ intermetallic particles can serve as voids nucleation sites at intermediate strain rate, because this strain rate is still in the solder matrix controlled region. Thus,

such $CeSn_3$ nucleated dimples are responsible for the improvement in ductility at intermediate strain rate.

Higher strain rates promoted more intermetallic layer cleavage fracture in both Sn-Ag-Cu and Sn-Ag-Cu-0.5Ce alloys. An increase in brittle cleavage fracture is due to the increase in solder yield strength and higher concentrated stress in the intermetallic layer. Therefore, at the highest strain rate, the fracture surface in both Sn-Ag-Cu and Ce-containing Sn-Ag-Cu joints consisted of cleavage fracture surface of the Cu_6Sn_5 IMC layer. Very little solder was found on the cleavage fracture surface, indicating that the mechanical properties of solder joints tested was dominantly controlled by the intermetallic layer. Therefore, the strain-to-failure of Ce-containing Sn-Ag-Cu alloys is comparable to that of Sn-Ag-Cu.

The fracture mechanisms in Sn-Ag-Cu and Sn-Ag-Cu-0.5Ce solder joints, as a function of strain rate, are summarized in Fig. 36. It is clear that the ultimate tensile strength of solder joints increased in the strain rate range 10^{-3} to 1.6 s^{-1} for both Sn-Ag-Cu and Sn-Ag-Cu-0.5Ce. The dynamic strengths of the solder joints then decreased monotonically when strain rate was larger than 1.6 s^{-1}. The strain-to-failure of both Sn-Ag-Cu and Sn-Ag-Cu-0.5Ce decreased rapidly with increasing strain rate, due to a transition in fracture from the solder to the brittle IMC. It is important to note that the strain-to-failure of Sn-Ag-Cu-0.5Ce is significantly larger than that of Sn-Ag-Cu solder joint when the strain rate is lower than 1.6 s^{-1}. The schematics of fracture behavior of Sn-Ag-Cu and Sn-Ag-Cu-0.5Ce solder joints at different strain rates are shown in Fig. 36. In the solder

controlled regime, strain homogenization bands, and voids in Sn-Ag-Cu-0.5Ce solder joints were nucleated by $CeSn_3$ intermetallic particles, and crack propagation along the intermetallic layer is less likely to take place in comparison to Sn-Ag-Cu joints, which results in a higher macroscopic ductility and better shock resistance in the Ce-containing solder.

7.5 Conclusions

The mechanical tensile behavior of Sn-Ag-Cu and Ce-containing Sn-Ag-Cu solder joints consists of solder-controlled and intermetallic-controlled strength regimes over a range of strain rates. In the solder-controlled regime, ductile fracture is dominant while in the intermetallic layer-controlled regime, cleavage fracture through the intermetallic layer dominates. The ductility of Sn-Ag-Cu can be improved by addition of Ce with a small penalty in ultimate tensile strength when the strain rate is in the solder matrix controlled regime. The fracture mechanism of the Ce-containing Sn-Ag-Cu alloy is dominated by $CeSn_3$ intermetallics, which homogenize the strain and contribute to void nucleation and growth in the solder-controlled regime. These mechanisms result in larger degree of homogeneous plastic strain, and cosenquently, higher ductility. The dynamic tensile strength and strain to failure of Sn-Ag-Cu and Sn-Ag-Cu-0.5Ce are comparable in the intermetallic layer-controlled regime.

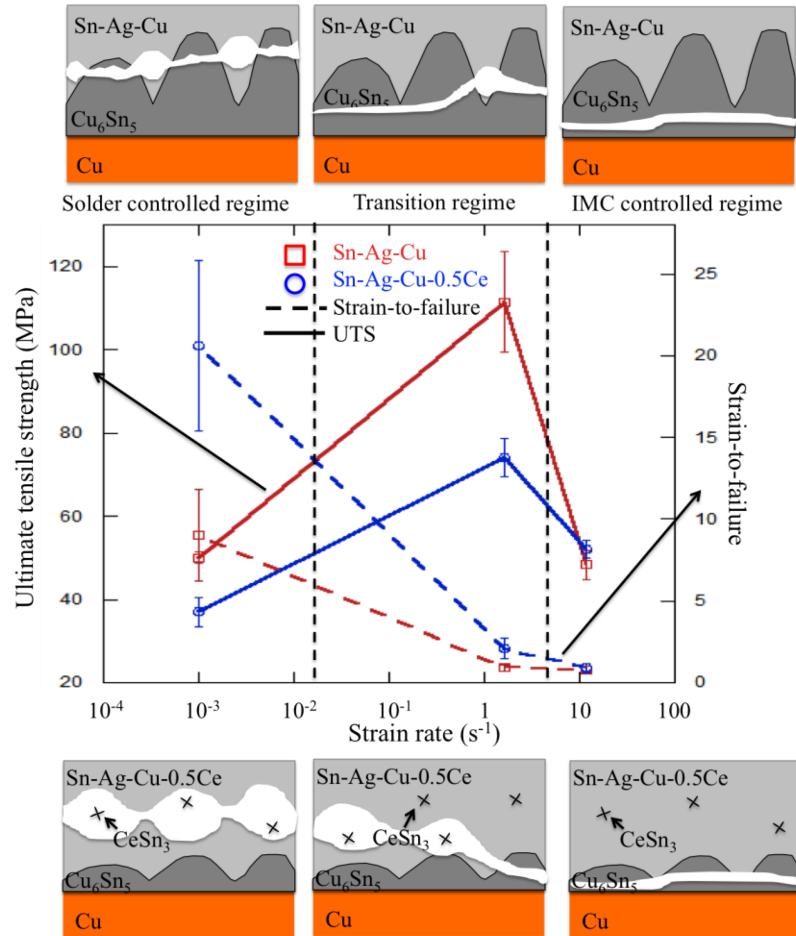

Figure 36. Ultimate tensile strength and strain-to-failure of Sn-Ag-Cu and Sn-Ag-Cu-0.5Ce solder joints, plotted as a function of strain rates. The fracture schematics for Sn-Ag-Cu and Sn-Ag-Cu-0.5Ce solder joints are shown at top and bottom, respectively.

7.6 References

1. N. Chawla, Inter. Mater. Reviews, 2009, 54(6), 368.

2 H. Ma, J. Suhling, J. Mater. Sci., 2009, 44(5), 1141.

3. S. Kang, A. Sarkhel, J. Electron. Mater., 1994, 23(8), 701.

4. D.A. Shnawah, M.F.M. Sabri, I.A. Badruddin, Microelectron. Reliab., 2012, 52(1), 9.

5. H. Lu, H. Balkan, K. Simon, JOM, 2005, 57(6), 30.

6. K.S. Kim, S.H. Huh, K. Suganuma, J. Alloys Compd., 2003, 352(1-2), 226.

7. D.H. Kim, P. Elenius, S. Barrett, IEEE Trans. Electron. Packaging Manufacturing, 2002, 25, 84.

8. M.E. Loomans, M.E. Fine, Metall. Mater. Trans. A, 2000, 31A, 1155.

9. C.M.L. Wu, D.Q. Yu, C.M.T. Law, L. Wang, Mater. Sci. Eng.: R: Reports, 2004, 44(1), 1.

10. F. Guo, M. Zhao, Z. Xia, Y. Lei, X. Li, X. Li, Y. Shi, JOM, 2009, 61(6), 39.

11. L. Zhang, S.-B. Xue, L.-L. Gao, G. Zeng, Z. Sheng, Y. Chen, S.-L Yu, J. Mater. Sci. Mater. Electron., 2009, 20(8), 685.

12. J. Shen, C. Wu, S. Li, J. Mater. Sci. Mater. Electron., 2012, 23(1), 156.

13. L. Gao, S. Xue, L. Zhang, Z. Sheng, G. Zeng, F. Ji, J. Mater. Sci. Mater. Electron., 2010, 21(7), 643.

14. L. Zhang, S. Xue, Y. Chen, Z. Han, J. Wang, S. Yu, F. Lu, J. Rare Earths, 2009, 27(1), 138.

15 Y. Shi, J. Tian, H. Hao, Z. Xia, Y. Lei, F. Guo, J. Alloys Compd., 2008, 453(1-2), 180.

16. H. Hao, J. Tian, Y.W. Shi, Y.P. Lei, Z.D. Xia, J. Electron. Mater., 2007, 36(7), 766.

17. M. Pei, J. Qu, Proc. 57th Electron. Comp. Technol. Conf., 2007, 198.

18. D.Q. Yu, J. Zhao, L. Wang, J. Alloys Compd., 2004, 376(1-2), 170.

19. B. Li, Y. Shi, Y. Lei, F. Guo, Z. Xia, B. Zong, J. Electron. Mater., 2005, 34(3), 217.

20. C. Wu, Y. Wong, J. Mater. Sci. Mater. Electron., 2007, 18(1), 77.

21. A.G. Ramirez, H. Mavoori, S. Jin, Appl. Phys. Lett., 2002, 80(3), 398.

22. H. He, G. Xu, F. Guo, J. Mater. Sci., 2009, 44(8), 2089.

23. Z. Chen, Y. Shi, Z. Xia, Y. Yan, J. Electron. Mater., 2003, 32(4), 235.

24. X.-Y. Zhao, M.-Q. Zhao, X.-Q. Cui, M.-X Tong, Trans. Nonferrous Metals Society of China, 2007, 17(4), 805.

25. M.A. Dudek, R.S. Sidhu, N. Chawla, JOM, 2006, 58(6), 57.

26. M.A. Dudek, R.S. Sidhu, N. Chawla, N. Renavikar, J. Electron. Mater., 2006, 35, 2088.

27. M.A. Dudek, N. Chawla, Metall. Mater. Trans. A, 2010, 41(3), 610.

28. M.A. Dudek, N. Chawla, J. Electron. Mater., 2009, 38(2), 210.

29. H.X. Xie, N. Chawla, K. Mirpuri, J. Electron. Mater., 2012, online first.

30. A. Schubert, H. Walter, R. Dudek, B. Michel, G. Lefranc, J. Otto, G. Mitic, Proc. Int. Symp. on Advanced Packaging Materials Processes, Properties and Interfaces, 129.

31. K.C. Ong, V.B. Tan, C.T. Lim, E.H. Wong, X.W. Zhang, in: Proceedings of the 54th IEEE Electronic Components and Technology Conference, 2004, Vol. 1, 1075.

32. D. Reiff, E. Bradley, in: Proceedings of the 55th IEEE Electronic Components and Technology Conference 2005, Vol. 2, 1519.

33. J.-M. Kim, S.-W. Woo, Y.-S. Chang, Y.-J. Kim, J.-B. Choi and K.-Y. Ji, Thin Solid Films, 2009, 517, 4255.

34. K.E. Yazzie, H.X. Xie, J. Williams, N. Chawla, Scripta Mater., 2012, 66, 586.

35. K.E. Yazzie, H.E. Fei, H. Jiang, N. Chawla, Acta Mater., 2012, 60, 4336.

36. M.A. Dudek, N. Chawla, Mater. Charact., 2008, 59, 1364.

37. H.X. Xie, N. Chawla, Y.-L Shen, Microelectron. Reliab., 2011, 51, 1142.

38. Y.-L. Shen, Constrained deformation of materials. New York: Springer, 2010.

39. S.M. Hayes, N. Chawla, D.R. Frear, Microelectron. Reliab., 2009, 49, 269.

40. H.F. Zhou, Z.F. Zhang, J. Mater. Res., 2008, 23, 1614.

41. P. Kumar, Z. Huang, I. Dutta, R. Sidhu, M. Renavikar, R. Mahajan, J. Electron. Mater., 2012, 41, 412.

8. ELECTROMIGRATION BEHAVIOR OF SN-3.9AG-0.8CU AND SN-3.9AG-0.8CU-0.5CE LEAD-FREE SOLDER JOINTS

8.1 Abstract

Our research has shown that Cerium (Ce)-containing Sn-3.9Ag-0.7Cu alloy exhibits desirable attributes of microstructural refinement, increased ductility and mechanical shock performance, while possess better oxidation resistance than other rare-earth containing solder. In addition to the beneficial mechanical properties, it is imperative to study reliability performance of the novel solder alloys in the form of electromigration experiments, in comparison to Sn-3.9Ag-0.7Cu. In this study, electromigration test was conducted on solder joints at elevated with a constant current using a V-groove testing methodology. The microstructural change of solder joints during electromigration was investigated by scanning electron microscopy, and the void growth was monitored utilizing three-dimensional X-ray microtomography imaging technique. The current density inside solder matrix was determined by 3-D structure based Finite Element Modeling. Finally, the product of diffusivity and effective charge number of solder joints during electromigration was calculated from both marker displacement and 3-D voids growth.

8.2 Introduction

The shift in semiconductor manufacturing from lead (Pb) based solder to Pb-free has caused reliability concerns for future electronic packaging platforms, due to the low ductility and poor mechanical shock resistance of Sn-Ag-Cu solder alloys [1-3]. Recently, a series of rare-earth containing Sn-3.9Ag-0.7Cu Pb-free

solders focused on solving these reliability issues has been proposed [4-6]. It has been shown that the addition of a trace amount rare-earth elements can refine the microstructure, reduce the interfacial intermetallic layer thickness, and, most importantly, increase ductility and shock performance of solder joints. Oxidation behavior studies on rare-earth containing solder indicate that Ce-based solder alloy possess the best oxidation resistance [7] and thermal stability [8] among the rare-earth containing solders.

Although previous studies have established the realistic feasibility of a Ce-based solder alloy as a replacement to conventional SAC alloys, eletromigration behavior of Ce-containing solder still need to be investigated, due to the concerns of increased current density in shrinking packaging size [9]. Electromigration behavior of SnAgCu lead free solder has also been studied and compared with conventional SnPb solder [10]. Generally, SnAgCu solder have much better electromigration performance, owing to high homologous temperature and high Young's modulus. However, very few studies have been carried out on the electromigration behavior of RE containing lead-free solder, and they show a large discrepancy in the literature. Lin et al. reported that the electromigration resistance of SnAgCu [11] and SnZn [12] solder decreased with addition of 0.5 wt.% Ce, which is attributed to finer microstructure in Ce-containing solder and current induced massive Cu diffusion. In contrast, He et al. [13] observed enhanced electromigration resistance in RE containing SnBi solder because of suppressed movement of dislocations and grain boundary. Much work remains to

be done in order to understand the electromigration behavior of Ce-based lead-free solder.

None-destructive X-ray tomography has been utilized as a powerful imaging tool to visualize intrinsic microstructure of solder joint, especially pore characteristics [14, 15]. In electromigration studies, 3D synchrotron tomography imaging technique has been conducted on SnPb solder bumper for fully understanding the shape and size evolution of current induced voids [16]. However, no such work has been reported on lead-free solders.

In this study, the electromigration behavior of Ce-containing Sn-3.9Ag-0.7Cu was compared with Sn-3.9Ag-0.7Cu by examining the microstructure evolution using SEM and X-ray tomography. The product of diffusivity and effective charge number of lead-free solder was also calculated based on the surface marker displacement and 3D voids growth. Finally, the current density distribution in the actual solder joint was studied using Finite Element Modeling (FEM), and the effect of preexisting voids on current distribution will be discussed.

8.3 Materials and Experimental Procedure

Vacuum-melted ingots of Sn-3.9Ag-0.7Cu with trace amounts of Ce (0.5 wt.%) were prepared. High purity Sn-3.9Ag-0.7Cu ingots (Indium, Clinton, NY) were cut into small rectangular pieces (6.5 mm × 6.5 mm × 13 mm) and mixed with Ce shot (ESPI, Ashland, OR). Due to the reactive nature of pure Ce with oxygen, materials were mixed in a quartz ampoule (12 mm in diameter) under a sealed glove box with helium atmosphere. The quartz ampoule then was then

evacuated to 10^{-5} torr and sealed. The sealed ampoules were heated to 1000 °C for 4 hours, and periodically mixed by rotation of the ampoule in order to homogenize the liquid metal. The ampoules were water quenched, removed from the ampoule and sectioned.

To study the effects of electromigration the microstructural change of Ce-containing Sn-3.9Ag-0.7Cu solder, micron-size Cu/Solder/Cu butt joints (500 μm in diameter) were fabricated, using a V-groove testing methodology [17, 18]. Silicon V-groove was made on a silicon wafer using photolithography and wet KOH etching techniques. The as-processed solder ingots were machined in to 500 μm thick solder disc, then punched to small solder disc with 500 μm in diameter. The copper wire end (500 μm in diameter) was polished to a 0.05 μm finish with colloidal silica solution. A rosin mildly activated (RMA) flux was applied to the Cu end bars to improve the wetting between the Cu wires and solder. The butt joints were assembled by aligning two Cu wires and solder disc on Si V-groove, then reflowed on a hotplate using a reflow profile consists of heating the fixture to 170 °C for 2 minutes to allow the excess flux to vaporize, then heating to 20 °C above the melting point and holding for 50 s, then cooling in air on Al blocks. A reproducible cooling rate of 1.4 °C/s was obtained.

Before electromigration tests, joints were re-enforced by a high temperature epoxy resin to avoid brittle failure while transferring the sample to the characterization tools. The as-reflowed sample was then polished down until half of the solder joint was grounded in order to reach high enough current density (10^4 A/cm^2), as well as for microstructure examination using microscopies. Butt

joint and test fixture were preheated inside a furnace at 100 °C for 1 hour to stabilize the sample and minimize thermal shock damage to the joints. Electromigration tests were performed at elevated temperature (100 °C) with a constant current that depends on the sample geometry. The actual temperature of specimen during testing was monitored by attaching a thermocouple at cathode side of solder joint.

The microstructural evolution of the Ce-containing solder joint during electromigration was examined by optical and scanning electron microscopy during current stressing, and compared with conventional Sn-3.9Ag-0.7Cu joints. The electromigration induced voids growth was examined by X-ray tomography technique. To reconstruct 3D structure of solder joints, 3D projection images of solder joints were collected by a MicroXCT system at Intel (Xradia, Concord, California). After data collection, it will be reconstructed by a commercial tomography reconstruction software (MIMICS, Materialise, Ann Arbor, MI) to create a 3D representation of the object. After obtaining a 3D reconstructed microstructure, Finite Element Modeling was utilized to predict the current density distribution based on the actual geometry and distribution of voids in the solder joint. To conduct Finite element analysis on the sample, the volume mesh of the reconstructed model was generated by commercial meshing software (Hypermesh, Altair Engineering Inc., Troy, MI) using linear tetrahedral elements. The meshed model will be then exported to Abaques (Dassault systems simulia, Providence, RI) for current density analysis. In the model, a concentrated current was applied on the cathode side of solder, while the anode side was set to be zero

potential boundary condition to get a current flow from cathode to anode. The electronic conductivity of Sn-3.9Ag-0.7Cu and Sn-3.9Ag-0.7Cu-0.5Ce solder was taken to be $8.66 \times 10^6/\Omega\bullet\text{m}$ and $8.39 \times 10^6/\Omega\bullet\text{m}$, respectively [19].

8.4 Results and Discussion

8.4.1 Finite Element Modeling results

It is well known that vaporized flux during reflow can produce pores near the solder/Cu interface [14]. The void formation inside solder joint is a complicate process with several different sources, and it is extremely difficult to control during the reflow process. It has been reported that the presence of voids can increase solder electronic resistivity [20] and electromigration resistance [21]. Therefore, it is important to determine the effect of void characteristics on the electromigration behavior of solder joint. Instead of characterizing voids size and distribution using metallographic techniques, x-ray microtomography was utilized to understand the effect of pore size, distribution and location on the current density distribution as a simple and non-destructive technique.

Fig. 37 shows a typical “virtual” cross-section through the 3D tomography reconstruction of a solder joint. The solder matrix and pores can be separated based on the different gray scale, which is determined by the attenuation of x-rays through the joint [22]. To accurately reconstruct the size and shape of pores, a novel and semi-automatic segmentation algorithm known as Livewire® was used to create 2D and 3D masks for all the pores (Mimics, Materialise, Ann Arbor, MI) [23]. The typical 3D reconstructed model of Sn-3.9Ag-0.7Cu is shown in Fig. 37. Most of the pores are distributed close to the interfaces between the Cu and solder

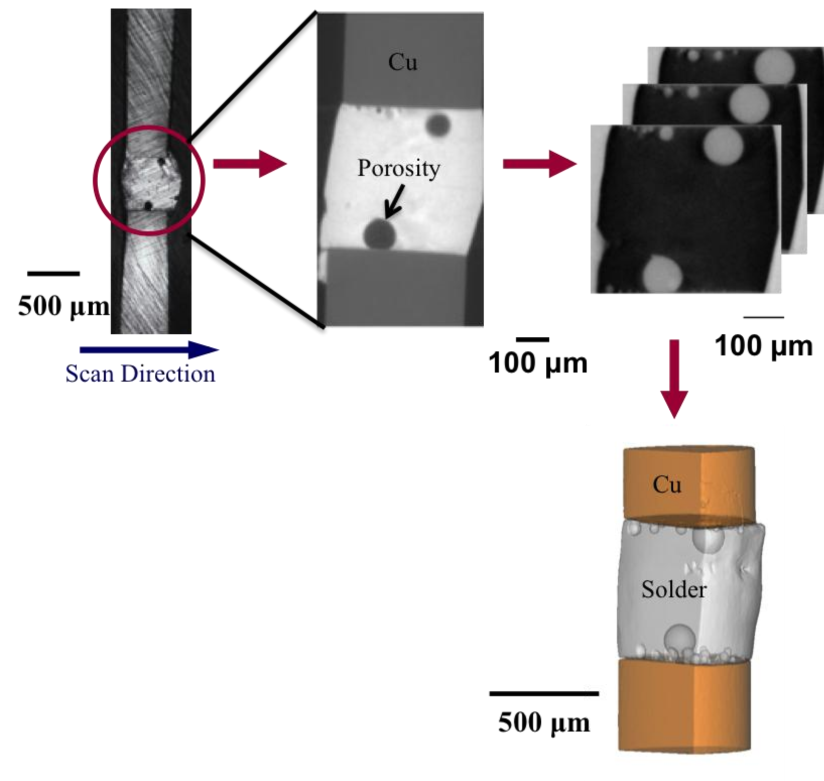

Figure 37. Image of butt solder/Cu joint showing direction of virtual cross-sectioning. 2D virtual cross-section data is also shown, along with segmented gray scale image and 3D reconstructed structure of solder joint

Some fairly large pores appear to accumulate at both the surfaces. Note that the pore size and distribution is extremely inhomogeneous, therefore the results from two-dimensional images always misrepresent pore characteristics. Using the Mimics software, the pore size and the volume of porosity can be quantitatively measured.

After obtaining 3D reconstructed microstructure, Finite Element Modeling was utilized to predict the current distribution based on the actual geometry and distribution of voids in the solder joint. Fig. 36 shows the simulation results of current density distribution in a joint with a total applied current of 10 A at cathode side, and compared to a joint with the same geometry but excluding all pre-existing voids. It is well known that eletromigration induced failure in conventional flip-chip structures is dominated by the current crowding effect in the solder region induced by the geometry of solder joint, where the maximum current density at contact window can be several orders higher than the solder matrix [24, 25]. Such current crowding effect increase the complexity of comparison between solders and accelerates the joints failure. In contrast, V-groove testing methodology provides more uniform current density distribution without this crowding effect [26]. It can be observed in Fig. 38 that the current distribution in the solder region is very uniform and no current crowding area can be observed in the solder joint without pre-existing voids. However, in solder joint with pre-existing voids, local geometry distortion by reflow porosity leads to current crowding at the interface between solder and porosity. It is important to note that the current density in the crowding region is only ~4 times larger than

that of the solder matrix, which is significantly lower than the current crowding effect in a flip-chip structure. The current crowding region is also relatively small and highly localized at solder/Cu interface, as the current distribution in the rest solder region is uniform. Therefore, that crowding effect induced by pre-existing void does not appear to play as crucial a role in V-groove methodology as it does in flip-chip structures, although the failure in current crowding region can be accelerated due to larger electromigration driving forces. Moreover, 3D structure-based finite element modeling results are also used to determine the applied current in Sn-3.9Ag-0.7Cu-0.5Ce joint in order to obtain same current density as Sn-3.9Ag-0.7Cu joint.

8.4.2 Microstructural evolution of Sn-3.9Ag-0.7Cu and Sn-3.9Ag-0.7Cu-0.5Ce during electromigration

Joule heating generated during current stressing caused higher local temperature in solder joints than ambience, which may accelerate the effect of electromigration and alter dominate diffusion species in solder joint. Kao et al. reported that test temperature plays crucial role on the degradation mechanism of electromigration (panacake-type void vs. metallization consumption) [27]. The actual temperature at the solder joint was monitored during the electromigration test by thermal couple attached at cathode side. To minimize thermal shock on joints, the test fixture was stabilized inside the furnace at elevated temperature (100 °C) before testing and the electromigration test was performed inside furnace

to obtain accelerated result. It was found that for current density around 10^4 A/cm^2, temperature increased 34 °C and 35 °C for Sn-3.9Ag-0.7Cu and Sn-3.9Ag-0.7Cu-0.5Ce respectively, which is reasonable because the resistance coefficient of Sn-3.9Ag-0.7Cu is similar to that of Sn-3.9Ag-0.7Cu-0.5Ce alloy [19]. Due to the elevated test temperature, the Sn self-diffusion induced panacake-type void formation can be expected to be dominant failure mechanism in this study.

To characterize electromigration induced microstructural evolution of Sn-3.9Ag-0.7Cu and Sn-3.9Ag-0.7Cu-0.5Ce solder joints, backscatter scanning electron microscopy was utilized due to its atomic number (Z) contrast. Fig. 39 and Fig. 40 showed microstructure of Sn-3.9Ag-0.7Cu and Sn-3.9Ag-0.7Cu-0.5Ce at different stressing time. The observed region was the Cu/solder interface because depletion and extrusion is most likely formed there, and the current crowding occurs in this region, as indicated by FEM results. For the as-reflowed joint, the scalloped Cu_6Sn_5 layer formed at Sn-3.9Ag-0.7Cu-0.5Ce /Cu interface is thinner than that of Sn-3.9Ag-0.7Cu solder joints, as was reported before. After 100 hours current stressing, noticeable amount of Cu was consumed and the intermetallic layer was becoming thinner at the cathode side indicating Cu dissolution into the solder matrix. Cu then diffused to cathode side and excessive intermetallic compounds formed at the anode side. It was also noted that the pancake type voids started to form between Cu_6Sn_5 layer and solder matrix at cathode side in Sn-3.9Ag-0.7Cu joint after 100 hours stressing, as a result of current accelerated Sn self-diffusion. Such a phenomenon is a clear indication that

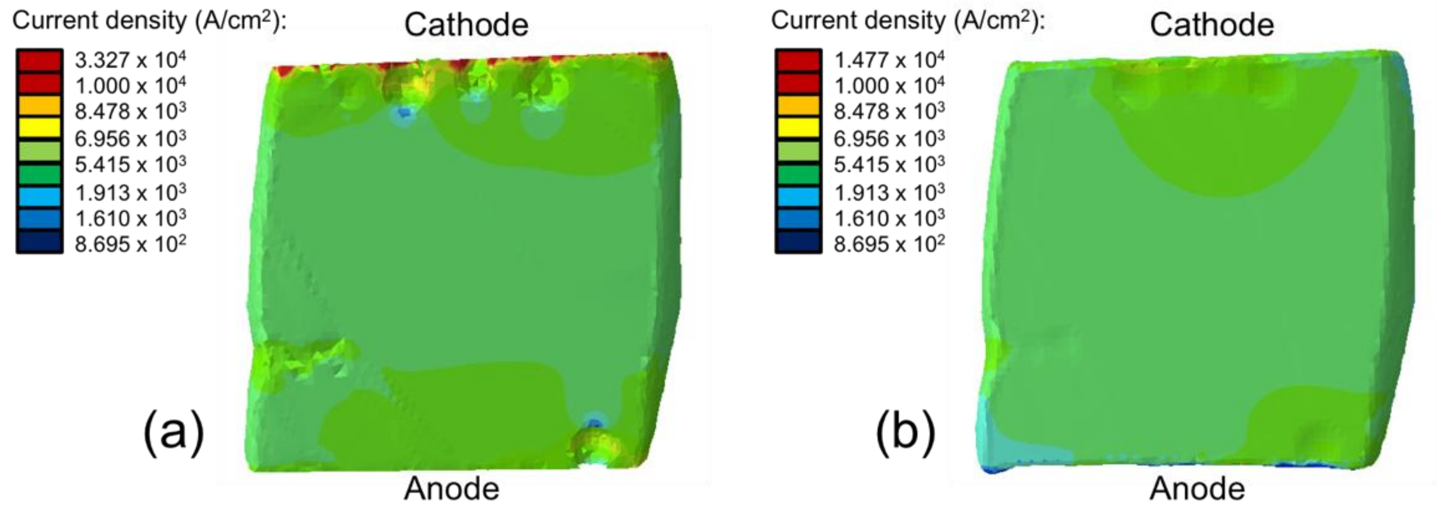

Figure 38. Finite element modeling results of current density inside Sn-3.9Ag-0.7Cu solder (a) with porosity; (b) without porosity

both Cu consumption and pancake-type voids formation in Sn-3.9Ag-0.7Cu joints are the dominant failure mechanism in Sn-3.9Ag-0.7Cu. This is consistent with literature that Sn and Cu electromigration flux turns to be comparable when the solder temperature is above 80 °C. As a result of Sn self-diffusion, compressive stresses built up inside solder joint. The cross-sectioned surface of Sn-3.9Ag-0.7Cu solder remained rather flat due to the mechanical harder solder matrix of Sn-3.9Ag-0.7Cu solder, as indicated in Fig. 40. The compressive stress was relaxed by squeezing out the hillocks of intermetallic at anode side [28].

In comparison to Sn-3.9Ag-0.7Cu solder joints, the microstructural evolution of Sn-3.9Ag-0.7Cu-0.5Ce solder joints is shown in Fig. 40. Similar as Sn-3.9Ag-0.7Cu, both voids formation and metallization consumption were observed at the cathode side. The pancake-type void formed at cathode side is significantly less than that of Sn-3.9Ag-0.7Cu, and substantial amount of Cu_6Sn_5 intermetallic compounds accumulated near the anode and centra regions. The reason for accelerated Cu atom diffusion in Ce-containing Sn-3.9Ag-0.7Cu solder can be explained by the finer microstructure [4], and fast diffusion path provided by grain boundary of Sn. As indicated in the Fig. 42, Sn grain sliding occurs at grain boundary to minimize the total resistance along the current direction due to the anisotropic resistance properties of Sn [29, 30]. Meanwhile, Cu_6Sn_5 intermetallic compound accumulated along the grain boundary and numerous newly formed Cu_6Sn_5 intermetallic dispersed in the middle of the solder alloy. The Cu_6Sn_5 intermetallic layer at the anode side also showed inhomogeneous growth rate respect to the Sn grain boundary, that Cu_6Sn_5 intermetallic at region A

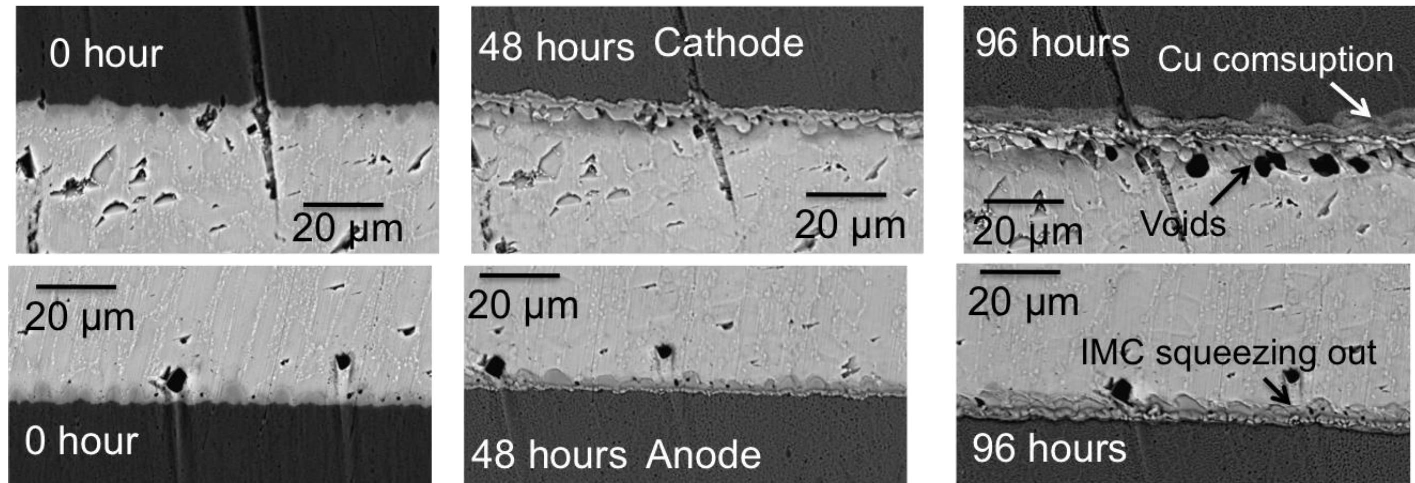

Figure 39. Backscatter electron microscopy images of cross-section of Sn-3.9Ag-0.7Cu/Cu solder joint after current stressing for: (a) 0 hour; (b) 48 hours; and (c) 96 hours.

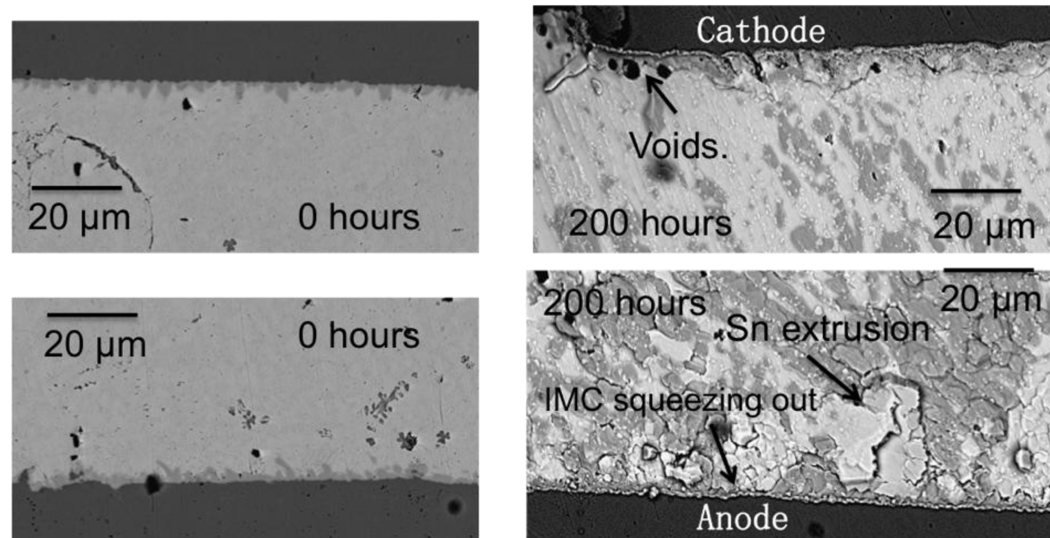

Figure 40. Backscatter electron microscopy images of the cross-section of Cu/Sn-3.9Ag-0.7Cu-0.5Ce/Cu butt joints after current stressing at current 10 A and 100 °C for: 0 hour and 300 hours.

(right side of grain boundary) grew faster than region B. These phenomena are clearly indicating Sn grain boundary can act as an effective diffusion barrier for migration of Cu atom driven by current [31]. In Sn-3.9Ag-0.7Cu-0.5Ce solder, one may expect more high-angle grain boundaries present inside the finer solder matrix than Sn-3.9Ag-0.7Cu. Therefore, excessive amount Cu_6Sn_5 intermetallic compound formed in the central region of the solder joint. Such accelerated Cu atom diffusion and substantial Cu_6Sn_5 intermetallic compound formation inside solder joint can greatly retard the Sn atom diffusion since critical product of Cu_6Sn_5 is 4-5 times larger than that of Sn [32]. It is interesting to note that unlike Sn-3.9Ag-0.7Cu, the Sn extrusion and surface bulge is observed in the solder central region, where $CeSn_3$ particles are densely distributed. Sn extrusion always formed at the top side relative to nearby $CeSn_3$ particles. Considering the current induced Sn diffusion direction is from top to bottom, it is hypothesized that the formation of Sn extrusion is due to the block effect of immobile $CeSn_3$ precipitates [33], as well as solder matrix softening by $CeSn_3$ particles [34]. Therefore, one may expect that current induced Sn atom migration is interrupted by $CeSn_3$ particles and the compressive stress localization at the anode side, which may initiate crack [28], can be branched. However, the blocking effect of $CeSn_3$ particles does not contribute to the enhanced electromigration resistance of Ce-containing solder in this case due to the existence of a free surface, as the back stress is released by forming Sn extrusion at the solder surface. Thus, the suppressed pancake-type voids formation in Ce-containing solder is mainly

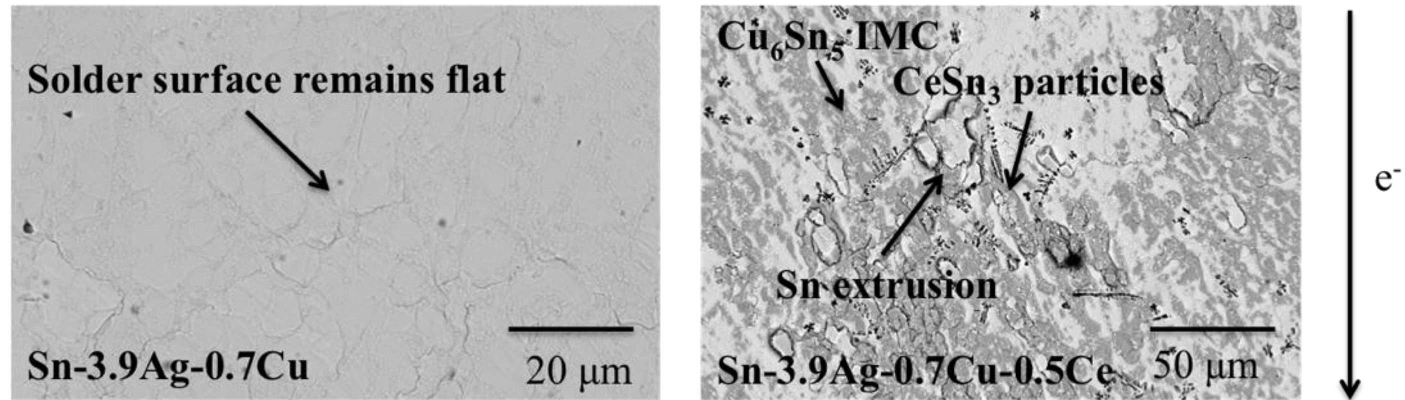

Figure 41. Backscatter electron microscopy images of central region of Sn-3.9Ag-0.7Cu and Sn-3.9Ag-0.7Cu-0.5Ce joints after current stress for 200 hours (Arrow indicating current direction).

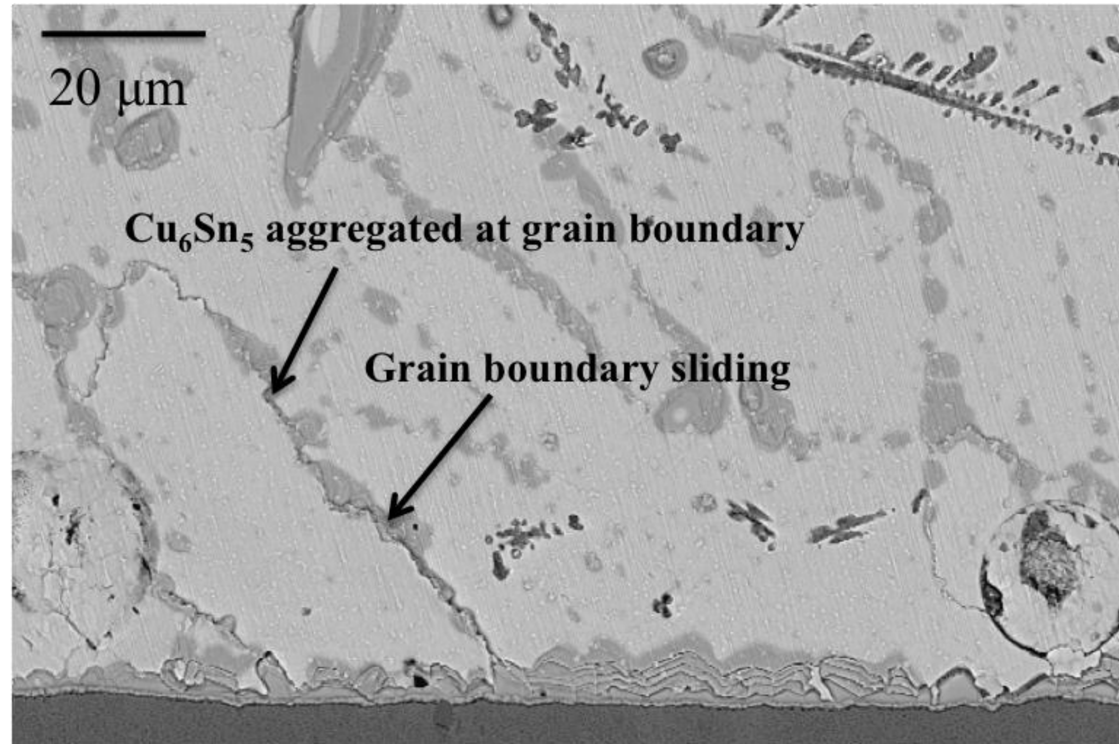

Figure 42. Backscatter electron microscopy images of anode side of Cu/Sn-3.9Ag-0.7Cu-0.5Ce/Cu butt joints after current stressing for 100 hours.

because of quick formation of the Cu_6Sn_5 intermetallic compound. Although consumption of Cu metallization could cause catastrophic failure in thin-film Cu UBM [11], rapid formation of Cu_6Sn_5 intermetallic compound is favorable for electromigration resistance in thick Cu UBM [35]. Moreover, the electromigration performance of Ce-containing solder can be further improved in actual solder bumper, where free surface does not exist.

8.4.3 Electromigration behavior of Sn-3.9Ag-0.7Cu and Sn-3.9Ag-0.7Cu-0.5Ce solders

The drift velocity of Sn atom and the product of diffusivity and effective charge are normally measured for quantitative comparison of electromigration resistance between different solder alloys. One way to quantitatively measure the drift velocity in butt solder joint is to measure the marker displacement on the solder surface. Markers can be polishing compound introduced during polishing or visible intermetallic compound, such as $CeSn_3$. Only markers that are 20 μm away from cathode side are selected for the measurement, to eliminate the effect of back stress gradient [36]. The average diffusivity can be calculated by assuming that current induced Sn migration is uniform across the solder cross-section:

$$J = \frac{D}{\Omega \cdot t}$$

Where D is the displacement measured from marker movement, Ω is the average atomic volume of Sn-rich solder alloy, which can be approximately calculated by the lattice parameter of Sn ($0.0027\ nm^3$) [37], t is the duration of the

electromigration test. Thus, the value of electromigration induced Sn atomic flux can be obtained: J_{EM}= 6.5 × 10^5 atoms/cm^2•s. As proposed by Huntington and Grone, the driving force for electromigration can be calculated by [38]:

$$F_{EM} = Z^* eE$$

Where Z* is the effective charge number of the migrating ion in electromigration (Sn in this case), e is the charge of an electron and E is the electric field. By assuming back stress is completely released at free surface, the atomic flux in units of atoms/cm^2 can then be taken as:

$$J_{EM} = C \frac{D}{kT} Z^* eE$$

Where C is the concentration of atoms per unit volume and D/kT is the atomic mobility of Sn atom. On the basis of the above equations, we can obtain the values of the product of diffusivity and effective charge number for Sn-3.9Ag-0.7Cu which is 0.774 × 10^{-10} cm^2/s. The result obtained from Blech strips test structure is slightly larger than was obtained in this study, because of the smaller current density and higher silver content in the this study [39]. And the DZ* of Sn-3.9Ag-0.7Cu is one order smaller than that of Sn-Pb solder, which is due to smaller modulus and lacking of diffusion barrier in Sn-Pb solder [16]. It should be noted that the DZ* of Ce in Sn-3.9Ag-0.7Cu solder could not be measured from marker displacement on the solder surface as the pancake-type voids growth in Sn-3.9Ag-0.7Cu-0.5Ce was extremely limited.

3D void growth of Sn-3.9Ag-0.7Cu and Sn-3.9Ag-0.7Cu-0.5Ce solder joint were also studied using high resolution X-ray tomography technique. 3D

rendering was performed at 0, 100, 200, 300 and 550 hours. The void at cathode and anode sides were reconstructed separately for side-by-side comparison of the samples, as shown in Fig. 43 and 44. It is clear that the Sn-3.9Ag-0.7Cu solder showed massive void growth and movement after only 100 hours stressing, which correlates very well with the surface observation. After 300 hours stress, the cathode side of Sn-3.9Ag-0.7Cu solder joint is saturated with voids. By examining the size and distribution of individual void during electromigration, it was found that the growth of preexisting voids is less pronounced than that of newly nucleated voids. Void also prefer to nucleate at void dense region, where current density is higher due to the current crowding effect. In comparison, almost no void growth and void nucleation take place on the Sn-3.9Ag-0.7Cu-0.5Ce solder joint, even after 550 hours current stressing. The volume change of the pancake-type void growth during electromigration can be accurately measured from 3-D render structure. The electromigration induced atomic flux calculated based on 3-D structure is $J_{EM} = 5.8 \times 10^5$ atoms/cm^2•s which is slightly smaller than that obtained from surface marker movement. This is reasonable because of the over-estimated cross-section area in previous result. The Sn flux in Sn-3.9Ag-0.7Cu-0.5Ce, however, cannot be measured due to smaller void growth in the Ce-containing solder. As the formation of Cu_6Sn_5 is the dominate phenomenon in Ce-containing solder, it would be interesting if one could resolve Cu_6Sn_5 phases from X-ray tomography images, which is possible due to the difference of X-ray attenuation coefficient between Cu_6Sn_5 and Sn. Unfortunately, the X-ray flux of a lab-scale X-ray tomography tool is too low to visualize contrast difference

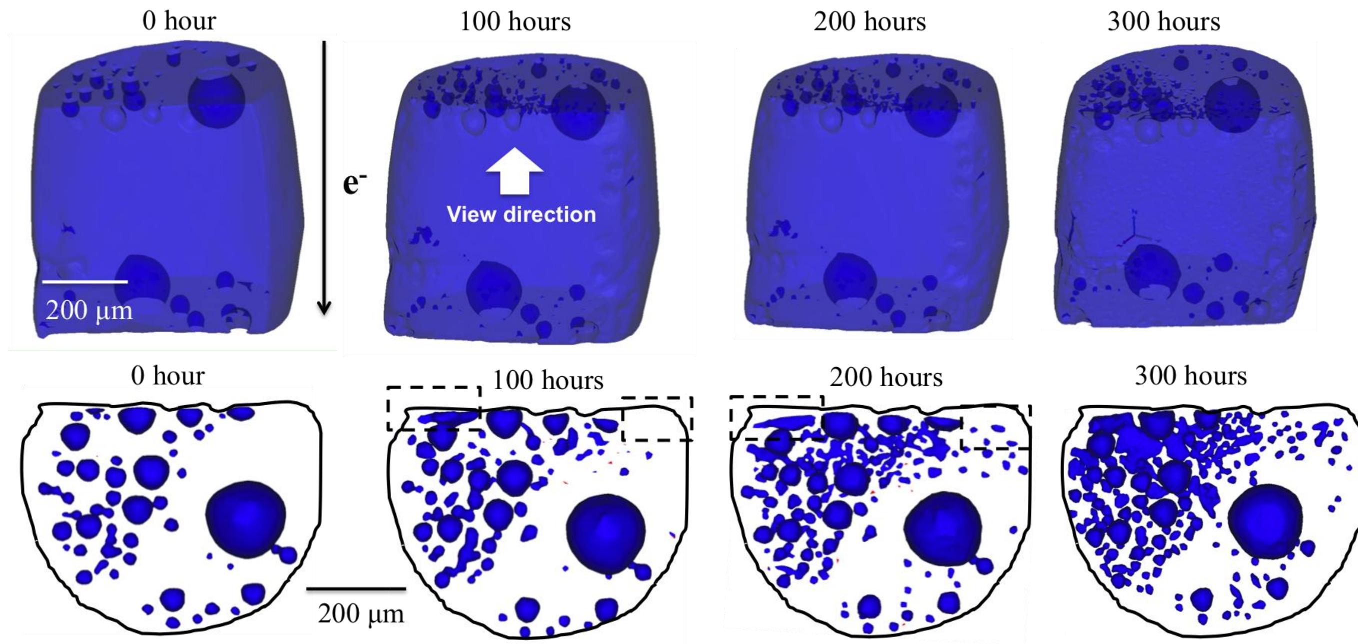

Figure 43. Sn-3.9Ag-0.7Cu void growth over time, showing 3-D rendering (top) and cathode void top view (bottom).

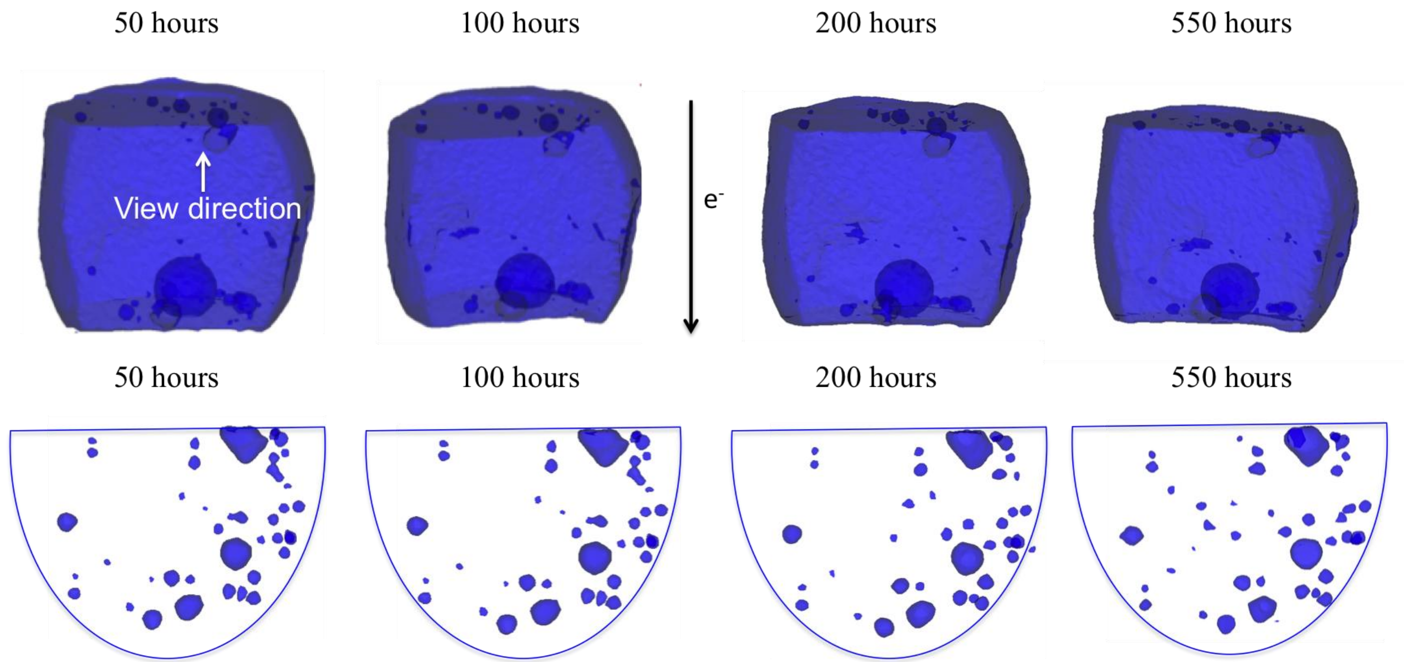

Figure 44. Sn-3.9Ag-0.7Cu-0.5Ce void growth over time, showing 3-D rendering (top) and cathode void top view (bottom).

between Cu_6Sn_5 and Sn is very close. This problem can be solved by utilizing synchrotron tomography [40].

8.5 Conclusions

The electromigration behavior of Sn-3.9Ag-0.7Cu-0.5Ce solder joint was studied by silicon V-groove methodology and compared with conventional Sn-3.9Ag-0.7Cu solder. Based on the experimental results, the following conclusion can be drawn.

1. Preexisting voids can alter current distribution inside solder by introducing current crowding region.
2. Microstructure characterization indicates that the dominant failure mechanism of Sn-3.9Ag-0.7Cu and Sn-3.9Ag-0.7Cu-0.5Ce in this study is both due to pancake-type voids formation and metallization consumption, respectively.
3. As a result of finer microstructure, Cu atom diffusion is accelerated in Sn-3.9Ag-0.7Cu-0.5Ce solder, and rapid Cu_6Sn_5 formation retard pancake-type voids formation at the cathode side.
4. $CeSn_3$ intermetallic particles can block the Sn diffusion by forming Sn extrusion, which may also benefit electromigration performance of Ce-containing solder.
5. The product of effective charge number and diffusivity is calculated based on the surface mark movement, and was found that electromigration resistance of Sn-3.9Ag-0.7Cu and Sn-3.9Ag-

0.7Cu-0.5Ce are significantly higher than that of Sn-Pb solder alloy.

8.6 References

1. N. Chawla, Int. Mater. Rev., 2009, 54, 368.
2. N.C. Lee, D. Lu, C.P. Wong, Mater. Adv. Packag., 2009, 181.
3. I.E. Anderson, J. Mater. Sci. Mater. Electron., 2007, 18(1-3), 55.
4. M.A. Dudek, N. Chawla, Metall. Mater. Trans. A, 2010, 41(3), 610
5. M.A. Dudek, R.S. Sidhu, N. Chawla, JOM, 2006, 58(6): 57.
6. M.A. Dudek, R.S. Sidhu, N. Chawla and N. Renavikar, J. Electron. Mater., 2002, 31, 1122.
7. M.A. Dudek, N. Chawla, J. Electron. Mater., 2009, 38(2), 210.
8. H.X. Xie, N. Chawla, K. Mirpuri, J. Electron. Mater., online first.
9. K.N. Tu, J. Appl. Phys., 2003, 94(9), 5451.
10. T.Y. Lee, K.N. Tu, D.R. Frear, J. Appl. Phys., 2001, 90(9), 4502.
11. H.-J. Lin, J.-S. Lin, T.-H, Chuang, J. Alloys Compd., 2009, 487(1-2), 506.
12. H.-J. Lin, T.-H Chuang, Mater. Lett., 2010, 64(4), 506.
13. H. He, G. Xu, F. Guo, J. Mater. Sci., 2009, 44(8), 2089.
14. L. Jiang, N. Chawla, M. Pacheco, V. Noveski, Mater. Charact., 2011, 62(10), 970.
15. M.A. Dudek, L. Hunter, S. Kranz, J.J. Williams, S.H. Lau, N. Chawla, Mater. Charact., 2010, 61(4), 433.
16. T. Tian, K. Chen, A.A. MacDowell, D. Parkinson, Y.-S. Lai, K.N. Tu, Scripta Mater., 2011, 65(7), 646.
17. F. Ren, J.W. Nah, J.O. Suh, K.N. Tu, B.S. Xiong, L.H. Xu, J.H.L. Pang, Mater. Res. Symp. Proc., Warrendale, PA, 2005, 863, B10.2.

18. M. Lu, D.-Y. Shih, P. Lauro, C. Goldsmith, D.W. Henderson, Appl. Phys. Lett., 2008, 92(21), 211909.

19. Z. Chen, Y. Shi, Z. Xia, Y. Yan, J. Electron. Mater., 2003, 32(4), 235.

20. M. Yunus, K. Srihari, J.M. Pitarresi, A. Primavera, Microelectron. Reliab., 2003, 43(12), 2077.

21. Z. Tang, F.G. Shi, Microelectron. J., 2001, 32(7), 605.

22. J.D.J. Ingle, Spectrochemical analysis, 1988, New Jersey, Prentic Hall.

23. W.A. Barrett, E.N. Mortensen, Med. Image Anal., 1997, 1(4), 331.

24. E.C.C. Yeh, W.J. Choi, K.N. Tu, P. Elenius, H. Balkan, Appl. Phys. Lett., 2002, 80(4), 580.

25. S.W. Liang, Y.W. Chang, T.L. Shao, C. Chen, K.N. Tu, Appl. Phys. Lett., 2002, 80(4), 580.

26. M. Lu, D.-Y, Shih, C. Goldsmith, T. Wassick, in Reliability Physics Symposium, 2009 IEEE International. 2009, 149.

27. J.H. Ke, T.L. Yang, Y.S. Lai, C.R. Kao, Acta Mater., 2011, 59(6), 2462.

28. T.Y. Lee, K.N. Tu, D.R. Frear, J. Appl. Phys., 2001, 90(9), 4502.

29. A.T. Wu, K.N. Tu, J.R. Lloyd, N. Tamura, B.C. Valek, C.R. Kao, Appl. Phys. Lett., 2004, 85(13), 2490.

30. A.T. Wu, A.M. Gusak, K.N. Tu, C.R. Kao, Appl. Phys. Lett., 2005, 86(24), 241902-4.

31. K. Lee, K.S. Kim, K. Suganuma, J. Mater. Res., 2011, 26(20), 2624.

32. L. Xu, J.-K, Han, J.J. Liang, K.N. Tu, Y.-S. Lai, Appl. Phys. Lett., 2008, 92(26), 262104.

33. Y.-M. Hung, C.-M. Chen, J. Electron. Mater., 2008, 37(6), 887.

34. H.X. Xie, N. Chawla, Y.-L Shen, Microelectron. Reliab., 2011, 51, 1142.

35. J.-W. Nah, J.O. Suh, K.N. Tu, S.W. Yoon, V.S. Rao, V. Kripesh, F. Hua, J. Appl. Phys., 100(12), 123513.

36. L. Xu, J.H.L. Pang, K.N. Tu, Appl. Phys. Lett., 2006, 89(22), 221909.

37. Q.T. Huynh, C.Y. Liu, C. Chen, K.N. Tu, J. Appl. Lett., 2001, 89, 4332.

38. H.B. Huntington, A.R. Grone, J. Phys. Chem. Solids, 1961, 20(1-2), 76.

39. Y.-C. Hsu, C.-K. Chou, P.C. Liu, C. Chen, D.J. Yao, T. Chou, K.N. Tu, J. Appl. Phys., 98(3), 033523.

40. K.E. Yazzie, J.J. Williams, N.C. Phillips, F. De Carlo, N. Chawla, Mater. Charact., 2012, 70, 33.

9. ENHANCING THE DUCTILITY OF SN-AG-CU LEAD-FREE SOLDER JOINTS BY ADDITION OF COMPLIANT INTERMETALLICS

9.1 Abstract

Tin (Sn)-rich lead (Pb)-free solders containing rare-earth (RE) elements have been shown to exhibit desirable attributes of microstructural refinement and enhanced ductility relative to conventional Sn-3.9Ag-0.7Cu lead-free solder, due to the unique mechanical properties of RE-Sn intermetallics. However, the roles of soft intermetallic phase in the enhanced ductility of Pb-free solder still needs to be further investigated. In this study, Ca and Mn were selected as doping elements for Sn-Ag-Cu solder. The mechanical properties of Ca-Sn and Mn-Sn intermetallics as a function of indentation depth were measured by nanoindentation using continuous stiffness method (CSM). The microstructure and mechanical properties of as-reflowed Ca and Mn-containing Sn-Ag-Cu solder joints were studied and compared with that of conventional Sn-Ag-Cu and RE-containing solder joints. It is shown that soft intermetallics result in higher ductility in Pb-free solders.

9.2 Introduction

Due to increasing demands to find a replacement of Pb-Sn solder [1], a series of rare earth (RE) doped lead (Pb)-free solder alloys have gained significant attention due to their superior physical and mechanical properties [2-4]. Previous investigations have shown that adding RE elements can refine the microstructure of Pb-free solders [5-7], refined intermetallic particle size [8-10], reduce melting

temperature [11,12], decrease the thickness of the intermetallic layer that forms between solder and substrate [5,13], improve wettability [4,12], and promote a strong bond to semiconductors [14,15]. Enhanced electromigration resistance [16], good thermal stability [17,18] and reasonable oxidation resistance [19] have also been shown. In particular, RE doped lead-free solders have been reported to have excellent mechanical properties, i.e., increased strength [20,21], strain-to-failure [9,22,23], and improved creep resistance [24,25].

We have shown that Pb-free solder alloys containing small amounts of La [17,22] and Ce [5,18,23] exhibit a significant enhancement in ductility, in comparison to conventional Sn-3.9Ag-0.7Cu (SAC) solder. The proposed mechanism for this is based on the soft RE-Sn intermetallics [5] formed inside RE-containing Pb-free solders [23]. However, while experiments do show that RE-Sn intermetallics enhance ductility of RE-containing solders, the precise mechanisms for this enhancement have not been studied in detail. In order to understand the relationship between soft intermetallic particle and enhanced ductility, it is necessary to conduct mechanical tests on the solder alloys with soft and hard particles, to simulate the effect of adding RE-Sn intermetallics to the microstructure. It has been reported that small addition of Mn can form $MnSn_2$ phase in Sn-rich Pb-free solder with modulus and hardness values (143.9 ± 1 GPa and 8.9 ± 0.1 GPa respectively) significantly higher than RE-Sn and other traditional intermetallics formed in Pb-free solder [26]. $CaSn_3$ is formed in Ca-containing Sn-rich alloys. More importantly, it has the same crystal structure as

$CeSn_3$ and $LaSn_3$ (cubic, L12) [27], but with a much lower melting point, indicating that it might be a softer phase [28].

In this study, Ca and Mn were each added to SAC. The geometry and composition of intermetallic phases formed in the as-processed alloys was studied using scanning electron microscopy (SEM) and energy dispersive spectroscopy (EDS). The Young's modulus and hardness of intermetallics were measured by nanoindentation (with a comparison to pure Sn and RE-Sn intermetallics). The microstructure and mechanical properties of Ca and Mn solders joint were examined, and compared to SAC and RE-containing SAC. It will be shown that the Young's modulus and hardness values of $CaSn_3$ are significantly lower than that of RE-Sn intermetallics, while $MnSn_2$ is a much stiffer and harder intermetallic. Only the solder joints containing soft intermetallic particles exhibited enhanced ductility compared to SAC. This study shows that one way to obtain softer, more ductile Pb-free solders, with properties approaching that of Pb-Sn, is to add compliant intermetallics to the microstructure.

9.3 Materials and Experimental Procedure

Vacuum-melted ingots of SAC with 2 wt.% Ca and Mn were prepared for nanoindentation, in order to obtain relatively large intermetallic particles. For mechanical testing, we have shown that alloying additions of less than 0.5 wt.% provide the best enhancement in ductility. So for shear tests, samples of SAC with 0.5 wt.% Ca and Mn were fabricated. High purity SAC ingots (Indium, Ithica, NY) were cut into small rectangular pieces ($6.5 \times 6.5 \times 13$ mm) and were mixed with Ca and Mn shot (ESPI, Ashland, OR). Due to their high reactivity, Ca, Mn

and solder were mixed in a sealed glove box in helium atmosphere, and then sealed in a quartz ampoule (12 mm in diameter). With a stopcock the quartz ampoule was evacuated to 10^{-5} torr and sealed. The sealed ampoules were heat treated at 700°C for 4 hours, and periodically mixed by rotating the ampoule, in order to homogenize the liquid metal. The ampoules were then furnace cooled for nanoindentation (to obtain larger particles) or water quenched for mechanical shear tests. The samples were removed from the ampoule, and sectioned.

Microstructural characterization was conducted on the as-processed ingot material. Ingots were sectioned and polished to a final finish of 0.05 μm colloidal silica. Optical microscopy, scanning electron microscopy (SEM), and quantitative image analysis (ImageJ, Gaithersburg, MD) were conducted to quantify the size and spacing of RE-containing intermetallic phases. The intermetallic phases of interest were fit to ellipses to estimate their size and aspect ratio. Energy dispersive spectroscopy (EDS) was also used to confirm the composition of the RE-containing intermetallics.

Nanoindentation was conducted on intermetallics in the as-processed bulk ingots, as well as on pure Sn. The ingots were sectioned and polished to a final finish of 0.05 μm colloidal silica. Samples were mounted on aluminum stubs for testing using a mounting adhesive (Crystalbond™, West Chester, PA). Nanoindentation was carried out by selecting 20 intermetallic particles randomly. The center of each of these intermetallics was indented. The nanoindenter was first calibrated by measuring Young's modulus and hardness of a silica standard at a strain rate of $0.05 s^{-1}$. A continuous stiffness measurement (CSM) technique

was used during indentation. With the CSM, a load is applied to the indenter tip to drive the indenter into the specimen surface while concurrently superimposing an oscillating force with a small amplitude (significantly smaller than the nominal load). An accurate measurement of the contact stiffness at all indentation depths is provided by separating the in-phase and out-of-phase components of the load-displacement data [29]. The advantage of CSM is that an instaneous measurement of modulus and hardness can be obtained during indentation. Thus, multiple indentations at different depths are not necessary.

For all indentations, Young's modulus was calculated as a function of indentation depth, to determine the onset of any pile-up, sink-in or cracking during indentation [30], as well as the thickness of oxidation layer. Indentation was carried out using a Berkovich indenter to an average depth of 1000-1500 nm per indentation. Young's modulus for an individual indentation was taken as the average value over a depth range where the modulus was independent of depth, i.e, approximately 500-1300 nm. An SEM equipped with Focused Ion Beam (FIB) and EDS was used after indentation to ensure that the indentations were located on the intermetallics, and to analyze the deformation during indentation. Indentation size was much smaller than the size of the individual intermetallic particles, so sink-in of the particle during testing was not likely to take place.

A FIB was used to cross-section oxidized samples of Sn-3.9Ag-0.7Cu-0.5Ca to study the thickness of oxide layer. Samples were first coated with a 1-μm-thick Pt layer using the ion beam to protect from subsequent beam damage. A trench was milled using the ion beam at 30 kV and a current of 5 nA. The initial

cleaning cross-section was perform at 30kV and 0.3 nA, with subsequent cleaning sections using smaller currents to a final ion bean current of 30 pA.

Mechanical shear tests and interrupted shear tests were conducted on solder/Cu single lap shear joints. As-processed solder ingots were machined into 6.35 × 6.35 × 0.5 mm squares. These were lightly polished to remove oxidation caused by the machining process, and ultrasonically cleaned in acetone. Oxygen free copper bars (50.8 mm in length and 6.35 mm in thickness) were polished to a 0.05 μm finish with colloidal silica solution. A graphite mask was applied to the Cu bars, leaving a 6.35 × 6.35 mm area for reflow. An RMA flux was applied to the unmasked portions of the copper bars to improve the wetting between the copper and the solder. The joint was assembled with the aid of a reflow fixture, to minimize misalignment, and maintain a consistent joint solder thickness of approximately 500 μm. The entire assembly was heated on the hot plate. The typical reflow profile consisted of heating the jig to 170°C and held at the same temperature for 120 sec, to allow excess flux to vaporize. The temperature was then raised until the solder reached 220 °C and was held for 40 s. The assembly was then removed from the hot plate and air-cooled on an aluminum heat sink. The actual temperature of solder during the reflow process was monitored using a thermocouple placed inside, and a reproducible cooling rate of 0.7°C/s was obtained. The cooling rate was measured from the peak temperature to 150°C, because the joint microstructure does not change significantly below this temperature during cooling [31-33]. A reproducible solder thickness of 500 μm was obtained in all joints. Shear testing was conducted using a servo-hydraulic

load frame (MTS systems, Minneapolis, MN) at room temperature and a shear strain rate of 10^{-3} s^{-1} in displacement control mode. To compensate for the variability in joint geometry, the joint thickness and reflowed area were measured in each case, after the experiment, to accurately measure the applied stress and strain.

9.4 Results and Discussion

9.4.1 Microstructural characterization

9.4.1.1 As-processed microstructure

Fig. 45 shows the microstructure of as-processed Sn-3.9Ag-0.7Cu-0.5Ca and Sn-3.9Ag-0.7Cu-0.5Mn water quenched ingots. All microstructure consisted of Sn-dendrites and a eutectic mixture of Ag_3Sn and Cu_6Sn_5 intermetallics distributed in the Sn-rich matrix. Both Ca and Mn-containing solder consisted of homogeneously distributed intermetallic phases (darker phases in the micrographs). Ca-Sn intermetallics had a dendritic geometry, which have been also observed in other rare-earth lead-free solder systems [5], while Mn-Sn intermetallic had a more needle-like geometry. To measure the mechanical properties of Ca-Sn and Mn-Sn intemetallics, furnace cooled solder ingots with 2 wt pct Ca and Mn were also prepared, as shown in Fig. 46. A slower cooling rate also yielded a microstructure consisting of Sn-rich dendrites and eutectic region, but relatively larger intermetallics were observed in the Sn-rich matrix. Note that all the Ca and Mn phases are considerably larger in size than obtained in the water quenched sample. Both furnace cooled Ca and Mn phases had a faceted geometry. Energy Dispersive Spectroscopy (EDS) analysis of the alloys was conducted to

confirm the composition of the particles, as summarized in Table 11. Analysis of the particles yielded an atomic ratio between Mn and Sn of approximately 2:1, indicating a stroichiometry of $MnSn_2$, which was also confirmed by the Mn-Sn phase diagram [35]. However, EDS results on the Ca-Sn intermetallic yielded an atomic ratio between Sn and Ca significantly larger than predicted by the Ca-Sn phase diagram (3:1), due to the oxidation of Ca-Sn intermetallics and Calcium oxide being dissolved during sample preparation, i.e., polishing. To study the composition of Ca-Sn intermetallic and measure the thickness of the oxidize layer, a small cross-section trench was milled on the surface of a partially oxidized Ca-Sn particle using FIB, and the concentrations of Sn, Ca, oxygen (O) elements were measured on cross-section by means of EDS line scans. A typical concentration profile is shown in Fig. 47. The concentration of Sn and Ca in oxide layer is very low. The dotted line in the figure denotes the depth of oxygen penetration, which is also indicated in the EDS line scan results. The thickness of oxide layer measured from EDS results was around 0.8 μm. The atomic ratio between Ca and Sn below the oxide layer is approximately 3:1, confirming the composition of the unoxidized intermetallic particle as $CaSn_3$.

Table 11. EDS analysis of Mn-Sn and Ca-Sn intermetallic phases in as-processed alloys.

Alloy	Sn (At. Pct)	Ca, Mn (At. Pct)	O (At. Pct)	Sn/Mn, Ca Ratio
SAC-0.5Ca	53.8 ± 2.0	8.3 ± 1.2	37.9 ± 2.5	6.6 ± 1.0
SAC-0.5Mn	67.6 ± 2.1	32.4 ± 2.1	0	2.1 ± 0.2

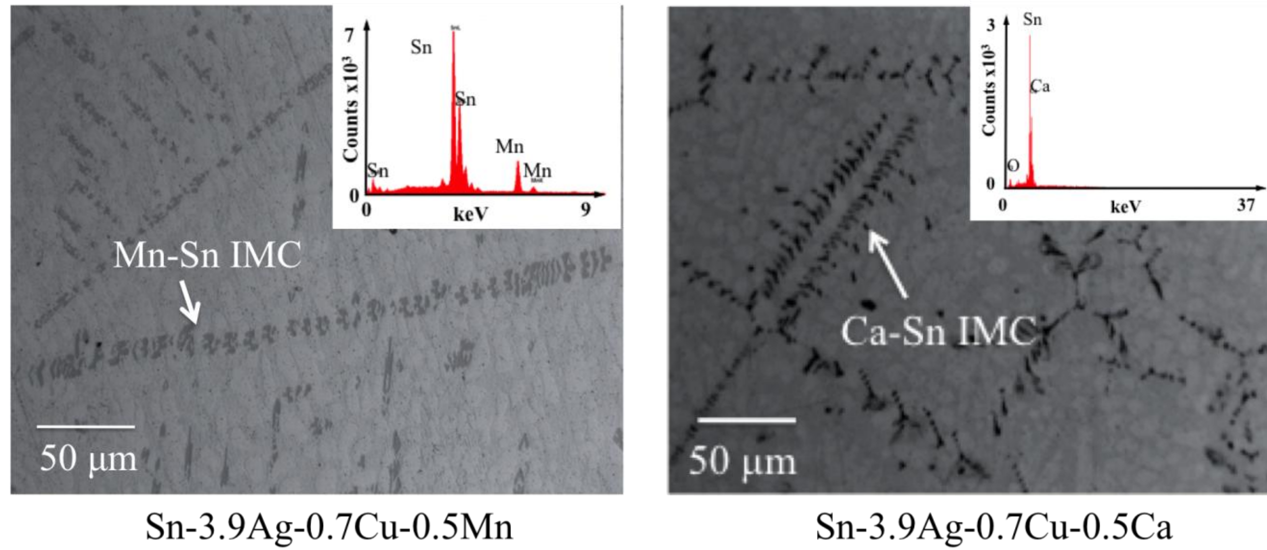

Figure 45. As-processed optical images of left: Sn-3.9Ag-0.7Cu-0.5Mn and Right: Sn-3.9Ag-0.7Cu-0.5Ca, and EDS spots scan results on intermetallic phases.

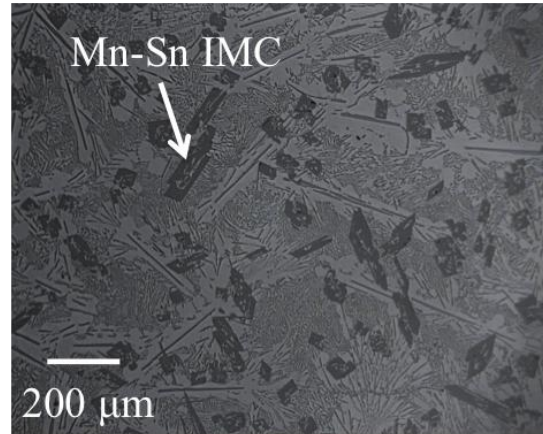

Furnace cooled Sn-3.9Ag-0.7Cu-2Mn ingot

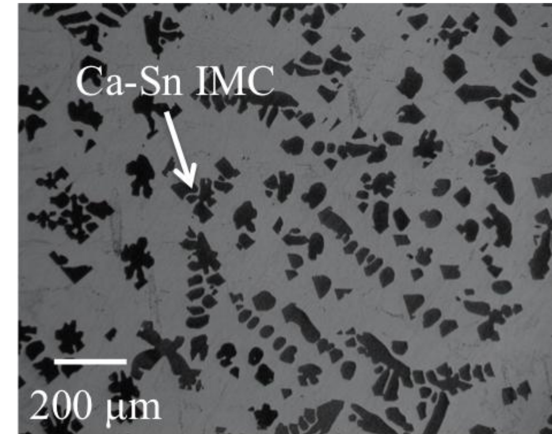

Sn-3.9Ag-0.7Cu-2Ca ingot

Figure 46. As-processed optical images of left: furnace cooled Sn-3.9Ag-0.7Cu-2Mn and Right: furnace cooled Sn-3.9Ag-0.7Cu-2Ca.

From Fig. 48 it appears that the size and distribution of the $CaSn_3$ and $MnSn_2$ intermetallics are nearly the same. This is further confirmed by the quantitative measurements as shown in Table 12, which includes particle size and aspect ratio for the intermetallics present in Ca and Mn containing Sn-3.9Ag-0.7Cu solder alloys. The size and aspect ratio of intermetallic particles were measured by fitting the phases of interest into ellipses. A more detailed description of this technique can be found elsewhere [5]. Note that the size of $CaSn_3$ and $MnSn_2$ intermetallics is much larger than the size of the individual indentation size. Thus, particle sink-in during testing is less likely to take place.

Table 12. Summary of microstructure characterization for as-processed solder alloys

	Water quenched		Furnace cooled	
	SAC-0.5Ca	SAC-0.5Mn	SAC-2Ca	SAC-2Mn
Major axis (μm)	58.3 ± 23.8	121.0 ± 42.1	527.1 ± 369.0	281.2 ± 112.4
Minor axis (μm)	23.3 ± 9.4	9.0 ± 2.3	140.7 ± 60.5	62.2 ± 17.9
Aspect ratio	2.9 ± 1.9	14.4 ± 6.7	3.8 ± 2.6	5.4 ± 3.5

9.4.1.2 Reflowed microstructure

In this section, we describe the microstructure of solder alloys after reflow. The as-reflowed microstructures of the solder joints with 0.5 wt. % Ca and Mn are shown in Fig. 48. Table 13 summarizes the microstructural features quantified in the as-reflowed solder joints, including secondary dendrite size and spacing, and the Cu_6Sn_5 intermetallic layer thickness. Compared to typical Sn-3.9Ag-0.7Cu solder joint, the average Sn dendrite size of Ca and Mn-containing

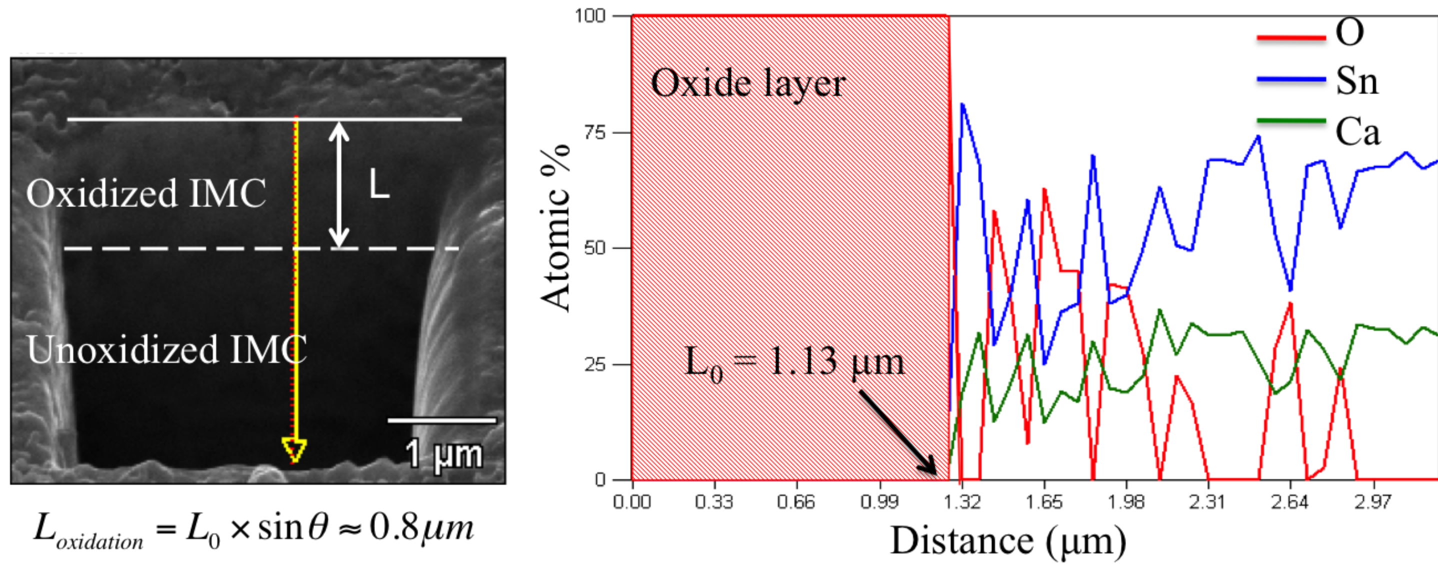

Figure 47. SEM image of cross-section of as-polished Ca-Sn intermetallic and EDS line scan results for partially oxidized Ca-Sn intermetallic alone the yellow arrow. Note that SEM image is viewed in a tilted angle (θ = 52°).

joints is approximately 70 and 50 % smaller than for Sn-Ag-Cu, respectively. Previously, it has been reported that the microstructure refinement in rare-earth containing solder is due to the suppressed undercooling during solidification by the large number of heterogeneous nucleation sites provided by $RESn_3$ particles [5]. Alloys doped with Ca and Mn did not exhibit significant segregation of the intermetallics (relative to the as-processed condition). Also, according to the phase diagrams, the melting point of $CaSn_3$ and $MnSn_2$ phases is above the peak temperature of the reflow profile. Therefore, it is reasonable for us to believe that $CaSn_3$ and $MnSn_2$ intermetallic particles remain solid during reflow and also serve as heterogeneous nucleation sites, with the Sn grains are nucleating and growing from the faceted edges of the primary intermetallics.

Table 13. Summary of microstructure characterization results for reflowed solder joints

	SAC	SAC-0.5Mn	SAC-0.5Ca	SAC-0.5Ce [18]
Sn dendrite length (μm)	27.7 ± 10.2	14.4 ± 8.8	8.3 ± 3.7	11.6 ± 4.1
Sn dendrite spacing (μm)	11.6 ± 4.1	10.2 ± 4.7	8.8 ± 2.4	7.6 ± 2.6
Cu_6Sn_5 IMC thickness (μm)	4.0 ± 2.1	2.0 ± 0.8	3.3 ± 1.1	2.6 ± 1.0

The interface between the solder and Cu substrate for all alloys is characterized by the formation of a thin Cu_6Sn_5 intermetallic layer [35,36]. This intermetallic layer is characterized by a nodular morphology (Fig. 49). It is interesting to note that the intermetallic layer thickness in the Ca-containing

alloys is much lower than that in Sn-Ag-Cu (approximately 60% less) and Ce and La-doped alloys (approximately 10% less). It has been reported that the lower intermetallic thickness of Cu_6Sn_5 in rare-earth containing solder joint is due to smaller degree of undercooling and less time for reaction between solder and Cu substrate [5]. For the Ca-containing solder joint, due to the lighter atomic mass of Ca, there are more heterogeneous nucleation sites in the similar joint volume compared to Ce and La-containing solder joints. Thus, one can expect that undercooling in Ca-containing solder is lower, which equates to less time for reaction with the substrate and a lower intermetallic thickness than that of Ce and La-containing solders. However, the intermetallic layer thickness of Mn-containing solder joint is only slightly thinner than that of Sn-Ag-Cu solder joint. This might be due to the different crystal structure and geometry of intermetallic phases (bulky vs. dendritic). The heterogeneous nucleation ability of different intermetallic systems requires further study.

9.4.2 Nanoindentation

Nanoindentation was carried out on pure Sn, $CaSn_3$, and $MnSn_2$ intermetallics at room temperature. Fig. 50 shows representative load-displacement curves for all the materials tested, to an indentation depth of 1500 nm for $CaSn_3$ and 1000 nm for other materials. The relatively larger indentation depth in $CaSn_3$ intermetallic phase is due to the existence of a fairly thick oxide layer as indicated in the previous section. It can be seen from the curves that for the same maximum indentation depth, the maximum loads obtained are different,

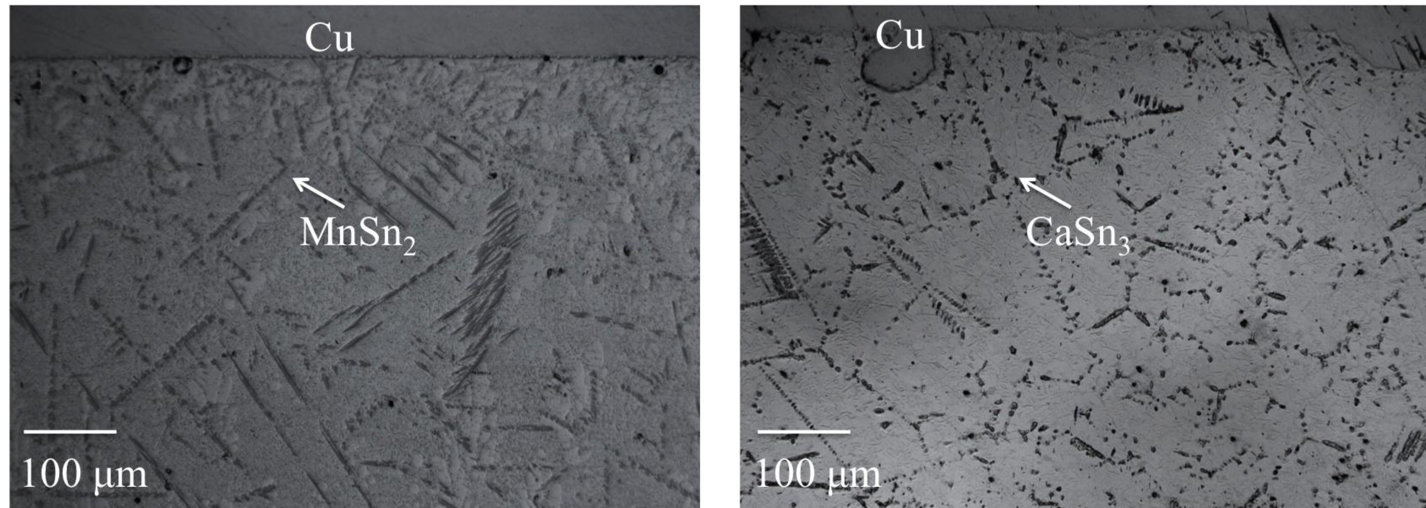

Figure 48. As-reflow optical images of left: Sn-3.9Ag-0.7Cu-0.5Mn and Right: Sn-3.9Ag-0.7Cu-0.5Ca solder joints.

indicating differences in hardness between the materials. All the intermetallics had maximum loads higher than that of pure Sn. The maximum load in $CaSn_3$ at 1000 nm indentation depth is only slightly higher than that obtained for pure Sn, while $MnSn_2$ exhibited highest maximum load. Pure Sn and $CaSn_3$ intermetallic phase are both very soft materials, and exhibited significant plasticity during testing. Also note multiple pop-in events in $MnSn_2$ intermetallic, which were also observed in Cu_6Sn_5 and Ag_3Sn under low-strain-rate nanoindention tests, indicating deformation in $MnSn_2$ consists of discrete events of isolated shear banding [37]. Young's modulus and hardness curves as a function of depth for pure Sn, $CaSn_3$ and $MnSn_2$ are shown in Figs. 51a and Fig. 51b, respectively. Young's modulus and hardness of $CaSn_3$ and $MnSn_2$ are summarized in Table 14 and compared to that of pure Sn. A summary of Young's modulus and hardness values for RE-Sn and other typical intermetallics in Sn-rich lead-free solders, i.e., $CeSn_3$, $LaSn_3$, YSn_3, Cu_6Sn_5, and Ag_3Sn, is also provided for comparison. Young's modulus of a material can be calculated from the reduced modulus according to the following equation [38]:

$$\frac{1}{E_r} = \frac{1 - v^2}{E} + \frac{1 - v_i^2}{E_i}$$

Where E and ν are Young's modulus and Poisson's ratio, respectively, and the subscript i refers to the indenter. Provided Poisson's ratio for the material is known, the calculation is straightforward. Unfortunately, the Poisson's ratios for the $MnSn_2$ intermetallic being studied here are yet to be determined. A Poisson's ratio of 0.3 was assumed for the intermetallic.

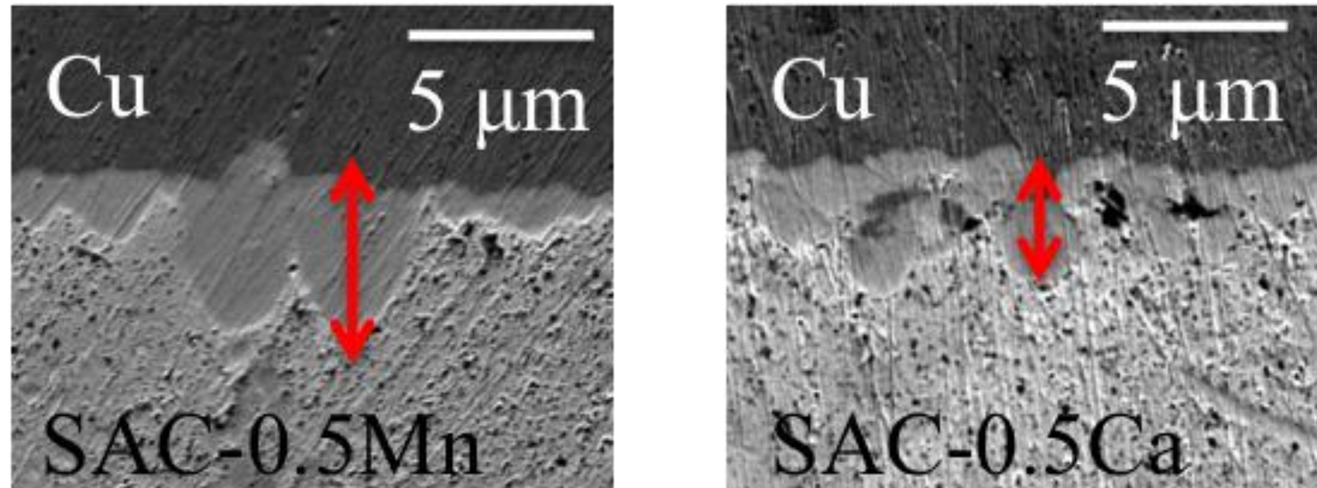

Figure 49. SEM images of the Cu substrate/solder interface in reflowed joints for Sn-3.9Ag-0.7Cu-0.5Mn (left) and Sn-3.9Ag-0.7Cu-0.5Ca (right).

This assumption can be validated: a change in the Poisson's ratio of 0.1 (the upper limit for the Poisson's ratio of the traditional Pb-free intermetallics) only produces a change of 1 GPa in the calculated Young's modulus, which is well within experimental error.

In Fig. 51a, note the "plateau" regions where the modulus is independent of depth. For $MnSn_2$ intermetallic phase, a stable plateau in Young's modulus was observed after approximately 300 nm, while it gradually decreased after 600 nm. Therefore the presence of the plateau indicates that the contribution from sink-in or crack effect is small up to depths of 600 nm for $MnSn_2$ intermetallic. Young's modulus of $CaSn_3$ intermetallic first increases up to an indentation depth of 800 nm, then reaches a stable plateau after 800 nm. Lower Young's modulus up to the 800 nm might be attributed to the porous oxide layer in $CaSn_3$. It's interesting to note that the thickness of oxide layer measured by nanoindentation method agreed well with the FIB results.

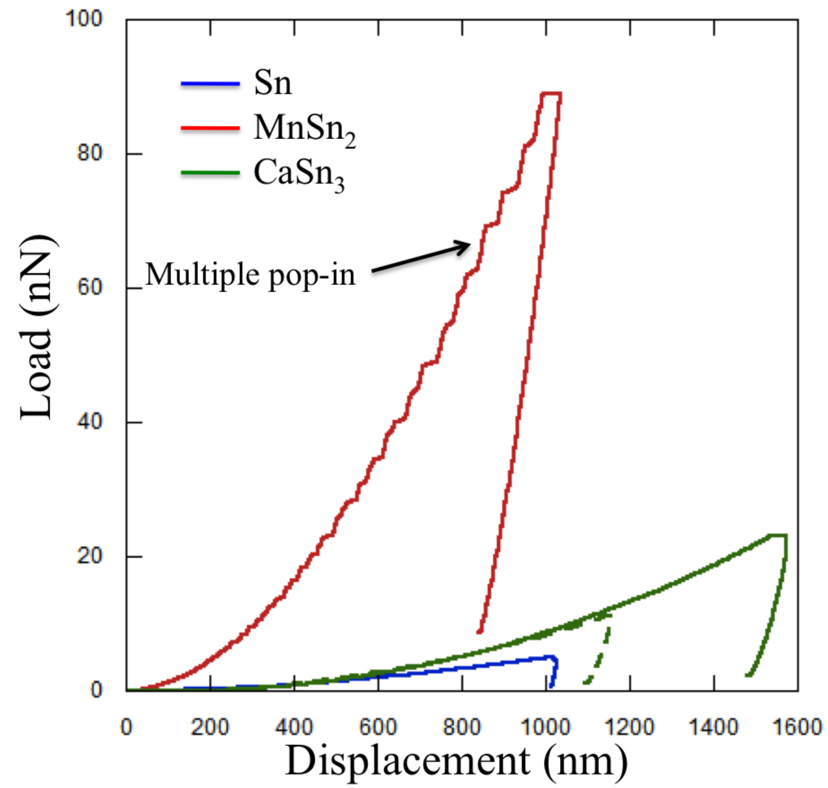

Figure 50. Representative load vs. displacement curves for pure Sn, $MnSn_2$ and $CaSn_3$, indented to a depth up to 1500 nm. Note large variation in maximum load for each phase.

Table 14. Young's moduli and hardness of intermetallics in Pb-free solder and pure Sn.

Phase	Young's modulus (GPa)	Hardness (GPa)
Pure Sn	49 ± 2	0.15 ± 0.03
$MnSn_2$	141 ± 4	8.00 ± 0.30
	143.9 ± 1 [26]	8.9 ± 0.1 [26]
$CaSn_3$	29 ± 5	0.34 ± 0.09
YSn_3	98 ± 4 [40]	3.47 ± 0.27 [40]
$CeSn_3$	69 ± 3 [40]	1.30 ± 0.03 [40]
Cu_6Sn_5	134.2 ± 6.7 [39]	6.12 ± 0.17 [39]
Ag_3Sn	78.9 ± 3.7 [39]	3.25 ± 0.18 [39]

Hardness and Young's modulus values obtained for pure Sn agree well with literature values obtained through nanoindentation [39]. $MnSn_2$ had the highest hardness of the intermetallics tested. The hardness value of $CaSn_3$ is very similar to that of pure Sn, and significantly less than traditional intermetallics formed in Pb-free and RE-Sn intermetallics, such as $CeSn_3$ and $LaSn_3$. As pointed out previously, we believe that these softer and less stiff RE-Sn intermetallic phases are directly responsible for the higher ductility observed in these materials, by undergoing a significant amount of plastic deformation and homogenizing the strain in the solder joint during loading. To further prove this assumption, it is

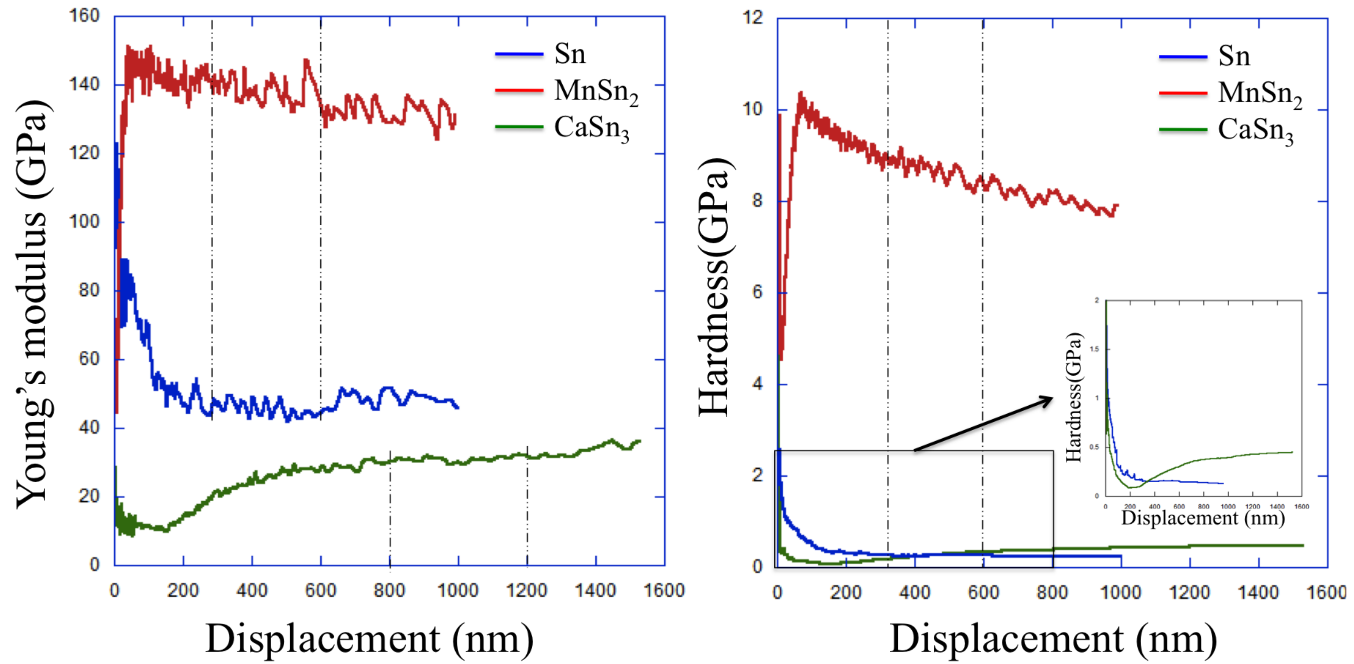

Figure 51. Nanoindentaion behavior of pure Sn, $CaSn_3$ and $MnSn_2$ intermetallics, (a) left: Young's modulus-displacement curve and (b) right: hardness-displacement curve. Young's modulus and hardness value were averaged from the plateau between 300-600 nm for Sn and $MnSn_2$, 800-1200 nm for $CaSn_3$.

interesting to compare the ductility of Sn-Ag-Cu solder ($CaSn_3$) with softer intermetallic to those with a stiffer intermetallic phase ($MnSn_2$). This is further discussed in the next section on mechanical properties of Ca and Mn-containing lead-free solders.

From the Table 14, it can be observed that Young's modulus of $CaSn_3$ is also lower than all the other intermetallics, even lower than that of pure Sn. Similar to the hardness, $MnSn_2$ intermetallic phase have highest Young's modulus among all the intermetallics, which is approximately 4 times higher than for $CaSn_3$, due to its lower Sn content. It have been reported that $CeSn_3$ and $LaSn_3$ formed in rare-earth containing solder have significantly lower modulus and hardness than that of traditional intermetallics formed in lead-free solder [40]. $CaSn_3$ has the same atomic ratio and crystal structure as $CeSn_3$ and $LaSn_3$ (cubic, L12), but has a much lower melting point [28]. Thus, one can expect $CaSn_3$ to be a softer and more compliant intermetallic, compared to $CeSn_3$ and $LaSn_3$. Although there were no direct measurements of mechanical properties of $CaSn_3$ in the literature, our experimentally measured values correspond well with the calculated Young's modulus using first-principle methods (24.9 GPa) [27].

Differences between the intermetallic phases may also be observed from the SEM images of the residual indents. Fig. 52 presents representative SEM images of as-polished $CaSn_3$ particles. A large degree of hillock type Sn whiskers growth can be seen on the surface of $CaSn_3$ particles. The formation of Sn whiskers can be explained by the oxidation of $CaSn_3$ particles during the sample preparation [41]. An explanation for this is as follows. In the oxidized $CaSn_3$

intermetallics, Sn atoms migration from oxidized $CaSn_3$ particles results in the phase separation between pure Sn and Ca oxide. The oxidation of these $CaSn_3$ phase may lead to a significant volume increase, which develops a compressive stress as the source of Sn whiskers. In addition, the migration of Sn to form whiskers also results in the formation of large degree porosity in these structures, which decreases modulus and hardness of oxide layer.

Indentation in the $MnSn_2$ intermetallics is smaller than in pure Sn and $CaSn_3$. Little evidence of pile-up or sink-in is present in the indentation micrographs for $CaSn_3$ and $MnSn_2$. Note that cracks are visible around the $MnSn_2$ indentation, and they are emanating from the corner of indenter. Cracking was only present in the stiffer, harder intermetallics, i.e., $MnSn_2$ and YSn_3 [40]. Neither cracks, nor nanoindentaion induced whiskering were observed around or within the indentation in the $CaSn_3$.

9.4.3 Mechanical shear behavior of Ca and Mn-containing Sn-3.9Ag-0.7Cu solder joints

In this section, we discuss the shear behavior of the Ca and Mn-containing Sn-Ag-Cu solder joints, and compare with Sn-Ag-Cu and RE-containing Sn-Ag-Cu lead-free solder joints. Table 15 summarizes the shear properties of SAC-0.5Ca and SAC-0.5Mn, compared with Sn-Ag-Cu-0.5RE (Ce and Y) solder joints. The relatively small wt. % of Ca and Mn is due to its lighter atomic mass than RE elements. Based on the nanoindentation test results, intermetallics formed inside the fourth element doped lead-free solder can be separated into two groups: soft ($CaSn_3$, $CeSn_3$) and brittle (YSn_3 and $MnSn_2$) intermetallics. All the alloys

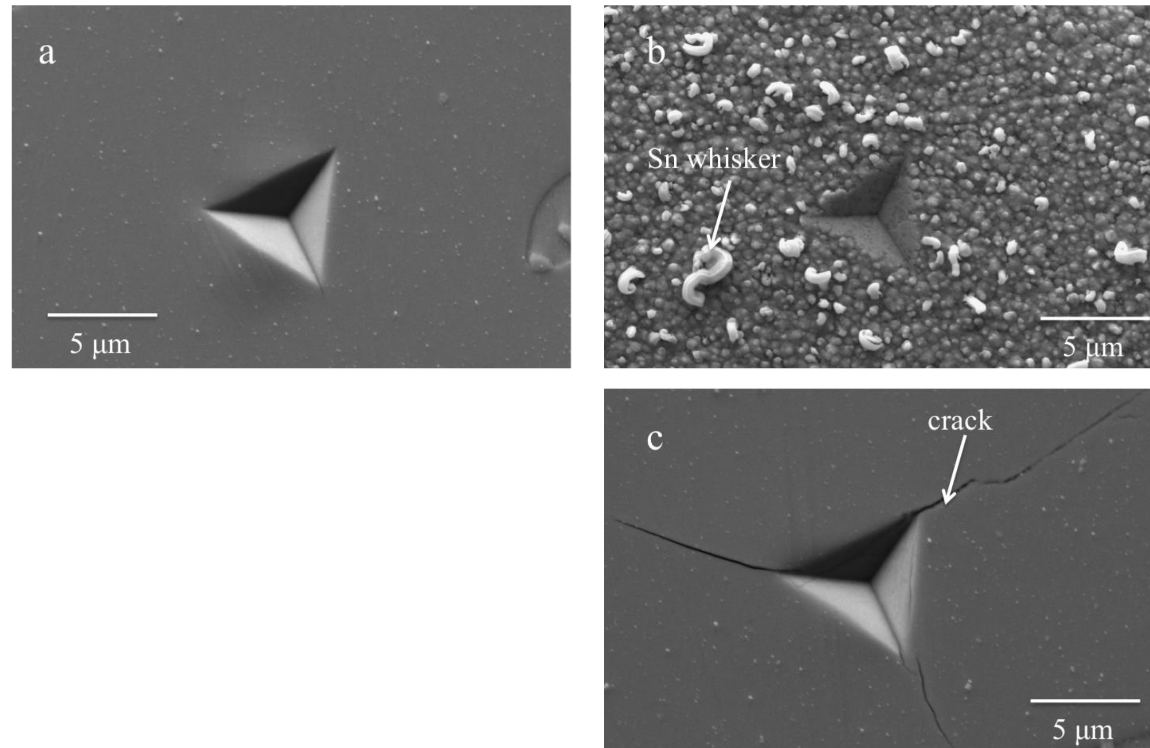

Figure 52. Scanning electron micrographs of indentations in (a) pure Sn, (b) $CaSn_3$ and (c) $MnSn_2$ intermetallics. Pile-up can be seen around the indentation edge in pure Sn. Sn whisker can be seen in $CaSn_3$, while cracks present around the indent in $MnSn_2$.

were compared with conventional Sn-Ag-Cu solder joints as a baseline. It is interesting to note that all the alloys containing soft intermetallic particles show a drop in strength compared to SAC, but with an increase in elongation. For example, the stain-to-failure of Sn-3.9Ag-0.7Cu-0.5Ca, increased by about 60% over that of Sn-3.9Ag-0.7Cu. In contrast, alloys containing hard intermetallic phases, such as YSn_3 and $MnSn_2$, exhibited elongations similar to that of Sn-Ag-Cu. Since $MnSn_2$ phases are significantly harder and stiffer than the other intermetallics in Pb-free solder alloys, this phase may act as strengtheners during loading, and Mn-containing alloy exhibits the highest ultimate shear strength among the 4th elements doped solder alloys. Such trend can be better revealed by plotting ultimate shear strength and strain to failure values of solder joints containing different intermetallics as a function of Young's modulus, as shown in Fig. 53. The red and blue lines are the ultimate shear strengths and strains to failure respectively. It is clear that a decrease in Young's modulus of intermetallics caused a reduction in ultimate tensile strength, but increase in strain to failure. An explanation for this will be discussed in details below.

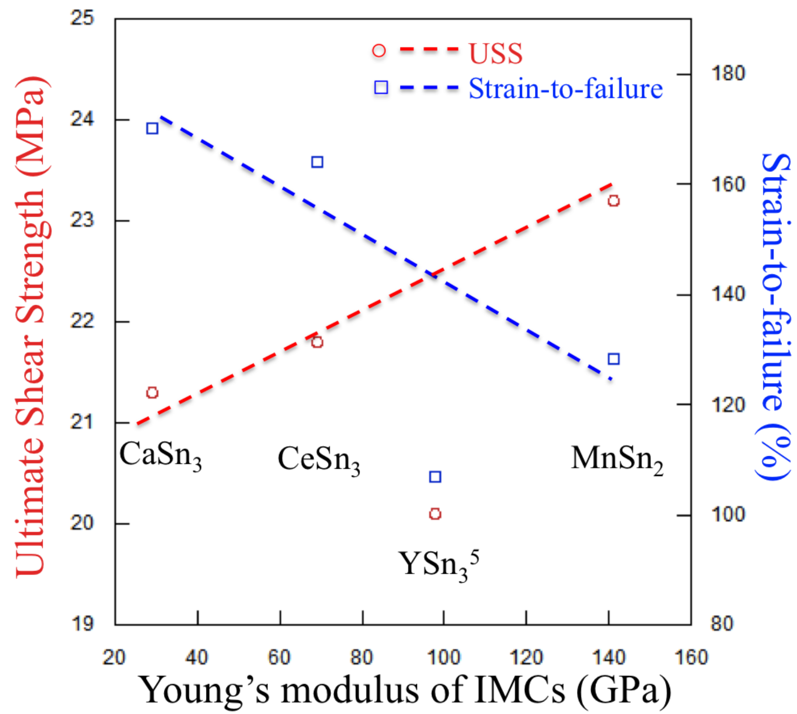

Figure 53. Ultimate shear strength and strain to failure of solder joints, plotted as a function of Young's modulus of intermetallics. Increase in Young's modulus of intermetallics increase the USS but reduce the strain to failure of solder joints.

Table 15. Monotonic shear results for Sn-3.9Ag-0.7Cu and Sn-3.9Ag-0.7Cu-0.5Ca and Mn.

Alloys		Ultimate shear strength (MPa)	Strain-to-failure
	Sn-3.9Ag-0.7Cu	24.2 ± 5.2	104.5 ± 3.7
Alloys containing soft intermetallic	Sn-3.9Ag-0.7Cu-0.5Ca	21.3 ± 0.3	170.0 ± 21.9
	Sn-3.9Ag-0.7Cu-0.5Ce	21.8 ± 2.3	164.0 ± 57.0
Alloys containing stiff intermetallic	Sn-3.9Ag-0.7Cu-0.5Mn	23.2 ± 1.1	118.3 ± 14.5
	Sn-3.9Ag-0.7Cu-0.5Y [5]	20.1 ± 3.7	107.0 ± 21.9

It has been reported that the increase in ductility with doping of Ce is caused by the $CeSn_3$ intermetallic, which nucleates and grow voids in the solder interior and minimizes strain localization along the brittle Cu_6Sn_5 intermetallic/solder interface [23]. Additionally, for the soft intermetallic particles, it is likely that an appreciable amount of deformation takes place in these phases as well, contributing to the enhancement in ductility. However, the solder joint containing harder intermetallic particles (YSn_3 and $MnSn_2$) behave in a different way, may be due to the morphology and individual properties of those intermetallic particles. It is likely that the change from dendritic ($CeSn_3$ and $CaSn_3$) to bulky ($MnSn_2$) and needlelike (YSn_3) microstructures adversely affects void nucleation. In addition, because those intermetallic particles are significantly

harder and stiffer, one can expect a negative contribution to ductility from the deformation of these intermetallics.

9.5 Conclusions

The Young's modulus and hardness of $CaSn_3$ and $MnSn_2$ intermetallics that form in 4th-element doped Sn-rich lead-free solders were measured utilizing nanoindentaion using the continuous stiffness measurement (CSM), and compared with the properties of pure Sn, RE-Sn and other traditional intermetallics formed in RE-containing lead-free solders. Both the Young's modulus and the hardness of $MnSn_2$ are significantly larger than that of other materials. In contrast, $CaSn_3$ is a much softer intermetallic with Young's modulus even lower than the pure Sn. The hardness value of $CaSn_3$ was comparable to pure Sn and was significantly lower than RE-Sn intermetallics and other intermetallics formed in Pb-free solder. Mechanical shear studies of Ca and Mn-containing solder indicate that only compliant intermetallics, such as $CeSn_3$ and $CaSn_3$, can improve the ductility of Sn-rich lead-free solders.

9.6 Reference

1. N. Chawla, Int. Mater. Rev., 2009, 54, 368

2. F. Guo, M. Zhao, Z. Xia, Y. Lei, X. Li, Y. Shi, JOM, 2009, 61(6), 39.

3. C.M.L. Wu, D.Q. Yu, C.M.T. Law, L. Wang, Mater. Sci. Eng. R-Reports, 2004, 44(1), 1.

4. L. Zhang, S.-B. Xue, L.-L Gao, G. Zeng, Z. Sheng, Y. Chen, S.L. Yu, J. Mater. Sci. Mater. Electron., 2009, 20(8), 685.

5. M.A. Dudek, N. Chawla, Metall. Mater. Trans. A, 2010, 41(3), 610.

6. J. Shen, C. Wu, S. Li, J. Mater. Sci. Mater. Electron., 2012. 23(1), 156.

7. L.-L Gao, S.-B Xue, L. Zhang, Z.-X Xiao, W. Dai, F. Ji, H. Ye, G. Zeng, J. Mater. Sci. Mater. Electron., 2010, 21(7), 643.

8. H. Hao, J. Tian, Y.W. Shi, Y.P. Lei, Z.D. Xia, J. Electron. Mater., 2007, 36(7), 766.

9. D.Q. Yu, J. Zhao, L. Wang, J. Alloy. Compd., 2004, 376(1-2), 170-175

10. B. Li, Y. Shi, Y. Lei, F. Guo, Z. Xia, B. Zong, J. Electron. Mater., 2005, 34(3), 217.

11. M. Dittes, H. Walter, Solder. Surf. Mt. Tech., 2003. 15(1), 50.

12. C. Wu, Y. Wong, J. Mater. Sci.: Materials in Electronics, 2007, 18(1): 77.

13. M.A. Dudek, R.S. Sidhu, N. Chawla, JOM, 2006, 58(6), 57.

14. A.G. Ramirez, H. Mavoori, S. Jin, Appl. Phys. Lett., 2002, 80(3), 398.

15. D.Q. Yu, C.M.L. Wu, Y.W. Wong, J. Mater. Sci. Mater. Electron., 2007, 18, 1057.

16. H. He, G. Xu, F. Guo, J. Mater. Sci., 2009, 44(8), 2089.

17. M.A. Dudek, N. Chawla, J. Electron. Mater., 2009, 38(2), 210.

18. H.X. Xie, N. Chawla, K. Mirpuri, J. Electron. Mater., 2012, online first.

19. L. Zhang, J.-G. Han, Y.-H Guo, C.-W. He, Sci. Tech. Weld. Join., 2012, 17(5), 424.

20. C.M.L. Wu, D.Q. Yu, C.M.T. Law, L.J. Wang, Mater. Res., 2002, 17, 3146.

21. L. Wang, D.Q. Wu, J. Zhao, M.L. Huang, Mater. Lett., 2002, 56, 1039.

22. M.A. Dudek, R.S. Sidhu, N. Chawla, N. Renavikar, J. Electron. Mater., 2006, 35, 2088.

23. H.X. Xie, N. Chawla, Y.-L Shen, Microelectron. Reliab., 2011, 51, 1142.

24. Z.G. Chen, Y.W. Shi, Z.D. Xia, Y.F. Yan, J. Electron Mater., 2002, 31, 1122.

25. Y. Shi, J. Tian, H. Hao, Z. Xia, Y. Lei, F. Guo, J. Alloys Compd. 2008, 453, 180.

26. L.-W. Lin, J.M. Song, Y.-S. Lai, Y.-T. Choi, N.-C. Lee, J.-Y. Uan, Microelectron. Reliab., 2009, 49, 235.

27. Z. Yang, D. Shi, B. Wen, R. Melnik, S. Yao, T. Li, J. Solid State Chem., 2010, 183(1), 136.

28. H. Okamoto, J. Phase Equilib. Diff., 2001, 22(5), 589.

29. Fischer-Cripps AC. Nanoindentation. 2nd ed. New York: Springer, 2004.

30. J.L. Hay, G.M.Pharr, Instrumented indentation testing. In: H. Kuhn, D. Medlin editors, ASM handbook, Materials Park, OH, ASM International, 2001, 232.

31. F. Ochoa, X. Deng, N. Chawla, J. Electron. Mater., 2004, 33(12), 1596.

32. N. Chawla, F. Ochoa, V.V. Ganesh, X. Deng, M. Koopman, K.K. Chawla, S. Scarriitt, J. Mater. Sci. Mater. Electron. 2004, 15, 385.

33. X. Deng, G. Piotrowski, J.J. Williams, N. Chawla, J. Electron. Mater., 2003, 32, 1403.

34. H. Okamoto, J. Phase Equilib., 1999, 20(5), 542.

35. X. Deng, R.S. Sidhu, P. Johnson, N. Chawla, Metall. Mater. Trans. A, 2005, 36A, 55.

36. P.G. Harris, K.S. Chaggar, Solder. Surf. Mt. Tech., 1998, 10(3), 38.

37. P.-F. Yang, Y.-S. Lai, S.-R. Jian, J. Chen, 8th International Conference on Electronic Packaging Technology, Shanghai, August, 2007, 1.

38. W.C. Oliver, G.M. Pharr, J. Mater. RES., 1992, 7, 1564.

39. X. Deng, M. Koopman, N. Chawla, K.K. Chawla, Mater. Sci. Eng. A, 2004, 364, 240.

40. M.A. Dudek, N. Chawla, Intermetallics, 2010, 18, 1016.

41. M.A. Dudek, N. Chawla, Acta Mater., 2009, 57, 4588.

10. CONCLUDING REMARKS

10.1 Summary of Research Findings

A synopsis of the most important results is presented in this section:

- The interrupted shear testing and characterization by optical microscopy and SEM shows that the $CeSn_3$ intermetallic particles are directly responsible for the higher ductility observed in Ce-containing SAC alloy. Plasticity around the particles, debonding, and fracturing of $CeSn_3$ intermetallic particles contribute to an increase in fracture energy as well as homogenization of the plastic strain in the solder region.
- Numerical finite element modeling illustrated that the existence of intermetallic particles in the solder serves to disturb the concentrated plastic deformation band during the lap-shear loading. The overall plastic flow field becomes more uniform, with a reduced maximum strain magnitude. Delayed fracture can thus be expected, leading to enhanced ductility.
- Studies on the effect of thinner Cu_6Sn_5 intermetallic layer thickness on ductility showed that the thin Cu_6Sn_5 intermetallic layer in SAC-Ce solder joint does not contribute to the enhanced ductility.
- The results of wetting behavior of SAC and SAC-0.5Ce indicate that SAC-Ce solder has comparable wetting behavior to SAC solder on Cu substrate.
- The microstructure of SAC can be refined with Ce addition. DSC result reveals that the refined microstructure as well as thinner Cu_6Sn_5

intermetallic layer may both be due to the reduction in undercooling, by increasing the amount of heterogeneous nucleation sites, i.e. $CeSn_3$ intermetallic.

- SAC-Ce alloy shows constant microstructure refinement with the variation of solder volume, indicating that both microstructure of solder matrix and interfacial intermetallic layer thickness is less affected by the volume variation.
- The shock behavior of Sn-Ag-Cu can be improved by addition of Ce with a small penalty in ultimate tensile strength when the strain rate is in the solder matrix controlled regime. The fracture mechanism of the Ce-containing Sn-Ag-Cu alloy dominated by $CeSn_3$ intermetallics nucleated voids and growth in the solder-controlled regime. Dynamic tensile strength and strain to failure of Sn-Ag-Cu and Sn-Ag-Cu-0.5Ce are comparable in the intermetallic layer-controlled regime.
- Microstructure characterization indicates that the dominant failure mechanism of Sn-3.9Ag-0.7Cu and Sn-3.9Ag-0.7Cu-0.5Ce in this study is both due to pancake-type voids formation and metallization consumption, respectively. The product of effective charge number and diffusivity calculated based on the surface mark movement indicates that electromigration resistance of Sn-3.9Ag-0.7Cu and Sn-3.9Ag-0.7Cu-0.5Ce are significantly higher than that of Sn-Pb solder alloy.
- The addition of Ca results in the formation of large, dendritic intermetallic particles ($CaSn_3$). Nanoindentation results indicate that $CaSn_3$ is a much

softer intermetallic with Young's modulus even lower than the pure Sn. The hardness value of $CaSn_3$ was comparable to pure Sn and was significantly lower than RE-Sn intermetallics and other intermetallics formed in Pb-free solder. Mechanical shear studies of Ca and Mn-containing solder indicate that only compliant intermetallics, such as $CeSn_3$ and $CaSn_3$, can improve the ductility of Sn-rich lead-free solders.

10.2 Recommendations

The current study has successfully established realistic feasibility of Ce-containing SAC lead-free solder alloy as a replacement to the conventional SAC alloys. In addition to the enhanced ductility and excellent oxidation resistance of Ce-containing SAC, it has been demonstrated that Ce-containing SAC alloy have enhanced mechanical shock and electromigration performance compared to traditional SAC alloys. The thermal stability and wettability of Ce-containing SAC alloy is comparable to the conventional SAC alloy. Studies on the mechanism for the enhanced ductility observed in Ce-containing SAC solder indicate that the soft $CeSn_3$ IMC particles play an important role in homogenizing the plastic strain in the solder and improving the shock resistance of SAC alloy.

While a significant amount of progress has been made, there are several areas of research which require attention in order to further develop high ductility lead-free solder alloys in the future:

- With decreasing size of electronic devices, the bump and pitch size decreases accordingly. However, studies on the volume effect in SAC-Ce solder showed that the refinement effect of Ce-containing intermetallics

decreases with decreasing the solder joint size due to the relatively large intermetallic particle size. Therefore, it is important to minimize the $CeSn_3$ particle size before implementation of this novel solder alloy into microelectronic packaging.

- Electromigration studies showed that the dominant phenomenon is current induced Cu diffusion. However, the X-ray flux of a lab-scale X-ray tomography tool is too low to visualize any constrast difference between Cu_6Sn_5 and Sn. Therefore, it would be informative to perform an in-situ synchrotron tomography study on solder joints during electromigration testing.
- The crystallographic orientation of Sn matrix may affect the mechanical and electromigration behavior of the solder joint. Therefore, it would be interesting to study the effect of Sn grain orientation on the electromigration behavior by performing in situ electromigration testing in a SEM coupled with an Orientation Image Mapping system.
- It was shown that the mechanical shear performance of conventional SAC alloys can be improved by the addition of soft intermetallic compounds, such as Ce-Sn and Ca-Sn intermetallics. However, both rare earth elements and calcium react with oxygen, which often results in the formation of Sn whiskers and the degradation of mechanical properties. Therefore it is necessary to develop a novel soft particle reinforced lead-free solder alloy, which is not suspectible to oxidation. Soft particles can

be introduced by either alloying with a 4th element which can react with the Sn-rich solder or nano-size particles.

REFERENCES

Chapter 1 and 2

1. M.R. Harrison, J.H.Vincent, H.A.H Steen, Sold. Surf. Mount Tech., 2001, 13(3),17.

2. E. Wood, K. Nimmo, J. Electron. Mater., 1994, 23(8), 709.

3. H. Ma and J. Suhling, J. Mater. Sci., 2009, 44(5), 1141.

4. N. Chawla, Inter. Mater. Reviews, 2009, 54(6), 368.

5. D. Lu, C. P. Wong, Materials for Advanced Packaging, Springer, 2009, 181.

6. K.N. Subramanian, I. E., Anderson, Lead-Free Electronic Solders, 2007, 55.

7. F. Guo, M. Zhao, Z. Xia, Y. Lei, X. Li, Y. Shi, JOM, 2009, 61(6), 39.

8. C.M.L. Wu, D.Q. Yu, C.M.T. Law, L. Wang, Mater. Sci. and Engineer. R: Reports, 2004, 44(1), 1.

9. L. Zhang, S.-B Xue, L.-L Gao, G. Zeng, Z. Sheng, Y. Chen, S.-L Yu, J. Mater. Sci. Mater. Electron., 2009, 20(8), 685.

10. M.A. Dudek, N. Chawla, Metall. Mater. Trans. A, 2010, 41(3), 610.

11. J. Shen, C. Wu, S. Li, J. Mater. Sci. Mater. Electron., 2012, 23(1), 156.

12. L. Gao S. Xue, L. Zhang Z. Sheng, G. Zeng, Z. Ji, J. Mater. Sci. Mater. Electron., 2010, 21(7), 643.

13. L. Zhang, S. Xue, Y. Chen, Z. Han, J. Wang, S. Yu, F. Lu, Journal of Rare Earths, 2009, 27(1), 138.

14. Y. Shi, J. Tian, H. Hao, Z. Xia, Y. Lei, F. Guo, J. Alloys and Compd., 2008, 453(1-2), 180.

15. H. Hao, J. Tian, Y.W. Shi, Y.P. Lei, Z.D. Xia, J. Electron. Mater., 2007, 36(7), 766.

16. P. Min, J. Qu, in Electronic Components and Technology Conference, 2007. ECTC '07. Proceedings. 57th. 2007.

17. D.Q. Yu, J. Zhao, L. Wang, J. of Alloys and Compd., 2004, 376(1-2), 170.

18. B. Li, Y. Shi, Y. Lei, F. Guo, Z. Xia, B. Zhong, J. Electron. Mater., 2005, 34(3), 217.

19. M. Dittes, H. Walter, Sold. Surf. Mount Tech., 2003, 15(1), 50.

20. C. Wu, Y. Wong, J. Mater. Sci.: Mater. Electron., 2007, 18(1), 77.

21. M. Dudek, R. Sidhu, N. Chawla, JOM, 2006, 58(6), 57.

22. A.G. Ramirez, H. Mavoori, S. Jin, Appl. Phys. Lett., 2002, 80(3), 398.

23. H. He, G. Xu, F. Guo, J. Mater. Sci., 2009, 44(8), 2089.

24. Z. Chen, Y. Shi, Z. Xia, Y. Yan, J. Electron. Mater., 2003, 32(4), 235.

25. X.-Y. Zhao, M.-Q. Zhao, X.-Q. Cui, M.-X. Tong, Transactions of Nonferrous Metals Society of China, 2007, 17(4), 805.

26. M.A. Dudek, R.S. Sidhu, N. Chawla, M. Renavikar, J. Electron. Mater., 2006, 35(12), 2088.

27. M.A. Dudek, N. Chawla, J. Electron. Mater., 2009, 38(2), 210.

28. S. Kang, A. Sarkhel, J. Electron. Mater., 1994, 23(8), 701.

29. F. Ochoa, X. Deng, N. Chawla, J. Electron. Mater., 2004, 33(12), 1596.

30. S. Wiese, K.J. Wolter, Microelectron. Reliab., 2004, 44(12), 1923.

31. S.K. Kang, P.A. Lauro, D.-Y. Shih, D.W. Henderson, K.J. Puttlitz, IBM Journal of Research and Development, 2005, 49(4-5), 607.

32. G. Henshall, R. Healey, R.S. Pandher, K. Sweatman, K. Howell, R. Coyle, T. Sack, P. Snugovsky, S. Tisdale F. Hua, in Microelectronics and Packaging Conference, 2009. European. 2009.

33. R.S. Sidhu, X. Deng, and N. Chawla, Metall. and Mater. Trans. A, 2008, 39(2), 349.

34. Y. Kariya, T. Hosoi, S. Terashima, M. Tanaka, M. Otsuka, J. Electron. Mater., 2004, 33(4), 321.

35. H.Y. Lu, H. Balkan, K.Y. Simon, JOM, 2005, 57(6), 30.

36. K.S. Kim, S.H. Huh, K. Suganuma, J. Alloys Compd., 2003, 352(1-2), 226.

37. D.Q. Yu, L. Wang, J. Alloys and Compd., 2008, 458(1-2), 542.

38. C.M. Liu, C.E. Ho, W.T. Chen, C.R. Kao, J. Electron. Mater., 2001, 30(9), 1152.

39. A. Kumar, M. He, Z. Chen, Surf. Coat. Tech., 2005, 198(1-3), 283.

40. K.S. Lin, H.Y. Huang, C.P. Chou, J. Mater. Engineer. Perfor., 2009, 18(2), 182.

41. J.-M. Koo, S.-B. Jung, Microelectron. Engineer., 2005, 82(3-4), 569.

42. Y. Xia, X. Xie, C. Lu, J. Chang, J. Alloys and Compd., 2006, 417(1-2), 143.

43. J.W. Jang, D.R. Frear, T.Y. Lee, K.N. Tu, J. Appl. Phys., 2000, 88(11), 6359.

44. S.K. Kang, D.Y. Shih, K. Fogel, P. Lauro, M.-J. Yim, G.G. Advocate, M. Griffin, C. Goldsmith, D.W. Henderson, T.A. Gosselin, D.E. King, J.J. Konrad, A. Sarkhel, K.J. Puttlitz, in Electronic Components and Technology Conference, 2001. Proceedings., 51st. 2001.

45. K. Zeng, V. Vuorinen, J.K. Kivilahti. in Electronic Components and Technology Conference, 2001. Proceedings., 51st. 2001.

46. A. Zribi, L. Zavalij, P. Borgesen, A. Primavera, G. Westby, E.J. Cotts, in Electronic Components and Technology Conference, 2001. Proceedings., 51st. 2001.

47. A. Sharif, Y.C. Chan, M.N. Islam, M.J. Rizvi, J. Alloys Compd., 2005, 388(1), 75.

48. D.Q. Yu, C.M.L. Wu, D.P. He, N. Zhao, L. Wang, J.K.L. Lai, J. Mater. Research, 2005, 20(8), 8.

49. Y.-D. Jeon, S. Nieland, A. Ostmann, H. Reichi, K.-W. Paik, J. Electron. Mater., 2003, 32(6), 548.

50. M.O. Alam, Y.C. Chan, K.N. Tu, J.K. Kivilahti, Chemistry of Materials, 2005, 17(9), 2223.

51. H. Ma, J.C. Suhling, P. Lall, M.J. Bozack, in Electronic Components and Technology Conference, 2006. Proceedings. 56th. 2006.

52. H. Ma, J.C. Suhling, Y. Zhang, P. Lall, M.J. Bozack, in Electronic Components and Technology Conference, 2007. ECTC '07. Proceedings. 57th. 2007.

53. X. Deng, R.S. Sidhu, P. Johnson, N. Chawla, Metall. Mater. Trans. A, 2005, 36(1), 55.

54. X. Ma, F. Wang, Y. Qian, F. Yoshida, Mater. Lett., 2003, 57(22-23), 3361.

55. D.Q. Yu, C.M.L. Wu, C.M.T. Law, L. Wang, J.K.L. Lai, J. Alloys Compd., 2005, 392(1-2), 192.

56. I. Dutta, P. Kumar, G. Subbarayan, JOM, 2009, 61(6), 29.

57. X. Deng, G. Piotrowski, J.J. Williams, N. Chawla, J. Electron. Mater., 2003, 32(12), 1403.

58. P. Vianco, K. Erickson, P. Hopkins, J. Electron. Mater., 1994, 23(8), 721.

59. S. Fubin, S.W.R. Lee. in Electronic Components and Technology Conference, 2006. Proceedings. 56th. 2006.

60. I. Anderson, J. Harringa, J. Electron. Mater., 2006, 35(1), 94.

61. K.N. Tu, K. Zeng, Mater. Sci. Engineer.: R: Reports, 2001, 34(1), 1.

62. J.-W. Yoon, S.-B. Jung, Surf. Coat. Tech., 2006, 200(14-15), 4440.

63. J.-W. Yoon, W.-C. Moon, S.-B. Jung, Microelectron. Engineer., 2006, 83(11-12), 2329.

64. P. Sun, C. Andersson X. Wei, Z. Chengm Z. Lai, D. Shangguan, J. Liu, J. Alloys Compd., 2006, 425(1-2), 191.

65. M. He, V. Acoff, J. Electron. Mater., 2006, 35(12), 2098.

66. L. Xu, J. Pang, J. Electron. Mater., 2006, 35(12), 2107.

67. Y. Miyazawa, T. Ariga. in Environmentally Conscious Design and Inverse Manufacturing, 1999. Proceedings. EcoDesign '99: First International Symposium On. 1999.

68. C.M. Chuang, T.S. Lui, L.H. Chen, J. Mater. Sci., 2002, 37(1),191.

69. S. Ou, Y. Xu, K.N. Tu, in Electronic Components and Technology Conference, 2005. Proceedings. 55th. 2005.

70. K. Zeng, K.N. Tu, Mater. Sci. Eng.: R: Reports, 2002, 38(2), 55.

71. J.-W. Yoon, H.-S. Chun, S.-B. Jung, J. Mater. Sci.: Mater. Electron., 2007, 18(5), 559.

72. M. Amagai, Y. Toyoda, T. Ohnishi, S. Akita, in Electronic Components and Technology Conference, 2004. Proceedings. 54th. 2004.

73. L. Zhang, S.B. Xue, G. Zeng, L.L. Gao, H. Ye, J. Alloys Compd., 2012, 510(1), 38.

74. B. Lu, H. Li, J.-H. Wang, H.-W. Zhu, X.-H. Jiao, Journal of Central South University of Technology, 2008, 15(3), 313.

75. H. Hao, Y. Shi, Z. Xia, Y. Lei, F. Guo, et al., J. Electron. Mater., 2008, 37(1), 2.

76. M. Pei, J. Qu, J. Electron. Mater., 2008, 37(3), 331.

77. C.M.T. Law, C.M.L. Wu, in High Density Microsystem Design and Packaging and Component Failure Analysis, 2004. HDP '04. Proceeding of the Sixth IEEE CPMT Conference on. 2004.

78. G. Li, Y. Shi, H. Hao, Z. Xia, Y. Lei, F. Guo, X. Li, J. Mater. Sci.: Mater. Electron., 2009, 20(2), 186.

79. C.M.L. Wu, C.M.T. Law, D.Q. Yu, L. Wang, J. Electron. Mater., 2003, 32(2), 63.

80. M. Abtew, G. Selvaduray, Mater. Sci. and Eng.: R: Reports, 2000, 27(5-6), 95.

81. K. Zhang, G. Cheng, Y. Yu, Y. Yan, H. Man, in Electronic Packaging Technology, 2005 6th International Conference on. 2005.

82. L. Zhang, S.-B. Xue, L.-L. Gao, Y. Chen, S.-L. Yu, Z. Sheng, G. Zeng, J. Mater. Sci.: Mater. Electron., 2009, 20(12), 1193.

83. L. Wang, D.Q. Yu, J. Zhao, M.L. Huang, Mater. Lett., 2002, 56(6), 1039.

84. D.Q. Yu, J. Zhao, L. Wang, J. Alloys Compd., 2004, 376(1-2), 170.

85. C.M.L. Wu, D.Q.Y., C.M.T. Law, L. Wang, J. Mater. Research, 2002, 17, 8.

86. C.M.T. Law, C.M.L. Wu, D.Q. Yu, L. Wang, J.K.L. Lai, J. Electron. Mater., 2006, 35(1), 89.

87. J.-X. Wang, S.-B. Xue, Z.-J. Han, S.-L Yu, Y. Chen, Y.-P. Shi, H. Wang, J. Alloys Compd., 2009, 467(1-2), 219.

88. A.O. Aggarwal, P. M. Raj, V. Sundaram, D. Ravi, S. Koh, R. Mullapudi, R.R. Tummala, in Electronic Components and Technology Conference, 2005. Proceedings. 55th. 2005.

89. M. Mueller, S. Wiese, M. Roellig, K.-J. Wolter, in Electronic Components and Technology Conference, 2007. ECTC '07. Proceedings. 57th. 2007.

90. Q.J. Zhai, Y.L. Gao, W.B. Guan, K.D. Xu, Mater. Sci. Eng. A, 2006, 441(1-2), 278.

91. Z. Huang, P.P. Conway, E. Jung, R.C. Thomson, C. Liu, T. Loeher, M. Minkus, J. Electron. Mater., 2006, 35(9), 1761.

92. M. Islam, A. Sharif, Y. Chan, J. Electron. Mater., 2005, 34(2), 143.

93. A. Betzwar-Kotas, G. Khatibi, A. Ziering, P. Zimprich, V. Groeger, B. Weiss, H. Ipser, Fracture of Nano and Engineering Materials and Structures, Springer, 2006, 645.

94. L.-M. Yin, W.-Y. Li, S. Wei, Z.-l. Xu, in Electronic Packaging Technology and High Density Packaging (ICEPT-HDP), 2011 12th International Conference on. 2011.

95. P. Zimprich, U. Saeed, A. Betzwar-Kotas, B. Weiss, H. Ipser, J. Electron. Mater., 2008, 37(1), 102.

96. L.M. Yin, X.P. Zhang, C. Lu, J. Electron. Mater., 2009, 38(10), 2179.

97. J. Cugoni, J. Botsis, J. Janczak-Rusch, Advanced Engineerin Materials, 2006, 8, 7.

98. N. Chawla, Y.-L Shen, X. Deng, E.S. Ege, J. Electron. Mater., 2004, 33(12), 1589.

99. Y.-L. Shen, N. Chawla, E.S. Ege, X. Deng, Acta Materialia, 2005, 53(9), 2633.

100. Y. Tian, C. Wang, S. Yang, P. Lin, L. Liang, in Electronic Packaging Technology & High Density Packaging, 2008. ICEPT-HDP 2008. International Conference on. 2008.

101. T.Y. Tee, H.S. Ng, C.T. Lim, E. Pek, Z. Zhong, Microelectron. Reliab., 2004, 44(7), 1131.

102. J. Luan, T.Y. Tee, E. Pek, C.T. Lim, Z. Zhong, Microelectron. Reliab., 2007, 47(2-3), 450.

103. Z.J. Xu, T.X. Yu, in Electronics Packaging Technology Conference, 2008. EPTC 2008. 10th. 2008.

104. K.T. Tsai, F.L. Liu, E.H. Wong, R. Rajoo, in High Density Microsystem Design and Packaging and Component Failure Analysis, 2005 Conference on. 2005.

105. M. Date, T. Shoji, M. Fujiyoshi, K. Sato, K.N. Tu, in Electronic Components and Technology Conference, 2004. Proceedings. 54th. 2004.

106. A.U. Telang, T.R. Bieler, M.A. Crimp, Mater. Sci. Eng. A, 2006, 421(1-2), 22.

107. Q. Yu, H. Kikuchi, S. Ikeda, M. Shiratori, M. Kakino, N. Fujiwara, in Thermal and Thermomechanical Phenomena in Electronic Systems, 2002. ITHERM 2002. The Eighth Intersociety Conference on. 2002.

108. Y. Liu, G. Tian, S. Gale, R.W. Johnson, L. Crane, Electronics Packaging Manufacturing, IEEE Transactions on, 2006, 29(1), 1.

109. Y. Liu, S. Gale, and R.W. Johnson, Electronics Packaging Manufacturing, IEEE Transactions on, 2007, 30(1), 63.

110. D. Suh, D.W. Kim, P. Liu, H. Kim, J.A. Weninger, C.M. Kumar, A. Parsad, B.W. Grimsley H.B. Tejada, Mater. Sci. Eng. A, 2007, 460-461(0), 595.

111. D.Y.R. Chong, F.X. Che, J.H.L. Pang, K. Ng, J.Y.N. Tan, T.H.P. Low, Microelectron. Reliab., 2006, 46(7), 1160.

112. Y.T. Chin, P.K. Lam, H.K. Yow, T.Y. Tou, Microelectron. Reliab., 2008, 48(7), 1079.

113. Z. Huang, P. Kumar, I. Dutta, J.H.L. Pang, R. Sidhu, M. Renavikar, R. Mahajan, J. Electron. Mater., 2012, 41(2), 375.

114. W. Liu, N.-C. Lee, A. Porras, M. Ding, A. Gallagher, A. Huang, S. Chen, C.J.Lee, in Electronic Components and Technology Conference, 2009. ECTC 2009. 59th. 2009.

115. W. Liu, N.-C. Lee, JOM, 2007, 59(7), 26.

116. L.-W. Lin, J.-M. Song, Y.-S. Lai, Y.-T. Chiu, N.-C. Lee, J.-Y. Uan, Microelectron. Reliab., 2009, 49(3), 235.

117. W. Liu, P. Bachorik, L. Ning-Cheng. in Electronic Components and Technology Conference, 2008. ECTC 2008. 58th. 2008.

118. M. Amagai, Y. Toyoda, T. Ohnishi, S. Akita, in Electronic Components and Technology Conference, 2004. Proceedings. 54th. 2004.

119. Y.S. Lai, J.M. Song, H.C. Chang, Y.T. Chiu, J. Electron. Mater., 2008. 37(2), 201.

120. S.K. Kang, D. Leonard, D.-Y. Shih, L. Gignac, D.W. Henderson, S. Cho, J. Yu, J. Electron. Mater., 2006, 35(3), 479.

121. K.N. Tu, J. Appl. Phys., 2003, 94(9), 5451.

122. C.Y. Liu, C. Chen, K.N. Tu, J. Appl. Phys., 2000, 88(10), 5703.

123. Q.T. Huynh, C.Y. Liu, C. Chen, K.N. Tu, J. Appl. Phys., 2001, 89(8), 4332.

124. M. Lu, D.-Y. Shih, C. Goldsmith, T. Wassick, in Reliability Physics Symposium, 2009 IEEE International. 2009.

125. Y.C. Hu, Y.H.L., C.R. Kao, K.N. Tu,. J. Mater. Research, 2003, 18, 4.

126. Y.L. Lin, C.W. Chang, C.M. Tsai, C.W. Lee, C.R. Kao, J. Electron. Mater., 2006, 35(5), 1010.

127. J.H. Ke, T.L. Yang, Y.S. Lai, C.R. Kao, Acta Mater., 2011, 59(6), 2462.

128. M. Lu, D.-Y. Shih, P. Lauro, C. Goldsmith, D.W. Henderson, Appl. Phys. Lett., 2008, 92(21), 211909.

129. E.C.C. Yeh, W.J. Choi, K.N. Tu, P. Elenius, H. Balkan, Appl. Phys. Lett., 2002, 80(4), 580.

130. K.N. Chiang, C.C. Lee, C.C. Lee, K.M. Chen, Appl. Phys. Lett., 2006. 88(7), 072102.

131. S.H. Chiu, T.L. Shao, C. Chen, D.J. Yao, C.Y. Hsu, Appl. Phys. Lett., 2006, 88(2), 022110.

132. M.O. Alam, B.Y. Wu, Y.C. Chan, K.N. Tu, Acta Mater., 2006, 54(3), 613.

133. S. Ou, K.N. Tu, in Electronic Components and Technology Conference, 2005. Proceedings. 55th. 2005.

134. H. Gan, K.N. Tu, in Electronic Components and Technology Conference, 2002. Proceedings. 52nd. 2002.

135. Y.-M. Hung, C.-M. Chen, J. Electron. Mater., 2008, 37(6), 887.

136. C.-M. Chen, C.-C. Huang, J. Alloys Compd., 2008. 461(1-2), 235.

137. F. Guo, G. Xu, H. He, J. Mater. Sci., 2009, 44(20), 5595.

138. L. Ma, G. Xu. F. Guo, X. Wang, in Electronic Packaging Technology and High Density Packaging (ICEPT-HDP), 2011 12th International Conference on. 2011.

139. X., Wang, M. Han, L. Ma, G. Xu, F. Guo, in Electronic Packaging Technology and High Density Packaging (ICEPT-HDP), 2011 12th International Conference on. 2011.

140. Y. Liu, S. Irving, T. Luk, L. Liang, S. Wang, Microelectron. Reliab., 2008, 48(6), 811.

141. J.D. Wu, C.W. Lee, P.J. Zheng, J.C.B Lee, S. Li, in Electronic Components and Technology Conference, 2004. Proceedings. 54th. 2004.

142. T.Y. Lee, K.N. Tu, D.R. Frear, J. Appl. Phys., 2001, 90(9), 4502.

143. L. Xu, J.H.L. Pang, in Electronic Components and Technology Conference, 2006. Proceedings. 56th. 2006.

144. L. Xu, J.K. Han, J.J. Liang, K.N. Tu, Y.S. Lai, Appl. Phys. Lett., 2008, 92(26), 262104.

145. L. Xu, J.H.L. Pang, K.N. Tu, Appl. Phys. Lett., 2006, 89(22), 221909.

146. H. Gan, W.J. Choi, G. Xu, K.N. Tu, JOM, 2002, 54(6), 34.

147. T.C. Chiu, K.L. Lin, J. Mater. Research, 2008, 23, 9.

148. H.-J. Lin, J.-S. Lin, T.-H. Chuang, J. Alloys Compd., 2009. 487(1-2), 458.

149. H.-J. Lin, T.-H. Chuang, Mater. Lett., 2010, 64(4), 506.

150. T. Tian, K. Chen, A.A. Macdowell, D. Parkinson, Y.S. Lai, K.N. Tu, Scripta Mater., 2011, 65(7), 646.

151. L. Ma, F. Guo, G. Xu, X. Wang, H. He, H. Zhao, J. Electron. Mater., 2012, 41(2), 425.

152. A.T. Wu, A.M. Gusak, K.N. Tu, C.R. Kao, Appl. Phys. Lett., 2004, 85(13), 2490.

Chapter 4

1. H. Ma, J.C. Suhling, J. Mater. Sci., 2009, 44: 1141.

2. D.H. Kim, P. Elenuysm S, Barrett, IEEE Trans Electron. Packaging Manufacturing, 2002, 25, 84.

3. M.E. Loomans, M.E. Fine, Metall. Mater. Trans., 2000, 31A, 1155.

4. N. Chawla, Int. Mater. Rev., 2009, 54, 368.

5. F. Guo, M. Zhao, Z. Xia, Y. Ler, X. Li, Y. Shi, JOM, 2009, 61, 39.

6. C.M.L. Wu, D.Q. Yu, C.M.T. Law, L. Wang, Mater. Sci. Eng., 2004, 44, 1.

7 L. Zhang, S. Xue, L.-L, Gao, G. Zeng, Z. Sheng, Y. Chen, S.-L, Yu, J. Mater. Sci. Mater. Electron., 2009, 20, 685.

8. M.A. Dudek, N. Chawla, Metall. Mater. Trans., 2010, 41A, 610.

9. L.-L Gao, S.-B Xue, L. Zhang, Z. Sheng, G. Zeng, F. Ji, J. Mater. Sci. Mater. Electron., 2010, 21, 643.

10. L. Zhang, S.-B Xue, L.-L Gao, Y. Chen, S.-L. Yu, Z. Sheng, G. Zeng, J. Mater. Sci. Mater. Electron., 2009, 20, 1193.

11. Y. Shi, J. Tian, H. Hao, Z. Xia, Y. Lei, F. Guo, J. Alloys Compd., 2008, 454, 180

12. C.M.L. Wu Y.W. Wong, J. Mater. Sci. Mater. Electron., 2007, 80, 398.

13. C.M.L. Wu, J. Electron. Mater., (2002), 31, 921.

14. A. Ramirez, H. Mavoori, S. Jin, Appl. Phys. Lett., 2002, 80, 398.

15. Z. Chen, Y. Shi, Z. Xia, Y. Yan, J. Electron. Mater., 2003, 32, 235.

16. X.-Y Zhao, M.-Q. Zhao, X.-Q. Cui, T.-H. Xu, M.-X. Tong, Trans. Nonferrous Met. Soc. China, 2007, 17, 805.

17. D.Q. Yu, J. Zhao, L. Wang, J. Alloys Compd., 2004, 376, 170.

18. M.A. Dudek, R.S. Sidhu, N. Chawla, M. Renavikar, J. Electron. Mater., 2006, 35, 2088.

19. M.A. Dudek, R.S. Sidhu, N. Chawla, JOM, 2006, 58, 57.

20. T. Chuang, Scripta Mater., 2006, 55, 983.

21. M.A. Dudek, N. Chawla, Acta Mater., 2009, 57, 4588.

22. M.A. Dudek, N. Chawla, J. Electron. Mater., 2009, 38, 210.

23. M.A. Dudek, N. Chawla, Mater. Charac., 2006, 59, 1364.

24. F. Ochoa, X. Deng, N. Chawla, J. Electron.. Mater., 2004, 33, 1596.

25. X. Deng, G. Piotrowski, J.J. Williams, N. Chawla, J. Electron. Mater., 2003, 32, 1403.

26. N. Chawla, F. Ochoa, V.V. Ganesh, X. Deng, M. Koopman, K.K. Chawla, S. Scarritt, J. Mater. Sci. Mater. Electron. 2004, 15, 385.

27. X. Deng, R.S. Sidhu, P. Johnson, N. Chawla, Metall. Mater. Trans., 2005, 36A, 55.

28. M.A. Dudek, N. Chawla, Intermetall. 2010, 18, 1016.

29. M. Amagai, Microelectron. Reliab., 2002, 42, 607.

30. S. Fubin, S.W.R. Lee, In Electronic components and technology conference 2006 proceedings, 2006,1196.

31. K.E. Yazzie, H.E. Fei, H. Jiang, N. Chawla, Acta Mater., 2012, 60, 4336.

32. I. Anderson, J. Harringa, J. of Electron. Mater., 2006, 35(1), 94.

33. M. Amagai, Y. Toyoda, T. Ohnishi, S. Akita, In Electronic Components and Technology conference, 2004 Proceeding, 54th, 2004, 2, 1304.

34. F. Ochoa, X. Deng, N. Chawla, J. Electron. Mater., 2004, 33(12), 1596.

35. X. Deng, R.S. Sindu, P. Johnson, N. Chawla, Metall. Mater. Trans. A, 2005, 36(1), 55.

36. D. Ma, W.D. Wang, S.K. Lahiri, J. Appl. Phys., 2002, 91, 3312.

37. K.E. Yazzie, H.X. Xie, J. Williams, N. Chawla, Scripta Mater., 2012, 66, 586.

38. Y.-L. Shen, N. Chawla, E. S. Ege, X. Deng, Acta Mater. 2005, 53, 2633.

39. W. H. Moy, Y.-L. Shen, Microelectron. Reliab. 2007, 47, 1300.

40. Y.-L. Shen, K. Aluru, Microelectron. Reliab. 2010, 50, 2059.

41. Abaqus 6.8, User's Manual, Dassault Systèmes Simulia Corp., Providence, RI.

42. H.X. Xie, N. Chawla, Y.-L. Shen, Microelectron. Reliab., 2011, 51, 1142.

43. N. Chawla, Y.-L. Shen, X. Deng, E.S. Ege, J. Electron. Mater. 33(12), 1589.

44. Y.-L. Shen, N. Chawla, E.S. Ege, X. Deng, Acta Mater., 53(9), 2633.

Chapter 5

1. H. Ma, J. Suhling, J. Mater. Sci., 2009, 44, 1141.

2. S. Kang, A. Sarkhel, J. Electron. Mater., 1994, 23, 701.

3. S. Wiese, K.J. Wolter, Microelectron. Reliab., 2004, 44, 1923.

4. S. Kang, IBM J. Res. Dev., 2005, 49, 607.

5. N. Chawla, Int. Mater. Rev., 2009, 54, 368.

6. I. E. Anderson, J. Mater. Sci.: Mater. Electron., 2007, 18, 55.

7. N.C. Lee, Mater.Adv. Packaging, 2009 p. 181.

8. M. Dudek, R.S. Sidhu, N. Chawla, M. Renavikar, J. of Electron. Mater., 2006, 35 2088.

9. M. Dudek, R. Sidhu, N. Chawla, JOM, 2006, 58, 57.

10. M. Dudek, N. Chawla, Metall. Mater. Trans. A, 2010, 41, 610.

11. M. Dudek, N. Chawla, J. of Electron. Mater., 2009, 38, 210.

12. Y. Shi, J. Tian, H. Hao, Z. Xia, Y. Lei, F. Guo, J. Alloys Compd., 2008, 453, 180.

13. L. Gao, S. Xue, L. Zhang, Z. Sheng, G. Zeng, F. Ji, J. Mater. Sci.: Mater. Electron., 2010, 21, 643.

14. C.M.L. Wu, D.Q. Yu, C.M.T. Law, L. Wang, Mater. Sci. Eng.: R, 2004, 44 1.

15. D.Q. Yu,, J. Zhao, L. Wang, J. of Alloys Compd.,2004, 376170.

16. T.-H. Chuang, Scripta Mater., 2006, 55, 983.

17. T.-H. Chuang, Metall. Mater. Trans. A, 2007, 38, 1048.

18. C.-Y. Lee, K.-L. Lin, Thin Solid Films, 1994, 249, 201.

19. A.J.G. Strandjord, S. Popelar, C. Jauernig, Microelectron. Reliab., 2002, 42, 265.

20. K. Zeng,, V. Vuorinen, J.K. Kivilahti. Electronic Components and Technology Conference, Proceedings, 2001.

21. A. Sharif, Y.C. Chan, M.N. Islam, M.J. Rizvi, J. Alloys Compd., 2005, 388, 75.

22. Y.-D. Jeon, S. Nieland, A. Ostmann, H. Reichi, K.-W Paik, et al., J. Electron. Mater., 2003, 32, 548.

23. C.M.T. Law, C.M.L. Wu, Proceeding of the Sixth IEEE CPMT Conference. 2004.

24. F. Ochoa,, X. Deng, N. Chawla, J. Electron. Mater., 2004, 33, 1596.

25. X. Deng, G. Piotrowski, J.J. Williams, N. Chawla, J. Electron. Mater. 2003, 32, 1403.

26. H.X. Xie, L. Jiang, N. Chawla, Unpublished research, 2012.

27. K.E. Yazzie, H.X. Xie, N. Chawla, Scripta Mater., 2012, 66, 586.

28. H.X. Xie, N. Chawla, unpublished research, 2012.

29. C. Wu, Y. Wong, J. Mater. Sci.: Mater. Electron., 2007, 18, 77.

30. L. Zhang, S. Xue, G. Zeng, L. Gao, Y. Huan, J. Alloys Compd., 2012, 510, 38.

31. B. Lu, H. Li, J. Wang, H. Zhu, X. Jiao, J. Central South University of Technology, 2008, 15, 313.

32. H. Hao, Y. Shi, Z. Xia, Y. Lei, F. Guo, J. of Electron. Mater., 2008, 37, 2.

33. A. Kumar, M. He, Z. Chen, Surface and Coatings Technology, 2005. 198(1-3), 283.

34. P. Sun, C. Anderson, X. Wei, Z. Cheng, D. Shangguan, J. Liu, J. Alloys Compd., 2006, 425(1-2), 191.

35. A. Kumar, M. He, Z. Chen, Surf. Coat. Technol., 2005, 198 283.

36. D.Q. Yu, C.M.L Wu, D.P. He, N. Zhao, L. Wang, J.K.L. Lai, J. Mater. Res., 2005, 20, 8.

37. H.X. Xie, N. Chawla, Y.-L Shen, Microelectron. Reliab., 2011, 51, 5.

38. M. Dudek, N. Chawla, Intermetallics, 2010, 18, 1016.

39. I. Dutta, P. Kumar, G. Subbarayan, JOM, 2009, 61, 29.

40. O. Shengquan, Y. Xu, K.N. Tu, M.O. Alam, Y.C. Chan, Electronic Components and Technology Conference, Proceedings. 2005.

41. X. Deng, R. Sidhu, P. Johnson, N. Chawla, Metall. Mater. Trans. A, 2005, 36, 55.

Chapter 6

1. E.P. Wood, K.L. Nimmo, J. Electron. Mater., 1994, 23(8), 709.

2. M. Abtew, G. Selvaduray, Mater. Sci. Eng., 2000, 20(5-6), 95.

3. N.-C. Lee, Soldering Surf. Mount Technol., 1997, 9(2), 65.

4 H. Ma, J. C. Suhling, J. Mater. Sci., 2009, 44(5), 1141.

5. N. Chawla, Int. Mater. Rev., 2009, 54, 368.

6. N.-C. Lee, International Microsystems, Packaging, Assembly and Circuits Technology (IMPACT) conference, (2007), Oct, 44.

7. I.E. Anderson: J. Mater. Sci., Mater. Electron., 2007, 18, 55.

8. M. Dittes, H. Walter, Soldering Surf. Mount. Technol., 2003, 15(1), 77.

9. C.M.L. Wu, Y.W. Wong, J. Mater. Sci. Mater. Electron., 2007, 18(1), 77.

10. C.M.L. Wu, D.Q. Yu, C.M.T. Law, L. Wang, J. Electron. Mater., 2002, 31, 921.

11. A. Ramirez, H. Mavoori, S. Jin, Appl. Phys. Lett., 2002, 80 (3), 398.

12. Y. Shi, J. Tian, H. Hao, Z. Xia, Y. Lei, F. Guo, J. Alloys Compd., 2008, 453(1-2), 180.

13. L. Zhang, S.-B. Xue, L.-L. Gao, Y. Chen, S.-L. Yu, Z. Sheng, G. Zeng, J. Mater. Sci. Mater. Electron., 2009, 20, 1193-9.

14. L.-L Gao, S.-B Xue, L. Zhang, Z.-X, Xiao, W. Dai, F. Ji, H. Ye, G. Zeng: J. Mater. Sci. Mater. Electron., 2010, 21(9), 910.

15. L.-L Gao, S.-B Xue, L. Zhang, Z. Sheng, G. Zeng, F. Ji, J. Mater. Sci. Mater. Electron., 2010, 21(7), 643.

16. Z. Chen, Y. Shi, Z. Xia, Y. Yan, J. Electron. Mater., 2003, 32(4), 235.

17. X.-Y. Zhao, M.-Q. Zhao, X.-Q. Cui, T.-H. Xu, M.-X. Tong, Trans. Nonferrous Met. Soc. China, 2007, 17(4), 805.

18. D.Q. Yu, J. Zhao, L. Wang, J. Alloys Compd., 2004, 376(1-2), 170.

19. M.A. Dudek, R.S. Sidhu, N. Chawla, M. Renavikar: J. Electron. Mater., 2006, 35(12), 2088.

20. M.A. Dudek, N. Chawla, Metall. Mater. Trans. A, 2010, 41(3), 610.

21. M.A. Dudek, R.S. Sidhu, N. Chawla, JOM, 2006, 58(6), 57.

22. H.X. Xie, N. Chawla, K. Mirpuri, J. Electron. Mater., 2012, online first.

23. M.A. Dudek, N. Chawla, Acta. Mater., 2009, 57, 4588.

24. M.A. Dudek, N. Chawla, J. Electron. Mater., 2009, 38(2), 210.

25. Z. Chen, Y. Shi, Z. Xia, Y. Yan, J. Electron. Mater., 2003, 32(4), 235.

26. L. Wang, D.Q. Yu, J. Zhao, M.L. Huang, Mater. Lett., 2002. 56(6), 1039.

27. A.O. Aggarwal, P.M. Raj, V.S.D. Ravi, S. Koh, R. Mukkapudi, R.R. Tummala, in Electronic Components and Technology Conference, 2005. Proceedings. 55th. 2005.

28. M. Mueller, S. Wiese, M. Roellig, K.-J. Wolter, in Electronic Components and Technology Conference, 2007. ECTC '07. Proceedings. 57th. 2007.

29. Z. Huang, P.P. Conway, E. Jung, R.C. Thomson, C. Liu, T. Loeher, M. Minkus, J. Electron. Mater., 2006.,35(9),1761.

30. M. Islam, A. Sharif, Y. Chan, J. Electron. Mater., 2005. 34(2), 143.

31. Karl J. Puttlitz, K.A.S., Marcel, Dekker, Handbook of lead-free solder technology for microelectronic assemblies. 2004, CRC Press, 349.

32. Wang L. D.Q. Yu, J. Zhao, M.L. Huang, Mater. Lett., 2002, 56(6), 1039.

33. H. Hao, J. Tian, Y.W. Shi, Y.P. Lei, Z.D. Xia, JEM, 2007, 36(7), 766.

34. I.E. Anderson, J. Mater. Sci.: Mater. Electron., 2007, 18, 55.

35. L-W. Lin, J-M. Song, Y-S. Lai, Y.-T. Chiu, N.-C. Lee, J-Y. Uan, Microelectron. Relib., 2009, 49, 235.

36. M.G. Cho, S.K. Kang, S-K. Seo, D-Y. Shih, H.M. Lee: J. Mater. Research, 2009, 24(2), 534.

37. S.K. Kang, D.-Y. Shih, D. Leonard, D.W. Henderson, T. Gosselin, S-I. Cho, J. Yu, W.K. Choi, JOM, 2004, 56(6), 34.

38. K.S. Kim, S.H. Huh, K. Suganuma, J. Alloys Compd., 2003. 352(1-2), 226.

39. D.Q. Yu, L. Wang, J. Alloys Compd., 2008. 458(1-2), 542.

40. M. Muller, S. Wiese, K.J. Wolter, in Electronics Systemintegration Technology Conference, 2006. 1st. 2006.

Chapter 7

1. N. Chawla, Inter. Mater. Reviews, 2009, 54(6), 368.

2 H. Ma, J. Suhling, J. Mater. Sci., 2009, 44(5), 1141.

3. S. Kang, A. Sarkhel, J. Electron. Mater., 1994, 23(8), 701.

4. D.A. Shnawah, M.F.M. Sabri, I.A. Badruddin, Microelectron. Reliab., 2012, 52(1), 9.

5. H. Lu, H. Balkan, K. Simon, JOM, 2005, 57(6), 30.

6. K.S. Kim, S.H. Huh, K. Suganuma, J. Alloys Compd., 2003, 352(1-2), 226.

7. D.H. Kim, P. Elenius, S. Barrett, IEEE Trans. Electron. Packaging Manufacturing, 2002, 25, 84.

8. M.E. Loomans, M.E. Fine, Metall. Mater. Trans. A, 2000, 31A, 1155.

9. C.M.L. Wu, D.Q. Yu, C.M.T. Law, L. Wang, Mater. Sci. Eng.: R: Reports, 2004, 44(1), 1.

10. F. Guo, M. Zhao, Z. Xia, Y. Lei, X. Li, X. Li, Y. Shi, JOM, 2009, 61(6), 39.

11. L. Zhang, S.-B. Xue, L.-L. Gao, G. Zeng, Z. Sheng, Y. Chen, S.-L Yu, J. Mater. Sci. Mater. Electron., 2009, 20(8), 685.

12. J. Shen, C. Wu, S. Li, J. Mater. Sci. Mater. Electron., 2012, 23(1), 156.

13. L. Gao, S. Xue, L. Zhang, Z. Sheng, G. Zeng, F. Ji, J. Mater. Sci. Mater. Electron., 2010, 21(7), 643.

14. L. Zhang, S. Xue, Y. Chen, Z. Han, J. Wang, S. Yu, F. Lu, J. Rare Earths, 2009, 27(1), 138.

15 Y. Shi, J. Tian, H. Hao, Z. Xia, Y. Lei, F. Guo, J. Alloys Compd., 2008, 453(1-2), 180.

16. H. Hao, J. Tian, Y.W. Shi, Y.P. Lei, Z.D. Xia, J. Electron. Mater., 2007, 36(7), 766.

17. M. Pei, J. Qu, Proc. 57th Electron. Comp. Technol. Conf., 2007, 198.

18. D.Q. Yu, J. Zhao, L. Wang, J. Alloys Compd., 2004, 376(1-2), 170.

19. B. Li, Y. Shi, Y. Lei, F. Guo, Z. Xia, B. Zong, J. Electron. Mater., 2005, 34(3), 217.

20. C. Wu, Y. Wong, J. Mater. Sci. Mater. Electron., 2007, 18(1), 77.

21. A.G. Ramirez, H. Mavoori, S. Jin, Appl. Phys. Lett., 2002, 80(3), 398.

22. H. He, G. Xu, F. Guo, J. Mater. Sci., 2009, 44(8), 2089.

23. Z. Chen, Y. Shi, Z. Xia, Y. Yan, J. Electron. Mater., 2003, 32(4), 235.

24. X.-Y. Zhao, M.-Q. Zhao, X.-Q. Cui, M.-X Tong, Trans. Nonferrous Metals Society of China, 2007, 17(4), 805.

25. M.A. Dudek, R.S. Sidhu, N. Chawla, JOM, 2006, 58(6), 57.

26. M.A. Dudek, R.S. Sidhu, N. Chawla, N. Renavikar, J. Electron. Mater., 2006, 35, 2088.

27. M.A. Dudek, N. Chawla, Metall. Mater. Trans. A, 2010, 41(3), 610.

28. M.A. Dudek, N. Chawla, J. Electron. Mater., 2009, 38(2), 210.

29. H.X. Xie, N. Chawla, K. Mirpuri, J. Electron. Mater., 2012, online first.

30. A. Schubert, H. Walter, R. Dudek, B. Michel, G. Lefranc, J. Otto, G. Mitic, Proc. Int. Symp. on Advanced Packaging Materials Processes, Properties and Interfaces, 129.

31. K.C. Ong, V.B. Tan, C.T. Lim, E.H. Wong, X.W. Zhang, in: Proceedings of the 54th IEEE Electronic Components and Technology Conference, 2004, Vol. 1, 1075.

32. D. Reiff, E. Bradley, in: Proceedings of the 55th IEEE Electronic Components and Technology Conference 2005, Vol. 2, 1519.

33. J.-M. Kim, S.-W. Woo, Y.-S. Chang, Y.-J. Kim, J.-B. Choi and K.-Y. Ji, Thin Solid Films, 2009, 517, 4255.

34. K.E. Yazzie, H.X. Xie, J. Williams, N. Chawla, Scripta Mater., 2012, 66, 586.

35. K.E. Yazzie, H.E. Fei, H. Jiang, N. Chawla, Acta Mater., 2012, 60, 4336.

36. M.A. Dudek, N. Chawla, Mater. Charact., 2008, 59, 1364.

37. H.X. Xie, N. Chawla, Y.-L Shen, Microelectron. Reliab., 2011, 51, 1142.

38. Y.-L. Shen, Constrained deformation of materials. New York: Springer, 2010.

39. S.M. Hayes, N. Chawla, D.R. Frear, Microelectron. Reliab., 2009, 49, 269.

40. H.F. Zhou, Z.F. Zhang, J. Mater. Res., 2008, 23, 1614.

41. P. Kumar, Z. Huang, I. Dutta, R. Sidhu, M. Renavikar, R. Mahajan, J. Electron. Mater., 2012, 41, 412.

Chapter 8

1. N. Chawla, Int. Mater. Rev., 2009, 54, 368.

2. N.C. Lee, D. Lu, C.P. Wong, Mater. Adv. Packag., 2009, 181.

3. I.E. Anderson, J. Mater. Sci. Mater. Electron., 2007, 18(1-3), 55.

4. M.A. Dudek, N. Chawla, Metall. Mater. Trans. A, 2010, 41(3), 610

5. M.A. Dudek, R.S. Sidhu, N. Chawla, JOM, 2006, 58(6): 57.

6. M.A. Dudek, R.S. Sidhu, N. Chawla and N. Renavikar, J. Electron. Mater., 2002, 31, 1122.

7. M.A. Dudek, N. Chawla, J. Electron. Mater., 2009, 38(2), 210.

8. H.X. Xie, N. Chawla, K. Mirpuri, J. Electron. Mater., online first.

9. K.N. Tu, J. Appl. Phys., 2003, 94(9), 5451.

10. T.Y. Lee, K.N. Tu, D.R. Frear, J. Appl. Phys., 2001, 90(9), 4502.

11. H.-J. Lin, J.-S. Lin, T.-H, Chuang, J. Alloys Compd., 2009, 487(1-2), 506.

12. H.-J. Lin, T.-H Chuang, Mater. Lett., 2010, 64(4), 506.

13. H. He, G. Xu, F. Guo, J. Mater. Sci., 2009, 44(8), 2089.

14. L. Jiang, N. Chawla, M. Pacheco, V. Noveski, Mater. Charact., 2011, 62(10), 970.

15. M.A. Dudek, L. Hunter, S. Kranz, J.J. Williams, S.H. Lau, N. Chawla, Mater. Charact., 2010, 61(4), 433.

16. T. Tian, K. Chen, A.A. MacDowell, D. Parkinson, Y.-S. Lai, K.N. Tu, Scripta Mater., 2011, 65(7), 646.

17. F. Ren, J.W. Nah, J.O. Suh, K.N. Tu, B.S. Xiong, L.H. Xu, J.H.L. Pang, Mater. Res. Symp. Proc., Warrendale, PA, 2005, 863, B10.2.

18. M. Lu, D.-Y. Shih, P. Lauro, C. Goldsmith, D.W. Henderson, Appl. Phys. Lett., 2008, 92(21), 211909.

19. Z. Chen, Y. Shi, Z. Xia, Y. Yan, J. Electron. Mater., 2003, 32(4), 235.

20. M. Yunus, K. Srihari, J.M. Pitarresi, A. Primavera, Microelectron. Reliab., 2003, 43(12), 2077.

21. Z. Tang, F.G. Shi, Microelectron. J., 2001, 32(7), 605.

22. J.D.J. Ingle, Spectrochemical analysis, 1988, New Jersey, Prentic Hall.

23. W.A. Barrett, E.N. Mortensen, Med. Image Anal., 1997, 1(4), 331.

24. E.C.C. Yeh, W.J. Choi, K.N. Tu, P. Elenius, H. Balkan, Appl. Phys. Lett., 2002, 80(4), 580.

25. S.W. Liang, Y.W. Chang, T.L. Shao, C. Chen, K.N. Tu, Appl. Phys. Lett., 2002, 80(4), 580.

26. M. Lu, D.-Y, Shih, C. Goldsmith, T. Wassick, in Reliability Physics Symposium, 2009 IEEE International. 2009, 149.

27. J.H. Ke, T.L. Yang, Y.S. Lai, C.R. Kao, Acta Mater., 2011, 59(6), 2462.

28. T.Y. Lee, K.N. Tu, D.R. Frear, J. Appl. Phys., 2001, 90(9), 4502.

29. A.T. Wu, K.N. Tu, J.R. Lloyd, N. Tamura, B.C. Valek, C.R. Kao, Appl. Phys. Lett., 2004, 85(13), 2490.

30. A.T. Wu, A.M. Gusak, K.N. Tu, C.R. Kao, Appl. Phys. Lett., 2005, 86(24), 241902-4.

31. K. Lee, K.S. Kim, K. Suganuma, J. Mater. Res., 2011, 26(20), 2624.

32. L. Xu, J.-K, Han, J.J. Liang, K.N. Tu, Y.-S. Lai, Appl. Phys. Lett., 2008, 92(26), 262104.

33. Y.-M. Hung, C.-M. Chen, J. Electron. Mater., 2008, 37(6), 887.

34. H.X. Xie, N. Chawla, Y.-L Shen, Microelectron. Reliab., 2011, 51, 1142.

35. J.-W. Nah, J.O. Suh, K.N. Tu, S.W. Yoon, V.S. Rao, V. Kripesh, F. Hua, J. Appl. Phys., 100(12), 123513.

36. L. Xu, J.H.L. Pang, K.N. Tu, Appl. Phys. Lett., 2006, 89(22), 221909.

37. Q.T. Huynh, C.Y. Liu, C. Chen, K.N. Tu, J. Appl. Lett., 2001, 89, 4332.

38. H.B. Huntington, A.R. Grone, J. Phys. Chem. Solids, 1961, 20(1-2), 76.

39. Y.-C. Hsu, C.-K. Chou, P.C. Liu, C. Chen, D.J. Yao, T. Chou, K.N. Tu, J. Appl. Phys., 98(3), 033523.

40. K.E. Yazzie, J.J. Williams, N.C. Phillips, F. De Carlo, N. Chawla, Mater. Charact., 2012, 70, 33.

Chapter 9

1. N. Chawla, Int. Mater. Rev., 2009, 54, 368

2. F. Guo, M. Zhao, Z. Xia, Y. Lei, X. Li, Y. Shi, JOM, 2009, 61(6), 39.

3. C.M.L. Wu, D.Q. Yu, C.M.T. Law, L. Wang, Mater. Sci. Eng. R-Reports, 2004, 44(1), 1.

4. L. Zhang, S.-B. Xue, L.-L Gao, G. Zeng, Z. Sheng, Y. Chen, S.L. Yu, J. Mater. Sci. Mater. Electron., 2009, 20(8), 685.

5. M.A. Dudek, N. Chawla, Metall. Mater. Trans. A, 2010, 41(3), 610.

6. J. Shen, C. Wu, S. Li, J. Mater. Sci. Mater. Electron., 2012. 23(1), 156.

7. L.-L Gao, S.-B Xue, L. Zhang, Z.-X Xiao, W. Dai, F. Ji, H. Ye, G. Zeng, J. Mater. Sci. Mater. Electron., 2010, 21(7), 643.

8. H. Hao, J. Tian, Y.W. Shi, Y.P. Lei, Z.D. Xia, J. Electron. Mater., 2007, 36(7), 766.

9. D.Q. Yu, J. Zhao, L. Wang, J. Alloy. Compd., 2004, 376(1-2), 170-175

10. B. Li, Y. Shi, Y. Lei, F. Guo, Z. Xia, B. Zong, J. Electron. Mater., 2005, 34(3), 217.

11. M. Dittes, H. Walter, Solder. Surf. Mt. Tech., 2003. 15(1), 50.

12. C. Wu, Y. Wong, J. Mater. Sci.: Materials in Electronics, 2007, 18(1): 77.

13. M.A. Dudek, R.S. Sidhu, N. Chawla, JOM, 2006, 58(6), 57.

14. A.G. Ramirez, H. Mavoori, S. Jin, Appl. Phys. Lett., 2002, 80(3), 398.

15. D.Q. Yu, C.M.L. Wu, Y.W. Wong, J. Mater. Sci. Mater. Electron., 2007, 18, 1057.

16. H. He, G. Xu, F. Guo, J. Mater. Sci., 2009, 44(8), 2089.

17. M.A. Dudek, N. Chawla, J. Electron. Mater., 2009, 38(2), 210.

18. H.X. Xie, N. Chawla, K. Mirpuri, J. Electron. Mater., 2012, online first.

19. L. Zhang, J.-G. Han, Y.-H Guo, C.-W. He, Sci. Tech. Weld. Join., 2012, 17(5), 424.

20. C.M.L. Wu, D.Q. Yu, C.M.T. Law, L.J. Wang, Mater. Res., 2002, 17, 3146.

21. L. Wang, D.Q. Wu, J. Zhao, M.L. Huang, Mater. Lett., 2002, 56, 1039.

22. M.A. Dudek, R.S. Sidhu, N. Chawla, N. Renavikar, J. Electron. Mater., 2006, 35, 2088.

23. H.X. Xie, N. Chawla, Y.-L Shen, Microelectron. Reliab., 2011, 51, 1142.

24. Z.G. Chen, Y.W. Shi, Z.D. Xia, Y.F. Yan, J. Electron Mater., 2002, 31, 1122.

25. Y. Shi, J. Tian, H. Hao, Z. Xia, Y. Lei, F. Guo, J. Alloys Compd. 2008, 453, 180.

26. L.-W. Lin, J.M. Song, Y.-S. Lai, Y.-T. Choi, N.-C. Lee, J.-Y. Uan, Microelectron. Reliab., 2009, 49, 235.

27. Z. Yang, D. Shi, B. Wen, R. Melnik, S. Yao, T. Li, J. Solid State Chem., 2010, 183(1), 136.

28. H. Okamoto, J. Phase Equilib. Diff., 2001, 22(5), 589.

29. Fischer-Cripps AC. Nanoindentation. 2nd ed. New York: Springer, 2004.

30. J.L. Hay, G.M.Pharr, Instrumented indentation testing. In: H. Kuhn, D. Medlin editors, ASM handbook, Materials Park, OH, ASM International, 2001, 232.

31. F. Ochoa, X. Deng, N. Chawla, J. Electron. Mater., 2004, 33(12), 1596.

32. N. Chawla, F. Ochoa, V.V. Ganesh, X. Deng, M. Koopman, K.K. Chawla, S. Scarriitt, J. Mater. Sci. Mater. Electron. 2004, 15, 385.

33. X. Deng, G. Piotrowski, J.J. Williams, N. Chawla, J. Electron. Mater., 2003, 32, 1403.

34. H. Okamoto, J. Phase Equilib., 1999, 20(5), 542.

35. X. Deng, R.S. Sidhu, P. Johnson, N. Chawla, Metall. Mater. Trans. A, 2005, 36A, 55.

36. P.G. Harris, K.S. Chaggar, Solder. Surf. Mt. Tech., 1998, 10(3), 38.

37. P.-F. Yang, Y.-S. Lai, S.-R. Jian, J. Chen, 8th International Conference on Electronic Packaging Technology, Shanghai, August, 2007, 1.

38. W.C. Oliver, G.M. Pharr, J. Mater. RES., 1992, 7, 1564.

39. X. Deng, M. Koopman, N. Chawla, K.K. Chawla, Mater. Sci. Eng. A, 2004, 364, 240.

40. M.A. Dudek, N. Chawla, Intermetallics, 2010, 18, 1016.

41. M.A. Dudek, N. Chawla, Acta Mater., 2009, 57, 4588.